Mechanisms of Action of Ribosome-Binding Antimicrobial Peptides

BY

TANJA FLORIN
B. Eng., University of Applied Sciences Jena, Germany 2011
M.S., University of Potsdam, Germany 2015

THESIS

Submitted as a partial fulfillment of the requirements
for the degree of Doctor of Philosophy in Pharmacognosy
in the Graduate College of the
University of Illinois at Chicago, 2019

Chicago, Illinois

Defense Committee:

Dr. Alexander Mankin, Chair and Advisor
Dr. Nora Vázquez-Laslop, Co-Advisor
Dr. Michael Federle
Dr. Terry Moore
Dr. Yury Polikanov, Biological Sciences
Dr. Don Morrison, Biological Sciences

CONTRIBUTIONS OF AUTHORS

Chapter 1 is an overview of the thesis contents.

Chapter 2 is a published manuscript. Pantel, L., Florin, T., Dobosz-Bartoszek, M., Racine, E., Sarciaux, M., Serri, M., Houard, J., Campagne, J.-M., Figueiredo, R., Midrier, C., Gaudriault, S., Givaudan, A., Lanois, A., Forst, S., Aumelas, A., Cotteaux-Lautard, C., Bolla, J.-M., Lundberg, C., Huseby, D., Hughes, D., Villain-Guillot, P., Mankin, A., Polikanov, Y., and Gualtieri, M. (2018) Odilorhabdins, Antibacterial Agents that Cause Miscoding by Binding at a New Ribosomal Site, *Mol Cell 70*, 83–94.e7. J.H. isolated and purified natural ODLs; A.A. performed and analyzed the NMR experiments; M.G. performed and analyzed the MS experiments; S.G. and A.G. identified the putative biosynthetic gene cluster. S.F. and A.L. constructed *X. nematophila* mutant strains. E.R., P.V.-G., and M.S. designed and synthesized NOSO-95179 and analogs. J.-M.C. and R.M.de F. determined the stereochemistry of the chiral centers of ODLs. L.P., C.L. and J.-M.B. evaluated bioactivity; D.H. and D.H. selected and sequenced resistant mutants; M.G., M.S. and L.P. designed and performed determination of mutant frequency, hemolytic activity and cell-free transcription-translation assay. C.V.L. evaluated *in vivo* efficacy, M.D.B and Y.S.P. designed and performed X-ray crystallography experiments; T.F. and A.S.M. designed *in vitro* biochemistry experiments, analyzed mode of action and *in vivo* activity of the inhibitors. All authors interpreted the results. M.G., Y.S.P., and A.S.M. wrote the manuscript.

Chapter 3 is a published manuscript. Gagnon, M. G., Roy, R. N., Lomakin, I. B., Florin, T., Mankin, A. S., and Steitz, T. A. (2016) Structures of proline-rich peptides bound to the ribosome reveal a common mechanism of protein synthesis inhibition., *Nucleic Acids Res. 44*, 2439–50. T.A.S lab (M.G.G., R.N.R., I.B.L., T.A.S.) carried out the structural studies, A.S.M lab (T.F., A.S.M.) carried out biochemical, microbiological and genetic experiments. M.G.G., R.N.R., I.B.L. and T.F. designed and performed experiments, analyzed data and wrote the manuscript; A.S.M. and T.A.S. analyzed data, wrote the manuscript and oversaw the project.

Chapter 4 is a published manuscript. Florin, T., Maracci, C., Graf, M., Karki, P., Klepacki, D., Berninghausen, O., Beckmann, R., Vázquez-Laslop, N., Wilson, D. N., Rodnina, M. V., and Mankin, A. S. (2017) An antimicrobial peptide that inhibits translation by trapping release factors on the ribosome., *Nat. Struct. Mol. Biol. 24*, 752–757. A.S.M./N.V.-L. lab (T.F**.**, D. K., N.V.-L, A.S.M.) carried out biochemical, microbiological and genetic experiments, M.V.R. lab (C.M, P.K., M.V.R.) performed kinetic analysis, D.N.W. lab (M.G., O.B., R.B., D.N.W.) carried out structural studies. N.V-L., A.S.M., M.V.R. and D.W. designed the study and oversaw the experiments. T.F**.**, C.M. and M.G. designed and performed the experiments, and analyzed the data. P.K. and D.K. performed the experiments. N.V-L., A.S.M., M.V.R., D.N.W., T.F**.**, C.M. and M.G. wrote the paper.

Chapter 5 is a preliminary manuscript about ongoing work in the Mankin/Vázquez-Laslop laboratory. D. Klepacki and T. Florin performed the experiments, T.F. designed the experiments, K. Mangano and T.F. analyzed the data. Vázquez-Laslop, N. and Mankin, A. S. designed the study and oversaw the experiments. T.F., N.V-L., A.S.M. wrote the manuscript.

Chapter 6 presents the overarching conclusions and future directions in the field.

TABLE OF CONTENTS

LIST OF TABLES

LIST OF FIGURES

LIST OF FIGURES (continued)

LIST OF FIGURES (continued)

LIST OF ABBREVIATIONS

Å	Angstrom
AMP	Antimicrobial peptide
Api	Apidaecin
ATP	Adenosine triphosphate
Bac	Bactenecin
bp	Base pair
CMCT	1-Cyclohexyl-(2-Morpholinoethyl)Carbodiimide metho-p-Toluene sulfonate
CRE	Carbapenem-resistant *Enterobacteriaceae*
cryo-EM	Cryo-electron microscopy
Da	Dalton
Dab(bOH)	αγ–diamino β–hydroxy butyric acid
Dbt	αδ–diamino butane
Dha	αβ–dehydro arginine
Dhl	δ–hydroxy lysine
DMS	Dimethylsulfate
EF	Elongation factor
IC_{50}	Half maximal inhibitory concentration
IF	Initiation factor
IGR	Intergenic region
LC-MS	Liquid chromatography / Mass spectrometry
MIC	Minimal inhibitory concentration
mRNA	Messenger RNA
NMR	Nuclear magnetic resonance
NRPS	Non-ribosomal peptide synthase
nt	Nucleotide
ODL	Odilorhabdin
Onc	Oncocin
PKS	Polyketide synthase
PostHC	Post hydrolysis complex
PrAMP	Proline-rich antimicrobial peptide
PreHC	Pre-hydrolysis complex
PTC	Peptidyl transferase center
RF	Release factor
RNA	Ribonucleic acid
Rpm	Reads per million
rRNA	Ribosomal RNA
RS	Aminoacyl-tRNA synthase
s_{in}	Initiation score
s_{rt}	Readthrough score
s_{term}	Termination score
tRNA	Transfer RNA
UTR	Untranslated region

1. INTRODUCTION

1.1 Antimicrobial peptides & Antibiotic resistance threat

1.1.1 An urgent need for new antimicrobials

Today, 90 years after the discovery of penicillin by Alexander Fleming, we are still facing a threat of infectious diseases. Formerly very effective antibiotics have been misused and overused, putting an enormous selective pressure on pathogenic bacteria that respond by evolving diverse antibiotic resistance traits. To make things worse, resistance mechanisms that emerge against one antibacterial agent often cripple the action of an entire class of antibiotics. The World Health Organization (WHO) has recently published a highest priority list of bacterial pathogens for which we are in urgent need of new antibiotics, which includes carbapenem-resistant gram-negative *Acinetobacter baumannii*, *Pseudomonas aeruginosa* and *Enterobacteriaceae* such as *Klebsiella pneumonia* and *Escherichia coli* (World Health Organization 2017).

Multiple strategies are being implemented to respond to the pressing demand for effective antibiotics. One approach is the revitalization of known antibiotics by using them in combinatorial therapy. Another strategy, favored by our research group, focuses on re-investigating mechanistic details of the action of classic and newer antibiotics to use this knowledge to rationally design better derivatives. Meanwhile, other research groups are screening large chemical libraries in hope to find novel structural scaffolds to use them as templates for the development of new drugs. Other platforms aim to discover natural antimicrobials produced by, for example, organisms adapted to understudied environments or participating in unusual symbiotic relationships (Wright 2017).

The projects that we present here focus on antibiotic candidates that derived from the latter approach, the search for natural products from unique environments. In chapter two, we describe an antibacterial produced by the bacterium *Xenorhabdus nematophila* which lives in a rather unusual ecological niche: a symbiotic relationship with soil-dwelling nematodes. To thrive as the

symbiotic partner of the worm, *Xenorhabdus* species produce a large variety of specialized metabolites (Tobias et al. 2017), among those the subject of our study, the new class of antimicrobial peptides named odilorhabdins. Chapters three and four are dedicated to our discoveries with proline-rich antimicrobial peptides (PrAMPs), which are products of the immune defense systems of different insects, crustaceans and mammals. That odilorhabdins and PrAMPs possess great potential to fight pathogens in the clinic is demonstrated by the studies showing that theses antimicrobial peptides are effective inhibitors in a mouse model of systemic infections of carbapenem-resistant *K. pneumoniae* and *E. coli* (Ostorhazi et al. 2014; Pantel et al. 2018).

1.1.2 Antimicrobial peptides as strong candidates to fight antibiotic resistance

Among promising candidates for new antibiotics are antimicrobial peptides (AMPs). AMPs are natural compounds found in all organisms, who produce them as effective weapons to fight bacterial infections. Even though AMPs are considered evolutionarily ancient weapons, we are only at the beginning of understanding their extreme diversity, their wide spectrum of mechanisms of action, and their full potential as therapeutics (Zasloff 2002; Fox 2013).

In general, AMPs which are produced as part of the immune system are referred to as host defense peptides, whereas non-ribosomally produced peptides are called peptide antibiotics. However, because peptide antibiotics have the ability to stop bacterial growth, we have included them in this thesis in the group of antimicrobial peptides (**Table 1.1**).

1.1.3 Structures and compositions of antimicrobial peptides

Antimicrobial peptides, being natural compounds, have already been subjected to evolutionary selection to inhibit bacterial cell growth efficiently without harming the producer. Because the producing organisms belong to all kingdoms of life it is not surprising that AMPs display a wide variety of structures, differing not only in amino acid composition but also in their modifications, charge and length. AMPs can be classified as i) anionic, ii) linear cationic alpha-helical iii) cationic peptides enriched for specific amino acids, iv) anionic and cationic peptides that contain cysteine

and form disulphide bonds, v) anionic and cationic peptide fragments of larger proteins (Brogden 2005).

1.1.4 Targets of antimicrobial peptides

The structural and compositional variety of AMPs is reflected in their specialized abilities to act on a wide range of targets in bacterial cells. For a long time, however, it was believed that the majority of AMPs, moreover the cationic peptides able to form pores in the bacterial envelope, cause bacterial cell death through lysis. More recently, it has been found that particular classes of AMPs work through completely non-lytic mechanisms and that their actions instead affect a variety of cellular compartments and functions ranging from membrane disruption (i.e. margainin 2, Wenk and Seelig 1998), nucleic acid synthesis (i.e. buforin II, Park, Kim, and Kim 1998), enzymatic activity (i.e. small histidine-rich human defense peptide histatin 5, De Smet and Contreras 2005) and protein synthesis (i.e. proline-rich antimicrobial peptides, PrAMPs, (Brogden 2005) (**Figure** 1.1).

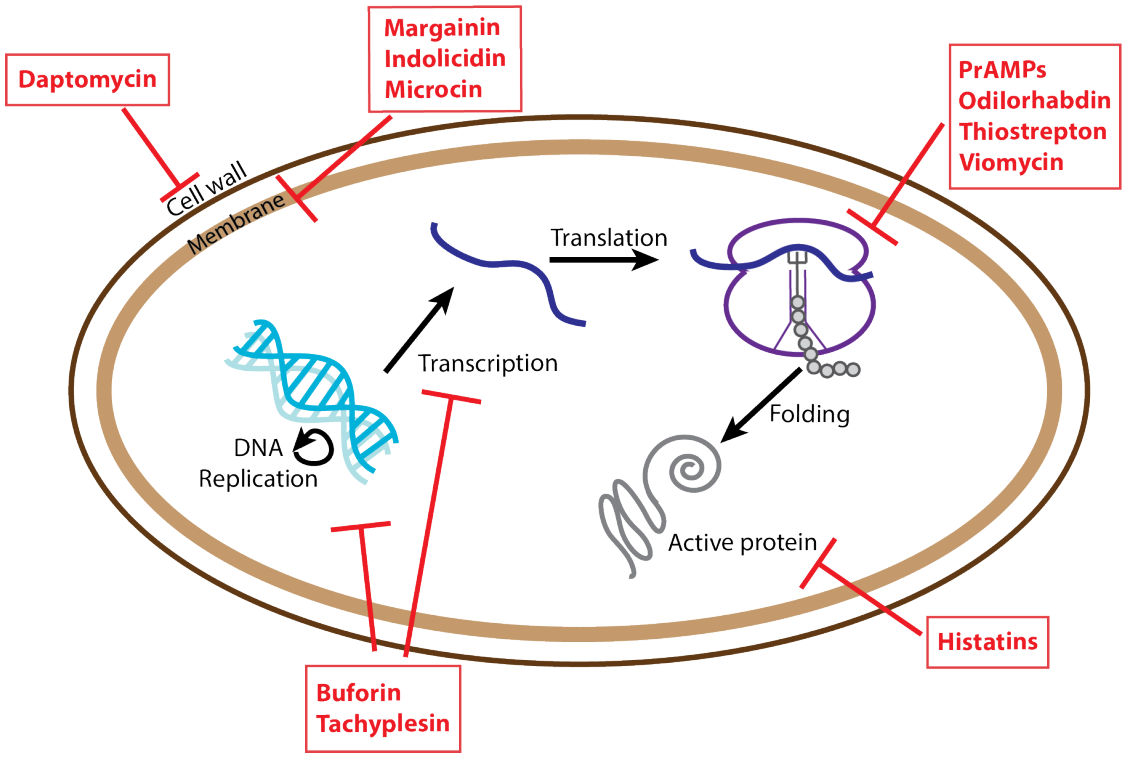

Figure 1.1: Overview of targets of antimicrobial peptides in the bacterial cell. Adapted from (Scocchi et al. 2016; Brogden 2005). Presented here is the bacterial cell (brown envelope) and its AMP target structures. The lipopeptide daptomycin changes the cell wall integrity. Margainin, Indolicidin and Microcin form pores in the cell membrane. Inside the cell, Buforin and Tachyplesin bind to DNA and thereby inhibit DNA replication and transcription. Translation is inhibited by multiple ribosome-targeting AMPs, among them PrAMPs, Odilorhabdins, Thiostrepton and Viomycin. The saliva-derived histatins inhibit enzymatic function through loss of ATP (Kavanagh and Dowd 2004).

A couple of decades ago, an unusual mechanism had been proposed for PrAMPs which, having the ability to bind to protein DnaK, were thought to inhibit bacterial growth by disrupting the function of cellular chaperones (Otvos et al. 2000). However, although interesting, this proposal was debunked when it was shown that *E. coli* cells lacking DnaK (*ΔdnaK*) are as susceptible to PrAMPs as the wild-type strain (Czihal et al. 2012; Scocchi et al. 2009). Shortly after, research of several groups showed that PrAMPs Bac-5, apidaecin, oncocin and their derivatives are able to bind to the bacterial ribosome (Mardirossian et al. 2014; Krizsan et al. 2014). Although these studies

suggested that the ribosome could be the primary intracellular target of PrAMPs, the mechanism leading to inhibition of protein synthesis remained completely undefined.

1.1.4.1 The bacterial ribosome as a target for antimicrobial peptides

One of the preferred targets for general antimicrobial agents, extending beyond antimicrobial peptides, is the bacterial ribosome, which synthesizes all the proteins of the cell. This highly sophisticated, evolutionarily conserved macromolecular machine is composed of ribosomal RNA (rRNA) and ribosomal proteins which, together, build the small and large subunits (30S and 50S, respectively, in bacteria). Many clinically important antibiotics target the functional centers of the ribosome, which include a) the decoding center in the 30S subunit which maintains the fidelity of interactions between mRNA codons and tRNA anticodons, b) the peptidyl transferase center (PTC) in the 50S subunit, where catalysis of peptide bond formation between a nascent polypeptide chain and an incoming amino acid takes place, and c) the nascent chain exit tunnel through which the newly synthesized peptide exits the ribosome (**Figure** 1.2). Blocking the activities of these functionally important ribosomal centers results in inhibition of specific steps of the process of protein synthesis (reviewed in Arenz and Wilson 2016). Indeed, biochemical and structural data have shown that a wide variety of antimicrobial peptides bind to the ribosome and perturb different stages of the translation cycle (reviewed in Polikanov et al. 2018) (**Figure** 1.2).

At the initiation of translation (step 1 in **Figure** 1.2), the 30S ribosomal subunit, together with the initiator fMet-tRNA and initiation factor (IF), initially bind messenger RNA (mRNA) that carries the information to build the proteins. Once associated to mRNA, the 50S subunit, aided by specific IFs, joins to form the 70S ribosome that enters the elongation phase of translation. Elongation (step 2 in **Figure** 1.2) occurs in a step-wise manner, starting with the binding of an aminoacyl-tRNA to the ribosome, followed by catalysis of peptide bond formation that results in the addition of one amino acid to the growing polypeptide chain. Selection of the cognate aminoacyl-tRNA and its proper accommodation in the ribosome is inhibited by odilorhabdin AMPs (Pantel et al. 2018) (Chapter 2), while formation of the first peptide bond is prevented by type I PrAMPs oncocin, Bac-

7, and their derivatives (Gagnon et al. 2016a; Roy et al. 2015; Seefeldt et al. 2016; Seefeldt et al. 2015) (Chapter three). After subsequent elongation steps, the ribosome reaches the stop codon of the mRNA, and release factors (RF1 or RF2) associate with the ribosome to prepare it for the termination phase (step 3 in **Figure 1.2**). RFs assist the ribosome to release the newly made protein into the cytoplasm and, in addition, allow dissociation of the ribosome from the mRNA. Following the termination step, ribosomes are recycled for subsequent rounds of translation. We found that the type II PrAMP apidaecin (Api) uniquely inhibits the termination phase of translation by trapping the RFs to the ribosomes after the nascent polypeptide has been hydrolyzed, an action that, in addition results in the blocking of recycling (step 4 in **Figure 1.2**) (Florin et al. 2017). Furthermore, we hypothesized that the Api-induced RF sequestration should lead to a depletion of free RFs in the cell and that if this is the case, Api action should ultimately result in a general inhibition of peptide-release. We tested this model by analyzing the effect of Api in global translation in living bacterial cells.

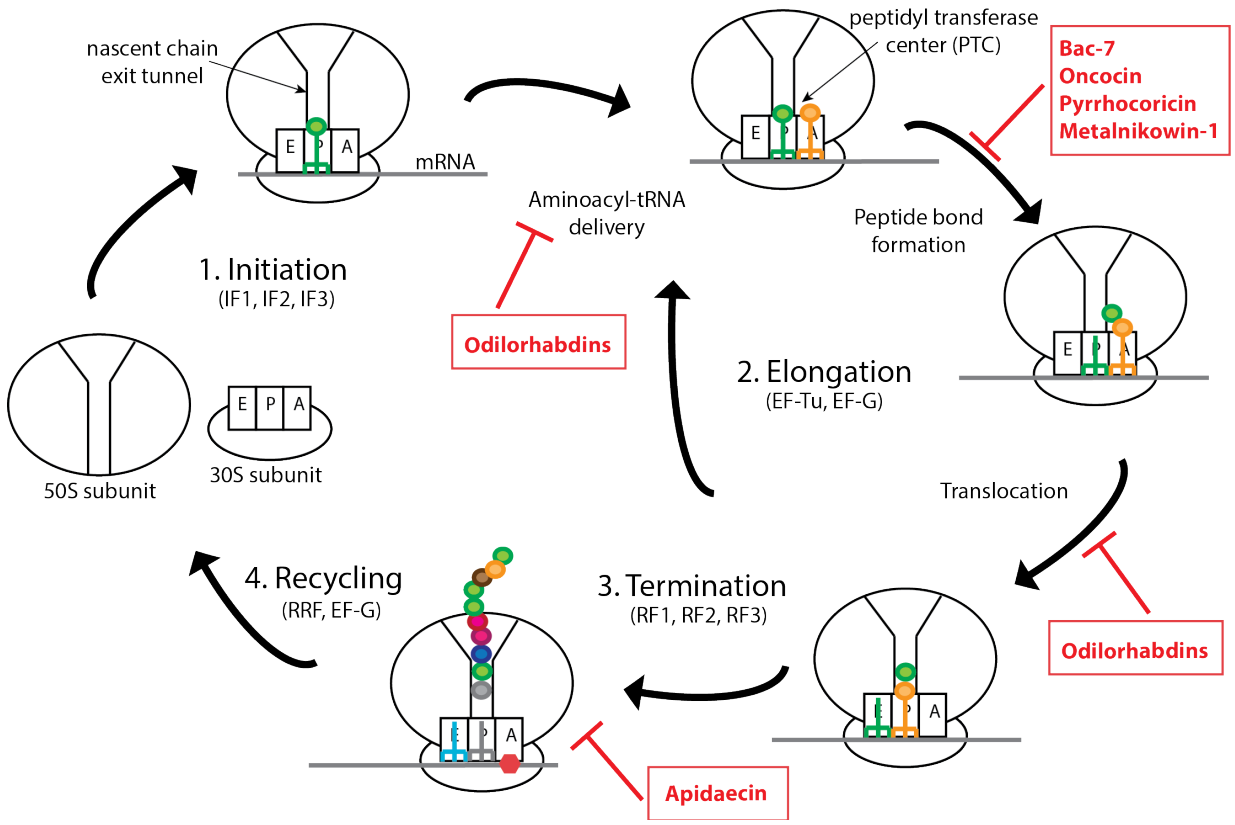

Figure 1.2: An overview of protein synthesis and the steps inhibited by examples of ribosome-targeting AMPs. For initiation of protein synthesis (step 1), the 70S pre-initiation complex formed by the ribosome and initiator tRNA binds to the mRNA at the start codon. This step is facilitated by initiation factors IF1, IF2 and IF3. During elongation (step 2), an aminoacyl-tRNA, corresponding to the mRNA codon in the ribosomal A-site, is delivered by EF-Tu. This step is inhibited by Odilorhabdins. Next, peptide bond formation between the two amino acids occurs in the PTC, which can be inhibited by type 1 PrAMPs Bac-7, Onc112, Pyrrhocoricin and Metalnikowin-1. After peptide bond formation, both tRNAs are translocated in the ribosome. Odilorhabdins can interfere with this step. Following multiple rounds of elongation, proceeding codon by codon along the mRNA, the ribosome will encounter a stop codon in its A-site, triggering the termination step of translation (step 3). The stop codon is decoded by class-1 release factors RF1 or RF2 which facilitate peptide bond hydrolysis and release of the newly synthesized polypeptide. RF3 aids in dissociation of class-1 release factors. The dissociation step is inhibited by the type 2 PrAMP Apidaecin. The terminated ribosome is now assisted by EF-G and RRF for recycling (step 4), allowing for dissociation and subsequent rounds of translation (adapted from Polikanov et al. 2018).

Table 1.1: Examples of ribosome-targeting antimicrobial peptides and peptide antibiotics

Name	Producer	Ribosomal Target	Mechanism	Reference
i) ribosomally-synthesized				
Oncocin	*Oncopeltus fasciatus* (milkweed bug)	50S, nascent chain exit tunnel	Elongation inhibition	(Schneider and Dorn 2001; Roy et al. 2015)
Bactenecin-7	*Bos taurus* (cattle)	50S, nascent chain exit tunnel	Elongation inhibition	(Gennaro, Skerlavaj, and Romeo 1989; Mardirossian et al. 2014; Gagnon et al. 2016b; Seefeldt et al. 2016)
Pyrrhocoricin	*Pyrrhocoris apterus* (firebeetle)	50S, nascent chain exit tunnel	Elongation inhibition	(Cociancich et al. 1994; Gagnon et al. 2016b)
Metalnikowin-1	*Palomena prasina* (green shield bug)	50S, nascent chain exit tunnel	Elongation inhibition	(Chernysh 1996, Gagnon 2016)
Apidaecin	*Apis mellifera* (honeybee)	50S, nascent chain exit tunnel	Termination inhibition, stop codon readthrough	(Casteels et al. 1989; Florin et al. 2017)
ii) ribosomally-sythesized and post translationally modified (RiPPs)				
Klebsazolicin	*Klebsiella pneumonia* (Gram-negative bacterium)	50S, nascent chain exit tunnel	Elongation inhibition	(Metelev et al. 2017)
iii) non-ribosomally synthesized (NRPSs)				
Odilorhabdin	*Xenorhabdus nematophila* (Gram-negative bacterium)	30S, decoding center	Elongation inhibition, miscoding	(Pantel et al. 2018)

1.2 Summary of the thesis

The works presented here are the result of our collaborative and multi-faceted investigations on the modes of action for two groups of AMPs: the odilorhabdins produced by the bacterium *Xenorabdus nematophilus* and the group of proline-rich antimicrobial peptides (PrAMPs) which are important components of the immune defense system of many insects, crustaceans and mammals.

The gammaproteobacteria of the *Xenorhabdus* species are known to dedicate a large portion of their genome to the production of specialized metabolites, produced by nonribosomal peptide synthetases (NRPS) and polyketide synthetases (PKS) (Tobias et al. 2017). One of the functions carried out by their various specialized metabolites is the eradication of competing bacteria (reviewed in Challinor and Bode 2015). In chapter two, we describe odilorhabdins (ODL), a novel class of peptide antibiotics that we detected in the supernatant of *Xenorhabdus nematophila*. We isolated and characterized the NRPS-derived ODL exhibiting excellent antibiotic properties: broad spectrum activity towards high priority pathogens, without exhibiting cross resistance to other antibiotics. That common resistance mechanisms turned out to be inefficient against ODLs pointed at the possible novel mode of action of these peptide antibiotics. Indeed, our biochemical and X-ray crystallography approaches revealed that ODLs specifically inhibit protein synthesis by binding to the bacterial ribosome in a site in the decoding center, which does not overlap with other decoding center targeting antibiotics. Interestingly, a consequence of this unique interaction is that ODLs show a dual mode of action: at high concentrations ODLs induce translation arrest while at lower concentrations, they decrease the fidelity of ribosomes during decoding, leading to incorporation of incorrect amino acids and production of faulty translation products, which ultimately leads to cidality (section 2.4 After publication). In addition, we demonstrate the high efficacy of ODLs *in vivo* by their ability to eradicate a *K. pneumonia* infection in a mouse model. Overall, our results from this study present ribosome-binding peptide antibiotics as promising compounds for treatment of infections caused by high priority strains of pathogenic bacteria.

Chapters three through six relate diverse aspects of the action of a different class of AMPs: proline-rich antimicrobial peptides, or PrAMPs. They are ribosomally produced by the immune system of a variety of higher organisms, among them mammals and insects, with insect-derived peptides being short (18 - 35 amino acids), whereas mammalian PrAMPs are slightly longer (40 - 60 amino acids). Even though the producers of PrAMPs are diverse, their overall structures are very similar, being characterized by their high proline and arginine content, which determines their linear secondary structure and cationic character (**Table 1.2**)

Table 1.2: Overview of sequences of selected PrAMPs and their derivatives. gu = N,N,N',N'-tetramethylguanidino, O = L-ornithine, r = D-arginine. Given are the amino acid lengths of the mature peptides. All sequences (except Apidaecin and Api137) were aligned ribosome-bound structure and the conserved Pro-Arg-Pro (PRP) motif (highlighted in red). Amino acid 11 of Oncocin in unknown and indicated with an X (adapted from Graf et al. 2017).

PrAMP	Length [aa]	Sequence
Apidaecin	18	GNNRPVYIPQPRPPHPRL
Api137	18	gu-ONNRPVYIPQPRPPHPRL-OH
Oncocin	20	VDKPPYLPRPXPRRIYNNR
Onc112	19	VDKPPYLPRPRPPRrIYNr-NH_2
Metalnikovin-1	15	VDKPDYRPRPRPPNM
Pyrrhocoricin	20	VDKGSYLPRPTPPTPIYNRN
Bactenecin-7	60	RRIRPRPPRLPRPRPRPLPFPPPGP…

In contrast to other cationic AMPs, PrAMP's primary target is not the cell membrane but instead, an intracellular one. To reach their target, PrAMPs are actively imported by the transporter protein SbmA or the YjiL-MdtM transporter system found in a variety of Gram-negative bacteria (Mattiuzzo et al. 2007; Krizsan, Knappe, and Hoffmann 2015), but not in Gram-positive species. While the need for specific transporters restricts PrAMP's action to gram-negative bacteria, it dramatically reduces the peptide's toxicity towards mammalian cells and, therefore, renders PrAMPs as promising antibiotics candidates. Thus, not surprisingly, different research groups are investigating their mode of action to further the development of PrAMPs as antibiotic agents. Interestingly, because a variety of PrAMPs were shown to have a high affinity for DnaK, bacterial chaperones were proposed to be the PrAMPs intracellular target. However, more recently, new data including ours, showed that the bacterial ribosome is the primary target of PrAMPs (reviewed in Graf et al. 2017). Structural methods combined with microbiological, biochemical, and genomic approaches have and will continues to uncover how PrAMPs inhibit ribosomal functions.

Chapter three describes our study of four different PrAMPs: the cattle-derived Bac7, and three PrAMPs produced by different insects. Importantly, our observations that mutations in the ribosome decrease the cell's sensitivity towards PrAMPs, strengthened the hypothesis of the ribosome being the primary target for PrAMPs. For PrAMPs Bac7, two oncocin derivatives, Pyrrhocoricin and Metalnikowin, our in vitro translation experiments showed that they have the ability to arrest ribosomes at the start codons of mRNAs. The data gathered from the high-resolution structures of these PrAMPs bound to the ribosome (see also Seefeldt et al. 2016; Seefeldt et al. 2015)., explained this mode of action. The studied PrAMPs penetrate into the nascent peptide exit tunnel of the ribosome which is about to initiate translation. The N-terminal end of the short PrAMPs reach into the peptidyl transferase center, block the binding of an incoming aminoacyl-tRNA, and impede formation of the first peptide bond.

Puzzlingly, although apidaecin (Api), an 18 amino acids long peptide produced by the honeybee *Apis mellifera* (Casteels et al. 1989), shares many properties with other PrAMPs (**Table 1.1** and **Table 1.2**), our pilot biochemical experiments failed to detect inhibition of translation initiation by Api. To add to the frustration, initial attempts to obtain a crystal structure of Api in complex with the *Thermus thermophilus* ribosome were unsuccessful. In chapter four we described the experiments that helped us elucidate the unique mechanism of Api: Instead of stalling ribosomes at the start codon, Api specifically blocks the termination step of translation. To our best knowledge, no other antibiotic has been described to specifically inhibit the termination phase of translation. Sophisticated kinetic experiments and further biochemical analysis revealed the series of steps necessary for Api's action. Briefly, after RF1 or RF2 help the ribosome catalyze hydrolysis of the newly made protein, Api takes the opportunity to penetrate the exit tunnel. However, unlike Bac7, Onc112 and others, Api does not stably bind to the tunnel's walls. To remain associated with the ribosome, Api needs to interact with RF, trapping it to the ribosome. Importantly, these biochemical data illuminated the strategy to finally obtain the cryo-electron (cryo-EM) structure of Api bound to the *E. coli* ribosome: the release factor, in this case RF1, needed to be present in the complex. Because ribosomes outnumber RFs, we then hypothesized that the Api-induced sequestration of RFs leads to their depletion in the cell, eventually causing ribosomes to remain stalled with fully-synthesized, but unreleased, proteins. In addition, if this model is correct, the A-site of the RF-depleted ribosomes stalled at stop codons should remain vacant, with a chance to accommodate a near-cognate aminoacyl-tRNAs, allowing the incorporation of an amino acid and, ultimately, resuming translation. In this case, an indirect consequence of Api action is increased stop codon readthrough, which we were able to demonstrate by using a readthrough reporter. Part of our ongoing studies (described in chapter five) is aimed towards understanding whether Api-induced stop codon readthrough is facilitated in certain genes.

Our study on Api's molecular mode of action was conducted using a variety of *in vitro* experiments. But in order to obtain the full picture of the protein syntheis inhibitory action in the bacterial cell, we sought out to analyze Api's mode of action *in vivo* in an inbiased and systematic approach using the ribosome profiling methodology, also known as RiboSeq. Ribo-Seq is an excellent tool to study the global translation status of cells under specific conditions (Ingolia et al., 2009), including the presence of inhibitors of protein synthesis for example the PrAMP Onc112 (Weaver et al. 2019). This powerful technique allows us to locate ribosomes, with codon precision, within an mRNA at a particular moment. To locate the translating ribosomes, we analyze the abundance of ribosome-protected mRNA fragments (footprints) and computationally map the footprints to the genome. As a result, we observe the overall ribosome density on every gene under different conditions (**Figure 1.3**).

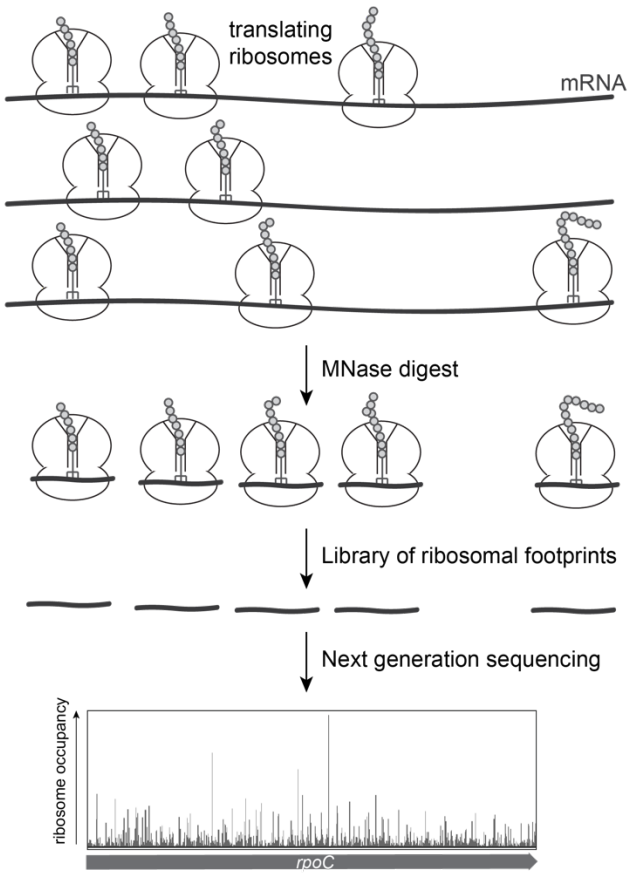

Figure 1.3: Overview of the RiboSeq (ribosome profiling) methodology to study the mode of action of protein synthesis inhibitors. Ribosomes are isolated from cells exposed to the translation inhibitor, followed by treatment with MNase to obtain ribosomal footprints which are subsequently sequenced and aligned to the genome. Changes of ribosome occupancy between cells exposed to the protein synthesis inhibitor and control cells are analyzed bioinformatically. (adapted from Vázquez-Laslop and Mankin, 2019).

By comparing the ribosomal footprints derived, in our case, from untreated and Api-treated cells, we were able to determine in an unbiased and systematic way how the Api affects translation globally and on single genes. Mapping of the ribosomal footprints resulted in the observation that exposure to Api leads to a genome-wide redistribution of ribosomes in *E. coli* cells., with three main Api137-induced phenomena: i) accumulation of ribosomes at the initiation region, ii) strong enrichment of ribosomes at the termination region and iii) high ribosome density in the 3' UTR, suggesting stop codon readthrough activity. Probably the most interesting aspect of the RiboSeq data is that the ribosome redistribution patterns differ from gene to gene, likely revealing a context specific component for the Api-induced effects on translation. To systematically analyze the effect in each gene, we developed a scoring system that quantifies each pattern. Our ongoing analysis involves grouping genes according to their ribosome density patterns, using the scoring system, to find determining factors, such as location of the gene within an operon, the nature of the stop codon, the sequence of the intergenic region, etc. This systematic analysis approach may illuminate not only mechanistic details of the action of Api but also could reveal basic principles of translation in the living bacterial cell.

1.3 Cited literature

Arenz, S., and D. N. Wilson. 2016. 'Bacterial Protein Synthesis as a Target for Antibiotic Inhibition', *Cold Spring Harb Perspect Med*, 6.

Brogden, K. A. 2005. 'Antimicrobial peptides: pore formers or metabolic inhibitors in bacteria?', *Nat Rev Microbiol*, 3: 238-50.

Casteels, P., C. Ampe, F. Jacobs, M. Vaeck, and P. Tempst. 1989. 'Apidaecins: antibacterial peptides from honeybees', *EMBO J*, 8: 2387-91.

Challinor, V. L., and H. B. Bode. 2015. 'Bioactive natural products from novel microbial sources', *Ann N Y Acad Sci*, 1354: 82-97.

Cociancich, S., A. Dupont, G. Hegy, R. Lanot, F. Holder, C. Hetru, J. A. Hoffmann, and P. Bulet. 1994. 'Novel inducible antibacterial peptides from a hemipteran insect, the sap-sucking bug Pyrrhocoris apterus', *Biochem J*, 300 (Pt 2): 567-75.

Czihal, P., D. Knappe, S. Fritsche, M. Zahn, N. Berthold, S. Piantavigna, U. Muller, S. Van Dorpe, N. Herth, A. Binas, G. Kohler, B. De Spiegeleer, L. L. Martin, O. Nolte, N. Strater, G. Alber, and R. Hoffmann. 2012. 'Api88 is a novel antibacterial designer peptide to treat systemic infections with multidrug-resistant Gram-negative pathogens', *ACS Chem Biol*, 7: 1281-91.

De Smet, K., and R. Contreras. 2005. 'Human antimicrobial peptides: defensins, cathelicidins and histatins', *Biotechnol Lett*, 27: 1337-47.

Florin, T., C. Maracci, M. Graf, P. Karki, D. Klepacki, O. Berninghausen, R. Beckmann, N. Vazquez-Laslop, D. N. Wilson, M. V. Rodnina, and A. S. Mankin. 2017. 'An antimicrobial peptide that inhibits translation by trapping release factors on the ribosome', *Nat Struct Mol Biol*, 24: 752-57.

Fox, J. L. 2013. 'Antimicrobial peptides stage a comeback', *Nat Biotechnol*, 31: 379-82.

Gagnon, M. G., R. N. Roy, I. B. Lomakin, T. Florin, A. S. Mankin, and T. A. Steitz. 2016a. 'Structures of proline-rich peptides bound to the ribosome reveal a common mechanism of protein synthesis inhibition', *Nucleic Acids Res*, 44: 2439-50.

Gagnon, Matthieu G., Raktim N. Roy, Ivan B. Lomakin, Tanja Florin, Alexander S. Mankin, and Thomas A. Steitz. 2016b. 'Structures of proline-rich peptides bound to the ribosome reveal a common mechanism of protein synthesis inhibition', *Nucleic Acids Research*.

Gennaro, R., B. Skerlavaj, and D. Romeo. 1989. 'Purification, composition, and activity of two bactenecins, antibacterial peptides of bovine neutrophils', *Infect Immun*, 57: 3142-6.

Graf, M., M. Mardirossian, F. Nguyen, A. C. Seefeldt, G. Guichard, M. Scocchi, C. A. Innis, and D. N. Wilson. 2017. 'Proline-rich antimicrobial peptides targeting protein synthesis', *Nat Prod Rep*, 34: 702-11.

Kavanagh, Kevin, and Susan Dowd. 2004. 'Histatins: antimicrobial peptides with therapeutic potential', *Journal of Pharmacy and Pharmacology*, 56: 285-89.

Krizsan, A., D. Knappe, and R. Hoffmann. 2015. 'Influence of the yjiL-mdtM Gene Cluster on the Antibacterial Activity of Proline-Rich Antimicrobial Peptides Overcoming Escherichia coli Resistance Induced by the Missing SbmA Transporter System', *Antimicrob Agents Chemother*, 59: 5992-8.

Krizsan, Andor, Daniela Volke, Stefanie Weinert, Norbert Sträter, Daniel Knappe, and Ralf Hoffmann. 2014. 'Insect-derived proline-rich antimicrobial peptides kill bacteria by inhibiting bacterial protein translation at the 70S ribosome', *Angewandte Chemie (International ed. in English)*, 53: 12236-39.

Mardirossian, M., R. Grzela, C. Giglione, T. Meinnel, R. Gennaro, P. Mergaert, and M. Scocchi. 2014. 'The host antimicrobial peptide Bac71-35 binds to bacterial ribosomal proteins and inhibits protein synthesis', *Chem Biol*, 21: 1639-47.

Mattiuzzo, Maura, Antonella Bandiera, Renato Gennaro, Monica Benincasa, Sabrina Pacor, Nikolinka Antcheva, and Marco Scocchi. 2007. 'Role of the Escherichia coli SbmA in the antimicrobial activity of proline-rich peptides', *Molecular Microbiology*, 66: 151-63.

Metelev, M., I. A. Osterman, D. Ghilarov, N. F. Khabibullina, A. Yakimov, K. Shabalin, I. Utkina, D. Y. Travin, E. S. Komarova, M. Serebryakova, T. Artamonova, M. Khodorkovskii, A. L. Konevega, P. V. Sergiev, K. Severinov, and Y. S. Polikanov. 2017. 'Klebsazolicin inhibits 70S ribosome by obstructing the peptide exit tunnel', *Nat Chem Biol*, 13: 1129-36.

Organization, World Health. 2017. "Global priority list of antibiotic-resistant bacteria to guide research, discovery, and development of new antibiotics." In.: World Health Organization.

Ostorhazi, E., E. Nemes-Nikodem, D. Knappe, and R. Hoffmann. 2014. 'In vivo activity of optimized apidaecin and oncocin peptides against a multiresistant, KPC-producing Klebsiella pneumoniae strain', *Protein Pept Lett*, 21: 368-73.

Otvos, L., Jr., I. O, M. E. Rogers, P. J. Consolvo, B. A. Condie, S. Lovas, P. Bulet, and M. Blaszczyk-Thurin. 2000. 'Interaction between heat shock proteins and antimicrobial peptides', *Biochemistry*, 39: 14150-9.

Pantel, L., T. Florin, M. Dobosz-Bartoszek, E. Racine, M. Sarciaux, M. Serri, J. Houard, J. M. Campagne, R. M. de Figueiredo, C. Midrier, S. Gaudriault, A. Givaudan, A. Lanois, S. Forst, A. Aumelas, C. Cotteaux-Lautard, J. M. Bolla, C. Vingsbo Lundberg, D. L. Huseby, D. Hughes, P. Villain-Guillot, A. S. Mankin, Y. S. Polikanov, and M. Gualtieri. 2018. 'Odilorhabdins, Antibacterial Agents that Cause Miscoding by Binding at a New Ribosomal Site', *Mol Cell*, 70: 83-94 e7.

Park, C. B., H. S. Kim, and S. C. Kim. 1998. 'Mechanism of action of the antimicrobial peptide buforin II: buforin II kills microorganisms by penetrating the cell membrane and inhibiting cellular functions', *Biochem Biophys Res Commun*, 244: 253-7.

Polikanov, Y. S., N. A. Aleksashin, B. Beckert, and D. N. Wilson. 2018. 'The Mechanisms of Action of Ribosome-Targeting Peptide Antibiotics', *Front Mol Biosci*, 5: 48.

Roy, Raktim N., Ivan B. Lomakin, Matthieu G. Gagnon, and Thomas A. Steitz. 2015. 'The mechanism of inhibition of protein synthesis by the proline-rich peptide oncocin', *Nature structural & molecular biology*.

Schneider, M., and A. Dorn. 2001. 'Differential infectivity of two Pseudomonas species and the immune response in the milkweed bug, Oncopeltus fasciatus (Insecta: Hemiptera)', *J Invertebr Pathol*, 78: 135-40.

Scocchi, M., M. Mardirossian, G. Runti, and M. Benincasa. 2016. 'Non-Membrane Permeabilizing Modes of Action of Antimicrobial Peptides on Bacteria', *Curr Top Med Chem*, 16: 76-88.

Scocchi, M., A. Pallavicini, R. Salgaro, K. Bociek, and R. Gennaro. 2009. 'The salmonid cathelicidins: a gene family with highly varied C-terminal antimicrobial domains', *Comp Biochem Physiol B Biochem Mol Biol*, 152: 376-81.

Seefeldt, A. C., M. Graf, N. Perebaskine, F. Nguyen, S. Arenz, M. Mardirossian, M. Scocchi, D. N. Wilson, and C. A. Innis. 2016. 'Structure of the mammalian antimicrobial peptide Bac7(1-16) bound within the exit tunnel of a bacterial ribosome', *Nucleic Acids Res*, 44: 2429-38.

Seefeldt, Carolin A., Fabian Nguyen, Stéphanie Antunes, Natacha Pérébaskine, Michael Graf, Stefan Arenz, Kishore K. Inampudi, Céline Douat, Gilles Guichard, Daniel N. Wilson, and Axel C. Innis. 2015. 'The proline-rich antimicrobial peptide Onc112 inhibits translation by blocking and destabilizing the initiation complex', *Nature structural & molecular biology*, 22: 470-75.

Tobias, N. J., H. Wolff, B. Djahanschiri, F. Grundmann, M. Kronenwerth, Y. M. Shi, S. Simonyi, P. Grun, D. Shapiro-Ilan, S. J. Pidot, T. P. Stinear, I. Ebersberger, and H. B. Bode. 2017. 'Natural product diversity associated with the nematode symbionts Photorhabdus and Xenorhabdus', *Nat Microbiol*, 2: 1676-85.

Weaver, J., F. Mohammad, A. R. Buskirk, and G. Storz. 2019. 'Identifying Small Proteins by Ribosome Profiling with Stalled Initiation Complexes', *MBio*, 10.

Wenk, M. R., and J. Seelig. 1998. 'Magainin 2 amide interaction with lipid membranes: calorimetric detection of peptide binding and pore formation', *Biochemistry*, 37: 3909-16.

Wright, G. D. 2017. 'Opportunities for natural products in 21(st) century antibiotic discovery', *Nat Prod Rep*, 34: 694-701.

Zasloff, Michael. 2002. 'Antimicrobial peptides of multicellular organisms', *Nature*, 415: 389-95.

2. ODILORHABDINS, ANTIBACTERIAL AGENTS THAT CAUSE MISCODING BY BINDING AT A NEW RIBOSOMAL SITE

(previously published as Pantel, L., Florin, T., Dobosz-Bartoszek, M., Racine, E., Sarciaux, M., Serri, M., Houard, J., Campagne, J.M., de Figueiredo, R.M., Midrier, C.*, et al.* (2018). Odilorhabdins, Antibacterial Agents that Cause Miscoding by Binding at a New Ribosomal Site. Mol Cell *70*, 83-94 e87)

2.1 Introduction

Antimicrobial resistance is one of the most serious threats to human health. Some strains of critical bacterial pathogens have acquired resistance to nearly all antibiotics available to date (Nordmann, Dortet, and Poirel 2012). Most of the known antibiotics that are currently used have been discovered in the 1940s – 1960s by extensive screening of soil actinomycetes. Over time, this source of new antibacterials has been significantly exhausted due to overmining and alternative drug-discovery strategies that have been explored. However, neither the high throughput screening of synthetic chemical libraries nor the search for new antibiotic targets with the help of bacterial genomics has yielded sufficiently potent new antibacterials (Payne et al. 2007). Therefore, finding new natural sources of bio-active antimicrobial scaffolds appears to be an alternative promising approach for overcoming the innovation gap in antibacterial drug discovery and identifying new antibiotic leads exploiting novel targets and mechanisms of action (Wright 2014; Ling et al. 2015).

Gram-positive actinomycetes have been traditionally used as the source of antibiotics because of their capacity to produce a great variety of secondary metabolites. The plasticity of the genomes of actinomycetes allows these microorganisms to stably maintain a large number of biosynthetic gene clusters, a large fraction of which is represented by the genes encoding non-ribosomal peptide synthetases (NRPSs) and polyketide synthases (PKS) (Walsh 2008; Lewis 2013; Berdy 2005). Intriguingly, members of the Gram-negative genus *Xenorhabdus* that belong to the family *Enterobacteriaceae,* also possess a high number of NRPS and PKS genes in their genomes, making these bacteria a promising alternative source for the discovery of new bioactive

compounds (Tobias et al. 2017). Nevertheless, *Xenorhabdus* bacteria have been largely understudied due in part to their idiosyncratic life cycle, which makes it difficult to isolate these organisms. *Xenorhabdus* genus is symbiotically associated with soil-dwelling nematodes. The bacterial symbiont produces toxins and immuno-modulators enabling the nematode to colonize and kill insects. *Xenorhabdus* further benefits the host nematode by releasing antibiotics that prevent the invasion of the insect's carcass by other competing bacteria and fungi. Indeed, the high potential of *Xenorhabdus* as a source for new antimicrobials has been demonstrated in several studies (Fodor et al. 2010; Gualtieri, Aumelas, and Thaler 2009).

Here we describe the discovery of a new class of modified peptide antibiotics, odilorhabdins (ODLs), produced by the enzymes encoded in an identified NRPS gene cluster present in the genome of *Xenorhabdus nematophila*. ODLs exhibit promising broad-spectrum antibacterial activity. The high-resolution crystal structure of the ribosome-ODL complex shows that these inhibitors bind to the decoding center of the small subunit of the bacterial ribosome at a site not exploited by any known ribosome-targeting antibiotic. Bound to the ribosome, ODLs make contacts with both the rRNA and tRNA and stimulate miscoding in cell-free translation system and in the living cell likely by promoting the illegitimate binding of non-cognate aminoacyl-tRNAs. The bactericidal activity of ODLs, their ability to cure the bacterial infection in the animal models, the novelty of the binding site and the demonstrated potential of the *de novo* chemical synthesis of natural and designer ODLs make them promising candidates for new drug development.

2.2 Materials and Methods

Table 2.3: Key resources

REAGENT or RESOURCE	SOURCE	IDENTIFIER
Bacterial and Virus Strains		
X. nematophila	CNCM	CNCM: I-4530 (K102)
K. pneumoniae	(clinical isolate, Denmark)	SSI#3010
K. pneumoniae	NCTC	NCTC: 13442
E. coli SQ110		CGSC: 12349
E. coli APV00028	Aptuit (Verona)	
E. coli CSH142	Laboratory of Kurt Frederick	CGSC: 8083

E. coli XAC-1 pGF1B	Laboratory of Ya-Ming Hou	N/A
E. coli BL21	New England Biolabs	Cat#: C2530H
E. aerogenes	ATCC	ATCC: 51697
E. cloacae	DSM	DSM: 30054
E. coli	TCC	ATCC: 25922
K. pneumoniae	ATCC	ATCC: 43816
P. mirabilis	ATCC	ATCC: 7002
S. marcescens	DSM	DSM: 30121
P. aeruginosa	DSM	DSM: 1117
A. baumannii	ATCC	ATCC: 19606
S. maltophilia	CIP	CIP: 60.71
S. aureus	ATCC	ATCC: 29213
E. faecalis	ATCC	ATCC: 29212
K. pneumoniae	ATCC	ATCC: BAA-1905
K. pneumoniae	ATCC	ATCC: BAA-1904
K. pneumoniae	NCTC	NCTC: 13438
K. pneumoniae	NCTC	NCTC: 13439
K. pneumoniae	ATCC	ATCC: BAA-2146
K. pneumoniae	ATCC	ATCC: BAA-2472
K. pneumoniae	ATCC	ATCC: BAA-2473
K. pneumoniae	NCTC	NCTC: 13443
K. pneumoniae	NCTC	NCTC: 13442
K. pneumoniae	ATCC	ATCC: BAA-2473
E. coli	ATCC	ATCC: BAA-2340
E. coli	ATCC	ATCC: BAA-2452
E. coli	ATCC	ATCC: BAA-2469
E. cloacae	ATCC	ATCC: BAA-2468
Thermus thermophilus HB8	ATCC	ATCC: 27634
Chemicals, Peptides, and Recombinant Proteins		
NOSO-95A	This study	N/A
NOSO-95B	This study	N/A
NOSO-95C	This study	N/A
NOSO-95179	This study	N/A
Ceftriaxon	Sigma-Aldrich	Cat#89434
Ciprofloxacin	Sigma-Aldrich	Cat#1134335
Gentamicin	Sigma-Aldrich	Cat#SLBB9265
Imipenem	Sigma-Aldrich	Cat#IO160
Polymyxin B	Sigma-Aldrich	Cat#92283
Tetracycline	Sigma-Aldrich	Cat#T8032
Tigecycline	Sigma-Aldrich	Cat#PZ0021
Chloramphenicol	Sigma-Aldrich	Cat#C0378
Kanamycin	Sigma-Aldrich	Cat#K1637
Erythromycin	Sigma-Aldrich	Cat#856193
Spectinomycin	Sigma-Aldrich	Cat#S4014
Onc112	GeneScript	N/A
AccuPrime DNA Polymerase	Thermo Fisher Scientific	Cat#12346-086
AMV Reverse Transcriptase	Sigma-Aldrich	Cat#10109118001
2-Methyl-2,4-pentanediol	Hampton Research	Cat# HR2-627
Polyethylene Glycol 20,000	Hampton Research	Cat# HR2-609

Experimental Models: Cell Lines		
Human: liver hepatocellular cells (hepg2)	ATCC	ATCC: HB-8065
Human: proximal tubule epithelial cells (HK-2)	ATCC	ATCC: CRL-2190
Experimental Models: Organisms/Strains		
Mouse: NMRI, female	Taconic Biosciences A/S, Lille Skensved, Denmark	N/A
Mouse: ICR, male	Charles River UK	N/A
Oligonucleotides		
Primers for toeprinting (see **Table 2.4**)	Integrated DNA Technologies	N/A
mRNA - GGC AAG GAG GUA AAA **AUG GUU** UUC UAA	Integrated DNA Technologies	N/A
E. coli initiator methionine-specific $tRNA_i^{Met}$	Laboratory of Dr. Andrey Konevega	N/A
E. coli valine-specific $tRNA^{Val}$	Laboratory of Dr. Andrey Konevega	N/A
Recombinant DNA		
Plasmid: p*lacZ* ($Glu537Gly_{GGG}$)	Laboratory of Dr. Phil Farabaugh	N/A
Plasmid: pEXP5-CT TOPO vector	Thermo Fisher	N/A
Software and Algorithms		
GraphPad Prism 6 Software	GraphPad Software	N/A
XWINNMR software	Bruker	N/A
CLC Genomics Workbench 8.0.2	CLC Bio	N/A
PHASER	McCoy et al., 2007	N/A
COOT	Emsley & Cowtan, 2004	N/A
PHENIX	Adams et al., 2010	N/A
PYMOL	www.pymol.org	N/A

Experimental model and subject details

Bacteria and human cell lines

Bacterial strains and human cell lines used can be found in **Table 2.3**.

Mouse models

Murine neutropenic peritonitis/sepsis model: Female NMRI mice (Taconic Biosciences A/S, Lille Skensved, Denmark) were used. Mice had *ad libitum* access to domestic quality drinking water and food (Rodents Diet, Harlan, USA). Light/dark period was in 12-hours interval. All animal experiments were approved by the National Committee of Animal Ethics, Denmark, and adhered to the standards of EU Directive 2010/63/EU.

Mouse lung infection model: Male ICR mice 6-8 weeks old (Charles River, UK) were rendered neutropenic by IP injection of cyclophosphamide. All animal experiments were performed under UK Home Office License 40/3644, and with local ethical committee clearance (The University of Manchester AWERB). All experiments were performed by technicians who had completed at least parts 1 to 3 of the Home Office Personal License course and held current personal licenses.

Cultivation of *X. nematophila* and isolation of natural ODLs.

X. nematophila CNCM I-4530 (K102) was cultivated for 72 h, at 28°C with shaking in a 2 l Erlenmeyer flask containing 500 ml of medium broth composed of bactopeptone (15 g/l), MgSO4.7H2O (2 g/l) and glucose (2 g/l). The culture was inoculated with 0.1% (v/v) of a pre-culture grown for 24 hours in the same medium. *X. nematophila* cells were pelleted by centrifugation at 6000 × g for 10 min at 4°C and supernatant was passed through 0.22 µm filter. After addition of an equal volume of 0.1 M NaCl, 20 mM Tris-HCl, pH 7.0, the solution was subjected to cation-exchange chromatography on a Sep Pack CarboxyMethyl cartridge (Accell Plus CM, Waters). The cartridge was washed with 50 ml of 0.1 M NaCl, 20 mM Tris-HCl, pH 7.0, and bound compounds were eluted with 200 ml of 1 M NaCl, 20 mM Tris-HCl, pH 7.0. After addition of 0.1% (v/v) trifluoroacetic acid (TFA) the eluate was subjected to reverse-phase chromatography on a Sep Pack C18 cartridge (Sep-Pak Plus C18, Waters). The cartridge was washed with 50 ml of 0.1% solution of TFA and the antibiotics were eluted with 40 ml of acetonitrile. After freeze-drying, the eluted material was resuspended in water. Pure compounds were isolated by reverse phase HPLC using a C18 column (Waters; Symmetry C18; 5 µm; 4.6X150 mm), using a linear gradient (0-30%) of acetonitrile in H_2O/0.1% TFA in 30 min, with a flow rate of 1 ml/min and UV detection in the range of 200 to 400 nm. The retention times of the bioactive ODLs were as follows: NOSO-95A - 14.16 min (purity: 98% by UV), NOSO-95B - 14.44 min (purity: 95% by UV), NOSO-95C - 14.6 min (purity: 94% by UV). The structure of the isolated ODLs was determined by NMR and mass-spectrometry analysis.

NMR and MS analysis.

For identifying the structures of the purified NOSO-95A, -B and -C, the compounds were analyzed by mass spectroscopy and NMR. LC-MS was first performed to obtain the m/z value of the protonated molecules of all ODL variants. MS-MS fragmentation was then carried out on NOSO-95A, -B and -C. ESI-LC-MS data were obtained in the positive mode on a Waters alliance LC-MS system (Waters ZQ mass detector, Waters photodiode array detector 2696, Waters alliance HPLC systems 2790). MS-MS fragmentation data were obtained on a Waters Micromass Q-Tof micro mass spectrometer.

The NMR analysis was carried out on a Bruker Avance spectrometer operating at 700 MHz equipped with a cryoprobe. The sample (10 mM) was solubilized in water (95/5 H_2O/D_2O v/v) and pH was adjusted to 3.5 with HCl. All data were recorded at 280 K. Protons chemical shifts are expressed with respect to sodium 4,4-dimethyl-silapentane-1-sulfonate, according to IUPAC recommendations. Double-quantum filtered-correlated spectroscopy (DQF-COSY), z-filtered total-correlated spectroscopy (z-TOCSY) and nuclear Overhauser effect spectroscopy (NOESY) spectra were acquired in the phase-sensitive mode, using the States-TPPI method. z-TOCSY spectra were obtained with a mixing time of 80 ms and NOESY spectra with mixing times of 220 ms. The ^{1}H-^{13}C HSQC and ^{1}H-^{13}C HSQC-TOCSY experiments were carried out with the same sample. The water resonance set at the carrier frequency was suppressed by the WATERGATE method (Piotto, Saudek, and Sklenar 1992). All data were processed with the XWINNMR software (Bruker Biospin). The non-classical residues were identified from the analysis of the homo- and hetero-nuclear data. The sequential assignment was achieved using the general strategy described by Wüthrich (Billeter, Braun, and Wuthrich 1982).The chemical structure of the 1296 Da (NOSO-95A) compound was determined by NMR and mass spectrometry.

NMR data were obtained in water and a set of experiments including DQF-COSY, TOCSY, NOESY, ^{1}H-^{13}C HSQC and ^{1}H-^{13}C HSQC-TOCSY experiments were recorded.

The 1D spectrum revealed features of a peptidic compound with at least 6 amide signals spanning the 8.9-7.0 ppm chemical shift area, alpha proton signals in the 4.8-3.7 ppm area, and beta proton

signals in the 3.7-1.1 ppm area. No methyl signal was observed in the high field area indicating the absence of Ala, Thr, Leu, Val and Ile residues. In contrast, unusual signals including the 9.60 ppm singlet and the 6.17 ppm triplet were observed suggesting the presence of non-classical residues. The TOCSY and COSY finger prints are displayed in **Figure 2.4A** and **B**, respectively. In addition, with homonuclear data, the ^{1}H-^{13}C heteronuclear data were particularly helpful to characterize the spin systems of the non-classical residues. The **Figure 2.4C** shows the main part of the ^{1}H-^{13}C HSQC-TOCSY map with some assignment of the non-classical residues.

The combined analysis of all these data allowed us to identify 11 spin systems including 4 types of non-classical residues: an $\alpha\gamma$-diamino β-hydroxy butyric acid (Dab(βOH), an δ-hydroxy lysine (Dhl), an $\alpha\beta$-dehydro arginine (Dha) and, an $\alpha\delta$-diamino butane (Dbt). The stereochemistry of the Dha_9 double bond was determined from the Dha_9 Hβ–Dh_{l1} HN dipolar interaction. Notice that the strong intensity of the Orn_5 Hα-Pro_6 H$\delta\delta$' NOE suggests that the Orn_5-Pro_6 amide bond adopts the trans conformation.

The sequence of this peptide was identified as following: Lys_1-Dab(βOH)$_2$-Dab(βOH)$_3$-Gly_4-Orn_5-Pro_6-His_7-Dhl_8-Dha_9-Dhl_{10}-Dbt_{11} and NMR data are reported in the **Table A1 in Appendix A.**

In order to determine the stereochemistry of each chiral center of NOSO-95A, Marfey's analysis was done. D- and L- enantiomers of Lys, Orn, Pro, His as well as Gly and 1,4-diaminobutane were purchased from Bachem (Germany). The 4 diastereoisomers of Dab(βOH) and of Dhl as well as the two diastereoisomers of the dipeptide Lys-(Z)-DhArg were synthesized. In all cases, only one enantiomer or diastereoisomer was observed. All chiral centers were found to be of S configuration, except the chiral center of Orn which was found to be of R configuration.

Chemical synthesis of NOSO-95179.

NOSO-95179 was synthesized via a solid phase peptide synthesis (SPPS) using a Fmoc-strategy (Amblard et al. 2006). The synthesis was run in six separate batches which were combined at the end of the synthesis. The crude product was dissolved in milliQ water (~400 mg/ml) and purified by semi-preparative HPLC on a C18 column (100 Å, 7 µm, 7.8 mm X 300 mm) with a 15 min

gradient of 0 to 15% MeCN in H_2O (0.1% TFA). Fractions containing pure product were combined and lyophilized. White foam (1016.5 mg, 98.2% purity by HPLC-MS) was obtained and characterized by HPLC, NMR and Marfey's analyses. 149 mg of the TFA salt of NOSO-95179 were dissolved in aqueous 0.05 M HCl solution (8 ml) and the solution was freeze-dried. This step was repeated twice. The procedure yielded 110 mg of HCl salt of NOSO-95179, 97.4% pure (HPLC-MS).

MIC and time-dependent killing.

MIC determination by microdilution and direct colony suspension methodologies and time-kill assays were performed according to the CLSI standards (CLSI 2012).

Cytotoxicity assay.

The cytotoxicity assay was carried out using microcultures of human liver hepatocellular cells (HepG2/ATCC HB-8065) and human proximal tubule epithelial cells (HK-2/ATCC CRL-2190) treated with NOSO-95179. Cell viability was fluorimetrically determined using a scanning fluorometer at 485/520 nm (Lindhagen, Nygren, and Larsson 2008).

Hemolytic activity assay.

Mouse red blood cells were washed with 0.9 % sodium chloride solution (saline solution) until the supernatant was clear after centrifugation and resuspended in saline solution to 10% (v/v). 300 μL of the suspension were added to an equal volume of NOSO-95179 to give final concentrations of 256 μg/ml. Saline solution and ultrapure water were used as 0% and 100% hemolytic control respectively. Microtubes were incubated at 35°C for 45 min. Then, the microtubes were centrifuged and the supernatants were transferred to monitor the release of hemoglobin at 540 nm. Experiments were performed in triplicate.

Mouse peritonitis/sepsis infection model.

NOSO-95179 was tested against *K. pneumoniae* SSI#3010 (clinical isolate, Denmark), with a MIC determined to 4 μg/ml in a murine neutropenic peritonitis/sepsis model. Female NMRI mice

(Taconic Biosciences A/S, Lille Skensved, Denmark) were used. Mice were allowed to acclimatize for 4 days and there after neutropenia was induced by i.p injections with cyclophosphamide (Baxter A/S Søborg Denmark) at 4 days (200 mg/kg) and 1 day (100 mg/kg) prior to inoculation. Overnight K. pneumoniae colonies were suspended in saline to 10^7 CFU/ml and mice were inoculated intraperitoneally with 0.5 ml of the suspension. At 1 h post inoculation, mice were treated with NOSO-95179 at 3.12, 6.25, 12.5 and 25 mg/kg, vehicle, PBS pH 7.4, or ciprofloxacin (Fresenius Kabi 2 mg/ml, Uppsala, Sweden) at 14 mg/kg, subcutaneously as a single dose in 0.2 ml. At 4 h after treatment, mice were anesthetized, and blood was collected by axillary cut-down. Blood samples were serially diluted and plated on blood agar plates (SSI Diagnostica, Hillerød, Denmark) with the subsequent counting of colonies after incubation overnight at 35°C in ambient air.

Mouse lung infection model

NOSO-95179 was tested against *K. pneumoniae* NCTC 13442 in a neutropenic mouse pulmonary infection model by Evotec (Manchester, UK). Mice were allowed to acclimatize for 7 days, then rendered neutropenic by IP injection of cyclophosphamide (200 mg/kg on day 4 and 150 mg/kg on day 1 before infection). Mice were infected by intranasal route (4 x 10^6 CFU/mouse) under parenteral anesthesia. At 2 h post infection, mice received treatment with NOSO-95179 at 10, 30 or 100 mg/kg administered by IV route in a single dose in a volume of 10 ml/kg (8 mice per dose). At 2 h and 14 h post infection, tigecycline was delivered by IV route at 80 mg/kg in a volume of 10 ml/kg to serve as positive control. At 2 h post infection, one infected group was humanely euthanized, and lungs processed for pre-treatment quantitative culture to determine *Klebsiella* burdens. At 24 h post infection, all remaining mice were humanely euthanized. Lungs were aseptically removed, homogenized, serially diluted, and plated on CLED (cystine lactose electrolyte deficient) agar for CFU titers.

Isolation of ODL resistant mutants.

E. coli strain SQ110 [Δ(*rrsH-aspU*)*794*(::*FRT*) Δ(*rrfG-rrsG*)*791*(::*FRT*) Δ(*rrfF-rrsD*)*793*(::*FRT*) Δ(*rrsC-trpT*)*795*(::*FRT*) Δ(*rrsA-rrfA*)*792*(::*FRT*) Δ(*rrsB-rrfB*)*790*(::*FRT*) *rph-1* λ⁻; ptRNA67] that carries only one copy of chromosomal *rrn* alleles (Quan et al. 2015) was used for isolation of ODL resistant mutants. Approximately $3.9x10^9$ CFU were plated onto a Mueller-Hinton Agar plate containing 10 x MIC of NOSO-95179 (80 µg/ml). Plates were incubated 48 hours at 35°C. Individual colonies that appeared on the plate were grown in liquid culture and genomic DNA was sequenced on the Illumina MiSeq platform. The sequences were processed and analyzed using CLC Genomics Workbench 8.0.2 (CLC bio).

Metabolic labeling assay.

The effect of NOSO-95179 on macromolecular synthesis in *E. coli* APV00028 was assessed by Aptuit (Verona). Overnight cultures were diluted in M9 medium with 0.25% (wt/vol) yeast extract and allowed to grow to an A_{600} of ~0.3. The culture was incubated at 37°C for 20 min with either 2.5 µCi/ml [^{14}C]leucine to measure protein synthesis, 1.0 µCi/ml [^{14}C]thymidine for DNA synthesis, 0.5 µCi/ml [^{14}C]uridine for RNA synthesis, 5.0 µCi/ml [^{14}C]acetic acid for fatty acid synthesis, or 1.0 µCi/ml [^{14}C]*N*-acetylglucosamine for cell wall synthesis, with increasing concentrations of NOSO-95C or NOSO-95179. Four antibacterial agents (tetracycline, rifampin, ciprofloxacin, and amoxicillin) with known mechanisms of action were tested as controls. Duplicate samples of 40 µl were precipitated with TCA at 20 min after compound addition and added to 100 ml of ice-cold 20% (wt/vol) TCA. After 60 min on ice, the samples were collected over vacuum on a 96-well glass fiber filter plate (Millipore MSFBNB50) and washed three times with 150 µl of ice-cold 10% (wt/vol) TCA. A 40-µl aliquot of scintillation cocktail was added to the dried filter plate, and counts were obtained in a MicroBeta Trilux 1450 scintillation counter (PerkinElmer) (Hernandez et al. 2013).

Crystallographic structure determination.

First, ribosome-mRNA-tRNA complex was pre-formed by programming 5 µM 70S *Tth* ribosomes with 10 µM mRNA and incubation at 55°C for 10 min, followed by addition of 20 µM P-site

($tRNA_i^{Met}$) and 20 μM A-site ($tRNA^{Val}$) substrates (with minor changes from (Polikanov et al. 2015)). Each of these two steps was allowed to reach equilibrium for 10 min at 37°C in the buffer containing 5 mM HEPES-KOH (pH 7.6), 50 mM KCl, 10 mM NH_4Cl, and 10 mM $Mg(CH_3COO)_2$, Then, NOSO-95179 dissolved in the same buffer was added to a final concentration of 250 μM to the pre-formed ribosome-mRNA-tRNA complex. Crystals were grown by vapor diffusion in sitting drop crystallization trays at 19°C. Initial crystalline needles were obtained by screening around previously published ribosome crystallization conditions (Selmer et al. 2006; Korostelev et al. 2006; Polikanov, Blaha, and Steitz 2012). The best-diffracting crystals were obtained by mixing 2-3 μl of the ribosome-NOSO-95179 complex with 3-4 μl of a reservoir solution containing 100 mM Tris-HCl (pH 7.6), 2.9% (w/v) PEG-20K, 7-12% (v/v) MPD, 100-200 mM Arginine, 0.5 mM β-mercaptoethanol (Polikanov et al. 2015). Crystals appeared within 3-4 days and grew up to 150 × 150 × 1600 μm in size within 10-12 days. Crystals were cryo-protected stepwise using a series of buffers with increasing MPD concentrations until reaching the final concentration of 40% (v/v) MPD, in which they were incubated overnight at 19°C. In addition to MPD, all stabilization buffers contained 100 mM Tris-HCl (pH 7.6), 2.9% (w/v) PEG-20K, 50 mM KCl, 10 mM NH_4Cl, 10 mM $Mg(CH_3COO)_2$ and 6 mM β-mercaptoethanol. NOSO-95179 was added to the final cryo-protection solution. After stabilization, crystals were harvested, and flash frozen in a nitrogen cryo-stream at 80°K.

Diffraction data were collected on the beamline 24ID-C at the Advanced Photon Source (Argonne National Laboratory, Argonne, IL). A complete dataset for each ribosome complex was collected using 0.979Å wavelength at 100K from multiple regions of the same crystal using 0.3° oscillations. The raw data were integrated and scaled using the XDS software package (Kabsch 2010). All crystals belonged to the primitive orthorhombic space group $P2_12_12_1$ with approximate unit cell dimensions of 210Å x 450Å x 620Å and contained two copies of the 70S ribosome per asymmetric unit. Each structure was solved by molecular replacement using PHASER from the CCP4 program suite (McCoy et al. 2007). The search model was generated from the previously published

structure of the *T. thermophilus* 70S ribosome with bound mRNA and tRNAs (PDB entry 4Y4P from (Polikanov et al. 2015)). The initial molecular replacement solutions were refined by rigid body refinement with the ribosome split into multiple domains, followed by 10 cycles of positional and individual B-factor refinement using PHENIX (Adams et al. 2010). Non-crystallographic symmetry restraints were applied to 4 domains of the 30S ribosomal subunit (head, body, spur, helix 44), and 4 domains of the 50S subunit (body, L1-stalk, L10-stalk, C-terminus of the L9 protein).

Atomic model of NOSO-95179 was generated from its known chemical structure using PRODRG online software (Schuttelkopf and van Aalten 2004), which was also used to generate restraints based on idealized 3D geometry. Atomic model and restraints were used to fit/refine NOSO-95179 into the obtained unbiased electron density. The final model of the 70S ribosome in complex with NOSO-95179 and mRNA/tRNAs was generated by multiple rounds of model building in COOT (Emsley and Cowtan 2004), followed by refinement in PHENIX (Adams et al. 2010). The statistics of data collection and refinement are compiled in **Table 2.6**. All figures and movie showing atomic models were generated using PYMOL (www.pymol.org).

Testing NOSO-95179 in the bacterial and mammalian cell-free transcription-translation assays.

The effect of NOSO-95179 and NOSO-95C on *in vitro* bacterial protein synthesis was tested in the Expressway™ Cell-Free *E. coli* Expression System (Invitrogen). The *gfp* gene was amplified from the pCmGFP plasmid (Srikhanta et al. 2009), cloned into pEXP5-CT TOPO vector (Thermo Fisher) and the resulting plasmid was used as a template for *in vitro* transcription-translation. The reactions were assembled following the manufacturer's protocol and carried out in 50 µl in the wells of polystyrene black 96 half-well microplate (Greiner ref. 675077) including the addition of feed buffer at 30 minutes of incubation to support optimal protein synthesis. Reactions were initiated by adding 1 µg of plasmid DNA, plates were incubated at 30°C and fluorescence was

measured every 20 minutes (λ_{ex}=475 nm, λ_{em}=520 nm) with a microplate reader. IC_{50} values were calculated at 1 hour after addition of feed buffer using GraphPad Prism 6 Software.

The Rabbit Reticulocyte Lysate System (L4960, Promega) was used to determine the inhibitory activity of NOSO-95179 and the natural compound NOSO-95C on eukaryotic translation. Assays were performed following the manufacturer's protocol in a white polystyrene 96 half-well microplates (Corning ref. 3693) and incubated 1 h at 30 °C using luciferase mRNA and recombinant ribonuclease inhibitor (both from Promega).

Toeprinting analysis.

The DNA templates for toeprinting were generated by PCR using AccuPrime DNA Polymerase (Thermo Fisher Scientific) and primers listed in

Table 2.4: DNA primers used for generating the templates for toeprinting analysis.

Primer name	**Nucleotide sequence (5' – 3')**
NV1	GGTTATAATGAATTTTGCTTATTAAC
T7-ermBL-fwd	TAATACGACTCACTATAGGGCTTAAGTATAAGGAGGAAAAAATATGTTGG TATTCCAAATGCGTAATGTAGATAAAACAATTACTATTTT
T7-ompX-fwd	TAATACGACTCACTATAGGGACTTATTTGAATCACATTTG
RBS-ompX$_{6}$-$_{7}$ermBL rev	GTTTTATCTACATTACGACATGCAATTTTTTTCATAACCACCTCAAATGTG ATTCAAAT
ompX$_{6}$-$_{7}$ermBL NV1 rev	GGTTATAATGAATTTTGCTTATTAACTTAAATAGTAATTGTTTTATCTACAT TACGACAT
ompX-NV1-rev	GGTTATAATGAATTTTGCTTATTAACTTAAGTACCTGCGGTGAAAGC
T7-csrA-fwd	TAATACGACTCACTATAGGGATACAGAGAGACCCGA
csrA-NV1-rev	GGTTATAATGAATTTTGCTTATTAACTTAAACTGTCACGGTGACCTCATC
T7-secM-fwd	TAATACGACTCACTATAGGGAGTTTTATAAGGAGGAAAACATATGGCGC ATTTTACCCCACAAG
SecM-NV1-rev	GGTTATAATGAATTTTGCTTATTAACGAGTTAATAAAATGAAGTAAAGG

The fusion template *ompX$_{1-6}$-ermBL$_{7-15}$* was prepared using 3 primers in a 2-step PCR reaction. First, the primers T7-ompX-fwd and RBS-ompX$_{6}$-$_{7}$ermBL-rev were used to generate the 5' fragment which was then re-amplified using primers T7 and ompX$_{6}$-$_{7}$ermBL-NV1-rev. The complete sequences of the templates are shown in **Table 2.5**.

Table 2.5: The nucleotide sequences of the templates used in the toeprinting experiments.

Blue – T7 promoter; bold – ORF; orange – annealing region of the toe printing primer NV1.

Template	Nucleotide sequence (5' – 3')
ompX$_{1-6}$ - *ermBL*$_{7-15}$	TAATACGACTCACTATAGGGACTTATTTGAATCACATTTGAGGTGG TT**ATGAAAAAAATTGCATGTCGTAATGTAGATAAAACAATTACTA TTTAA**GTTAATAAGCAAAATTCATTATAACC
secM	TAATACGACTCACTATAGGGAGTTTTATAAGGAGGAAAACAT**ATGG CGCATTTTACCCCACAAGCAAAATTCAGCACGCCCGTCTGGATA AGCCAGGCGCAAGGCATCCGTGCTGGCCCTCAACGCCTCACCTA A**CAACAATAAACCTTTACTTCATTTTATTAACTCGTTAATAAGCAAA ATTCATTATAACC
ompX	TAATACGACTCACTATAGGGACTTATTTGAATCACATTTGAGGTGG TT**ATGAAAAAAATTGCATGTCTTTCAGCACTGGCCGCAGTTCTGG CTTTCACCGCAGGTACTTAA**GTTAATAAGCAAAATTCATTATAACC
csrA	TAATACGACTCACTATAGGGATACAGAGAGACCCGACTCTTTTAAT CTTTCAAGGAGCAAAGA**ATGCTGATTCTGACTCGTCGAGTTGGTG AGACCCTCATGATTGGGGATGAGGTCACCGTGACAGTTTAA**GTTA ATAAGCAAAATTCATTATAACC

Toeprinting reactions were carried out in 5 µl of PURExpress transcription-translation system (New England Biolabs). The final concentrations of inhibitors in the reactions were 50 µM unless otherwise indicated; NOSO-95C and NOSO-95719 were added as stock solutions in water. PCR-generated templates were transcribed and translated for 20 minutes at 37°C, followed by primer extension (15 min) using radio-labeled NV1 primer and reverse transcriptase (Roche).

The PCR-generated DNA template was expressed in a cell-free transcription-translation system (PURExpress *In Vitro* Protein Synthesis kit, New England BioLabs). For a typical reaction, 2 µl of solution A (kit), 1 µl of solution B (kit), 0.5 µl of DNA template (0.5 pmol/µl), 0.5 µl of radioactive primer (1 pmole), 0.2 µl of Ribolock RNAse inhibitor (40 U/µl, Thermo Scientific), 0.5 µl of the compound to be tested and 0.3 µl of H_2O were combined in the reaction tube chilled on ice. Samples were incubated at 37°C for 20 min. Primer extension was performed using freshly prepared reverse transcriptase (RT) mix by combining five volumes of the dNTPs solution (4 mM each), 4 volumes of the Pure System Buffer (9 mM $Mg(CH_3COO)_2$, 5 mM potassium phosphate (pH 7.3), 95 mM potassium glutamate, 5 mM NH_4Cl, 0.5 mM $CaCl_2$, 1 mM spermidine, 8 mM

putrescine, 1 mM DTT) and one volume of AMV RT (Roche, 20-25 U/µl). One µl of the RT mix was added to the 5 µl of translation reaction, and samples were incubated at 37°C for 15 min. Reactions were terminated by addition of 1 µl of 10 M NaOH and incubation for 10 min at 37°C. The samples were then neutralized by the addition of 0.8 µl of 12 N HCl. 200 µl of resuspension buffer (0.3 M sodium acetate (pH 5.5), 5 mM EDTA, 0.5% SDS) was added to the reactions, and samples were extracted with phenol [Tris-saturated (pH 7.5–7.7)] and then with chloroform. DNA was precipitated by addition of 3 volumes of ethanol. After removal of supernatants, the pellets were washed with 500 µl of 70% ethanol, air-dried and resuspended in 6 µl of formamide loading buffer (a 1-ml stock solution contains 980 µl of formamide (deionized, nuclease-free, Ambion), 20 µl of 0.5 M EDTA (pH 8.0), 1 mg of bromophenol blue and 1 mg of xylene cyanol). Gel electrophoresis was run in a 6% sequencing gel. Gels were transferred onto Whatman paper, dried and exposed to the phosphorimager screen for 2 hours or overnight. Gels were visualized in a Typhoon phosphorimager (GE Healthcare) (Orelle, Szal, et al. 2013; Vazquez-Laslop, Thum, and Mankin 2008).

In vivo miscoding and stop codon readthrough.

The missense reporter plasmid encoding *lacZ* (Glu537Gly$_{GGG}$) (Manickam et al. 2014) was propagated in *E. coli* CSH142 (F-, *ara-600* del*(gpt-lac)*5 LAM^{-} *relA1 spoT1 thi-1*) cells that were grown in LB medium supplemented with 30 µg/ml chloramphenicol. For testing the stop codon suppressing activity of NOSO-95179, *E. coli* XAC-1 pGF1B cells (F′ *lacI*$_{373}$*lacZ*$_{\mu 118am}$ *pro*B^{+}/F^{-} Δ(*lac-proB*)$_{XIII}$ *nalA rif arg*E$_{am}$ *ara*) carrying a *lacZ* gene with a premature stop codon (Tyr17TAG) (Normanly et al. 1986) were grown in LB medium supplemented with 100 µg/ml of ampicillin. Upon reaching A_{600} of 1.0, 0.5 ml of cell culture were mixed with 3.5 ml of LB soft agar (0.6%) kept at 50^{o}C and poured onto an LB-agar plate containing the respective antibiotic (chloramphenicol (20 µg/ml) or ampicillin (100µg/ml)), IPTG (0.2 mM) and X-gal (80 µg/ml). After soft agar solidification, 1 µl of 25 mg/ml solution of streptomycin (25 µg), 1 µl of 10 mg/ml solution of tetracycline (10 µg) or 1 µl of 10 mM solution of NOSO-95179 (13 µg) were spotted on top of the cell lawn. The plates

were incubated overnight at 37°C. Miscoding- or stop-codon read-through activity was revealed by a blue halo around the spotted antibiotic.

2.2 Experimental results

Identification of ODLs as a new class of antimicrobial agents

In the search for new antibacterials, we screened supernatants of eighty cultured *Xenorhabdus* strains for the presence of antimicrobial activity. The three most abundant and chemically related antibacterial compounds with molecular masses of 1296 Da (NOSO-95A), 1280 Da (NOSO-95B) and 1264 Da (NOSO-95C) were isolated from the supernatant of *Xenorhabdus nematophila* strain K102 (CNCM I-4530). Chemical structures of the compounds, solved by NMR and verified by *de novo* chemical synthesis (**Table A1 in Appendix A, Figure 2.4**) revealed them as representatives of a new chemical class of antibiotics, which we named odilorhabdins (ODLs) (**Figure 2.5A**).

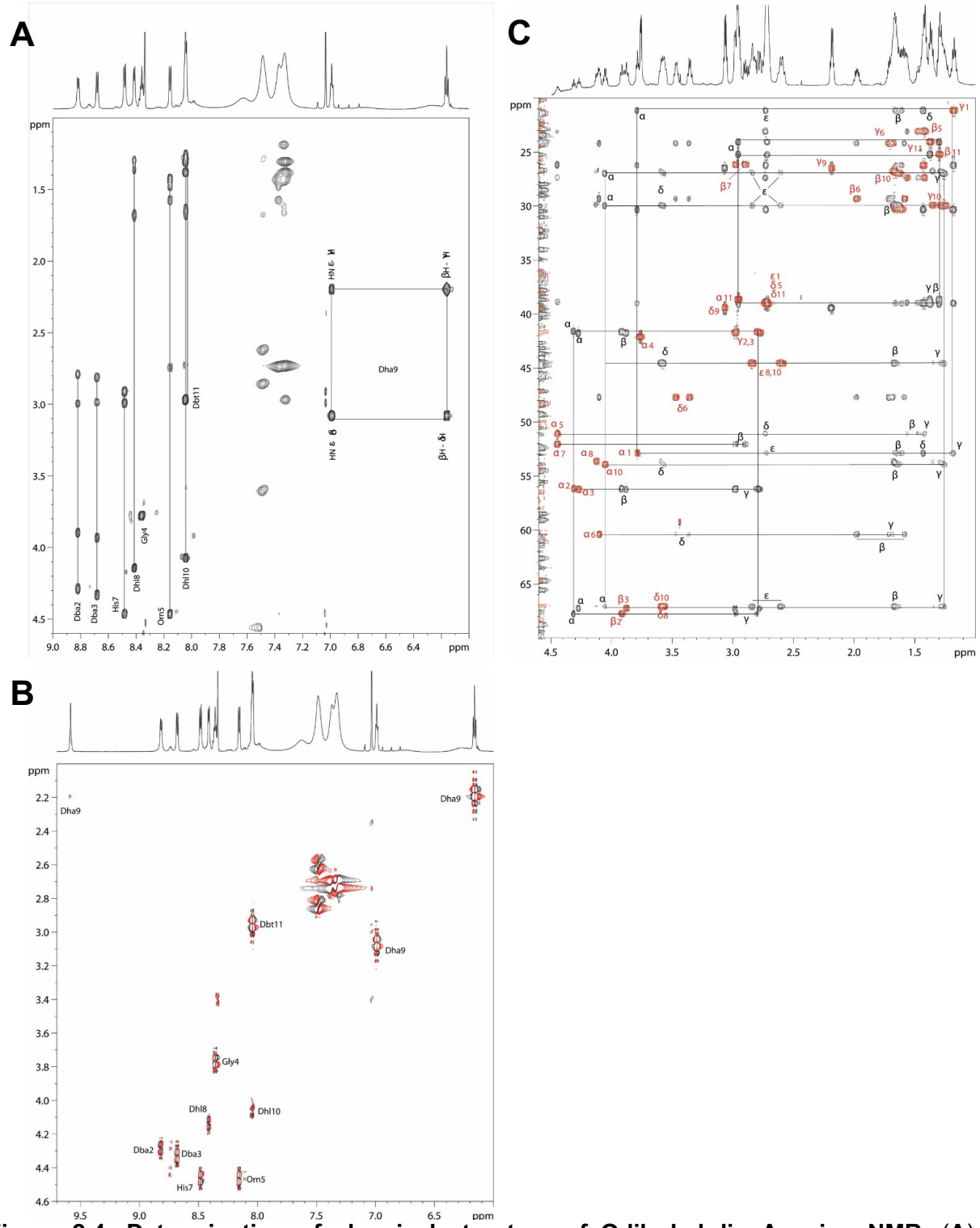

Figure 2.4: Determination of chemical structure of Odilorhabdin A using NMR. (**A**) Fingerprint of the TOCSY experiment with Odilorhabdin A with the assignment of spin systems (H_2O/D_2O, 95/5 v/v, pH 3.5, 280 K). (**B**) Part of the COSY experiment with Odilorhabdin A showing the amide-alpha proton cross-peaks. Notice that for the non-classical Dha_9 residue three cross-peaks are observed. The 9.6/2.2 ppm cross peak of weak intensity corresponds to the $^5J_{HN\text{-}H\gamma}$ long-range coupling constant, the 7.0/3.06 ppm cross peak to the $^3J_{HN\varepsilon\text{-}H\delta}$ coupling constant and the 6.17/2.2 ppm cross peak to the $^3J_{H\beta\text{-}H\delta}$ coupling constant. (H_2O/D_2O, 95/5 v/v,

pH 3.5, 280 K). (**C**) Superposition of the HSQC (red cross-peaks) and the HSQC-TOCSY (black cross-peaks) maps of Odilorhabdin A. Red labels (type of carbon and residue number) are for the HSQC and black labels (type of proton) show the TOCSY transfers used to identify the spin systems of all residues (H_2O/D_2O, 95/5 v/v, pH 3.5, 280 K). Only some spin systems are labeled for clarity.

The sequence of NOSO-95A was determined as Lys_1-Dab(βOH)$_2$-Dab(βOH)$_3$-Gly_4-Orn_5-Pro_6-His_7-Dhl_8-Dha_9-Dhl_{10}-Dbt_{11}, including four types of non-standard amino-acid residues: αγ-diamino β-hydroxy butyric acid (Dab(βOH) in positions 2 and 3; δ-hydroxy lysine (Dhl) in positions 8 and 10; αβ-dehydro arginine (Dha) in position 9; and αδ-diamino butane (Dbt) in position 11 (**Figure 2.5A**). NOSO-95B and C differ from NOSO-95A by the substitution in position 10 of the Dhl by a lysine (NOSO-95B) and by the substitutions in position 8 and 10 of the Dhl by lysines (NOSO-95C).

The apparent peptidic structure of ODLs suggested that they are the products of the NRPSs. Using an anti-SMASH prediction, we identified the putative biosynthetic gene cluster (ENA accession number: PRJEB17644) consisting of four large NRPS-coding genes (**Figure 2.5A**) in the genome of *X. nematophila* strain CNCM I-4530. Similar *odl* clusters could be also found in other sequenced *X. nematophila* strains. Inactivation of the first gene of the cluster in the reference strain *X. nematophila* ATCC19061, XNC1_2467 (*odl1* in **Figure 2.5A**), abolished production of all three antimicrobial compounds as revealed by LC-MS (data not shown) confirming that the NRPS cluster is responsible for the production of bioactive ODLs. The peptidic nature and relative simplicity of ODLs opened room for improvement of their activity by modifying the structure via *de novo* chemical synthesis. This experimental effort resulted in the development of a derivative, NOSO-95179 (**Figure 2.5B**), which exhibits a better selectivity for bacterial *versus* eukaryotic target compared to natural ODLs and thus, represents a preferable lead for further drug development. NOSO-95179 derives from NOSO-95C by the substitution in position 3 of the Dab(βOH) by an alanine and by the truncation of the lysine and the Dbt in positions 10 and 11. It

has been used in our studies, along with the native prototype NOSO-95C, to identify the site of binding and the mode of action of ODLs.

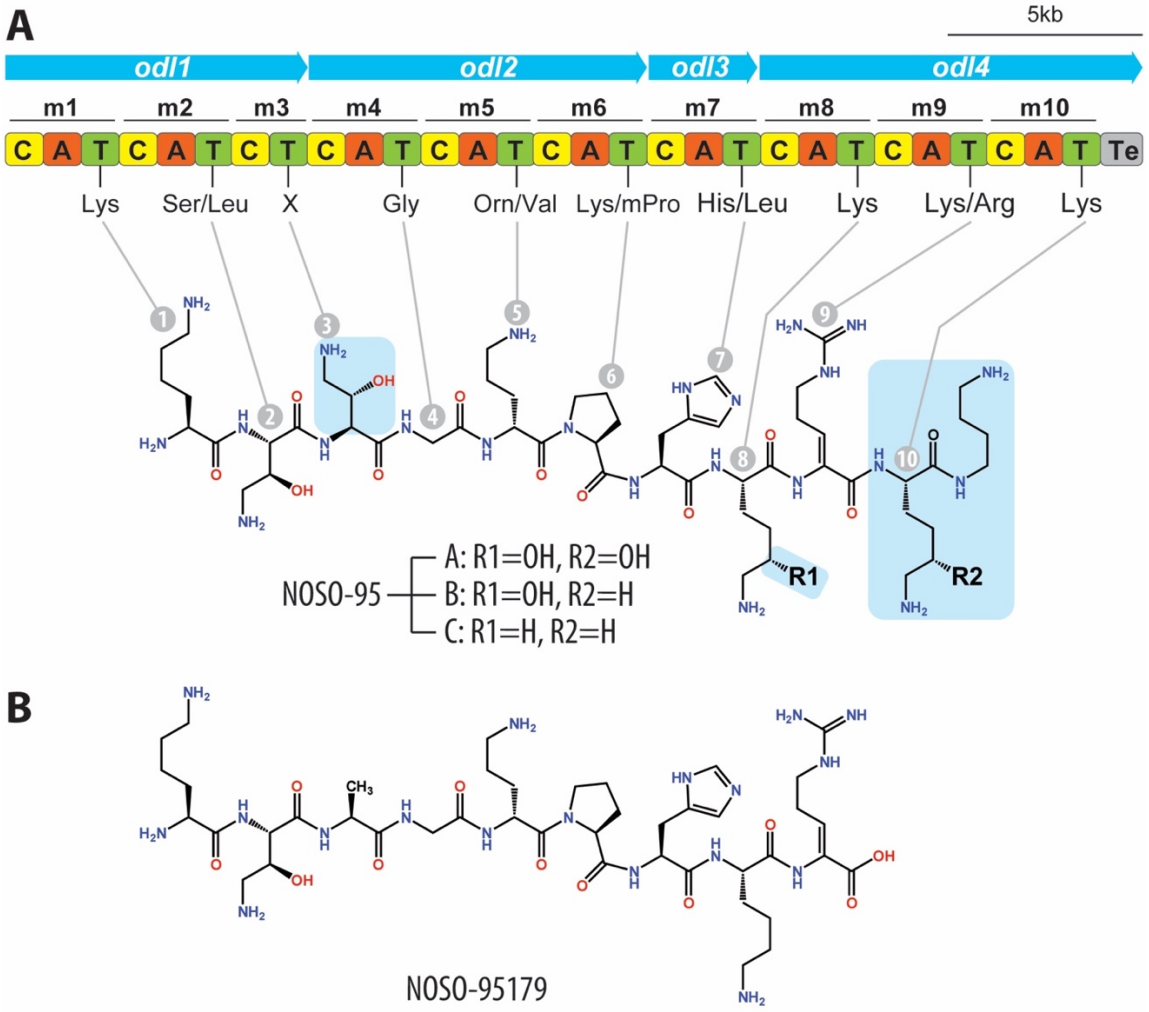

Figure 2.5: Chemical structures of ODLs and the organization of the biosynthetic gene cluster in the ODL producer. (**A**) Chemical structures of natural ODLs NOSO-95A, -B, -C, and the structure of the gene cluster in the X. nematophila K102 (CNCM I-4530) genome encoding NRPS proteins responsible for the ODL biosynthesis. The predicted NRPS modules (m1-m10), each composed of a condensation domain (C), an adenylation domain (A) and a thiolation/peptide carrier domain (T) are indicated alongside with the amino acids incorporated by the respective modules. 'X' indicates a module whose specificity was difficult to assign on the basis of in silico analysis. The sequence of this pseudopeptide was determined as Lys_1-$Dab(\beta OH)_2$-$Dab(\beta OH)_3$-Gly_4-Orn_5-Pro_6-His_7-Dhl_8-Dha_9-Dhl_{10}-Dbt_{11}. Chemical moieties of natural ODLs that are absent or altered in the synthetic NOSO-95179 compound are highlighted in light blue. (**B**) Chemical structure of the fully-synthetic ODL derivative NOSO-95179 with the sequence Lys_1-$Dab(\beta OH)_2$-Ala_3-Gly_4-Orn_5-Pro_6-His_7-Lys_8-Dha_9.

ODLs inhibit protein synthesis by acting upon the ribosome

In order to elucidate the mode of action and intracellular target of ODLs, we first tested the effect of NOSO-95179 and NOSO-95C on the incorporation of radiolabeled precursors into biopolymers in bacterial (*E. coli*) cells. These metabolic labeling experiments demonstrated that ODLs primarily interfere with protein synthesis in living bacteria (**Figure 2.6A**). Although the antibiotic also inhibited cell wall biosynthesis, our subsequent findings made us believe that this was a secondary effect resulting from inhibition of translation. Consistent with this conclusion, NOSO-95179 and NOSO-95C readily inhibits production of the green fluorescent protein in an *E. coli* cell-free transcription-translation system (IC_{50} = 0.55 ± 0.12 μM and IC_{50} = 0.63 ± 0.05 μM, respectively) (**Figure 2.6B**). Importantly, NOSO-95179 is more than 300-fold more active in inhibiting bacterial translation compared to eukaryotic protein synthesis, while this ratio is only 16-fold for NOSO-95C (**Figure 2.6C**). Altogether, these experiments reveal ODLs as potent and selective inhibitors of bacterial protein synthesis.

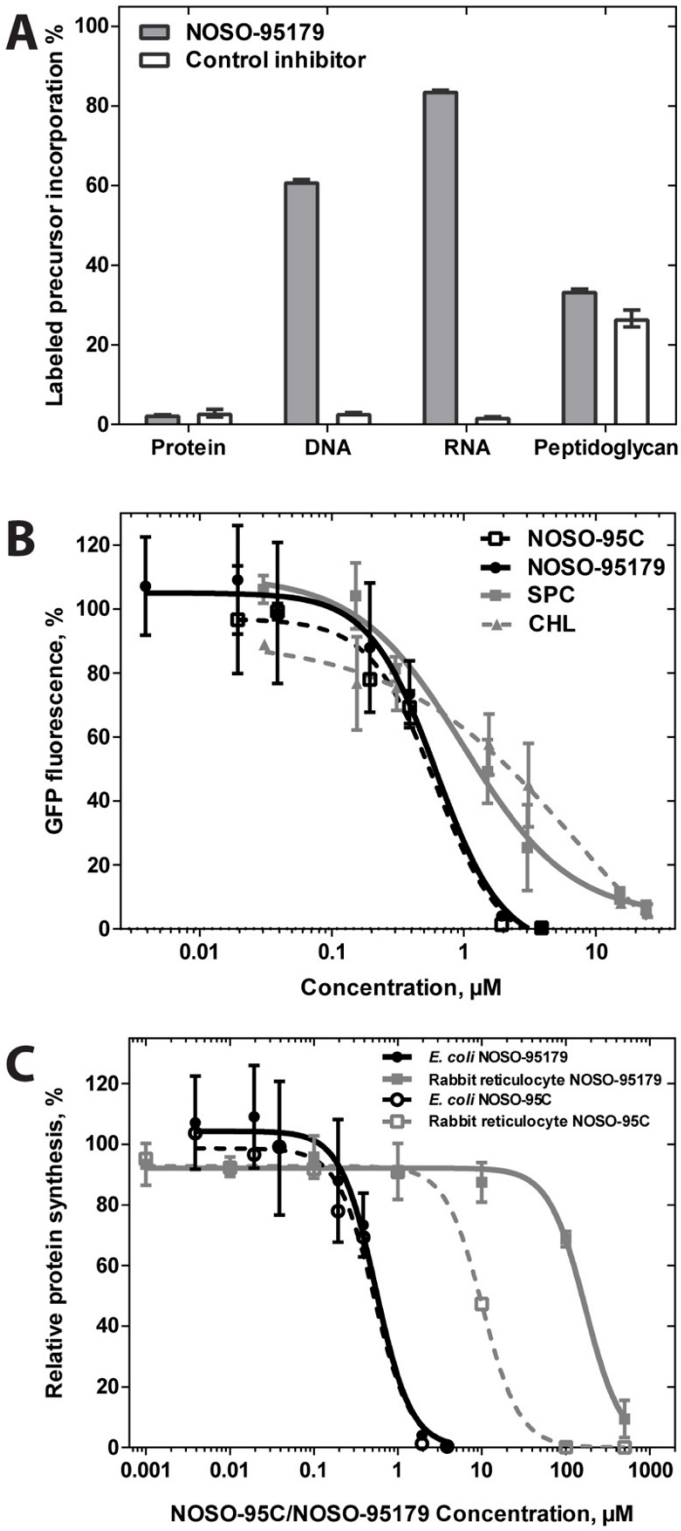

Figure 2.6: ODLs interfere with protein synthesis *in vivo* and *in vitro*. (**A**) Impact of NOSO-95179 on macromolecular biosynthesis in *E. coli*. Incorporations of [^{3}H] L-leucine (protein), [^{3}H] thymidine (DNA), [^{3}H] uridine (RNA), and [^{3}H] N-acetyl-D-glucosamine (peptidoglycan) were determined in *E. coli* cells treated with NOSO-95179 and NOSO-95C at 32 μg/ml (16-fold MIC) for 30 min (grey bars). Tetracycline (8 μg/ml), ciprofloxacin (0.125 μg/ml), rifampicin (128 μg/ml), and amoxicillin (128 μg/ml) were used as positive controls (white bars). Data

represent means of two independent experiments ± SD. (**B**) Inhibition of synthesis of the GFP reporter protein in the *E. coli* cell-free transcription-translation system. The known protein synthesis inhibitors spectinomycin (SPC) and chloramphenicol (CHL) were used as positive controls. (**C**) Comparison of protein synthesis inhibition by NOSO-95179 (squares, solid curve) and NOSO-95C (open squares, dashed curve) in the bacterial and in rabbit reticulocyte cell-free translation systems. Error bars represent standard deviation of duplicates.

In order to identify the primary target of the NOSO-95179 action, we selected resistant mutants carrying alterations in the drug target site. To this end, we used the *E. coli* strain SQ110, which lacks 6 out of 7 chromosomal *rrn* alleles and is particularly suited for isolating resistance mutations in the components of protein synthesis apparatus, including rRNA (Orelle, Carlson, et al. 2013; Quan et al. 2015). After 10^9 *E. coli* cells were applied onto an agar plate containing 10-fold MIC (80 μg/mL) of NOSO-95179, twenty drug-resistant colonies appeared. Whole-genome sequencing of the resistant clones showed that one of the clones had a mutation in the *rpsJ* gene encoding ribosomal protein S10 (**Table A2 in Appendix A**), whereas all the other analyzed ODL resistant isolates carried mutations in the 16S rRNA gene of the small ribosomal subunit (**Figure 2.7A, Table A2 in Appendix A**). In addition, we tested several of the previously isolated 16S rRNA mutants from our collection (Orelle, Carlson, et al. 2013; Polikanov et al. 2014) and found one more 16S rRNA mutation, G1058C, conferring resistance to NOSO-95179 (**Table A2 in Appendix A**). All the identified 16S rRNA mutations are clustered in the vicinity of the **d**ecoding center. This functional center of the ribosome is targeted by several clinically-useful ribosomal antibiotics (e.g., tetracyclines, aminoglycosides, negamycin) (Brodersen et al. 2000; Pioletti et al. 2001; Polikanov et al. 2014; Olivier et al. 2014; Cocozaki et al. 2016). However, most of the ODL resistance mutations conferred no cross-resistance to other ribosomal inhibitors (**Table A2 in Appendix A**). The activity of the NOSO-95179 compound was also unaffected by TetM, a ribosome protection protein that confers resistance to tetracycline by displacing the drug from the ribosome (Donhofer et al. 2012; Arenz et al. 2015). Altogether, these results revealed the ribosome as the primary

target of ODLs and suggested that inhibitors belonging to this new class of antibiotics bind at a location distinct from the sites of action of the known drugs targeting the small ribosomal subunit.

ODL binding site in the bacterial ribosome

To unambiguously identify the mode of binding of ODLs to their target, we solved the crystal structure of the *Thermus thermophilus* 70S ribosome associated with mRNA, A-, P- and E-site tRNAs and NOSO-95179 at 2.6Å resolution (**Table 2.6**). In this study we used deacylated valine-specific tRNA as the A-site substrate and initiator methionine-specific tRNA as the P-site substrate. E site of the ribosome contained $tRNA^{Val}$. The difference electron density maps ($\boldsymbol{F}_{obs} - \boldsymbol{F}_{calc}$) were used to localize the antibiotic on the ribosome. A strong peak of positive electron density (**Figure 2.7B**) resembling distinct features of the NOSO-95179 chemical structure was observed in the vicinity of the decoding center in both copies of the ribosome in the asymmetric unit. Atomic models of the ribosome-bound NOSO-95179, generated from its chemical structure and the restraints based on idealized 3D geometry were used to fit the drug into the observed electron density (**Figure 2.7B**). The proximity of the resistance mutations to this site of NOSO-95179 binding confirmed that this is the primary site of ODL action on the bacterial ribosome (**Figure 2.7C, D**).

Table 2.6: X-ray data collection and refinement statistics.

Crystals	**70S ribosome complex with A-, P- and E-tRNAs and NOSO-95179**
Diffraction data	
Space Group	$P2_12_12_1$
Unit Cell Dimensions, Å (a x b x c)	209.17 x 448.69 x 618.53
Wavelength, Å	0.9795
Resolution range (outer shell), Å	363-2.60 (2.67-2.60)
I/σI (outer shell with I/σI=1)	8.60 (0.85)
Resolution at which I/σI=1, Å	2.60
Resolution at which I/σI=2, Å	2.83
CC(1/2) at which I/σI=1, %	18.0

CC(1/2) at which I/σI=2, %		50.1
Completeness (outer shell), %		99.0 (97.3)
R_{merge} (outer shell)%		13.7 (179.4)
No. of crystals used		1
No. of Reflections Used:	Observed	6,968,917
	Unique	1,740,501
Redundancy (outer shell)		4.00 (3.95)
Wilson B-factor, Å^2		56.9
Refinement		
R_{work}/R_{free}, %		21.2/24.9
No. of Non-Hydrogen Atoms		
RNA		200,298
Protein		90,976
Ions (Mg, K, Zn, Fe)		2,856
Waters		5,101
Ramachandran Plot		
Favored regions, %		94.17
Allowed regions, %		5.01
Outliers, %		0.82
Deviations from ideal values (RMSD)		
Bond, Å		0.004
Angle, degrees		0.837
Chirality		0.040
Planarity		0.005
Dihedral, degrees		14.4
Average B-factor (overall), Å^2		62.9

$R_{merge} = \Sigma |I - \langle I \rangle| / \Sigma I$, where I is the observed intensity and <I> is the average intensity from multiple measurements.
$R_{work} = \Sigma|F_{obs} - F_{calc}| / \Sigma F_{obs}$. For calculation of R_{free}, 5% of the truncated dataset was excluded from the refinement.

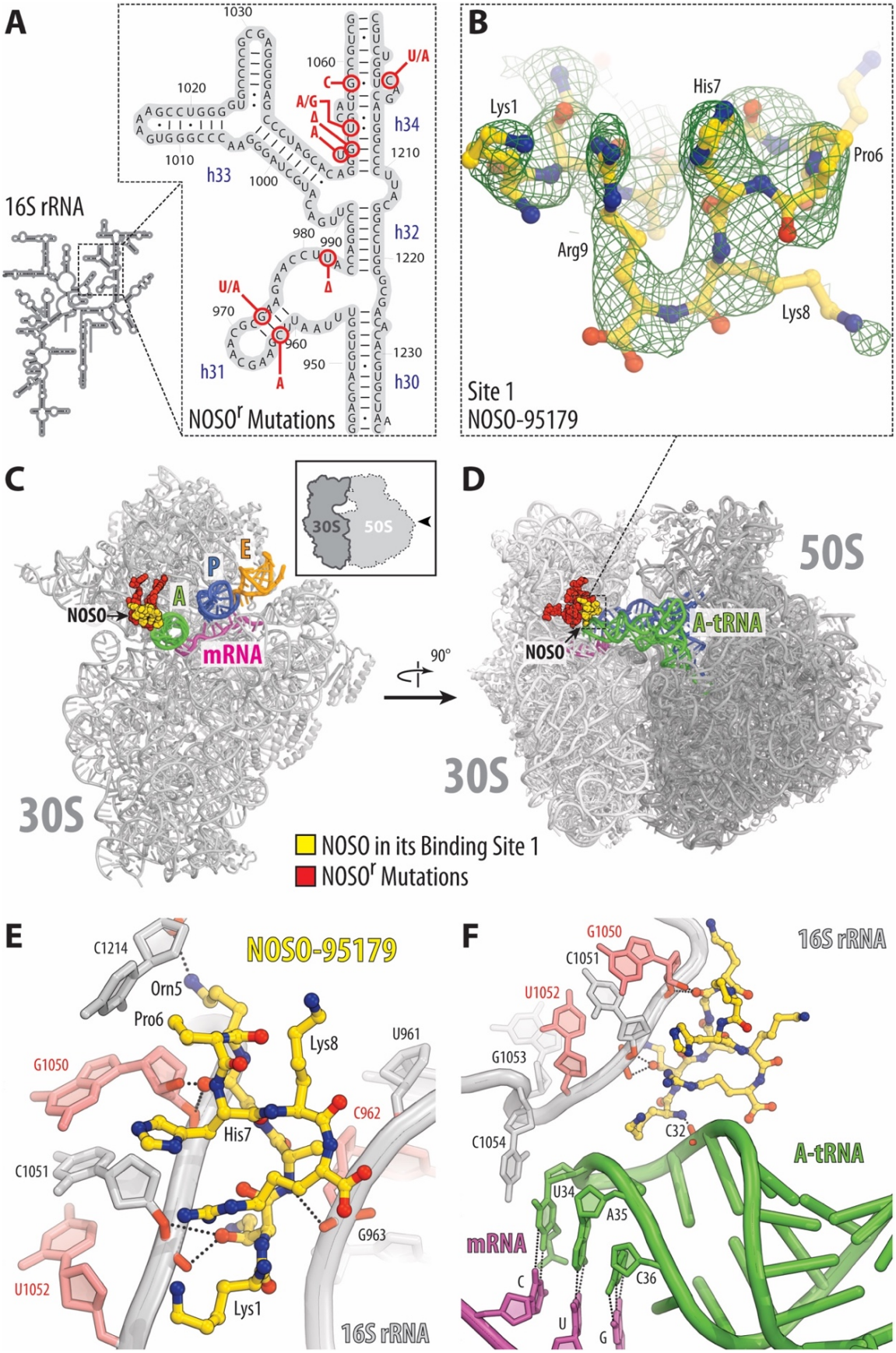
A
16S rRNA
NOSO^r Mutations
h34
h33
h32
h31
h30
B
Lys1
His7
Pro6
Arg9
Lys8
Site 1
NOSO-95179
C
30S
50S
P
E
A
NOSO
mRNA
30S
D
50S
A-tRNA
NOSO
30S
90°
NOSO in its Binding Site 1
NOSO^r Mutations
E
NOSO-95179
C1214
Orn5
Pro6
Lys8
U961
G1050
C962
His7
C1051
G963
U1052
Lys1
16S rRNA
F
16S rRNA
G1050
C1051
U1052
G1053
C1054
C32
A-tRNA
U34
A35
mRNA
C36
C
U
G

Figure 2.7: Structure of NOSO-70S ribosome complex. (**A**) The secondary structure of the 16S rRNA and positions of the resistance mutation identified in *E. coli*. Relevant helices of the 16S rRNA are labeled. (**B**) Chemical structure of NOSO-95179 fitted into the difference Fourier map at a primary site within the *T. thermophilus* 70S ribosome (green mesh). The refined model of the compound is displayed in its respective electron density before the refinement and viewed from two different perspectives. The unbiased ($F_{obs} - F_{calc}$) difference electron density map is contoured at 3.0σ. Carbon atoms are colored yellow, nitrogens are blue, oxygens are red. Some amino acids are labeled to indicate the orientation of the inhibitor molecule. (**C, D**) Overview of the NOSO-95C binding sites (yellow) on the *T. thermophilus* 30S subunit (A) and 70S ribosome (B). 30S subunit is light grey, the 50S subunit is dark grey. mRNA is shown in magenta and tRNAs are displayed in green for the A site, in blue for the P site, and in orange for the E site. In (C), the 30S subunit is viewed from the subunit interface, as indicated by the inset; 50S subunit and parts of tRNAs are removed for clarity. The 16S rRNA nucleotides whose mutations cause resistance to NOSO-95179 are highlighted in red. (**E, F**) Interactions of NOSO-95179 with the 16S rRNA (E, F) and with tRNA (F). 16S rRNA residues whose mutations cause resistance to NOSO-195179 are highlighted in light red. In (F), the nucleotides of the mRNA A-site codon and the tRNA anticodon are shown as sticks.

In this primary binding site, the extended NOSO-95179 molecule folds up and adopts a compact conformation, in which it forms multiple hydrogen bonds with 16S rRNA residues of helices 31, 32 and 34 (**Figure 2.7E, F**). None of the contacts directly involves rRNA bases. Rather, the drug recognizes sugar-phosphate backbone atoms, whose spatial arrangement defines the placement of the drug in its binding site. This conclusion is consistent with the lack of protection of the rRNA bases from chemical modification by ODLs (data not shown). The 16S rRNA resistance mutations, all of which disrupt base pairs in helices 31 and 34 (**Figure 2.7A)**, likely interfere with drug binding by changing the geometry of the rRNA backbone. Bound in this site, NOSO-95179 closely approaches the anticodon loop of the A-site tRNA where the α-amine of the Lys1 residue of the antibiotic forms a hydrogen bond with the non-bridging phosphate oxygen of C32 in the anticodon loop of the A-site tRNA (**Figure 2.7F**). As it has been described for negamycin (Polikanov et al. 2014; Olivier et al. 2014), the simultaneous interaction of the inhibitor with the ribosome and tRNA is expected to increase the affinity of aminoacyl-tRNA during decoding and potentially decrease the accuracy of translation by stimulating binding of near-cognate aminoacyl-tRNAs. Tighter binding may also interfere with the translocation of the A-site tRNA into the P site.

Several different classes of ribosome-targeting inhibitors bind and act upon the decoding center. Superposition of the structure of NOSO-95179 in complex with the 70S ribosome with the known structures of negamycin, tetracycline, and aminoglycoside antibiotic paromomycin and streptomycin shows no overlap with the binding site of NOSO-95179 (**Figure 2.8A, B**). Thus, NOSO-95179 has a unique binding site within the ribosome that is not exploited by any other known inhibitor.

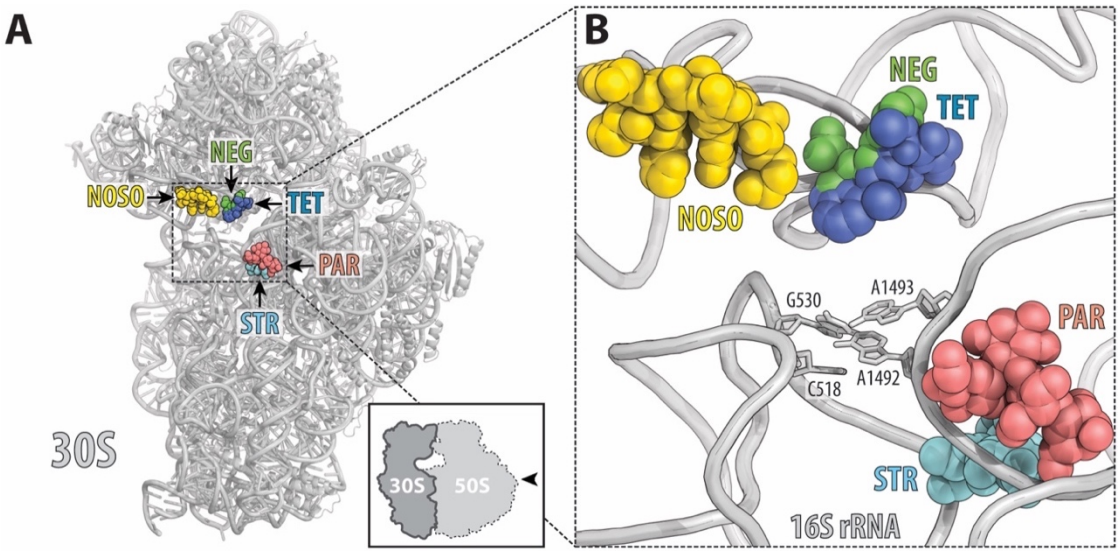

Figure 2.8: Antibiotics that bind in the decoding center on the small ribosomal subunit. (**A, B**) The location of the NOSO-95179 binding site relative to the binding sites of other antibiotics known to target the decoding center of the small ribosomal subunit: streptomycin (STR, cyan), paromomycin (PAR, salmon), tetracycline (TET, blue), negamycin (NEG, green). In (B), the 16S rRNA nucleotides critical for decoding are shown as sticks.

The producers of ribosome-targeting antibiotics often protect their own ribosomes by post-transcriptionally modifying of the rRNA nucleotides located in the inhibitor binding site. Knowing the primary site of the ODL action, we analyzed by primer extension the corresponding segments

of the 16S rRNA isolated from the *X. nematophilia,* a strain that produces ODL, and from a closely related, but non-ODL producing strain. However, we did not detect any specific difference in the primer extension patterns (data not shown) suggesting that either the protective rRNA modification does not affect the progression of the reverse transcriptase, or more likely, that other mechanisms, e.g. ODL efflux, protects the producer from the inhibitor.

In addition to the primary site of NOSO-95179 action, we also observed electron density peak at the interface between the two subunits, where helix 44 of the 16S rRNA and helix 64 of the 23S rRNA interact with each other (**Figure 2.9A, B**). We attributed this density to binding of the second molecule of the inhibitor (**Figure 2.9C**). In the secondary binding site, NOSO-95179 interacts with the backbones of the nucleotides 1472-1474 of the 16S rRNA and the nucleotides 1987-1989 of 23S rRNA (**Figure 2.9D**) and with the Glu45 side chain of the ribosomal protein L14. Unlike the primary binding site in the decoding center, the second ODL site is far from known ribosome functional centers and is likely functionally irrelevant; it probably results from promiscuous binding of the positively charged flexible ODL to the polyanionic rRNA scaffold.

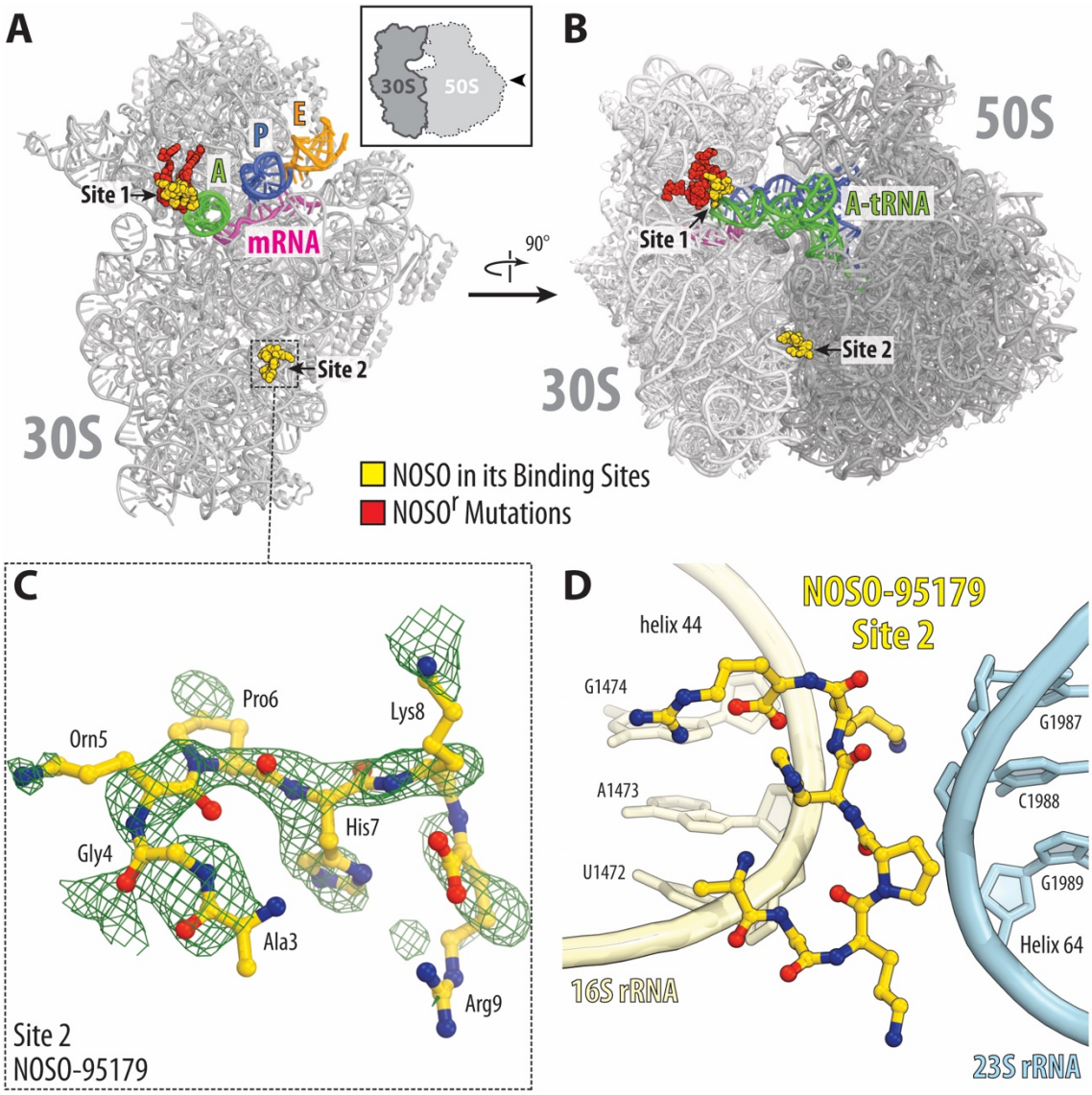

Figure 2.9: The secondary binding site of NOSO-95179 in the bacterial ribosome. (**A, B**) Overview of the NOSO-95C binding sites (yellow) on the *T. thermophilus* 30S subunit (A) and 70S ribosome (B). Color scheme is the same as in Figures 2.4C, D. (**C**) Chemical structure of NOSO-95179 fitted into the difference Fourier map at site 2 within the *T. thermophilus* 70S ribosome (green mesh). (**D**) Interactions of the NOSO-95179 with the elements of the 70S ribosome at site 2.

Binding of ODLs stalls the ribosome and causes miscoding.

To elucidate the mode of action of ODLs we used toeprinting analysis. This technique uses primer extension to detect antibiotic-induced ribosome stalling during *in vitro* translation of a model mRNA (Orelle, Carlson, et al. 2013; Hartz et al. 1988). The translation reactions were additionally supplemented with an inhibitor of one of the aminoacyl-tRNA synthetases (RS); the resulting depletion of the corresponding aminoacyl-tRNA makes the ribosome to stop at the 'hungry' codon of the open reading frame (ORF) (Vazquez-Laslop et al. 2011) (**Figure 2.10A**). For instance, addition of the Thr-RS inhibitor borrelidin arrests translation of the model *ermBL* ORF at the 11th codon, when the Thr_{12} codon enters the ribosomal A site (**Figure 2.10B**, lane 1, the upper red arrowhead). Such antibiotic-independent translation arrest helps to assess the efficiency of inhibition of translation by the investigated antibiotic at the preceding codons of the ORF.

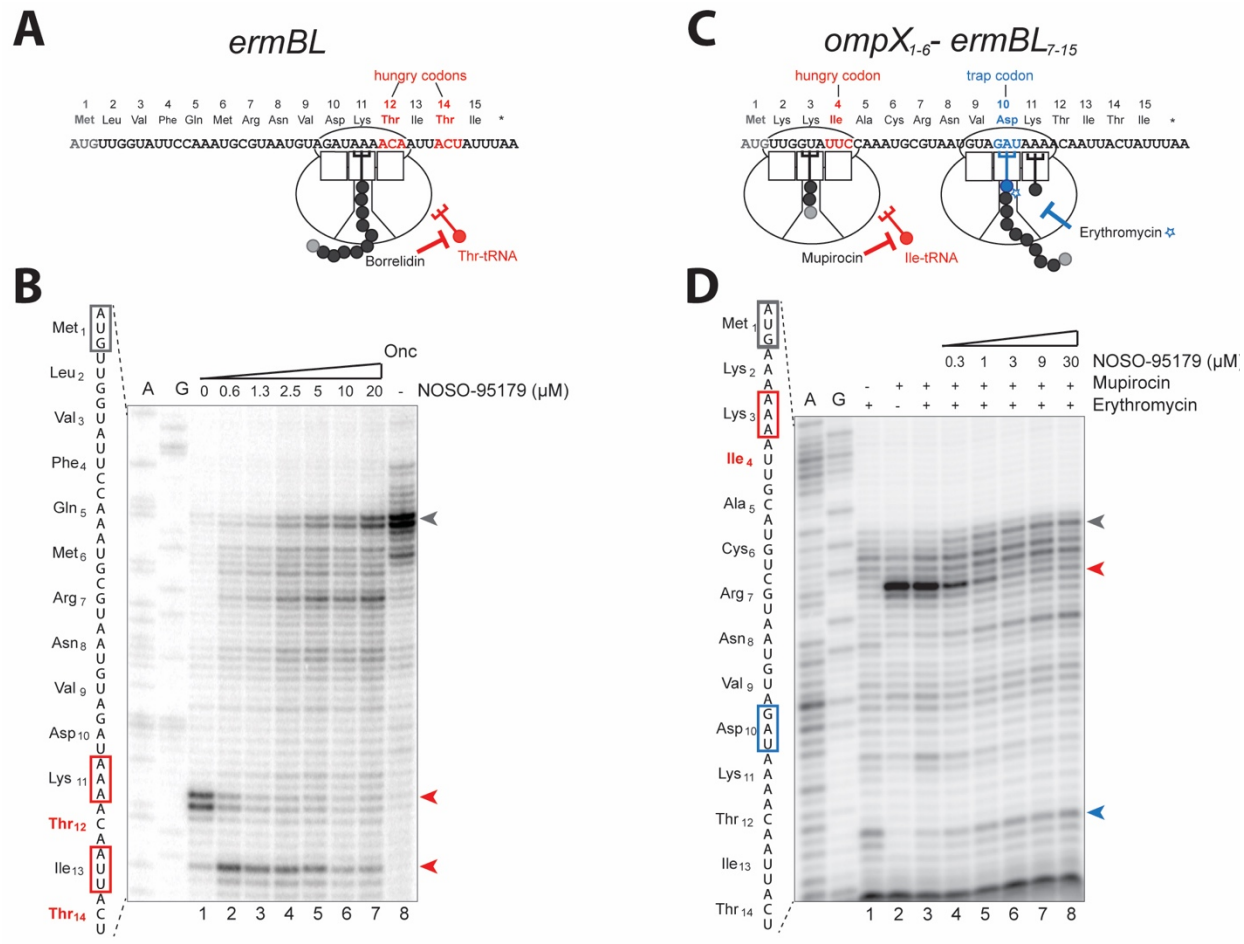

Figure 2.10: Mechanism of ODL action. (**A-D**) Toeprinting analysis of the ODL-induced hungry codon bypass. (**A**) Cartoon representation of the toeprinting experiment with the *ermBL* gene. Hungry codons Thr_{12} and Thr_{14} are indicated. (**B**) Toeprinting analysis of the ribosome stalling during translation of the *ermBL* gene in the presence of increasing concentrations of NOSO-95179. Note that at low concentrations of the inhibitor (lane 2), the ribosomes are able to bypass the first hungry (Thr_{12}) codon (the upper red arrowhead) and then get arrested at the next hungry codon (Thr_{14}) (the lower red arrowhead). Translation initiation inhibitor Onc112 was included as a control (Onc) (lane 8) (Gagnon et al. 2016). (**C**) Cartoon representation of the toeprinting experiment with the *ompX*$_{1-6}$ *–ermBL*$_{7-15}$ gene. Hungry codon Ile_4 (red) and trap-codon Asp_{10}, at which ribosomes stall in the presence of erythromycin (blue), are indicated. (**D**) NOSO-95179-stimulated hungry codon bypass in the *ompX*$_{1-6}$ *–ermBL*$_{7-15}$ fusion gene. Erythromycin (50μM) induces ribosome stalling at the Asp_{10} codon (blue arrowhead). In the presence of 50μM of the Ile-RS inhibitor mupirocin, translation is arrested at the hungry Ile_4 codon (red arrowhead). Addition of NOSO-95179 to the reactions induces readthrough of the hungry codon and increased stalling at the erythromycin-dependent arrest site (lanes 4–8). The start codon band is indicated by a grey arrowhead.

At high concentrations (≥ 20 μM) of NOSO-95179, translation of the *ermBL* ORF was primarily arrested at the early codons, preventing ribosomes from reaching the Thr_{12} codon as can be judged by the low intensity of the hungry codon toeprint band and appearance of the new bands corresponding to the ribosome stalling at the previous codons (**Figure 2.10B**, lane 7). Interestingly, the ODL-induced ribosome pausing appears to be context-specific. Thus, during translation of the *ompX* or *csrA* genes, NOSO-95179 arrests ribosome at specific codons of the ORF while allowing relatively unimpeded progression through other codons (**Figure 2.11**).

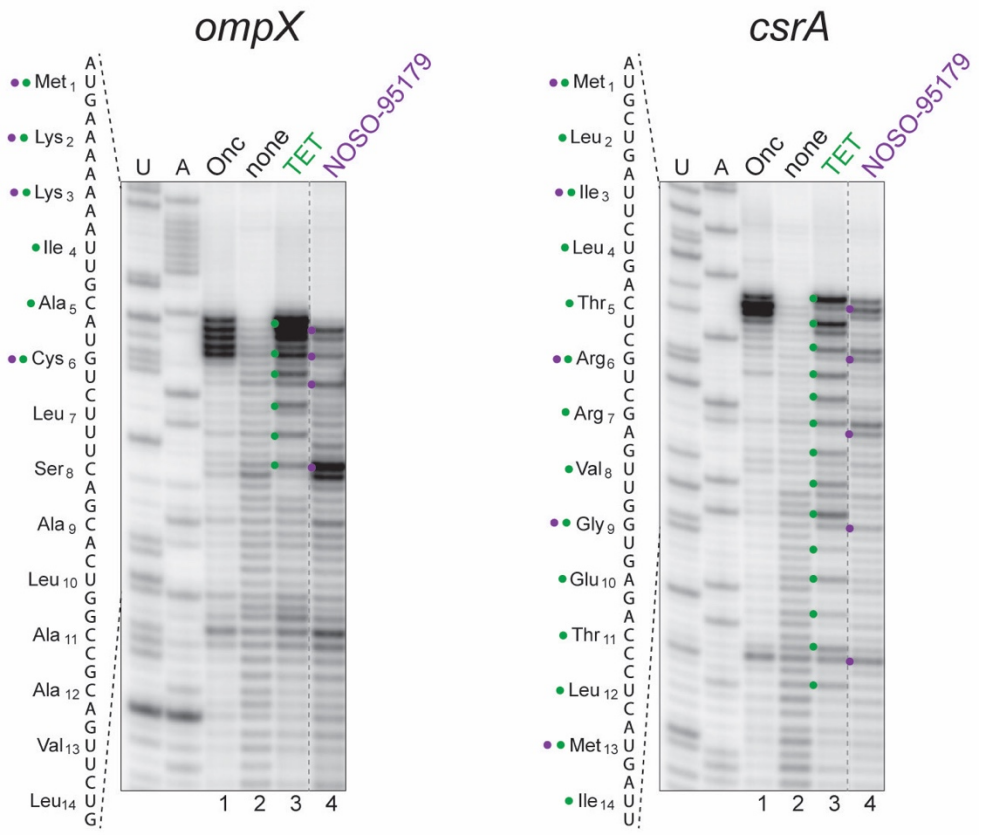

Figure 2.11: Context-specificity of action of NOSO-95179. Toe-printing analysis of the effects of NOSO-95179 and elongation inhibitor tetracycline (TET) on translation of the *E. coli* genes *ompX* and *csrA*. While TET evenly pauses ribosomes at every codon (lanes 3, green dots), NOSO-95179 preferentially stalls ribosomes at specific codons (lanes 4, purple dots). Note that toeprinting bands in the NOSO-95179-treated sample are shifted one nucleotide

down in respect to the TET-stalled ribosomes. This observation points towards a different A-site occupation of the arrested ribosomes (Jerinic and Joseph 2000) and suggests that, in contrast to TET-treated ribosomes, NOSO-95179-bound ribosomes stall with the A-site occupied with tRNA. The control inhibitor Onc112 (Onc) normally arrests the ribosome at the start codons of the genes (Seefeldt et al. 2015; Gagnon et al. 2016). However, with *ompX*, it reproducibly generates toeprinting bands corresponding to the ribosome occupying the first two codons of the genes. We are not sure of the nature of this effect.

Strikingly, at low concentrations of NOSO-95179 (0.6 μM) while the intensity of the toeprint band at the *ermBL* Thr_{12} codon was dramatically reduced compared to the borrelidin-only control, a prominent new band, that corresponded to ribosomes stalled at the Thr_{14} codon, appeared (**Figure 2.10B**, lanes 1 and 2). Apparently, low concentrations of NOSO-95179 allowed the ribosome to easily bypass the first hungry codon (Thr_{12}).

The high efficiency of the ODL-induced hungry codon readthrough prompted us to test this effect in more detail. We modified our experimental setup by introducing a bypass-resistant ribosome trap downstream from the hungry codon. For this, we took advantage of the macrolide antibiotic erythromycin, which binds in the exit tunnel of the large ribosomal subunit (away from the ODL binding sites) and arrests translation at the 10^{th} codon of *ermBL* by interfering with peptide bond formation (Arenz et al. 2014) (**Figure 2.10C and D,** lane 1, blue arrowhead). Accordingly, erythromycin-induced stalling should be largely unaffected by the ODL-promoted readthrough. Upstream from this ribosome trap site, we introduced a new unique hungry codon, Ile_4, by replacing the first 6 codons of *ermBL* with codons 1-6 of the *E. coli ompX* gene and supplementing the translation reaction with the Ile-RS inhibitor mupirocin (**Figure 2.10C and D,** lane 2, red arrowhead). In the presence of mupirocin and erythromycin, almost all ribosomes were trapped at the hungry Ile_4 codon and were unable to reach the site of erythromycin-dependent stalling (**Figure 2.10D**, lane 3). However, when the reactions were additionally supplemented with increasing concentrations of NOSO-95179, stalling at the hungry Ile_4 codon dramatically decreased, and a larger fraction of ribosomes could reach the trap-codon Asp_{10} (**Figure 2.10D**, lanes 4-8).

Qualitatively similar results were obtained with the use of a principally different model gene, *secM*, where NOSO-95179 could stimulate bypass of a hungry Trp_{15} codon (**Figure 2.12**).

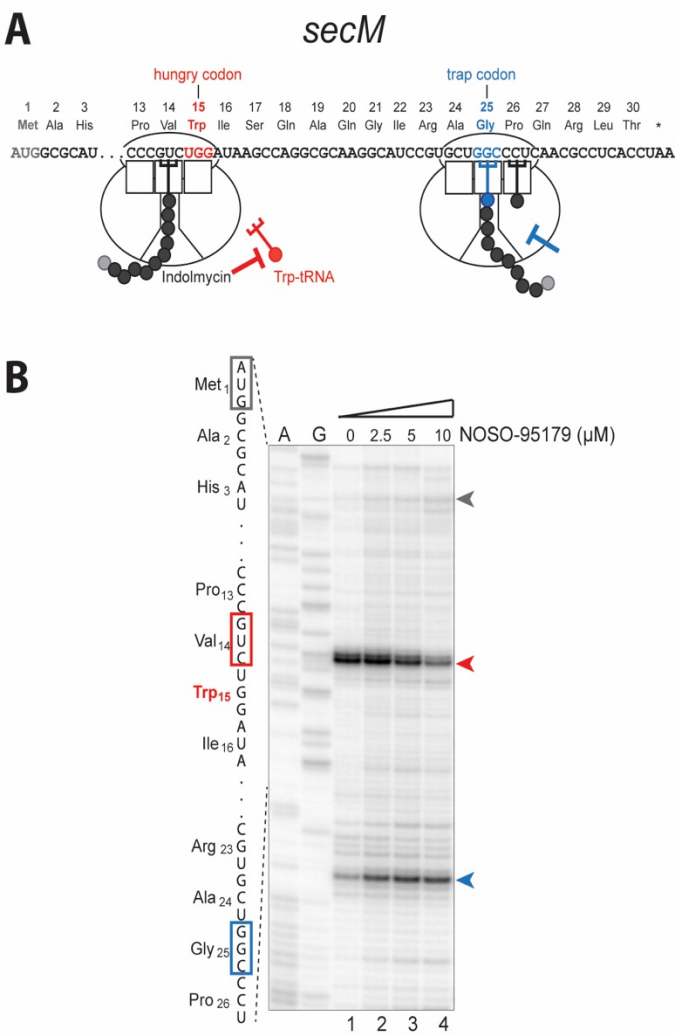

Figure 2.12: NOSO-95179 induces efficient bypass of a hungry codon in the *secM* gene. (**A**) Cartoon representation of the experiment with the *secM* mini-gene, which contains thirty 3' terminal codons of the native *E. coli secM* gene. Hungry codon Trp_{15} is generated by addition of the Trp-RS inhibitor indolmycin. Ribosomes that are able to bypass the hungry codon are arrested at the 'trap' codon Gly_{25} (Gly_{165} in the wt *secM*) due to the interaction of the SecM stalling nascent peptide with the ribosomal exit tunnel (Nakatogawa and Ito 2002). (**B**) Toeprinting analysis of *in vitro* translation of the truncated *secM* gene in the presence of indolmycin and NOSO-95179. The toeprint band representing translation arrests at the hungry codon is indicated by red arrowhead. Ribosomes that reached and were arrested at the trap codon generate the toeprint band shown by blue arrowhead. Noteworthy, the intensity of the

toeprint band at the trap (Gly_{25}) codon underrepresents the fraction of the ribosomes able to bypass the hungry codon because Trp_{15} is important for the stalling activity of the SecM peptide, whereas in the presence of NOSO-95179 it is replaced by a 'wrong' amino acid.

Thus, our results obtained with different model systems consistently show that NOSO-95179 strongly stimulates the bypass of the hungry codon during *in vitro* translation. The most plausible explanation of this effect is binding of an illegitimate (likely, near-cognate) aminoacyl-tRNA at the hungry codon suggesting that the primary mode of ODL action is rendering translation error-prone.

In order to test whether the miscoding activity of ODLs is manifested in living cells, we examined the effect of NOSO-95179 on *in vivo* expression of a *lacZ* reporter, in which the codon 537 (GAA/GAG), encoding a functionally critical glutamate, was replaced with a near-cognate glycine codon (GGG) (Manickam et al. 2014). The Gly537 mutant of the *lacZ*-encoded β-galactosidase is catalytically inactive and misincorporation of Glu instead of the Gly537 is required to restore the activity. When NOSO-95179 was spotted on an X-gal indicator plate with a lawn of the reporter *E. coli* cells, a blue halo appeared at the edge of the no-growth zone indicating that the antibiotic increased the frequency of decoding of the *lacZ* Gly537 codon by the near-cognate Glu-tRNA (**Figure 2.13**). In an independent experiment, we used a *lacZ* reporter with a premature stop codon (TAG), which replaced the wild-type Tyr17 codon (UAU) preventing the production of full size β-galactosidase (Normanly et al. 1986). We observed that at permissive concentrations NOSO-95179 restored the β-galactosidase activity (blue halo in **Figure 2.13**) likely due to misincorporation of an aminoacyl-tRNA at the premature stop codon. Thus, the results of *in vitro* and *in vivo* experiments demonstrate that ODLs render translation error-prone.

Figure 2.13: The miscoding activity of NOSO-95179 *in vivo*. NOSO-95179 induces 'correction' of the *lacZ* missense mutation (Glu537Gly) by amino acid misincorporation (left) or readthrough of the premature stop codon (Tyr17TAG) (right). Cells with the corresponding reporters were plated on agar plates and 1 µl antibiotic drops containing 13 µg of NOSO-95179, 25 µg of streptomycin (STR) or 10 µg of tetracycline (TET) were applied at the points indicated by the dots. In the left panel control antibiotics streptomycin (STR) and tetracycline (TET) were included. In the left panel, the blue halo appeared at the edge of the growing cells around the clear no-growth zone. In the TET sample, the edges of the no-growth zone, not clearly reproduced in the picture, are indicated by the dashed circle.

ODLs are active against a wide spectrum of pathogens and exhibit therapeutic efficacy in animal models

Binding of ODLs to a ribosomal site not exploited by any known antibiotic, and the favorable mode of action of these inhibitors, prompted us to evaluate the clinical prospects of ODLs as a new class of ribosomal antibiotics. Microbiological testing showed that NOSO-95179 exhibited activity against a wide range of Gram-negative and Gram-positive bacterial pathogens (*Klebsiella pneumoniae, Escherichia coli, Enterobacter aerogenes, Enterobacter cloacae, Proteus mirabilis, Serratia marcescens, Staphylococcus aureus, Enterococcus faecalis*) including difficult-to-treat drug-resistant strains as carbapenemase-producing *Enterobacteriaceae* (**Table 2.7 and Table A3 in Appendix A)**. Similar to some other miscoding antibiotics, NOSO-95179 shows strong bactericidal activity (> 3-$\log_{10}$ reduction in colony-forming units) against *K. pneumoniae* and *E. coli* (**Figure 2.14A, B**). At the same time, NOSO-95179 did not exhibit cytotoxicity against mammalian

HepG2 and HK-2 cells even at concentrations up to 256 µg/ml which exceeded the typical MIC for *K. pneumoniae* or *E. coli* by 16- and 64-fold. NOSO-95179 also did not show any hemolytic activity at 256 µg/ml (the highest tested concentration). NOSO-95179-resistant mutants of wild-type *E. coli* or *K. pneumoniae* strains appeared only with very low frequency at 24 hours (3.5×10^{-9} and 4.6×10^{-9}, respectively), even when cells were plated at low (4-fold MIC) concentrations of the ODL.

Table 2.7: Activity of NOSO-95179 against reference strains. See also Tables A2 and A3 in Appendix A.

[a] ATCC: American Tissue Culture Collection; [b] DSM: Deutsche Sammlung von Mikroorganismen und Zellkulturen; [c] CIP: Collection de l'Institut Pasteur

Microorganism (Strain)	**MIC µg/ml**
Enterobacter aerogenes ATCC [a] 51697	16
Enterobacter cloacae DSM [b] 30054	8
Escherichia coli ATCC 25922	8
Klebsiella pneumoniae ATCC 43816	4
Proteus mirabilis ATCC 7002	16
Serratia marcescens DSM 30121	8
Pseudomonas aeruginosa DSM 1117	>64
Acinetobacter baumannii ATCC 19606	>64
Stenotrophomonas maltophilia CIP [c] 60.71	>64
Staphylococcus aureus ATCC 29213	16
Enterococcus faecalis ATCC 29212	16

Encouraged by the results of microbiological testing, we further investigated the therapeutic potential of ODLs. The *in vivo* efficacy of NOSO-95179 was studied in mouse models of *K. pneumoniae* septicemia and lung infection. At a dose of 25 mg/kg, subcutaneous administration of NOSO-95179 resulted in a 2.9 $\log_{10}$ reduction in the viable bacterial cells (colony forming units) compared to the untreated control (**Figure 2.14C**). At a dose of 100 mg/kg, in the lung infection model, the inhibitor reduced the bacterial load by more than three $\log_{10}$ (**Figure 2.14D**). These results demonstrate the therapeutic potential of ODLs as a new class of antibacterials.

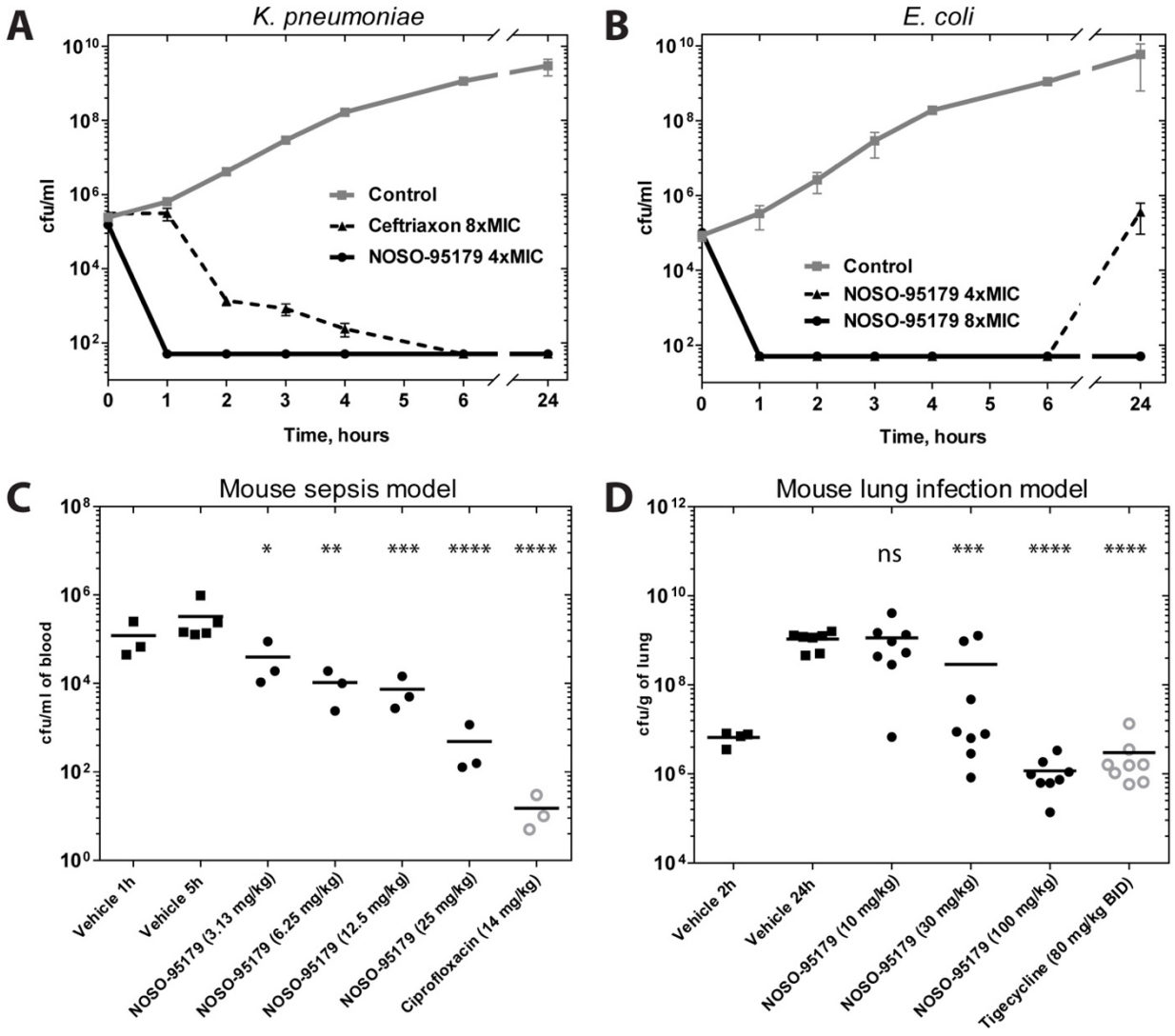

Figure 2.14: NOSO-95179 is a potent therapeutic agent. (**A, B**) Bactericidal activity of NOSO-95179 against *K. pneumoniae* (A) or *E. coli* (B). Cells were exposed to 4x MIC of NOSO-95179 or 8x MIC of the control bactericidal antibiotic ceftriaxone and the fraction of cells surviving after various incubation times was determined by plating and counting colony forming units (cfu). (**C, D**) Therapeutic efficiency of NOSO-95179 (C) Sepsis model. Single dose subcutaneous treatment with NOSO-95179 or a control antibiotic ciprofloxacin 1 h post inoculation with the *K. pneumoniae* strain SSI#3010. One-way ANOVA, Dunnett's comparison *vs.* vehicle control (5 hr) control. (D) A lung model of infection using *K. pneumoniae* strain NCTC 13442. Single dose intravenous treatment 2 h post infection with NOSO-95179 or double doses treatment 2 h and 14 h post infection with tigecycline. For drug-treated animals, lung cfu values were determined 24 h post-infection. For controls, lung cfu values were determined at 2 h and 24 h post-infection. One-way ANOVA, Dunnett's comparison *vs.* vehicle control where "ns" – non-significant $P>0.05$, * – $P \leq 0.05$, ** – $P \leq 0.01$, *** – $P \leq 0.001$, **** – $P \leq 0.0001$.

2.3 Discussion

We discovered a new class of antibiotics, ODLs, produced by a nematode-symbiotic bacterium *X. nematophila.* ODLs selectively abolish bacterial growth by interfering with protein synthesis. They achieve their inhibitory action by binding at a new site in the small ribosomal subunit. By interacting simultaneously with the 16S rRNA and with the anticodon loop of the A-site tRNA, ODLs likely increase the affinity of aminoacyl-tRNA to the ribosome resulting in a decreased accuracy of translation. At high concentrations, ODLs impede progression of the ribosome along mRNA.

Although ODLs bind at the ribosomal decoding center, which is targeted by several classes of antibiotics, their binding site is clearly distinct from those of other ribosome inhibitors. The tetracycline and negamycin sites are the closest to the site of binding of NOSO-95179. However, even these drugs do not overlap with NOSO-95179 (**Figure 2.8A, B**). Aminoglycosides bind the ribosome ~25Å farther away - on the other side of the decoding center at the top of the helix 44 of the 16S rRNA.

The overall mechanism of action of ODLs conceptually resembles that of aminoglycosides or negamycin whose mode of translation inhibition depends on the drug concentration. At lower concentrations, these antibiotics induce amino acid misincorporation by reducing the fidelity of decoding, whereas at higher concentrations they interfere with the progression of the ribosome along mRNA (Polikanov et al. 2014; Olivier et al. 2014; Wang et al. 2012). Both activities likely reflect a tighter binding of the tRNA in the A site induced by the inhibitor. However, different classes of antibiotics achieve this effect via different mechanisms. Aminoglycosides, for example, interact exclusively with the 16S rRNA and increase tRNA affinity by stabilizing the flipped-out conformation of the 16S rRNA bases 1492 and 1493 that interact with the tRNA anticodon (Demeshkina et al. 2012; Ogle and Ramakrishnan 2005). In contrast, negamycin and ODLs establish direct contacts with the A-site tRNA. However, due to the different binding sites on the ribosome, these drugs establish principally different contacts with tRNA. While negamycin interacts with the non-bridging oxygen atoms of the nucleotide 34 phosphate of the A-site tRNA,

NOSO-95179 is located within H-bonding distance from the phosphate of the nucleotide 32 of the tRNA anticodon (**Figure 2.8D**). The direct interaction between ODL and tRNA anticodon not only promotes miscoding, but also likely hinders the transition of tRNA from the A site into the P site thus inhibiting translocation at the higher concentrations of the antibiotic. This effect was context-specific, and the ribosome was preferentially arrested at the defined codons within the gene (**Figure 2.10B, D** and **Figure 2.11**). With the few templates that were tested in our toeprinting experiments, we observed preferential ODL-induced pausing at the Leu (CUG and CUU), Gln (CAA), Arg (CGA), Ile (AUU) and Lys (AAA) codons. Because ODL interacts with the tRNA anticodon loop, specificity of the drug action is likely defined by tRNA. Although, we were unable to identify a unique sequence or posttranscriptional modification signature that distinguishes the corresponding tRNAs, it is conceivable that the observed context-specificity of ODL action could reflect variations in the conformational dynamics of different tRNAs (Vare et al. 2017). Translocation could be additionally slowed down due to the ODL-induced binding of near cognate tRNAs in the A site and subsequent poor accommodation of the mismatched codon-anticodon structure in the P site (Alejo and Blanchard 2017).

Although at high concentrations ODLs arrest ribosome progression, their primary effect at lower concentrations is manifested as miscoding. Due to this activity ODLs stimulate bypass of hungry codons during cell-free translation, make possible readthrough of the premature stop codon *in vivo* and allow amino acid misincorporation at a site of inactivating missense mutation (**Figure 2.10**). The miscoding activity of ODLs should lead to production of erroneous proteins in the cells treated by the antibiotic. By analogy with the aminoglycosides, another class of miscoding-inducing inhibitors, this is a likely cause of the bactericidal activity of ODLs (**Figure 2.14A, B**). Although aminoglycosides are very potent antibiotics, their use in the clinic has been curbed due to toxicity often mediated by the action of the drugs on the mitochondrial ribosome. Specific familial mutations in the vicinity of the aminoglycoside binding site (e.g. A1555G or C1494U, **Figure 2.15**) can predispose patients to the side effects of these antibiotics resulting in an irreversible hearing

loss (Hobbie et al. 2008). Because of the distance from the ODL binding site, the mutations that sensitize mitochondrial ribosomes to aminoglycosides are not expected to affect binding or action of ODLs (**Figure 2.15**). This raises the hope that ODLs could be developed into a new class of clinically-useful bactericidal ribosome inhibitors with an improved safety profile.

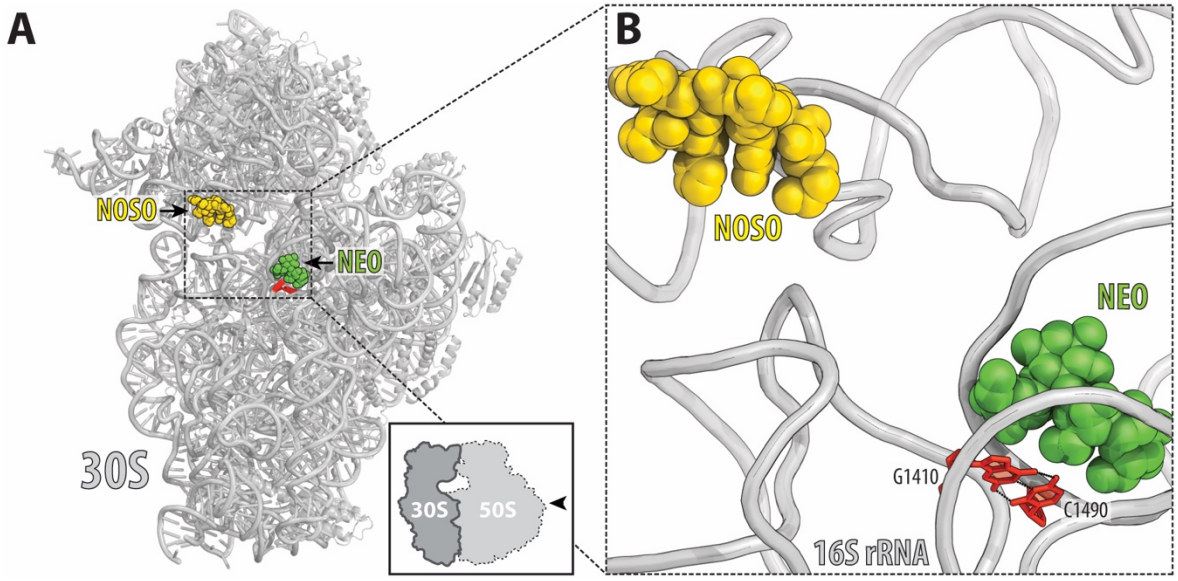

Figure 2.15: Binding site of NOSO-95179 relative to the rRNA nucleotides, whose mutations in mitochondrial ribosome confer familiar hypersensitivity to aminoglycosides. The binding sites of NOSO-95179 (NOSO, yellow) and neomycin (NEO, green) are shown within the context of the bacterial small ribosomal subunit; the small subunit rRNA nucleotides, whose mutations are associated with increased ototoxicity due to hypersensitivity of mitochondrial translation to aminoglycosides are shown in red (C1490 and G1410 in eubacterial 16S rRNA are equivalent to A1555 or C1494 in mitochondrial 12S rRNA, respectively). The long distance (27Å) of the sites of mutation to the NOSO-95179 binding site makes it unlikely that they would affect the antibiotic action.

These hopes are further fueled by the demonstrated activity of ODLs *in vitro* and *in vivo* against a number of the Gram-positive and Gram-negative bacterial pathogens, including carbapenem-

resistant *Enterobacteriaceae* (CRE). The latter observation is particularly important because CRE strains frequently exhibit resistance to other classes of antibacterials (Nordmann, Dortet, and Poirel 2012) and severe infections caused by CRE are associated with mortality rates exceeding 50% (van Duin et al. 2013). The *in vivo* efficacy of ODLs in murine sepsis and lung infection models, the absence of toxicity and the low frequency of bacterial resistance make this new class of the ribosome-targeting antibiotics an attractive starting point for medicinal chemistry programs aimed at obtaining ODL clinical candidates.

2.4 After publication

We showed that NOSO-95179 is cidal against *K. pneumonia* and *E. coli* (**Figure 2.14A, B**). Antibiotics that block protein synthesis, i.e. tetracycline, are known to have bacteriostatic activity, while miscoding inducers, i.e. aminoglycosides, are thought to result in the synthesis of faulty proteins whose accumulation is toxic for the cell.

We showed that ODLs have a dual mode of action which is concentration dependent and we wondered if ODL's cidal effect is based on its miscoding activity. To test this possibility, we exposed exponentially growing *E. coli* cells to different concentrations of NOSO-95179 with or without pretreatment using a bacteriostatic antibiotic to prevent ribosomes from producing erroneous proteins. As expected from previous experiments (**Figure 2.14A, B**), *E. coli* cells exposed to NOSO-95179 induced cell death, as observed in a spot assay (**Figure 2.16**). In contrast, when cells were pretreated, cells survived even 8-fold MIC of NOSO-95179 over 3 hours. This result indicates that indeed, ODL's miscoding activity is responsible for its bacteriocidal activity.

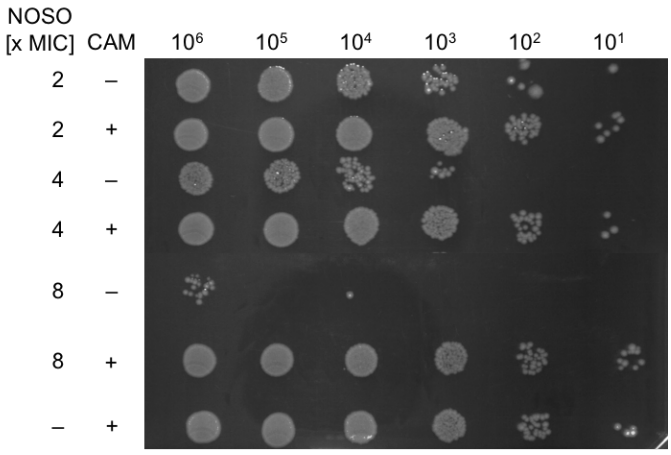

Figure 2.16: NOSO-95179's bacteriocidal effect is due to its miscoding activity. Exponentially grown *E. coli* cells were exposed to NOSO-95179 at different concentrations (2-, 4- and 8-fold MIC) for 3 hours and subsequently serially diluted in PBS and spotted onto LB agar.

2.5 Cited literature

Adams, P. D., P. V. Afonine, G. Bunkoczi, V. B. Chen, I. W. Davis, N. Echols, J. J. Headd, L. W. Hung, G. J. Kapral, R. W. Grosse-Kunstleve, A. J. McCoy, N. W. Moriarty, R. Oeffner, R. J. Read, D. C. Richardson, J. S. Richardson, T. C. Terwilliger, and P. H. Zwart. 2010. 'PHENIX: a comprehensive Python-based system for macromolecular structure solution', *Acta Crystallogr. D Biol. Crystallogr.*, 66: 213-21.

Alejo, J. L., and S. C. Blanchard. 2017. 'Miscoding-induced stalling of substrate translocation on the bacterial ribosome', *Proc. Natl. Acad. Sci. USA*, 114: E8603-E10.

Amblard, M., J. A. Fehrentz, J. Martinez, and G. Subra. 2006. 'Methods and protocols of modern solid phase Peptide synthesis', *Mol. Biotechnol.*, 33: 239-54.

Arenz, S., F. Nguyen, R. Beckmann, and D. N. Wilson. 2015. 'Cryo-EM structure of the tetracycline resistance protein TetM in complex with a translating ribosome at 3.9-A resolution', *Proc. Natl. Acad. Sci. USA*, 112: 5401-06.

Arenz, S., H. Ramu, P. Gupta, O. Berninghausen, R. Beckmann, N. Vazquez-Laslop, A. S. Mankin, and D. N. Wilson. 2014. 'Molecular basis for erythromycin-dependent ribosome stalling during translation of the ErmBL leader peptide', *Nat. Commun.*, 5: 3501.

Berdy, J. 2005. 'Bioactive microbial metabolites', *J. Antibiot. (Tokyo)*, 58: 1-26.

Billeter, M., W. Braun, and K. Wuthrich. 1982. 'Sequential resonance assignments in protein 1H nuclear magnetic resonance spectra. Computation of sterically allowed proton-proton distances and statistical analysis of proton-proton distances in single crystal protein conformations', *J. Mol. Biol.*, 155: 321-46.

Brodersen, D. E., W. M. Clemons, Jr., A. P. Carter, R. J. Morgan-Warren, B. T. Wimberly, and V. Ramakrishnan. 2000. 'The structural basis for the action of the antibiotics tetracycline, pactamycin, and hygromycin B on the 30S ribosomal subunit', *Cell*, 103: 1143-54.

CLSI. 2012. 'Methods for dilution antimicrobial susceptibility tests for bacteria that grow aerobically. ', *Approved standard. CLSI document M07-A9*, 26.

Cocozaki, A. I., R. B. Altman, J. Huang, E. T. Buurman, S. L. Kazmirski, P. Doig, D. B. Prince, S. C. Blanchard, J. H. Cate, and A. D. Ferguson. 2016. 'Resistance mutations generate divergent antibiotic susceptibility profiles against translation inhibitors', *Proc. Natl. Acad. Sci. USA*, 113: 8188-93.

Demeshkina, N., L. Jenner, E. Westhof, M. Yusupov, and G. Yusupova. 2012. 'A new understanding of the decoding principle on the ribosome', *Nature*, 484: 256-59.

Donhofer, A., S. Franckenberg, S. Wickles, O. Berninghausen, R. Beckmann, and D. N. Wilson. 2012. 'Structural basis for TetM-mediated tetracycline resistance', *Proc. Natl. Acad. Sci. USA*, 109: 16900-05.

Emsley, P., and K. Cowtan. 2004. 'Coot: model-building tools for molecular graphics', *Acta Crystallogr. D Biol. Crystallogr.*, 60: 2126-32.

Fodor, A., A. M. Fodor, S. Forst, Hogan J. S., M. G. Klein, K. Lengyel, G. Sáringer, E. Stackebrandt, R. A. J. Taylor, and E. Lehoczky. 2010. 'Comparative analysis of antibacterial activities of Xenorhabdus species on related and non-related bacteria in vivo', *Journal of Microbiology and Antimicrobials*, 2: 36-46.

Gagnon, M. G., R. N. Roy, I. B. Lomakin, T. Florin, A. S. Mankin, and T. A. Steitz. 2016. 'Structures of proline-rich peptides bound to the ribosome reveal a common mechanism of protein synthesis inhibition', *Nucleic Acids Res.*, 44: 2439-50.

Gualtieri, M., A. Aumelas, and J. O. Thaler. 2009. 'Identification of a new antimicrobial lysine-rich cyclolipopeptide family from Xenorhabdus nematophila', *J. Antibiot. (Tokyo)*, 62: 295-302.

Hartz, D., D. S. McPheeters, R. Traut, and L. Gold. 1988. 'Extension inhibition analysis of translation initiation complexes', *Methods Enzymol.*, 164: 419-25.

Hernandez, V., T. Crepin, A. Palencia, S. Cusack, T. Akama, S. J. Baker, W. Bu, L. Feng, Y. R. Freund, L. Liu, M. Meewan, M. Mohan, W. Mao, F. L. Rock, H. Sexton, A. Sheoran, Y. Zhang, Y. K. Zhang, Y. Zhou, J. A. Nieman, M. R. Anugula, M. Keramane el, K. Savariraj, D. S. Reddy, R. Sharma, R. Subedi, R. Singh, A. O'Leary, N. L. Simon, P. L. De Marsh, S. Mushtaq, M. Warner, D. M. Livermore, M. R. Alley, and J. J. Plattner. 2013. 'Discovery of a novel class of boron-based antibacterials with activity against gram-negative bacteria', *Antimicrob. Agents Chemother.*, 57: 1394-403.

Hobbie, S. N., S. Akshay, S. K. Kalapala, C. M. Bruell, D. Shcherbakov, and E. C. Bottger. 2008. 'Genetic analysis of interactions with eukaryotic rRNA identify the mitoribosome as target in aminoglycoside ototoxicity', *Proc. Natl. Acad. Sci. USA*, 105: 20888-93.

Jerinic, O., and S. Joseph. 2000. 'Conformational changes in the ribosome induced by translational miscoding agents', *J. Mol. Biol.*, 304: 707-13.

Kabsch, W. 2010. 'Xds', *Acta Crystallogr. D Biol. Crystallogr.*, 66: 125-32.

Korostelev, A., S. Trakhanov, M. Laurberg, and H. F. Noller. 2006. 'Crystal structure of a 70S ribosome-tRNA complex reveals functional interactions and rearrangements', *Cell*, 126: 1065-77.

Lewis, K. 2013. 'Platforms for antibiotic discovery', *Nat. Rev. Drug Discov.*, 12: 371-87.

Lindhagen, E., P. Nygren, and R. Larsson. 2008. 'The fluorometric microculture cytotoxicity assay', *Nat. Protoc.*, 3: 1364-69.

Ling, L. L., T. Schneider, A. J. Peoples, A. L. Spoering, I. Engels, B. P. Conlon, A. Mueller, T. F. Schaberle, D. E. Hughes, S. Epstein, M. Jones, L. Lazarides, V. A. Steadman, D. R. Cohen, C. R. Felix, K. A. Fetterman, W. P. Millett, A. G. Nitti, A. M. Zullo, C. Chen, and K. Lewis. 2015. 'A new antibiotic kills pathogens without detectable resistance', *Nature*, 517: 455-59.

Manickam, N., N. Nag, A. Abbasi, K. Patel, and P. J. Farabaugh. 2014. 'Studies of translational misreading in vivo show that the ribosome very efficiently discriminates against most potential errors', *RNA*, 20: 9-15.

McCoy, A. J., R. W. Grosse-Kunstleve, P. D. Adams, M. D. Winn, L. C. Storoni, and R. J. Read. 2007. 'Phaser crystallographic software', *J. Appl. Crystallogr.*, 40: 658-74.

Nakatogawa, H., and K. Ito. 2002. 'The ribosomal exit tunnel functions as a discriminating gate', *Cell*, 108: 629-36.

Nordmann, P., L. Dortet, and L. Poirel. 2012. 'Carbapenem resistance in Enterobacteriaceae: here is the storm!', *Trends Mol. Med.*, 18: 263-72.

Normanly, J., J. M. Masson, L. G. Kleina, J. Abelson, and J. H. Miller. 1986. 'Construction of two Escherichia coli amber suppressor genes: tRNAPheCUA and tRNACysCUA', *Proc Natl Acad Sci USA*, 83: 6548-52.

Ogle, J. M., and V. Ramakrishnan. 2005. 'Structural insights into translational fidelity', *Annu Rev Biochem*, 74: 129-77.

Olivier, N. B., R. B. Altman, J. Noeske, G. S. Basarab, E. Code, A. D. Ferguson, N. Gao, J. Huang, M. F. Juette, S. Livchak, M. D. Miller, D. B. Prince, J. H. Cate, E. T. Buurman, and S. C. Blanchard. 2014. 'Negamycin induces translational stalling and miscoding by binding to the small subunit head domain of the Escherichia coli ribosome', *Proc Natl Acad Sci USA*, 111: 16274-79.

Orelle, C., S. Carlson, B. Kaushal, M. M. Almutairi, H. Liu, A. Ochabowicz, S. Quan, V. C. Pham, C. L. Squires, B. T. Murphy, and A. S. Mankin. 2013. 'Tools for characterizing bacterial protein synthesis inhibitors', *Antimicrob. Agents Chemother.*, 57: 5994-6004.

Orelle, C., T. Szal, D. Klepacki, K. J. Shaw, N. Vazquez-Laslop, and A. S. Mankin. 2013. 'Identifying the targets of aminoacyl-tRNA synthetase inhibitors by primer extension inhibition', *Nucleic Acids Res*, 41: e144.

Payne, D. J., M. N. Gwynn, D. J. Holmes, and D. L. Pompliano. 2007. 'Drugs for bad bugs: confronting the challenges of antibacterial discovery', *Nat. Rev. Drug Discov.*, 6: 29-40.

Pioletti, M., F. Schlunzen, J. Harms, R. Zarivach, M. Gluhmann, H. Avila, A. Bashan, H. Bartels, T. Auerbach, C. Jacobi, T. Hartsch, A. Yonath, and F. Franceschi. 2001. 'Crystal structures of complexes of the small ribosomal subunit with tetracycline, edeine and IF3', *EMBO J.*, 20: 1829-39.

Piotto, M., V. Saudek, and V. Sklenar. 1992. 'Gradient-tailored excitation for single-quantum NMR spectroscopy of aqueous solutions', *J. Biomol. NMR*, 2: 661-65.

Polikanov, Y. S., G. M. Blaha, and T. A. Steitz. 2012. 'How hibernation factors RMF, HPF, and YfiA turn off protein synthesis', *Science*, 336: 915-18.

Polikanov, Y. S., S. V. Melnikov, D. Soll, and T. A. Steitz. 2015. 'Structural insights into the role of rRNA modifications in protein synthesis and ribosome assembly', *Nat. Struct. Mol. Biol.*, 22: 342-44.

Polikanov, Y. S., T. Szal, F. Jiang, P. Gupta, R. Matsuda, M. Shiozuka, T. A. Steitz, N. Vazquez-Laslop, and A. S. Mankin. 2014. 'Negamycin interferes with decoding and translocation by simultaneous interaction with rRNA and tRNA', *Mol. Cell*, 56: 541-50.

Quan, S., O. Skovgaard, R. E. McLaughlin, E. T. Buurman, and C. L. Squires. 2015. 'Markerless Escherichia coli rrn Deletion Strains for Genetic Determination of Ribosomal Binding Sites', *G3 (Bethesda)*, 5: 2555-57.

Schuttelkopf, A. W., and D. M. van Aalten. 2004. 'PRODRG: a tool for high-throughput crystallography of protein-ligand complexes', *Acta Crystallogr. D Biol. Crystallogr.*, 60: 1355-63.

Seefeldt, A. C., F. Nguyen, S. Antunes, N. Perebaskine, M. Graf, S. Arenz, K. K. Inampudi, C. Douat, G. Guichard, D. N. Wilson, and C. A. Innis. 2015. 'The proline-rich antimicrobial peptide Onc112 inhibits translation by blocking and destabilizing the initiation complex', *Nat. Struct. Mol. Biol.*, 22: 470-75.

Selmer, M., C. M. Dunham, F. V. th Murphy, A. Weixlbaumer, S. Petry, A. C. Kelley, J. R. Weir, and V. Ramakrishnan. 2006. 'Structure of the 70S ribosome complexed with mRNA and tRNA', *Science*, 313: 1935-42.

Srikhanta, Y. N., S. J. Dowideit, J. L. Edwards, M. L. Falsetta, H. J. Wu, O. B. Harrison, K. L. Fox, K. L. Seib, T. L. Maguire, A. H. Wang, M. C. Maiden, S. M. Grimmond, M. A. Apicella, and M. P. Jennings. 2009. 'Phasevarions mediate random switching of gene expression in pathogenic Neisseria', *PLoS Pathog.*, 5: e1000400.

Tobias, N. J., H. Wolff, B. Djahanschiri, F. Grundmann, M. Kronenwerth, Y. M. Shi, S. Simonyi, P. Grun, D. Shapiro-Ilan, S. J. Pidot, T. P. Stinear, I. Ebersberger, and H. B. Bode. 2017. 'Natural product diversity associated with the nematode symbionts Photorhabdus and Xenorhabdus', *Nat. Microbiol.*, 82: 1354-63.

van Duin, D., K. S. Kaye, E. A. Neuner, and R. A. Bonomo. 2013. 'Carbapenem-resistant Enterobacteriaceae: a review of treatment and outcomes', *Diagn. Microbiol. Infect. Dis.*, 75: 115-20.

Vare, V. Y., E. R. Eruysal, A. Narendran, K. L. Sarachan, and P. F. Agris. 2017. 'Chemical and conformational diversity of modified nucleosides affects tRNA structure and function', *Biomolecules*, 7.

Vazquez-Laslop, N., D. Klepacki, D. C. Mulhearn, H. Ramu, O. Krasnykh, S. Franzblau, and A. S. Mankin. 2011. 'Role of antibiotic ligand in nascent peptide-dependent ribosome stalling', *Proc. Natl. Acad. Sci. USA*, 108: 10496-501.

Vazquez-Laslop, N., C. Thum, and A. S. Mankin. 2008. 'Molecular mechanism of drug-dependent ribosome stalling', *Mol Cell*, 30: 190-202.

Walsh, C. T. 2008. 'The chemical versatility of natural-product assembly lines', *Acc. Chem. Res.*, 41: 4-10.

Wang, L., A. Pulk, M. R. Wasserman, M. B. Feldman, R. B. Altman, J. H. Cate, and S. C. Blanchard. 2012. 'Allosteric control of the ribosome by small-molecule antibiotics', *Nat. Struct. Mol. Biol.*, 19: 957-63.

Wright, G. D. 2014. 'Something old, something new: revisiting natural products in antibiotic drug discovery', *Can. J. Microbiol.*, 60: 147-54.

3. STRUCTURES OF PROLINE-RICH PEPTIDES BOUND TO THE RIBOSOME REVEAL A COMMON MECHANISM OF PROTEIN SYNTHESIS INHIBITION

(previously published as Gagnon, M.G., Roy, R.N., Lomakin, I.B., Florin, T., Mankin, A.S. and Steitz, T.A. (2016) Structures of proline-rich peptides bound to the ribosome reveal a common mechanism of protein synthesis inhibition. *Nucleic Acids Res*, **44**, 2439-2450.)

3.1 Introduction

The vital role of the ribosome in protein synthesis and its low mutational propensity due to the redundancy of ribosomal RNA (rRNA) genes in bacterial genomes make it an ideal target for antimicrobials. Indeed, a large number of clinically useful antibiotics, most of which are of natural origin, target the ribosome. They usually inhibit protein synthesis by binding to one of the functional sites in the ribosome (McCoy, Xie, and Tor 2011). The knowledge of the atomic structure of the vacant ribosome (Selmer et al. 2006), and of an array of ribosome-antibiotic complexes (Amunts et al. 2015; Polikanov, Szal, et al. 2014; Polikanov, Osterman, et al. 2014; Garreau de Loubresse et al. 2014; Bulkley et al. 2014; Bulkley, Johnson, and Steitz 2012; Blaha, Polikanov, and Steitz 2012; Stanley et al. 2010; Polikanov, Starosta, et al. 2015; Bulkley et al. 2010; Gurel et al. 2009), allows the rational design of new inhibitors that are highly active against bacterial pathogens. However, the rise of resistant bacteria represents a daunting challenge that has not been yet met with a corresponding development of effective new antibiotics. This serious public health concern has revived interest in the discovery and development of new therapeutics, especially those targeting Gram-negative microorganisms.

The sources of most of the naturally produced small-molecule antibiotics now in use are primarily bacteria and fungi. However, antimicrobial peptides (AMP) are produced as an innate immune response by many multicellular organisms (Li et al. 2014; Zasloff 2002; Yi et al. 2014). Proline-rich antimicrobial peptides (PrAMPs), which were among the first AMPs to be discovered, were identified in the late 1980s independently in honeybees (Casteels et al. 1989) and cattle (Gennaro, Skerlavaj, and Romeo 1989). PrAMPs, with motifs enriched in proline and arginine residues arranged in recurring patterns (Scocchi, Tossi, and Gennaro 2011), have thus evolved in both vertebrates and invertebrates.

The majority of eukaryotic PrAMPs, unlike most other AMPs which act on bacterial membranes (Nguyen, Haney, and Vogel 2011), are actively transported across the bacterial membrane into the cytoplasm by specialized transporters such as SbmA in Gram-negative bacteria (Runti et al. 2013). The first intracellular AMP target identified was the heat-shock protein DnaK (Otvos 2000; Mattiuzzo et al. 2007). However, the findings that a DnaK null mutant retained susceptibility to PrAMPs suggested that they have other targets (Berthold and Hoffmann 2014). It was recently reported that the PrAMPs oncocin and apidaecin preferentially target and inhibit the bacterial ribosome (Krizsan et al. 2014), and a structure of oncocin bound to the 70S ribosome was also reported (Seefeldt et al. 2015; Roy et al. 2015). This structure revealed that oncocin inhibits protein synthesis at the initiation stage by binding in the peptide exit tunnel in such a way as to interfere with the binding of the aminoacyl-tRNA in the A site (Seefeldt et al. 2015; Roy et al. 2015).

The bovine peptide bactenecin 7 (Bac7) is the most studied mammalian PrAMP and it belongs to the cathelicidin family of innate immune effectors, which are defined by a conserved, cathelin-like proline-region followed by a highly variable C-terminal domain (Tomasinsig and Zanetti 2005). Bac7 is a 60-residue peptide that is derived from a protein precursor (Scocchi, Romeo, and Zanetti 1994). Previous studies showed that Bac7, and its C-terminal truncated form $Bac7_{1-35}$, have a potent activity against many Gram-negative bacteria *in vitro* (Marlow et al. 2009; Podda et al. 2006; Benincasa et al. 2004). Similar to oncocin, Bac7 was shown to bind to chaperone DnaK (Zahn et al. 2014), but more recently, $Bac7_{1-35}$ was reported to bind bacterial ribosomal proteins and to inhibit protein synthesis (Mardirossian et al. 2014). Other PrAMPs like Pyrrhocoricin, isolated from the insect *Pyrrocoris apterus* (Cociancich et al. 1994), and Metalnikowin, isolated from *Palomena prasina* (Chernysh et al. 1996) show similar antimicrobial properties (Narayanan et al. 2014; Kragol et al. 2001). Pyrrhocoricin and Metalnikowin, even though isolated from different sources, are approximately 70% conserved with Onc112 in sequence, suggesting that they have the same target.

We report here the crystal structures of $Bac7_{1-35}$, Pyrrhocoricin, Metalnikowin, and two oncocin derivatives bound to the *Thermus thermophilus* 70S ribosome at 2.7–3.0 Å resolution (**Table 3.8**). The binding mode of $Bac7_{1-35}$ in the ribosome peptide exit tunnel is reminiscent to that of oncocin previously reported (Seefeldt et al. 2015; Roy et al. 2015), with its N-terminal residues overlapping with the binding site for the CCA-end of A-site tRNA in the peptidyl transferase center (PTC). We observe 19 amino acid residues of $Bac7_{1-35}$ extending by more than 45 Å along the exit tunnel down to the constriction formed by the apical loops of ribosomal proteins uL4 and uL22. Foot-printing experiments confirm that the binding mode observed in the crystalline complex resembles the interaction between $Bac7_{1-35}$ and the ribosome in solution. Using a toe-printing assay, we also show that $Bac7_{1-35}$ and several other PrAMPs block the ribosome at the initiation codon, thereby preventing subsequent transitioning into the elongation phase of protein synthesis. We compare the $Bac7_{1-35}$-ribosome structure with a series of 70S-ribosome structures in complex with other PrAMPs and delineate the molecular determinants of PrAMPs that are responsible for ribosome binding and thus for their antibiotic activity. We show that mutations of rRNA residues in the vicinity of the PrAMP binding site confer resistance to oncocin, revealing the ribosome as the key cellular target for this and likely other PrAMPs. This study reveals a common binding mode and mechanism of action of PrAMPs on the ribosome and thus provides a basis for designing improved antibacterial compounds that target the ribosome.

3.2 Materials and Methods

mRNA and tRNA

The mRNA with a Shine-Dalgarno sequence and an initiation codon in the P site was synthesized by integrated DNA technologies with the sequence 5′ GGC AAG GAG GUA AAA AUG UUC UAA 3′. The fMet-$tRNA^{fMet}$ was prepared as previously described (Junemann et al. 1996). All peptides used in this study were chemically synthetized by GenScript USA.

Complex formation and crystallization

The 70S ribosomes from *T. thermophilus* HB8 or its mutant strain in which ribosomal protein rpL9 is truncated (70S:$L9_{58}$) (Lin et al. 2015; Gagnon et al. 2014) were prepared and crystallized as previously described (Lin et al. 2015; Polikanov, Blaha, and Steitz 2012; Gagnon et al. 2012). Essentially, 4 μM ribosomes were incubated with 8 μM mRNA and fMet-$tRNA^{fMet}$ in 50 mM KCl, 5 mM HEPES-KOH, pH 7.6, 10 mM NH4Cl, 10 mM Mg acetate and 6 mM β-mercaptoethanol at 55 °C for 6 min. The complex was further incubated at room temperature for 15 min in the presence of either 50 μM $Bac7_{1-35}$, Metalnikowin, Onc10wt, OncΔ15-19, Pyrrhocoricin or OncΔVD. We obtained the structure of $Bac7_{1-35}$ bound to both 70S:$L9_{58}$ and 70S-wt ribosomes. With the 70S:$L9_{58}$ ribosomes, the complex was prepared as previously described in the presence of 5 μM EF-G fused to ribosomal protein L9 (Lin et al. 2015) and 50 μM $Bac7_{1-35}$. Crystals were grown in sitting-drop trays in which 3 μl of ribosome complex was mixed with 3.5–4.5 μl reservoir solution containing 0.1 M Tris-HCl, pH 7.3 – 7.6, 2.6 – 2.9% (w/v) PEG 20000, 9 – 10% (v/v) 2-methyl-2,4-pentanediol, 0.15 M L-arginine and 0.5 mM β-mercaptoethanol, and incubated at 19 °C. Crystals were cryoprotected by gradually increasing the concentration of 2-methyl-2,4-pentanediol while all other buffer components were held constant, except that each stabilization step also contained 100 μM of peptide. The crystals were left to equilibrate overnight at 19 °C and were frozen at 80 °K in a nitrogen stream before being plunged in liquid nitrogen.

X-ray data collection and structure refinement

Data were collected at beamline 24ID-C at the Advanced Photon Source at Argonne National Laboratory. The collected data were processed using the XDS package (Kabsch 1993), and we used PHASER from the CCP4 suite (Winn et al. 2011) to determine the initial solution for the structure by molecular replacement. The search model used was generated from the previously published high-resolution structure of the *T. thermophilus* 70S ribosome (PDB 1VY4 (Polikanov, Steitz, and Innis 2014)) with all its ligands removed. Structures were refined with two 70S ribosomes in the asymmetric unit by rigid-body refinement, and then by five cycles of position and

B-factor refinement with the PHENIX package (Adams et al. 2010). The P-site tRNA, mRNA and the peptide bound in the ribosome peptide exit tunnel were built into the $F_{obs} - F_{calc}$ electron density map with Coot (Emsley and Cowtan 2004), and the models were further refine with PHENIX (Adams et al. 2010). The final statistics of refinement are provided in **Table 3.8**.

Table 3.8: Data collection and refinement statistics.

	Bac7$_{1-35}$ + *T. Th.* 70S:L9$_{58}$ + EF-G	Metalnikowin + *T. Th.* 70S	Onc10wt + *T. Th.* 70S	OncΔ15-19 + *T. Th.* 70S	Pyrrhocoricin + *T. Th.* 70S
Unit cell dimensions (Space group: $P2_12_12_1$)					
a	209 Å	210 Å	210 Å	210 Å	210 Å
b	449 Å	450 Å	451 Å	451 Å	450 Å
c	619 Å	623 Å	623 Å	623 Å	623 Å
Data processing					
Resolution (Å)	50.0 – 3.0 (3.18 – 3.0)	50.0 – 2.89 (3.07 – 2.89)	50.0 – 2.80 (2.97 – 2.80)	50.0 – 2.80 (2.97 – 2.80)	50.0 – 2.70 (2.86 – 2.70)
R_{merge} (%)	26.3 (119.8)	21.6 (124.1)	22.1 (164.5)	16.1 (139.5)	16.3 (134.0)
($I/\sigma I$)	7.04 (1.34)	9.07 (1.24)	7.79 (1.01)	10.8 (1.29)	9.54 (1.12)
Completeness (%)	99.1 (98.1)	98.6 (94.7)	99.0 (97.8)	99.6 (98.9)	99.3 (98.2)
Redundancy	4.6 (4.5)	4.9 (4.6)	5.0 (4.9)	5.0 (5.0)	4.9 (4.9)
Refinement					
R_{work} (%)	19.80	21.30	20.70	19.45	21.29
R_{free} (%)	25.38	27.99	26.94	25.03	27.47
Bond dev. (Å)	0.011	0.012	0.012	0.012	0.012
Angle dev. (°)	1.732	1.688	1.698	1.694	1.718

Toe printing analysis

Toe-printing analysis was performed using the RST2 template (Orelle, Szal, et al. 2013) as previously described (Vazquez-Laslop, Thum, and Mankin 2008). Cell-free translation reactions, carried out in the PURExpress in vitro protein synthesis system, (New England Biolabs) were supplemented with 50 μM thiostrepton or 100 μM of peptides which were added in water and samples (5 μl volume) were incubated for 15 min at 37°C prior to the primer extension phase of the procedure. The control reaction had no inhibitor. Primer extension was carried out for 15 min, after which the samples were processed as described (Vazquez-Laslop, Thum, and Mankin 2008).

Foot printing experiments

E. coli ribosomes were prepared as described (Shimizu, Kanamori, and Ueda 2005). The wild-type *T. thermophilus* ribosomes used in crystallization experiments were also used in foot-printing experiments. Ribosomes (0.2 μM) were pre-incubated with 100 μM of $Bac7_{1-35}$ or Onc112 and then modified with dimethylsulfate (DMS) or *N*-cyclohexyl-*N'*-(2-morpholinoethyl) carbodiimide methyl-*p*-toluenesulfonate (CMCT) as described (Merryman and Noller 1998). rRNA was extracted and distribution of base modifications was analyzed by primer extension.

Determination of PrAMP's minimal inhibitory concentration (MIC)

MIC of PrAMPs were tested for *E. coli* strains SQ110 which contains a single *rrn* allele or its derivatives with a mutation in the *lptD* gene (SQ110 LPTD) or knock-out of the *tolC* gene (SQ110DTC) (Orelle, Carlson, et al. 2013). The A2503C and A2059G mutants were previously selected for their resistance to chloramphenicol or erythromycin, respectively (Orelle, Carlson, et al. 2013). The A2503C/A2059G double mutant was selected by plating the A2503C mutant on the plate with the macrolide antibiotic solithromycin. For the MIC determination, cells were exponentially grown in LB medium, diluted to A_{650} of 0.005 and placed in the wells of a 96-well plate. PrAMPs were added in LB medium to the highest final concentration of 25 μM in one column of wells. After 2-fold serial dilutions, the plate was incubated overnight at 37°C with shaking and cell growth was analyzed by addition of the alamarBlue dye. When MIC was tested with the SQ110DTC mutants, the highest concentration of Onc112 and $Bac7_{1-35}$ was 100 μM.

3.3 Results and Discussion

Characterization of PrAMPs

The AMP $Bac7_{1-35}$ and a series of PrAMPs (**Table 3.9**) were chemically synthesized and used to elucidate the determinants required for their ribosome binding and antimicrobial activity.

Table 3.9: Sequence alignment of selected PrAMPs.

Peptide	Sequence	Reference
Bac7$_{1-35}$	RRIRPRPPRLPRPRPRP-LPFPRPGPRPIPRPLPFP	(Scocchi, Romeo, and Zanetti 1994; Gennaro, Skerlavaj, and Romeo 1989; Frank et al. 1990)
Onc112	VDKPPYLPRPRPPR-rIYNr	(Krizsan et al. 2014)
Pyrrhocoricin	VDKGSYLPRPTPPR-PIYNRN	(Cociancich et al. 1994)
Metalnikowin	VDKPDYRPRPRPPN-M	(Chernysh et al. 1996)
OncΔ15-19	VDKPPYLPRPRPPR------	
OncΔVD	--KPPYLPRPRPPR-RIYNR	
Onc10wt	VDKPPYLPRPRPPR-RIYNR	(Knappe et al. 2010)

r = D-Arginine

The conserved and non-conserved residues among selected PrAMPs are red and blue, respectively. The underlined residues correspond to the common core region.

They were tested for their inhibitory activity against the SQ110 LPTD strain of *Escherichia coli,* which is defective in outer membrane structure (**Table 3.10**) (Orelle, Carlson, et al. 2013). All peptides, except Onc-ΔVD and Metalnikowin, show detectable activity with minimal inhibitory concentrations (MIC) ranging between 0.75 and 25 μM, which agrees well with previous data (Benincasa et al. 2015; Knappe et al. 2011; Narayanan et al. 2014). It is noteworthy that the activity of the peptides against the parental SQ110 strain was reduced in most cases (**Table 3.10**), indicating that crossing the outer membrane of Gram-negative bacteria presents a challenge for PrAMPs.

Table 3.10: Minimal inhibitory concentration (MIC) values for selected PrAMPs against *E. coli* strains. The SQ110LPTD strain is defective in the lipopolysaccharide assembly of the outer membrane and is more sensitive to some antibiotics (Orelle, Carlson, et al. 2013).

Peptide	SQ110 (LPTD) (μM)	SQ110 (μM)
Bac7(1-35)	0.75	1.5
Onc112	0.75	12.5
Pyrrhocoricin	4	>25
Metalnikowin	62.5	>25
OncΔ15-19	25	>25
OncΔVD	62.5	>25
Onc10wt	1	25

As the cellular growth inhibitory activity of PrAMPs depends both on their ability to cross the cell membrane (Runti et al. 2013) and their stabilities, their inhibitory effect on protein synthesis was also assessed *in vitro* using a toe-printing assay (**Figure 3.17**A). While most peptides inhibited the initiation stage of protein synthesis and arrested the ribosome at the initiator codon, as previously reported for Onc112 (Seefeldt et al. 2015; Mattiuzzo et al. 2007), the deletion peptide Onc-ΔVD was inactive.

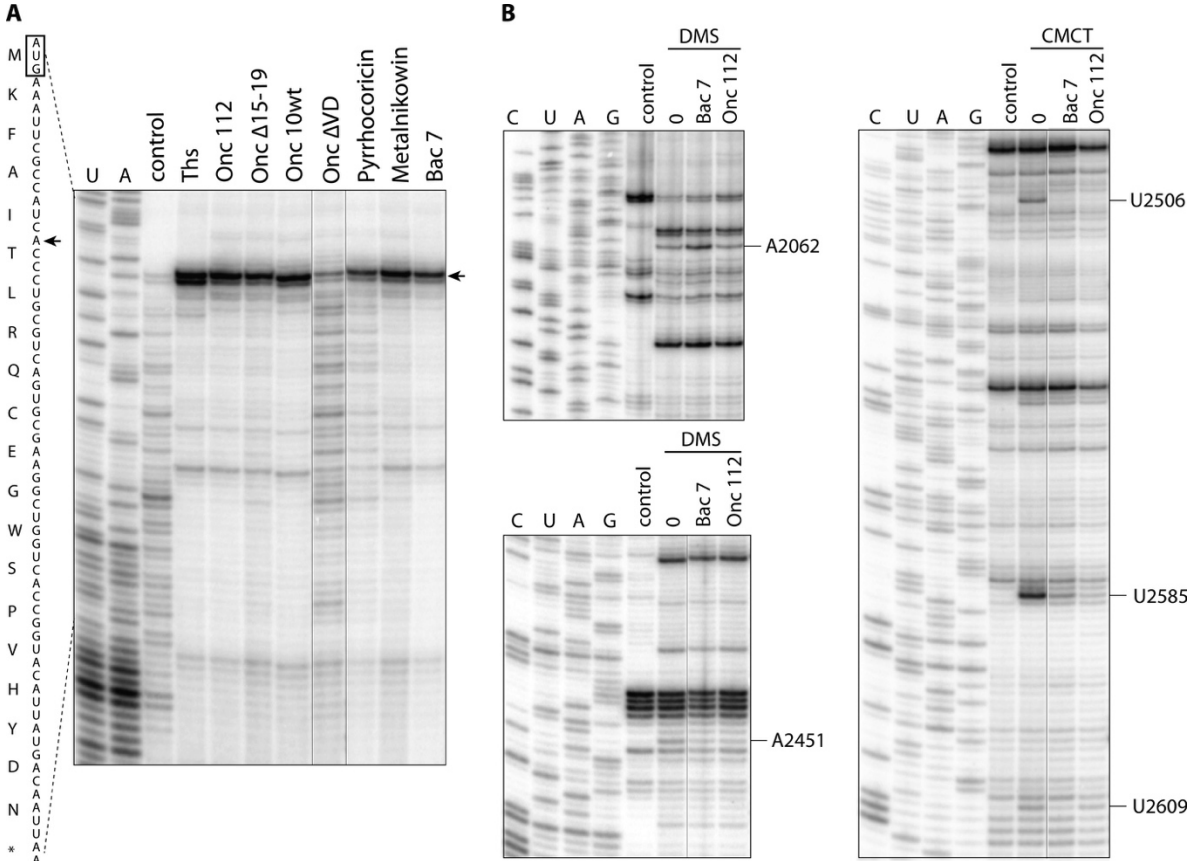

Figure 3.17: Toe-printing (A) and foot-printing (B) experiments reveal the mode of action and verify PrAMP binding mode in solution. (A) The 20-codon synthetic RST2 ORF containing codons for all 20 amino acids (Orelle, Szal, et al. 2013) was translated in the PURExpress cell-free transcription-translation system by *E. coli* ribosomes in the presence of 100 μM of PrAMPs or 50 μM of the control antibiotic thiostrepton (Ths), and the position of the stalled ribosome was determined by primer extension. U- and A- specific reactions were used

as a sequencing ladder. The toeprint band (marked by an arrow in the gel and in the sequence of the gene), which occurs at position +16 counting from the first nucleotide of the codon in the ribosomal P site, places the arrested ribosome at the initiator codon (boxed on the RST2 sequence on the left from the gel). **(B)** Foot-printing analysis of interaction of $Bac7_{1-35}$ and Onc112 with the *E. coli* ribosome in solution. Ribosomes were pre-incubated with no PrAMP ('none') or 50 μM of $Bac7_{1-35}$ or Onc112 and subjected to modification with CMCT or DMS. Control sample remained unmodified. Some of the lanes in gels shown in A and B, which contained samples irrelevant to the current study, have been computationally removed.

Structure determination of PrAMPs bound to the ribosome

To further elucidate the ribosome binding mode of all the peptides studied, each was co-crystallized with the *T. thermophilus* 70S ribosome bound to mRNA and initiator tRNA (**Table 3.8**). The resulting 70S-complex structures were determined by the molecular replacement method using a high-resolution model of the vacant 70S ribosome (Polikanov, Steitz, and Innis 2014). The difference Fourier maps calculated at 2.7–3.0 Å resolution using initially phased diffraction data showed clear unbiased electron density for the mRNA, $tRNA^{fMet}$ in the P site and the antimicrobial peptide located inside the peptide exit tunnel of the 50S subunit (**Figure 3.19**A and **Figure 3.18**). The absence of electron density for Onc-ΔVD in the ribosome peptide exit tunnel (data not shown) is consistent with the toe-printing experiments (**Figure 3.17**A).

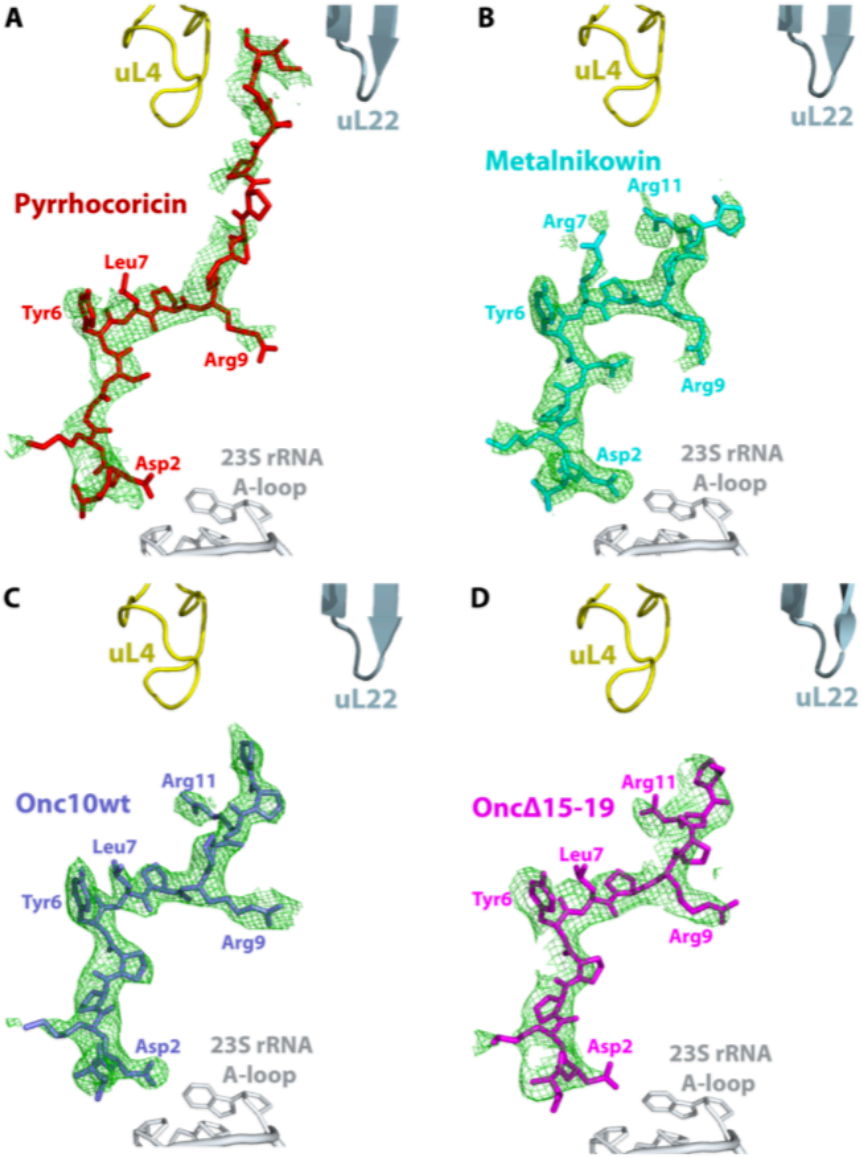

Figure 3.18: Structures of Pyrrhocoricin **(A)**, Metalnikowin **(B)**, Onc10wt **(C)** and OncΔ15-19 **(D)** bound inside the peptide exit tunnel of the ribosome with their difference Fourier $F_{obs} - F_{calc}$ (green) electron density maps shown and contoured at ~2.5σ. The 23S rRNA A-loop and ribosomal proteins uL4 and uL22 are shown. Each peptide is colored as in **Figure 3.19**.

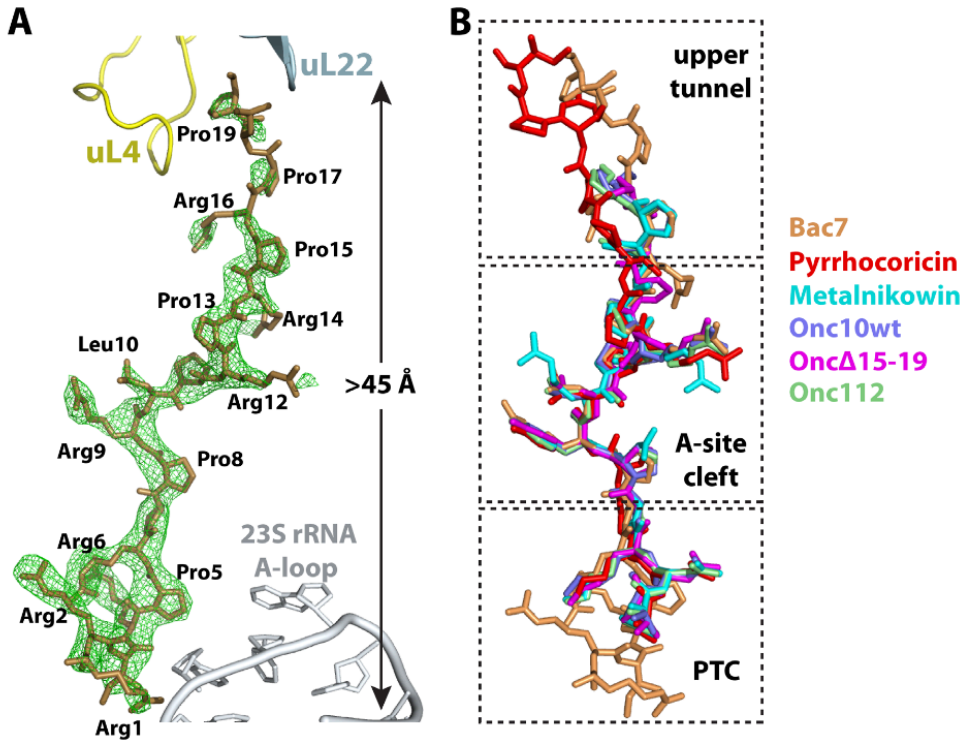

Figure 3.19: The structure of PrAMPs in their ribosome-bound conformation. (A) Structure of $Bac7_{1-35}$ bound in the peptide exit tunnel of the ribosome. The difference Fourier map calculated at 3.0 Å resolution using initially phased diffraction data ($F_{obs} - F_{calc}$, green) contoured at 3σ shows clear unbiased electron density for 19 residues of $Bac7_{1-35}$. The 23S rRNA A-loop and ribosomal proteins uL4 and uL22 are shown. **(B)** The superposition of all PrAMPs bound to the ribosome reveals that the common core (middle) region overlaps almost perfectly. $Bac7_{1-35}$ is colored brown, Onc112 is green (PDB 4Z8C (Roy et al. 2015)), Metalnikowin is cyan, Onc10wt is slate, OncΔ15-19 is magenta and Pyrrhocoricin is red.

The interactions of the N-terminus of PrAMPs with the 23S rRNA are not conserved, but are crucial for ribosome binding

Nineteen residues of the $Bac7_{1-35}$ peptide, spanning more than 45 Å from the CCA-binding site of the aminoacyl-tRNA in the A site to the constriction of the peptide exit tunnel in the upper chamber, could be unambiguously fitted into the unbiased electron density of the difference Fourier map for the complex (**Figure 3.19**A). Compared to Onc112 (Seefeldt et al. 2015; Roy et al. 2015), the N-terminal region of $Bac7_{1-35}$ extends further into the A site of the 50S subunit (**Figure 3.20**A), and would collide with the acceptor stem of a tRNA bound in the A site if there were one (**Figure 3.20**B). The many interactions of this extended region of $Bac7_{1-35}$ with the 23S rRNA stabilize the

peptide inside the PTC and may also be essential for the entry of $Bac7_{1-35}$ into the peptide exit tunnel. Indeed, the antimicrobial activity of deletion variants of $Bac7_{1-35}$ is known to require the integrity of the first 16 residues of the highly cationic N-terminus, which is also known to be required for its activity against Gram-negative bacteria (Benincasa et al. 2004; Sadler et al. 2002). In addition, it has been proposed that the loss of activity for the deletion variants of $Bac7_{1-35}$ is due to impaired interaction with the intra-cellular target, because the peptides remained cell-permeable (Sadler et al. 2002).

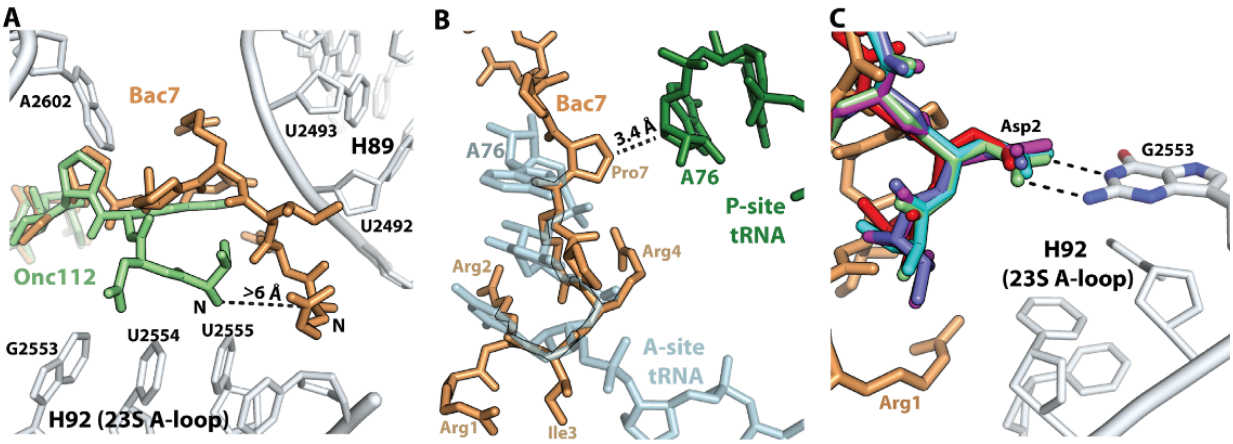

Figure 3.20: Conformation of the N-terminal region of PrAMPs in the ribosome. (A) The N-terminal of $Bac7_{1-35}$ (brown) extends further than Onc112 (green, PDB ID: 4Z8C, Roy et al. 2015) into the A site of the 50S subunit, establishing interactions with H89 of 23S rRNA. **(B)** The N-terminal of $Bac7_{1-35}$ is not compatible with the presence of the CCA-end of A-site tRNA (light blue; PBD ID 4Y4P, (Polikanov, Melnikov, et al. 2015)). **(C)** The Asp2 residue at the N-termini of PrAMPs Pyrrhocoricin, Metalnikowin, Onc10wt, OncΔ15-19 and Onc112 interact with the Watson-Crick edge of nucleotide G2553 in the 23S rRNA A-loop.

The structure of $Bac7_{1-35}$ bound to the ribosome reveals that the N-terminal region of $Bac7_{1-35}$ makes several interactions with Helix 92 (H92), which forms the A-loop of the 23S rRNA, and Helix 89 (H89), which is part of the PTC (**Figure 3.21**). The epsilon nitrogen atom of residue Arg1 is within hydrogen bonding distance to the O2 atom of nucleotide U2555 and the O4' atom of

nucleotide C2556, both in H92 (**Figure 3.21**A) (*E. coli* nucleotide numbers are used throughout the text). Residues Arg2, Arg4 and Arg6 all make interactions with the sugar-phosphate backbone of H89 (**Figure 3.21**B-D). Finally, residue Arg2 makes a π-stacking interaction with the nucleotide base of C2573 and with Arg6, which in turn stacks on Arg4 (**Figure 3.21**E). Compared to other PrAMPs studied here and previously (Seefeldt et al. 2015; Roy et al. 2015), the N-terminal region of $Bac7_{1-35}$ extends further by more than 6 Å toward H89 of 23S rRNA into the A site of the 50S subunit (**Figure 3.20**A), which may provide a clue about why this segment of the peptide is important for the antimicrobial activity of $Bac7_{1-35}$. The sugar-phosphate backbone of H89 has been proposed to be involved in the tRNA accommodation by mediating the first binding interactions of the aminoacyl-tRNA with the ribosome (Sanbonmatsu, Joseph, and Tung 2005). By interacting closely with H89 and hindering the path to the PTC for the acceptor stem of the aminoacyl-tRNA, the N-terminal region of $Bac7_{1-35}$ may be more efficient at inhibiting translation initiation than Onc112 (**Table 3.10**). Each arginine residue of the 'RRIR' motif in $Bac7_{1-35}$ participates in dual interactions involving the epsilon nitrogen and the amino group (**Figure 3.21**). These interactions would not be possible if arginines were substituted for lysines or other residues, thereby providing a structural basis for their high conservation in $Bac7_{1-35}$, bactenecin 5 (Bac5) and PR-39 (Agerberth et al. 1991; Gennaro, Skerlavaj, and Romeo 1989). This argument is supported by previous data reporting an appreciable loss of activity for $Bac7_{1-35}$ N-terminal variants in which Arg1 and Arg2 residues were substituted for lysine (Guida et al. 2015). Similarly, it has been shown that arginine residues at the N-terminus of a PR-39 variant and of Bac5 are important for the antimicrobial activity of those PrAMPs (Chan et al. 2001; Raj and Edgerton 1995).

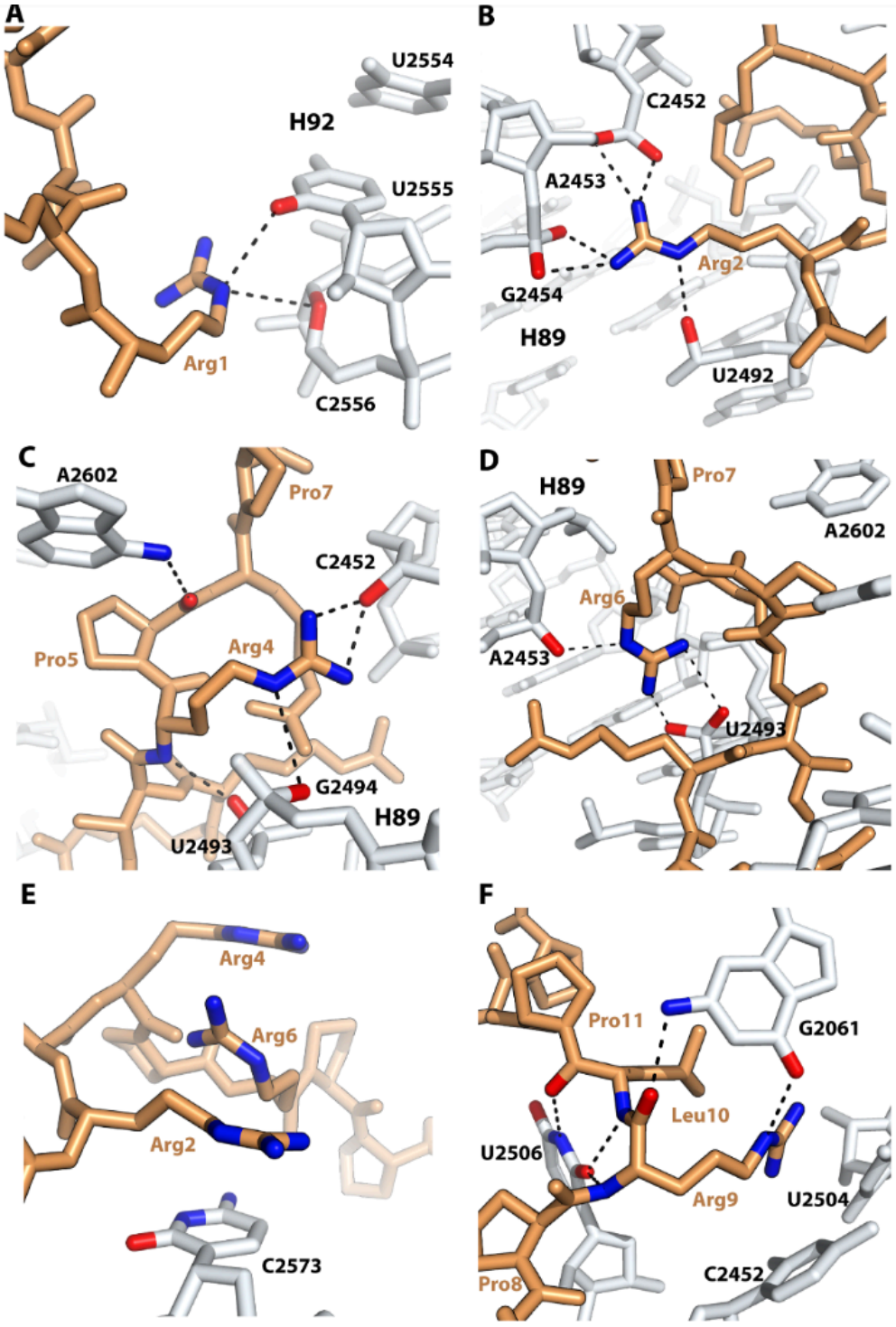

Figure 3.21:. Interactions of the N-terminal (A – E) and the core (middle) (F) regions of Bac7$_{1-35}$ with the ribosome. Residues Arg 1 **(A)**, Arg2 **(B)**, Arg4 **(C)** and Arg6 **(D)** establish multiple interactions with nucleotides in H89 and H92 of 23S rRNA. Each arginine residue of the N-terminal 'RRIR' motif in Bac7$_{1-35}$ participates in dual interactions involving the epsilon nitrogen and the amino group. **(E)** Four-layer π-stacking interaction formed between residues Arg2, Arg6, Arg4 and nucleotide C2573. **(F)** Residue Arg9 of the core region in Bac7$_{1-35}$ stacks with the conserved base pair formed between nucleotides C2452 and U2504 of the A-site cleft and also forms a hydrogen bond with G2061. The Leu10 residue stacks with residue Arg9.

To investigate the role of the N-terminal region in other PrAMPs, we tested an N-terminally truncated version of oncocin, OncΔVD, which lacks the first two residues (**Table 3.9**). This mutant exhibited a MIC value 80-fold higher than that of Onc112 (**Table 3.10**). Moreover, the toe-printing assay shows thatOncΔVD did not block the ribosome at the initiation codon and allows translation to continue through the entire gene (**Figure 3.17**A), indicating that the mutant peptide does not inhibit the ribosome function at the concentration tested (see 'Materials and Methods' section). This observation correlates with our inability to observe electron density for OncΔVD in the ribosome complex (data not shown). Thus, our data provide a structural explanation for the importance of the N-terminal domain in PrAMPs for ribosome binding.

Despite the high conservation of the A-site cavity in the PTC, the structures obtained for $Bac7_{1-35}$ and the other PrAMPs bound to the ribosome show that their N-terminal parts interact with the ribosome in different manners. Most of them form an interaction between the Asp2 residue and the Watson-Crick edge of nucleotide G2553 of the 23S rRNA A-loop. In contrast, the N-terminal region of $Bac7_{1-35}$ is displaced toward H89 by more than 6 Å (**Figure 3.20**A), thereby positioning the carbonyl oxygen of Pro5 and the N6 atom of A2602, a universally conserved nucleotide in the PTC, within hydrogen bonding distance (**Figure 3.21**C).

The core region of PrAMPs uses a common ribosome binding mode

The superposition of the 50S subunits of ribosome-PrAMP complexes shows a similar peptide binding mode in their core regions. Residues 6 to 13 of $Bac7_{1-35}$ overlap perfectly with the corresponding region in other PrAMPs bound to the ribosome (**Figure 3.19**B). This segment in all peptides interacts with conserved nucleotides of the peptide exit tunnel, such as U2585 and U2506 (**Figure 3.17**B, **Figure 3.21**F and **Figure 3.22**), two nucleotides known to change their conformation in response to substrates binding into the PTC and the exit tunnel (Voorhees et al. 2009; Sothiselvam et al. 2014). This region of the ribosome is also known to bind several antibiotics like chloramphenicol (Bulkley et al. 2010), homoharingtonine (Garreau de Loubresse et al. 2014; Gurel et al. 2009) and hygromycin A (Polikanov, Starosta, et al. 2015). Sequence

alignment of the peptides studied here shows that the core region consists of multiple proline-arginine repeats (underlined in **Table 3.9**). The tyrosine-leucine (YL) motif, which is surrounded by the proline-arginine repeats, is generally conserved but appears to accommodate variations. The sequence alignment shows that the tyrosine residue can be substituted by arginine (**Table 3.9**). In the 70S-ribosome-Bac7$_{1-35}$ complex, the position occupied by Arg9 is the same as the one occupied by Tyr6 in the 70S-Onc112 complex (**Figure 3.21**F and **Figure 3.22**A) (Seefeldt et al. 2015; Roy et al. 2015), which is also reminiscent of the position occupied by the phenylalanine residue attached to the A-site tRNA (**Figure 3.22**B) (Polikanov, Steitz, and Innis 2014). Correspondingly, both Arg9 (in Bac7$_{1-35}$) and Tyr6 (in Onc112) residues form similar π-stacking interactions with the conserved base pair formed between nucleotides C2452 and U2504 of the A-site cleft (**Figure 3.21**F). The high sequence conservation of this region reflects the analogous interactions that occur with the nucleotides of the peptide exit tunnel in the ribosome. In Bac7$_{1-35}$, the interaction of the Arg9 side chain with the A-site cleft of the PTC is stabilized by the Leu10 side chain that forms a stacking interaction with Arg9 (**Figure 3.21**F), as previously observed in the Onc112 complex (Roy et al. 2015). The crystal structures of all other PrAMPs show that this interaction is maintained and is mediated by a leucine residue, with the exception of peptide Metalnikowin where this residue is replaced by arginine (**Table 3.9**) that nevertheless forms a similar π-stacking interaction with Tyr6 (**Figure 3.22**C).

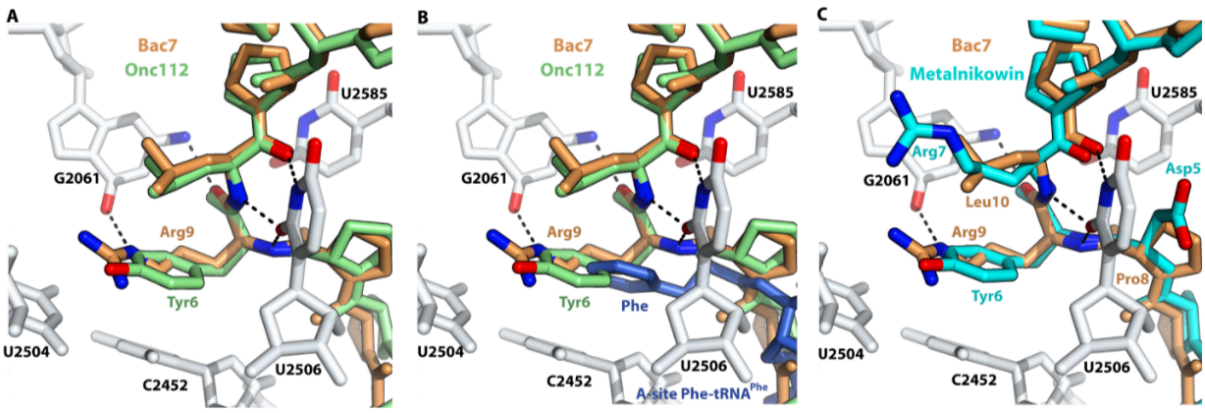

Figure 3.22: Interactions of different PrAMPs with the A-site cleft of the peptide exit tunnel. (A) Residue Arg9 in Bac7$_{1-35}$ overlaps with residue Tyr6 in Onc112 [PDB 4Z8C], thereby forming a similar π-stacking interaction with nucleotide C2452. **(B)** The phenylalanine residue attached to the A-site tRNA occupies the same position in the A-site cleft [PDB 1VY4]. **(C)** Even though the amino acid sequence of peptide Metalnikowin is slightly different, its Arg7 residue stacks with the previous residue similarly as in the Bac7$_{1-35}$ peptide.

The variable C-terminal region of PrAMPs is flexible in the upper chamber of the peptide tunnel

We did not detect any electron density in the difference Fourier map for residues 20 to 35 of Bac7$_{1-35}$ probably due to their flexibility (**Figure 3.19**A). In the previously reported 70S-Onc112 structure, residues 14 to 19 of Onc112 were also not visible (Roy et al. 2015). In the structure of peptide Pyrrhocoricin bound to the ribosome, 17 residues out of 20 are visible, which allows us to visualize the path taken by the C-terminal region of Pyrrhocoricin (**Figure 3.19**B and **Figure 3.23**D and **Figure 3.18**A). The superposition of ribosomes bound to Bac7$_{1-35}$ and Pyrrhocoricin reveals that the C-terminal region of those peptides diverge from residue 14 in Bac7$_{1-35}$ (11 in Pyrrhocoricin), with the main chain peptide backbone laterally displaced by more than 5 Å along the constriction formed by the loops of ribosomal proteins uL4 and uL22 (**Figure 3.23**D). The high flexibility of this region in PrAMPs indicates that the interactions of the C-terminal region with the peptide exit tunnel of the ribosome – if any – contribute less to binding than the core and N-terminal segments.

Consistent with this hypothesis, a C-terminal truncation of the $Bac7_{1-35}$ peptide, giving $Bac7_{1-16}$, has been reported to retain good antimicrobial activity (Benincasa et al. 2004; Guida et al. 2015). However, deletion of Arg16, producing $Bac7_{1-15}$, abolishes activity (Benincasa et al. 2004; Sadler et al. 2002). This effect is likely due to a loss of binding affinity to the ribosome because $Bac7_{1-15}$ is still transported inside the cell (Sadler et al. 2002). This agrees with our structure showing that Arg16 makes multiple interactions with the ribosome (**Figure 3.23**A and C). The side chain of Arg16 forms a π-stacking interaction with His69 of protein uL4 on one side, while on the other side Arg16 is is within hydrogen bonding distance to atom N1 of nucleotide A2062 (**Figure 3.23**A). The interaction between Arg16 and protein uL4 seen in this ribosome-$Bac7_{1-35}$ complex is substituted by Arg11 in our previous 70S-Onc112 complex structure (Roy et al. 2015), where it interacts with A2062 of the 23S rRNA (**Figure 3.23**A). Accordingly, a substitution of Arg11 in Onc112 to alanine decreases the binding affinity of oncocin to the ribosome by about 6-fold (Krizsan et al. 2014).

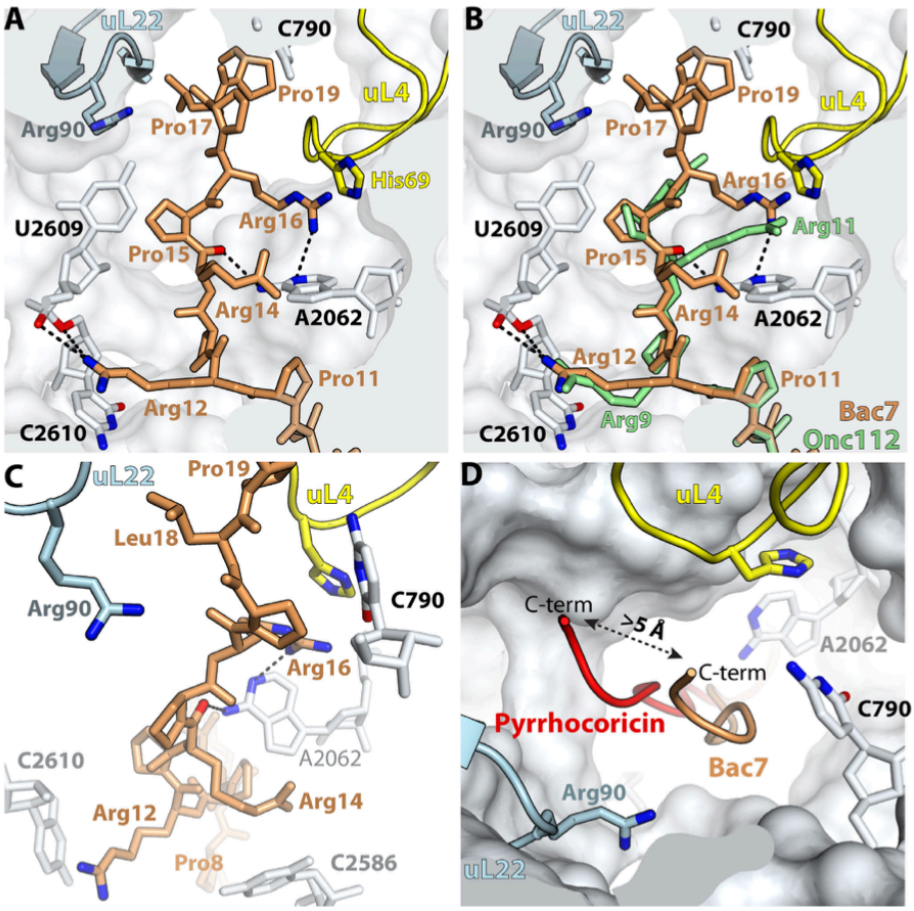

Figure 3.23: Interactions of the C-terminal region of Bac$_{1-35}$ with the upper chamber of the peptide exit tunnel (A) Residue Arg16 forms a π-stacking interaction with Hist69 of ribosomal protein uL4 and also makes multiple interactions with the ribosome. **(B)** The interactions mediated by residue Arg16 in Bac$_{1-35}$ (brown) are compensated by Arg11 on Onc112 (green) **(C)** Residue Arg14 stacks with nucleotide C2586 and the main chain peptide backbone of residues 17-19 forms a stacking interaction with nucleotides C790 across the tunnel, and with residue Arg90 of ribosomal protein uL22. **(D)** Lateral displacement of the C-terminus of Pyrrhocoricin (red) compared with Bac$_{1-35}$ (brown) by more than 5 Å along the constriction formed by the loops of proteins uL4 and uL22.

To further explore the contribution of the PrAMP's C-terminal residues to ribosome binding and activity, we designed a truncated version of Onc112 in which the last five residues are removed (OncΔ15-19). Based on the sequence alignment of other selected PrAMPs with Bac7$_{1-35}$ (**Table 3.9**), such truncation should not inhibit its binding to the ribosome, and therefore its antimicrobial activity. As expected, we observed electron density inside the peptide tunnel for OncΔ15-19,

indicating that removal of the last five residues does indeed not affect its binding to the ribosome. Correspondingly, this oncocin mutant preserves its inhibitory activity against the ribosome as it blocks the initiation step of protein synthesis (**Table 3.10** and **Figure 3.17**A).

In the upper chamber of the peptide exit tunnel, nucleotide A2062 adopts the same conformation in both the 70S-Bac7$_{1-35}$ and 70S-Onc112 complexes; however, while Arg11 of Onc112 interacts with A2062 (**Figure 3.23**B) (Roy et al. 2015), the corresponding Arg14 in Bac7$_{1-35}$ forms an alternative stacking interaction with nucleotide C2586, not seen previously with Onc112 (**Figure 3.23**C). Residues 16 to 19 of Bac7$_{1-35}$ pack along the side of the peptide exit tunnel wall formed by residues 69 and 70 of protein uL4. The main chain peptide backbone of residues 17 to 19 of Bac7$_{1-35}$ is sandwiched between nucleotide C790 across the tunnel and residue Arg90 of protein uL22 (**Figure 3.23**C). The various interactions observed between the ribosome and the C-terminal region of PrAMPs may reflect the plasticity of the upper chamber of the ribosome exit tunnel in accommodating different nascent peptide chains during translation. This correlates with recent studies of macrolide antibiotics, which bind 50S ribosomal subunit in the exact same region, revealing that some nascent polypeptide chains can escape the inhibitory effect of the antibiotic in a sequence dependent manner (Kannan, Vazquez-Laslop, and Mankin 2012).

Taken together, our results and the available data on truncated variants of Bac7$_{1-35}$ suggest that the binding determinants for Bac7$_{1-35}$ and other PrAMPs reside within the first 14 to 15 residues of the peptide, with the main contribution to ribosome binding being provided by the residues of the N-terminal and middle segments of the peptides.

While crystallographic studies can provide critical insights into the interactions of inhibitors with the ribosome in the crystalline state, the intrinsic dynamics of the ribosome in solution could hypothetically lead to alternative or additional binding modes. Therefore, in order to verify that the binding of Bac7$_{1-35}$ and Onc112 inferred from the X-ray analysis adequately reflects interaction of PrAMPs with the ribosome in solution, we carried out foot-printing experiments, in which we identified rRNA nucleotides protected by PrAMPs from chemical modification in the *E. coli* or *T.*

thermophilus ribosomes (**Figure 3.17**B, and **Figure 3.24**). Consistent with our structural data (**Figure 3.21**A and **Figure 3.22**A), we observed strong protection of U2506, U2585 and A2451 by both peptides in the ribosome from mesophylic and thermophilic bacteria. Interestingly, $Bac7_{1-35}$ completely protected U2609 from modification with carbodiimide (CMCT), but Onc112 afforded only partial protection in the *E. coli* ribosome, indicating differences in PrAMPs binding to the upper chamber of the peptide exit tunnel. Correspondingly, $Bac7_{1-35}$ provides increased accessibility of A2062 to dimethylsulfate (DMS) modification in *E. coli* over Onc112 (**Figure 3.17**B), which is in agreement with differences in interaction of Onc112 and $Bac7_{1-35}$ with A2062 (**Figure 3.23**B).

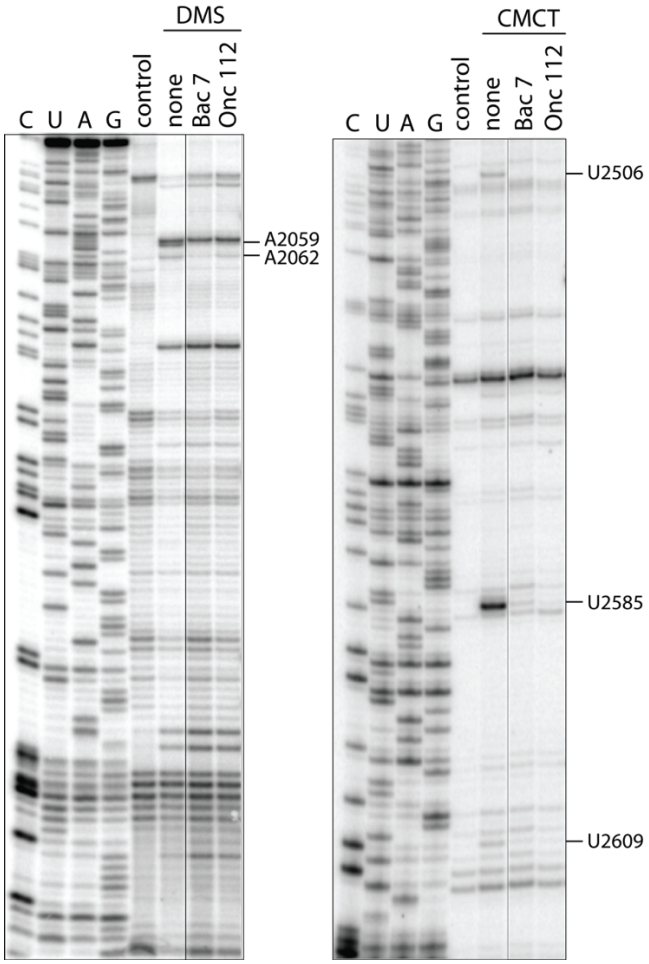

Figure 3.24: Foot-printing of $Bac7_{1-35}$ and Onc112 on the *T. thermophilus* ribosome. The 70S ribosome was pre-incubated with no PrAMP ('none') or 50 μM of $Bac7_{1-35}$ or Onc112 and subjected to modification by DMS or CMCT. The rRNA residues whose accessibility to the modifying reagents was affected by PrAMPs are marked.

Ribosomal mutations affect the activity of PrAMPs

The primary intra-cellular target for PrAMPs has long been thought to be the chaperone DnaK because PrAMPs can bind to DnaK and inhibit its activity (Knappe et al. 2011; Kragol et al. 2001; Zahn et al. 2014; Zahn et al. 2013). However, the sensitivity of an *E. coli* strain lacking DnaK to PrAMPs suggests another key target (Berthold and Hoffmann 2014). The new data presented here highlight the importance of a different target for oncocins and $Bac7_{1-35}$ – the ribosome (Mardirossian et al. 2014; Seefeldt et al. 2015; Roy et al. 2015; Krizsan et al. 2014). However, neither structural, nor biochemical data can distinguish between the primary target of antibiotic action, whose inhibition results in growth arrest, and a fortuitous binding. Therefore, in order to test whether the ribosome is indeed a target for PrAMPs in the bacterial cell, we tested whether rRNA mutations in the PrAMP binding site can render *E. coli* resistant to $Bac7_{1-35}$ or Onc112. Guided by antibiotic binding studies (Dunkle et al. 2010), we used the previously selected resistant mutants with alterations at 23S rRNA residues A2503 and A2059 (**Table 3.11**) (Orelle, Carlson, et al. 2013). For $Bac7_{1-35}$, the selected mutations did not provide any clear advantage over the wild-type strain, however the A2503C or A2059C mutations in the peptide exit tunnel increased resistance against Onc112 by about 4-fold (**Table 3.11**). When present together in the A2503C/A2059G double mutant, the mutations increased *E. coli* resistance to Onc112 by more than 15-fold (**Table 3.11**).

Table 3.11: rRNA mutations confer resistance to Onc112.

SQ110 DTC [a]	MIC [µmol L^{-1}]	
	Bac 7	Onc 112
"wild type" [b]	0.75	3
2503C	0.75	12.5
2059C	0.75	12.5
2503C/2059G	0.75	50

[a] The *E. coli* strain SQ110DTC and its derivatives used in these experiments carry a single chromosomal *rrn* allele and lack the *tolC* transporter gene (Orelle, Carlson, et al. 2013).
[b] The parental SQ110DTC strain lacking rRNA mutations is designated "wild type".

Both of these residues interact with A2062 (**Figure 3.22**) which in turn forms stacking interactions with the peptide (**Figure 3.23**B). Because of the enhanced stacking between Onc112 and A2062 (2083) compared to $Bac7_{1-35}$ (**Figure 3.23**B), any mutation which affects the position of A2062 is expected to have a greater effect on the binding of Onc112 than $Bac7_{1-35}$. The results of mutational analysis suggest that the proper positioning of A2062 influences the activity of Onc112 and establish the ribosome as the immediate cellular target of Onc112 and likely other PrAMPs.

3.4 Conclusion

We have established the molecular determinants required for ribosome binding of several PrAMPs. Our data show that the variable N-terminal domain makes different types of interactions with the ribosome, providing a rationale for the observed sequence diversity of the N-terminal domain in PrAMPs. For all selected PrAMPs here, the location occupied by their N-terminal region is sterically incompatible with the simultaneous binding of the aminoacyl-tRNA in the ribosomal A site, thereby interfering with the initiation step of protein synthesis. The conserved middle region of all PrAMPs presented here superposes surprisingly well and correspondingly forms homologous interactions with the peptide tunnel. This region of the peptide tunnel is known to be the binding site of several antibiotics, including chloramphenicol, homoharingtonine, hygromycin A and other antibiotics, and also to accommodate the amino acid attached to the aminoacyl-tRNA bound in the A site. The variable C-terminal region interacts with different elements of the ribosome and overlaps with the binding site of macrolide and streptogramin B antibiotics. The binding in the peptide exit tunnel by different PrAMPs and their common mechanism of action of protein synthesis inhibition afforded by interaction with multiple rRNA residues encompassing three antibiotic-binding sites indicates that it has been conserved throughout evolution, suggesting an efficient way to inactivate the bacterial ribosome. The common ribosome binding and mechanism of translation inhibition by the multiple PrAMPs reported here establishes a structural basis for the design of new and more effective antibiotics.

3.5 Cited literature

Adams, P. D., P. V. Afonine, G. Bunkoczi, V. B. Chen, I. W. Davis, N. Echols, J. J. Headd, L. W. Hung, G. J. Kapral, R. W. Grosse-Kunstleve, A. J. McCoy, N. W. Moriarty, R. Oeffner, R. J. Read, D. C. Richardson, J. S. Richardson, T. C. Terwilliger, and P. H. Zwart. 2010. 'PHENIX: a comprehensive Python-based system for macromolecular structure solution', *Acta Crystallogr. D Biol. Crystallogr.*, 66: 213-21.

Agerberth, B., J. Y. Lee, T. Bergman, M. Carlquist, H. G. Boman, V. Mutt, and H. Jornvall. 1991. 'Amino acid sequence of PR-39. Isolation from pig intestine of a new member of the family of proline-arginine-rich antibacterial peptides', *Eur J Biochem*, 202: 849-54.

Amunts, A., K. Fiedorczuk, T. T. Truong, J. Chandler, E. Peter Greenberg, and V. Ramakrishnan. 2015. 'Bactobolin A binds to a site on the 70S ribosome distinct from previously seen antibiotics', *Journal of molecular biology*, 427: 753-5.

Benincasa, M., M. Scocchi, E. Podda, B. Skerlavaj, L. Dolzani, and R. Gennaro. 2004. 'Antimicrobial activity of Bac7 fragments against drug-resistant clinical isolates', *Peptides*, 25: 2055-61.

Benincasa, M., S. Zahariev, C. Pelillo, A. Milan, R. Gennaro, and M. Scocchi. 2015. 'PEGylation of the peptide Bac7(1-35) reduces renal clearance while retaining antibacterial activity and bacterial cell penetration capacity', *Eur J Med Chem*, 95: 210-9.

Berthold, N., and R. Hoffmann. 2014. 'Cellular uptake of apidaecin 1b and related analogs in Gram-negative bacteria reveals novel antibacterial mechanism for proline-rich antimicrobial peptides', *Protein and peptide letters*, 21: 391-8.

Blaha, G. M., Y. S. Polikanov, and T. A. Steitz. 2012. 'Elements of ribosomal drug resistance and specificity', *Curr Opin Struct Biol*, 22: 750-8.

Bulkley, D., L. Brandi, Y. S. Polikanov, A. Fabbretti, M. O'Connor, C. O. Gualerzi, and T. A. Steitz. 2014. 'The antibiotics dityromycin and GE82832 bind protein S12 and block EF-G-catalyzed translocation', *Cell Report*, 6: 357-65.

Bulkley, D., C. A. Innis, G. Blaha, and T. A. Steitz. 2010. 'Revisiting the structures of several antibiotics bound to the bacterial ribosome', *Proceedings of the National Academy of Sciences of the United States of America*, 107: 17158-63.

Bulkley, D., F. Johnson, and T. A. Steitz. 2012. 'The antibiotic thermorubin inhibits protein synthesis by binding to inter-subunit bridge B2a of the ribosome', *Journal of molecular biology*, 416: 571-8.

Casteels, P., C. Ampe, F. Jacobs, M. Vaeck, and P. Tempst. 1989. 'Apidaecins: antibacterial peptides from honeybees', *The EMBO journal*, 8: 2387-91.

Chan, Y. R., M. Zanetti, R. Gennaro, and R. L. Gallo. 2001. 'Anti-microbial activity and cell binding are controlled by sequence determinants in the anti-microbial peptide PR-39', *J Invest Dermatol*, 116: 230-5.

Chernysh, S., S. Cociancich, J. P. Briand, C. Hetru, and P. Bulet. 1996. 'The inducible antibacterial peptides of the hemipteran insect Palomena prasina: Identification of a unique family of proline-rich peptides and of a novel insect defensin', *J. Insect Physiol.*, 42: 81-89.

Cociancich, S., A. Dupont, G. Hegy, R. Lanot, F. Holder, C. Hetru, J. A. Hoffmann, and P. Bulet. 1994. 'Novel inducible antibacterial peptides from a hemipteran insect, the sap-sucking bug Pyrrhocoris apterus', *Biochem J*, 300 (Pt 2): 567-75.

Dunkle, J. A., L. Xiong, A. S. Mankin, and J. H. Cate. 2010. 'Structures of the Escherichia coli ribosome with antibiotics bound near the peptidyl transferase center explain spectra of drug action', *Proceedings of the National Academy of Sciences of the United States of America*, 107: 17152-7.

Emsley, P., and K. Cowtan. 2004. 'Coot: model-building tools for molecular graphics', *Acta Crystallogr. D Biol. Crystallogr.*, 60: 2126-32.

Frank, R. W., R. Gennaro, K. Schneider, M. Przybylski, and D. Romeo. 1990. 'Amino acid sequences of two proline-rich bactenecins. Antimicrobial peptides of bovine neutrophils', *The Journal of biological chemistry*, 265: 18871-4.

Gagnon, M. G., J. Lin, D. Bulkley, and T. A. Steitz. 2014. 'Crystal structure of elongation factor 4 bound to a clockwise ratcheted ribosome', *Science*, 345: 684-7.

Gagnon, M. G., S. V. Seetharaman, D. Bulkley, and T. A. Steitz. 2012. 'Structural basis for the rescue of stalled ribosomes: structure of YaeJ bound to the ribosome', *Science*, 335: 1370-2.

Garreau de Loubresse, N., I. Prokhorova, W. Holtkamp, M. V. Rodnina, G. Yusupova, and M. Yusupov. 2014. 'Structural basis for the inhibition of the eukaryotic ribosome', *Nature*, 513: 517-22.

Gennaro, R., B. Skerlavaj, and D. Romeo. 1989. 'Purification, composition, and activity of two bactenecins, antibacterial peptides of bovine neutrophils', *Infect Immun*, 57: 3142-6.

Guida, F., M. Benincasa, S. Zahariev, M. Scocchi, F. Berti, R. Gennaro, and A. Tossi. 2015. 'Effect of size and N-terminal residue characteristics on bacterial cell penetration and antibacterial activity of the proline-rich peptide Bac7', *Journal of medicinal chemistry*, 58: 1195-204.

Gurel, G., G. Blaha, P. B. Moore, and T. A. Steitz. 2009. 'U2504 determines the species specificity of the A-site cleft antibiotics: the structures of tiamulin, homoharringtonine, and bruceantin bound to the ribosome', *Journal of molecular biology*, 389: 146-56.

Junemann, R., J. Wadzack, F. J. Triana-Alonso, J. U. Bittner, J. Caillet, T. Meinnel, K. Vanatalu, and K. H. Nierhaus. 1996. 'In vivo deuteration of transfer RNAs: overexpression and large-scale purification of deuterated specific tRNAs', *Nucleic acids research*, 24: 907-13.

Kabsch, W. 1993. 'Automatic processing of rotation diffraction data from crystals of initially unknown symmetry and cell constants', *J. Appl. Cryst.*, 26: 795-800.

Kannan, K., N. Vazquez-Laslop, and A. S. Mankin. 2012. 'Selective protein synthesis by ribosomes with a drug-obstructed exit tunnel', *Cell*, 151: 508-20.

Knappe, D., S. Piantavigna, A. Hansen, A. Mechler, A. Binas, O. Nolte, L. L. Martin, and R. Hoffmann. 2010. 'Oncocin (VDKPPYLPRPRPPRRIYNR-NH2): a novel antibacterial peptide optimized against gram-negative human pathogens', *Journal of medicinal chemistry*, 53: 5240-7.

Knappe, D., M. Zahn, U. Sauer, G. Schiffer, N. Strater, and R. Hoffmann. 2011. 'Rational design of oncocin derivatives with superior protease stabilities and antibacterial activities based on the high-resolution structure of the oncocin-DnaK complex', *Chembiochem : a European journal of chemical biology*, 12: 874-6.

Kragol, G., S. Lovas, G. Varadi, B. A. Condie, R. Hoffmann, and L. Otvos, Jr. 2001. 'The antibacterial peptide pyrrhocoricin inhibits the ATPase actions of DnaK and prevents chaperone-assisted protein folding', *Biochemistry*, 40: 3016-26.

Krizsan, A., D. Volke, S. Weinert, N. Strater, D. Knappe, and R. Hoffmann. 2014. 'Insect-derived proline-rich antimicrobial peptides kill bacteria by inhibiting bacterial protein translation at the 70 s ribosome', *Angew. Chem. Int. Ed. Engl.*, 53: 12236-9.

Li, W., J. Tailhades, N. M. O'Brien-Simpson, F. Separovic, L. Otvos, Jr., M. A. Hossain, and J. D. Wade. 2014. 'Proline-rich antimicrobial peptides: potential therapeutics against antibiotic-resistant bacteria', *Amino Acids*, 46: 2287-94.

Lin, J., M. G. Gagnon, D. Bulkley, and T. A. Steitz. 2015. 'Conformational changes of elongation factor G on the ribosome during tRNA translocation', *Cell*, 160: 219-27.

Mardirossian, M., R. Grzela, C. Giglione, T. Meinnel, R. Gennaro, P. Mergaert, and M. Scocchi. 2014. 'The host antimicrobial peptide Bac71-35 binds to bacterial ribosomal proteins and inhibits protein synthesis', *Chemical Biology*, 21: 1639-47.

Marlow, V. L., A. F. Haag, H. Kobayashi, V. Fletcher, M. Scocchi, G. C. Walker, and G. P. Ferguson. 2009. 'Essential role for the BacA protein in the uptake of a truncated eukaryotic peptide in Sinorhizobium meliloti', *J Bacteriol*, 191: 1519-27.

Mattiuzzo, M., A. Bandiera, R. Gennaro, M. Benincasa, S. Pacor, N. Antcheva, and M. Scocchi. 2007. 'Role of the Escherichia coli SbmA in the antimicrobial activity of proline-rich peptides', *Mol Microbiol*, 66: 151-63.

McCoy, L. S., Y. Xie, and Y. Tor. 2011. 'Antibiotics that target protein synthesis', *Wiley Interdiscip Rev RNA*, 2: 209-32.

Merryman, C., and H. F. Noller. 1998. 'Footprinting and modification-interference analysis of binding sites on RNA.' in Smith CWJ (ed.), *RNA:Protein Interactions* (Oxford Univ Press, UK).

Narayanan, S., J. K. Modak, C. S. Ryan, J. Garcia-Bustos, J. K. Davies, and A. Roujeinikova. 2014. 'Mechanism of Escherichia coli resistance to Pyrrhocoricin', *Antimicrobial agents and chemotherapy*, 58: 2754-62.

Nguyen, L. T., E. F. Haney, and H. J. Vogel. 2011. 'The expanding scope of antimicrobial peptide structures and their modes of action', *Trends in biotechnology*, 29: 464-72.

Orelle, C., S. Carlson, B. Kaushal, M. M. Almutairi, H. Liu, A. Ochabowicz, S. Quan, V. C. Pham, C. L. Squires, B. T. Murphy, and A. S. Mankin. 2013. 'Tools for characterizing bacterial protein synthesis inhibitors', *Antimicrobial agents and chemotherapy*, 57: 5994-6004.

Orelle, C., T. Szal, D. Klepacki, K. J. Shaw, N. Vazquez-Laslop, and A. S. Mankin. 2013. 'Identifying the targets of aminoacyl-tRNA synthetase inhibitors by primer extension inhibition', *Nucleic acids research*, 41: e144.

Otvos, L., Jr. 2000. 'Antibacterial peptides isolated from insects', *J. Pept. Sci.*, 6: 497-511.

Podda, E., M. Benincasa, S. Pacor, F. Micali, M. Mattiuzzo, R. Gennaro, and M. Scocchi. 2006. 'Dual mode of action of Bac7, a proline-rich antibacterial peptide', *Biochimica et biophysica acta*, 1760: 1732-40.

Polikanov, Y. S., G. M. Blaha, and T. A. Steitz. 2012. 'How hibernation factors RMF, HPF, and YfiA turn off protein synthesis', *Science*, 336: 915-8.

Polikanov, Y. S., S. V. Melnikov, D. Soll, and T. A. Steitz. 2015. 'Structural insights into the role of rRNA modifications in protein synthesis and ribosome assembly', *Nat Struct Mol Biol*, 22: 342-44.

Polikanov, Y. S., I. A. Osterman, T. Szal, V. N. Tashlitsky, M. V. Serebryakova, P. Kusochek, D. Bulkley, I. A. Malanicheva, T. A. Efimenko, O. V. Efremenkova, A. L. Konevega, K. J. Shaw, A. A. Bogdanov, M. V. Rodnina, O. A. Dontsova, A. S. Mankin, T. A. Steitz, and P. V. Sergiev. 2014. 'Amicoumacin a inhibits translation by stabilizing mRNA interaction with the ribosome', *Molecular cell*, 56: 531-40.

Polikanov, Y. S., A. L. Starosta, M. F. Juette, R. B. Altman, D. S. Terry, W. Lu, B. J. Burnett, G. Dinos, K. A. Reynolds, S. C. Blanchard, T. A. Steitz, and D. N. Wilson. 2015. 'Distinct tRNA Accommodation Intermediates Observed on the Ribosome with the Antibiotics Hygromycin A and A201A', *Molecular cell*.

Polikanov, Y. S., T. A. Steitz, and C. A. Innis. 2014. 'A proton wire to couple aminoacyl-tRNA accommodation and peptide-bond formation on the ribosome', *Nat. Struct. Mol. Biol.*, 21: 787-93.

Polikanov, Y. S., T. Szal, F. Jiang, P. Gupta, R. Matsuda, M. Shiozuka, T. A. Steitz, N. Vazquez-Laslop, and A. S. Mankin. 2014. 'Negamycin interferes with decoding and translocation by simultaneous interaction with rRNA and tRNA', *Molecular cell*, 56: 541-50.

Raj, P. A., and M. Edgerton. 1995. 'Functional domain and poly-L-proline II conformation for candidacidal activity of bactenecin 5', *FEBS Lett*, 368: 526-30.

Roy, R. N., I. B. Lomakin, M. G. Gagnon, and T. A. Steitz. 2015. 'The mechanism of inhibition of protein synthesis by the proline-rich peptide oncocin', *Nat. Struct. Mol. Biol.*, 22: 466-9.

Runti, G., C. Lopez Ruiz Mdel, T. Stoilova, R. Hussain, M. Jennions, H. G. Choudhury, M. Benincasa, R. Gennaro, K. Beis, and M. Scocchi. 2013. 'Functional characterization of SbmA, a bacterial inner membrane transporter required for importing the antimicrobial peptide Bac7(1-35)', *J Bacteriol*, 195: 5343-51.

Sadler, K., K. D. Eom, J. L. Yang, Y. Dimitrova, and J. P. Tam. 2002. 'Translocating proline-rich peptides from the antimicrobial peptide bactenecin 7', *Biochemistry*, 41: 14150-7.

Sanbonmatsu, K. Y., S. Joseph, and C. S. Tung. 2005. 'Simulating movement of tRNA into the ribosome during decoding', *Proceedings of the National Academy of Sciences of the United States of America*, 102: 15854-9.

Scocchi, M., D. Romeo, and M. Zanetti. 1994. 'Molecular cloning of Bac7, a proline- and arginine-rich antimicrobial peptide from bovine neutrophils', *FEBS Letters*, 352: 197-200.

Scocchi, M., A. Tossi, and R. Gennaro. 2011. 'Proline-rich antimicrobial peptides: converging to a non-lytic mechanism of action', *Cell Mol. Life Sci.*, 68: 2317-30.

Seefeldt, A. C., F. Nguyen, S. Antunes, N. Perebaskine, M. Graf, S. Arenz, K. K. Inampudi, C. Douat, G. Guichard, D. N. Wilson, and C. A. Innis. 2015. 'The proline-rich antimicrobial peptide Onc112 inhibits translation by blocking and destabilizing the initiation complex', *Nat. Struct. Mol. Biol.*, 22: 470-5.

Selmer, M., C. M. Dunham, F. V. th Murphy, A. Weixlbaumer, S. Petry, A. C. Kelley, J. R. Weir, and V. Ramakrishnan. 2006. 'Structure of the 70S ribosome complexed with mRNA and tRNA', *Science*, 313: 1935-42.

Shimizu, Y., T. Kanamori, and T. Ueda. 2005. 'Protein synthesis by pure translation systems', *Methods*, 36: 299-304.

Sothiselvam, S., B. Liu, W. Han, H. Ramu, D. Klepacki, G. C. Atkinson, A. Brauer, M. Remm, T. Tenson, K. Schulten, N. Vazquez-Laslop, and A. S. Mankin. 2014. 'Macrolide antibiotics allosterically predispose the ribosome for translation arrest', *Proceedings of the National Academy of Sciences of the United States of America*, 111: 9804-9.

Stanley, R. E., G. Blaha, R. L. Grodzicki, M. D. Strickler, and T. A. Steitz. 2010. 'The structures of the anti-tuberculosis antibiotics viomycin and capreomycin bound to the 70S ribosome', *Nat. Struct. Mol. Biol.*, 17: 289-93.

Tomasinsig, L., and M. Zanetti. 2005. 'The cathelicidins--structure, function and evolution', *Curr Protein Pept Sci*, 6: 23-34.

Vazquez-Laslop, N., C. Thum, and A. S. Mankin. 2008. 'Molecular mechanism of drug-dependent ribosome stalling', *Molecular cell*, 30: 190-202.

Voorhees, R. M., A. Weixlbaumer, D. Loakes, A. C. Kelley, and V. Ramakrishnan. 2009. 'Insights into substrate stabilization from snapshots of the peptidyl transferase center of the intact 70S ribosome', *Nat Struct Mol Biol*, 16: 528-33.

Winn, M. D., C. C. Ballard, K. D. Cowtan, E. J. Dodson, P. Emsley, P. R. Evans, R. M. Keegan, E. B. Krissinel, A. G. Leslie, A. McCoy, S. J. McNicholas, G. N. Murshudov, N. S. Pannu, E. A. Potterton, H. R. Powell, R. J. Read, A. Vagin, and K. S. Wilson. 2011. 'Overview of the CCP4 suite and current developments', *Acta Crystallogr. D Biol. Crystallogr.*, 67: 235-42.

Yi, H. Y., M. Chowdhury, Y. D. Huang, and X. Q. Yu. 2014. 'Insect antimicrobial peptides and their applications', *Applied microbiology and biotechnology*, 98: 5807-22.

Zahn, M., N. Berthold, B. Kieslich, D. Knappe, R. Hoffmann, and N. Strater. 2013. 'Structural studies on the forward and reverse binding modes of peptides to the chaperone DnaK', *Journal of molecular biology*, 425: 2463-79.

Zahn, M., B. Kieslich, N. Berthold, D. Knappe, R. Hoffmann, and N. Strater. 2014. 'Structural identification of DnaK binding sites within bovine and sheep bactenecin Bac7', *Protein and peptide letters*, 21: 407-12.

Zasloff, M. 2002. 'Antimicrobial peptides of multicellular organisms', *Nature*, 415: 389-95.

4. AN ANTIMICROBIAL PEPTIDE THAT INHIBITS TRANSLATION BY TRAPPING RELEASE FACTORS ON THE RIBOSOME

(previously published as Florin, T. et al. An antimicrobial peptide that inhibits translation by trapping release factors on the ribosome. *Nat Struct Mol Biol* **24**, 752-757 (2017).)

4.1 Introduction

The release of the polypeptide from the ribosome is an essential step of protein synthesis. When the translating ribosome reaches the end of an open reading frame (ORF), it carries the completed protein chain attached to the P-site tRNA and has a stop codon in the A site. In bacteria, termination requires the action of three release factors (RFs), RF1, RF2 and RF3. RF1 or RF2 recognize the stop codon in the A site of the small (30S) subunit while their conserved GGQ motif is placed in the active site of the peptidyl transferase center (PTC) of the large (50S) subunit where it facilitates the hydrolysis of the peptidyl-tRNA ester bond, releasing the completed protein (reviewed in Korostelev 2011). Because the number of ribosomes in the cell greatly exceeds the number of RF1 and RF2 molecules (Bremer and Dennis 1996; Schmidt et al. 2016), continuous translation relies upon the rapid turnover of these factors in order to serve the needs of all the cellular ribosomes. RF3 is a GTPase that facilitates recycling of RF1 and RF2 subsequent to polypeptide release (Koutmou et al. 2014; Shi and Joseph 2016). Finally, the ribosome recycling factor (RRF) together with the elongation factor G (EF-G) dislodge the ribosome from the mRNA and splits it into subunits (Kaji et al. 2001). Inhibition of any of these reactions should reduce fitness and viability of the bacterial cell. Strikingly, in spite of the complexity and importance of the translation termination, no specific inhibitors of this key step in protein synthesis have so far been identified.

Antimicrobial peptides constitute an important component of the innate immune defense system of multicellular organisms against bacterial infection (Zasloff 2002). While many antibacterial peptides lyse cells by disrupting their membrane, a specific class of non-lytic peptides, called proline-rich antimicrobial peptides (PrAMPs), act upon the intracellular target, the ribosome (Scocchi et al. 2016; Li et al. 2014; Seefeldt et al. 2016; Roy et al. 2015; Seefeldt et al. 2015;

Gagnon et al. 2016). Several investigated PrAMPs, such as oncocin 112 (Onc112) and others, whose size range from 15 to 20 amino acids, bind to the nascent peptide exit tunnel of the ribosome and, by encroaching upon the A site of the peptidyl transferase center (PTC), prevent binding of aminoacyl-tRNA (Seefeldt et al. 2016; Roy et al. 2015; Seefeldt et al. 2015; Gagnon et al. 2016). This mode of action results in the arrest of the ribosome at the mRNA start codon before the first peptide bond can be formed (Seefeldt et al. 2016; Roy et al. 2015; Seefeldt et al. 2015; Gagnon et al. 2016).

Among PrAMPs, the 18-20 amino acid long antimicrobial peptides called apidaecins, which are produced by bees, hornets and wasps, remain outliers. Compared to other PrAMPs, they compete with a different subset of ribosomal antibiotics for binding (Krizsan et al. 2015). Furthermore, while Onc112 and other PrAMPs readily inhibited protein synthesis in vivo and in vitro, apidaecins efficiently interfered with protein synthesis in living cells, but are a poor inhibitors of in vitro translation (Castle et al. 1999; Krizsan et al. 2014; Krizsan et al. 2015). We sought to understand the mechanism of action of apidaecins using Api137 (**Figure 2.4**a), an 18- amino acid derivative of the natural apidaecin 1b, which was optimized to have improved antibacterial properties and serum stability (Berthold et al. 2013).

4.2 Materials and Methods

Peptides and oligonucleotides

Api137 was synthesized by NovoPro Biosciences Inc. Onc112 was synthesized by GenScript. The ‘start-stop’ mRNA (**Table 4.12**) was purchased from IBA GmbH. The 2XermCL_S10_UAG construct was synthesized by Eurofins. DNA oligonucleotides were synthesized by Integrated DNA Technologies.

Table 4.12: DNA & RNA templates: Promotor – blue, ORF – red, annealing site for toeprinting primer – purple, annealing site for oligonucleotide for RNase H treatment of disomes – green. Start codons of the ORFs are shown in bold, stop codons are underlined.

Name	DNA Sequence (5' – 3')
yrbA-fs	TAATACGACTCACTATAGGGCTTAAGTATAAGGAGGAAAACATA **TG**ATATACCCCTGCGGAGTGGGCGCGCGATCGCAAACTGAACG GCTTTAGGCCGACCTCGACAGTTGGATTCACGTGCTGAATCCT GATGCGATGTCGAGTTAATAAGCAAAATTCATTATAACC
ermCL-UAG	TTAATACGACTCACTATAGGGAATTGTGAGCGGATAACAATTGC TAGTCTTAAGTTTTATAAGGAGGAAAAAAT**ATG**GGCATTTTTAGT ATTTTTGTAATCAGCACAGTTCATTATCAACCAAACAAAAAATAG GTGGTTATAATGAATCGTTAATAAGCAAAATTCATTATAACCAAA TTAAAGAGGGTTATAA
RST2	TAATACGACTCACTATAGGGCTTAAGTATAAGGAGGAAAACAT **ATG**AAATTCGCCATCACCCTGCGTCAGTGCGAAGGCTGGTCAC CGGTACATTATGACAATTAATAATAATAAAAAAAGTGATAGAATT CTATCGTTAATAAGCAAAATTCATTATAACC
ermBL	TAATACGACTCACTATAGGGCTTAAGTATAAGGAGGAAAAAAT**A** **TG**TTGGTATTCCAAATGCGTAATGTAGATAAAACATCTACTATTT AAGTGATAGAATTCTATCGTTAATAAGCAAAATTCATTATAACC
start-stop	GGCAAGGAGGUAAAUA**AUG**UAAACGAUU
tnaC-UAG	TTGACAATTAATCATCGGCTCGTATAATGTGTGGAAGTTTTATAA GGAGGAAAACAT**ATG**AATATCTTACATATATGTGTGACCTCAAA ATGGTTCAATATTGACAACAAAATTGTCGATCACCGCCCTTAG
tnaC-UGA	TTGACAATTAATCATCGGCTCGTATAATGTGTGGAAGTTTTATAA GGAGGAAAACAT**ATG**AATATCTTACATATATGTGTGACCTCAAA ATGGTTCAATATTGACAACAAAATTGTCGATCACCGCCCTTGA
2XermCL_S10_UAG	UAAUACGACUCACUAUAGGGAGUUUUAUAAGGAGGAAAAAAUA **UG**GGCAUUUUUAGUAUUUUUGUAAUCUAGACAGUUCAUUAUC AACCAAACAAAAAAUAAAGUUUUAUAAGGAGGAAAAAAU**AUG**G GCAUUUUUAGUAUUUUUGUAAUCUAGACAGUUCAUUAUCAAC CAAACAAAAAAUAA

Generation of templates for in vitro translation and toeprinting

The DNA templates for toeprinting were generated by PCR using AccuPrime DNA Polymerase (Thermo Fisher Scientific) and primers listed in **Table 4.13**. The synthetic template *yrbA-fs15* was prepared using 3 overlapping primers (T7-IR-AUG, IR-yrbA-fs15-RF1 and posT-NV1) in a single PCR reaction. The *ermCL* template was created by PCR amplification of the gene from the plasmid pERMCT7-M (Vazquez-Laslop, Thum, and Mankin 2008) using primers T7 and ermCL-UAG. The complete sequences of the templates are shown in **Table 4.12**.

Toeprinting reactions were carried out in 5 µl of PURExpress transcription-translation system (New England Biolabs) as previously described (Vazquez-Laslop, Thum, and Mankin 2008; Orelle

et al. 2013). The reverse transcription on the *ermCL* template was carried out using primer ermCL-TP-term. The final concentrations of Api137 and Onc112 in the reactions were 50 μM; the PrAMPs were added as stock solutions in water.

Table 4.13: Oligonucleotides used in this study.

Name	Sequence
T7-IR-AUG	TAATACGACTCACTATAGGGCTTAAGTATAAGGAGGAAAACATATG
IR-yrbA-fs15-RF1	GTATAAGGAGGAAAACATATGATATACCCCTGCGGAGTGGGCGCGCGA TCGCAAACTGAACGGCTTTAGGCCGACCTCGACAGTTGGAT
posT-NV1	GGTTATAATGAATTTTGCTTATTAACTCGACATCGCATCAGGATTCAGC ACGTGAATCCAACTGTCGAGGTCG
T7	TAATACGACTCACTATAGGG
ermCL-UAG	TTATAACCCTCTTTAATTTGGTTATAATGAATTTTGCTTATTAACGATTCA T TATAACCACCTATT
ermCL-TP-term	TTATAACCCTCTTTAATTTGGTT
SbmA-seq-fwd	CATTTGGCTGACGCTTTGTA
SbmA-seq-rev	TACTACACCCCGCTAAAACC
SbmA-EcoRI-rev	TGACGCGCGGAATTCCTTCT
PrfA-seq-fwd	CTGAATATTCTGCGCGACAG
PrfA-seq-rev	CAGGATTTCAGCATCACGC
PrfB-seq-fwd	GCTCTTATCACCGCATTTTG
PrfB-seq-rev	GTTCATTGTTAAGATCGACTACC
PrfC-seq-fwd	GAAGGTAAGCTGGATATGCTG
PrfC-seq-rev	GCTTCTGATAACGTAGCCAG
rplP-seq-fwd	CGTTAAAGTGTGGATCTTCAAAGG
rplP-seq-rev	CACTTGCTTCAACAGGTGAG
L2667	GGTCCTCTCGTACTAGGAGCAG
L2180	GGGTGGTATTTCAAGGTCGG
Ptrc-tnaC	ACATGGATTCTTGACAATTAATCATCGGCTCGTATAATGTGTGGAAGTT TTATAAGGAGGAAAACATATG
M13 rev (-44)	AGCGGATAACAATTTCACACAGGA
tnaC-UAG-rev	GCAAACTAAGGGCGGTGATCGAC
tnaC-UGA-rev	GCAAATCAAGGGCGGTGATCGAC

Selection of Api137-resistant mutants

The first round of selection of Api137 resistant mutants was performed with the *E. coli* strain SQ110, derived from the K12 strain (**Table 4.14**). An overnight culture grown in Luria-Bertani (LB) medium was diluted 100-fold into fresh medium containing subinhibitory concentration of Api137 (10 μM). After 24 h growth at 37°C, the culture was diluted 100-fold into 1 ml fresh LB medium containing 50 μM Api137. The culture was passaged one more time at 100 μM Api137 (8-fold MIC). The dilutions of cell culture were plated on LB agar. After overnight incubation, the *sbmA* gene was PCR amplified from 20 individual colonies using primers SbmA-seq-fwd and SbmA-seq-rev and sequenced. All but one clone had mutations in the *sbmA* gene. The Api137-resistant clone

with the wt *sbmA* sequence (clone SQ110 ApiR21 in **Table 4.14**) was grown in liquid culture; genomic DNA was isolated and prepared for sequencing using a Nextera XT kit (Illumina). Sequencing was performed on an Illumina NextSeq500 instrument (paired-end, 2x150 base reads) at the DNA Services facility at UIC. After mapping the reads to the genome of the strain SQ110(Quan et al. 2015), the single mutation A722G in the *prfA* gene was identified. The presence of the mutation was verified by PCR-amplification of the *prfA* gene using primers PrfA-seq-fwd and PrfA-seq-rev from the parent and mutant strains and sequencing.

E. coli strain BL21(DE3) (**Table 4.14**) was used in the second selection experiment. In order to avoid selection of *sbmA* mutants, prior to selection cells were transformed with the multicopy plasmid pZα-SbmA encoding the functional SbmA transporter. The pZα-SbmA plasmid was prepared by amplifying the *E. coli sbmA* gene using primers SbmA-seq-fwd and SbmA-EcoRI-rev, cutting the PCR product with restriction enzymes *Nde*I and *Eco*RI, and ligating the resulting DNA fragment into the pZα plasmid (Bailey, Chettiath, and Mankin 2008) cut with the same enzymes. For selection of Api137-resistant mutants, the overnight culture of BL21(DE3)/pZα-SbmA cells was diluted 1:100 in LB medium containing ampicillin (100 μg/ml) and 0.1 μM isopropyl-b-D-1-thiogalactopyranoside (IPTG) and grown at 37°C until reaching A_{600} of 0.5. Two ml (approximately 10^9 cells) were plated on LB agar supplemented with 100 μg/ml ampicillin, 0.1 μM IPTG and 12 μM (4-fold MIC) Api137. After overnight incubation at 37°C, 10 colonies appeared. The *prfA*, *prfB* and *prfC* genes were PCR amplified using pairs of primers PrfA-seq-fwd with PrfA-seq-rev, PrfB-seq-fwd and PrfB-seq-rev, or PrfC-seq-fwd with PrfC-seq-rev, respectively, and sequenced. Five clones had mutations in the *prfB* gene: three of these had the C784T and two clones had the A839T mutation. The genome of one of the remaining five clones was sequenced and revealed the presence of the G241A mutation in the *rplP* gene encoding ribosomal protein uL16. The presence of this mutation in this and four remaining clones was verified by PCR-amplification of the *rplP* gene using primers RplP-seq-fwd and RplP-seq-rev and sequencing.

Table 4.14: Bacterial strains used in this study

Strain	Type	Source
SQ171	K-strain; F-, *Δ(rrsH-aspU)794(::FRT)*, *λ*$^-$, *Δ(rrfG-rrsG)791(::FRT)*, *Δ(rrfF-rrsD)793(::FRT)*, *rph-1*, *Δ(rrsC-trpT)795(::FRT)*, *Δ(rrsA-rrfA)792(::FRT)*, *Δ(rrsB-rrfB)790(::FRT)*, *Δ(rrsE-rrfE)789(::FRT)*, ptRNA67, pKK3535	[32]
SQ110	K-strain, F-, *Δ(rrsH-aspU)794(::FRT)*, *λ*$^-$, *Δ(rrfG-rrsG)791(::FRT)*, *Δ(rrfF-rrsD)793(::FRT)*, *rph-1*, *Δ(rrsC-trpT)795(::FRT)*, *Δ(rrsA-rrfA)792(::FRT)*, *Δ(rrsB-rrfB)790(::FRT)*, ptRNA67	[32]
SQ110 ApiR2	derived from SQ110, *sbmA*(C752A)	*this study*
SQ110 ApiR21	derived from SQ110, *prfA*(A722G)	*this study*
BL21 (DE3)	B-strain; F-, *lon-11*, *Δ(ompT-nfrA)885*, *Δ(galM-ybhJ)884*, *λDE3 [lacI, lacUV5-T7 gene 1, ind1, sam7, nin5]*, *Δ46*, *[mal*$^+$*]*$_{K-12}$(λ^S), *hsdS10*	[58, 59]
BL21 ApiR10	derived from BL21 (DE3), *rplP*(G241A), pZα-SbmA	*this study*
BL21 ApiR11	derived from BL21 (DE3), *prfB*(C784T), pZα-SbmA	*this study*
BL21 ApiR12	derived from BL21 (DE3), *prfB*(A839T), pZα-SbmA	*this study*
AB301	K-strain; Hfr(PO21), *relA1*, *spoT1*, *metB1*	[60]
N281	K-strain; Hfr(PO21), *relA1*, *rplV281*, *spoT1*, *metB1*	[61, 62]
N282	K-strain; Hfr(PO21), *relA1*, *rplD282*, *spoT1*, *metB1*	[61, 62]
SQ171-ΔtolC	derived from SQ171; Δ*tolC*, pCSacB	[63]
SQ171-ΔtolC/W3	derived from SQ171-Δ*tolC*, *lacZ*(C2035T) pCSacB	*this study*

Preparation of PreHC for fast kinetics experiment

All experiments were performed in buffer A (50 mM Tris-HCl, pH 7.5, 70 mM $MgCl_2$, 30 mM KCl, 7 mM $MgCl_2$) at 37°C if not stated otherwise. Ribosomes from the *E. coli* strain MRE600, *E. coli* initiation factors IF1, IF2 and IF3, f[^{3}H]Met-tRNA^{fMet} and its fluorescein-labeled version f[^{3}H]Met-tRNA^{fMet}(Flu) were prepared as described (Rodnina and Wintermeyer 1995; Milon et al. 2007). PreHC was assembled on the synthetic 'start-stop' mRNA (**Table 4.12**) and purified through sucrose cushion as described (Peske et al. 2014). The extent of f[^{3}H]Met-tRNA^{fMet} binding was better than 95% as determined by nitrocellulose filter binding. The pellets of PreHC were resuspended in buffer A, flash-frozen in liquid nitrogen, and stored at -80°C.

Single-cysteine mutants RF1(S167C), RF1(S167C/D241G) and the K12-type RF2(A246T) variant were generated by site-directed mutagenesis of the corresponding plasmids. C-terminally 6xHis-tagged RF1 and RF2 were purified and *in vitro* methylated by PrmC according to the published

protocol (Kuhlenkoetter, Wintermeyer, and Rodnina 2011). RF3 was purified as described (Peske et al. 2014).

Peptide hydrolysis assay

f[^{3}H]Met-tRNA^{fMet} hydrolysis was monitored at single round conditions, by mixing [^{3}H]-PreHC (0.1 μM), preincubated with 0-100 μM Api137, with RF1 (1 μM) in a quench-flow apparatus at 37°C. Reactions were quenched with a 10% trichloroacetic acid (TCA) solution in 50% ethanol. The extent of hydrolysis was assessed by liquid scintillation counting of the supernatants after centrifugation for 30 min at 16000 x *g* at 4°C. For measuring peptide release under multi-turnover conditions, [^{3}H]-PreHC (0.1 μM) was preincubated with RF3 (0.1 μM), GTP (1 mM), pyruvate kinase (0.1 mg/ml), and phosphoenol pyruvate (3 mM) for 15 min at 37°C. The concentration of Api137, when present, was 1 μM. Time courses were started by addition of RF1/2 (10 nM) and after quenching the reactions with a 10% TCA solution in 50% ethanol, the samples were processed as described above.

Preparation of quencher-labeled RF1$_{Qsy}$

Prior to labeling, RF1s containing a single cysteine was incubated for 30 min at room temperature with a 10-fold molar excess of Tris(2-carboxyethyl)phosphine (TCEP, Sigma). The quencher dye QSY9 (Thermo Fisher) was dissolved in dimethyl sulfoxide (DMSO) and added to the RF1 solution at a 10-fold molar excess. Labeling reaction was incubated for 1 h at room temperature with vigorous shaking and stopped by addition of 2 mM dithiothreitol (DTT). The excess dye was removed by gel filtration on a PD10 column (GE Healthcare) and protein purity was checked by SDS-PAGE. The extent of RF1 labeling (as analyzed by absorbance) was greater than 80%.

Prior to labeling, RF1s containing a single cysteine was incubated for 30 min at room temperature with a 10-fold molar excess of Tris(2-carboxyethyl)phosphine (TCEP, Sigma). The quencher dye QSY9 (Thermo Fisher) was dissolved in dimethyl sulfoxide (DMSO) and added to the RF1 solution at a 10-fold molar excess. Labeling reaction was incubated for 1 h at room temperature with

vigorous shaking and stopped by addition of 2 mM dithiothreitol (DTT). The excess dye was removed by gel filtration on a PD10 column (GE Healthcare) and protein purity was checked by SDS-PAGE. The extent of RF1 labeling (as analyzed by absorbance) was greater than 80%.

Measuring kinetics of RF1 binding and dissociation

Rapid kinetics measurements were performed on an SX-20MV stopped-flow apparatus (Applied Photophysics, Leatherhead, UK). Experiments were performed by rapidly mixing equal volumes (60 µl) of f[^{3}H]Met-tRNA^{fMet}(Flu)-carrying PreHC (0.05 µM), preincubated with Api137 for 2 min at room temperature and $RF1_{Qsy}$ (0.15 µM) at 37°C. Fluorescein was excited at 470 nm and fluorescence emission was monitored after passing a KV500 filter (Schott). Time courses were evaluated by fitting using exponential functions by GraphPad Prism software. Dissociation rates (k_{off}) were determined by chase experiments: $PreHC_{flu}$ (0.05 µM) was preincubated with 0.15 µM $RF1_{Qsy}$ to generate $PostHC_{flu}$ in the absence or presence of 1 µM Api137. PreHC was then rapidly mixed with a 10-fold excess of unlabeled RF1 and RF3·GTP (1 mM); pyruvate kinase (0.1 mg/ml), and phosphoenol pyruvate (3 mM) were present in both syringes. The increase of fluorescence upon dissociation of $RF1_{Qsy}$ was monitored as described above.

Chemical probing of Api137 interaction with the ribosome

PostHC was prepared by incubating 70S ribosomes (9 µM) with tRNA^{fMet} (18 µM) and start-stop mRNA (18 µM) at 37°C for 30 min in buffer A containing 20 mM $MgCl_2$. PostHC (0.2 µM) was incubated in 50 µl of reaction buffer B (250 mM K-Borate, 50 mM $MgCl_2$, 500 mM NH_4Cl) with RF1 (1 µM) and/or Api137 (50 µM) at 37°C for 10 min. Modification with dimethylsulfate (Sigma-Aldrich) and quenching were carried out at 37°C for 10 min as described (Merryman and Noller 1998). rRNA was isolated by phenol extraction and the distribution of modifications was analyzed by primer extension using primers L2667 and L2180.

Cell-free translation and analysis of peptidyl-tRNA accumulation

To prepare the templates for translation in the *E. coli* S30 Extract System for Linear Templates (Promega), the *tnaC* gene was first amplified by PCR from genomic DNA of *E. coli* MG1655 using primer Ptrc-tnaC-2 in combination with either tnaC-UGA-rev or tnaC-UAG-rev. These PCR fragments were cloned into the SmaI site of pUC18 and the *tnaC* template was re-amplified with primers Ptrc-eCLi and rev-44.

The transcription–translation reactions were carried out in a total volume of 5 µl. The reactions contained 0.5 pmol of the *tnaC* DNA template, 2 µCi [^{35}S]-L-methionine (specific activity 1,175 Ci/mmol, MP Biomedicals). When needed, the reactions were supplemented with 50 µM of Api137 or 5 mM tryptophan, or 3.7 µM of purified RF1. The reactions were incubated at 37°C for 30 min and then, when needed, split in two aliquots, one of which was treated for 5 min at 37°C with 0.5 µg RNase A (Sigma-Aldrich). The translation products were precipitated with four volumes of cold acetone and resolved in a 16.5% Tris-Tricine gels that preserve the integrity of peptidyl-tRNA (Schägger and von Jagow 1987). Gels were dried, exposed to the phosphoimager screen and scanned on a Typhoon scanner (GE).

In vivo suppression of premature stop codon

The *E. coli* strain with a premature stop codon in the *lacZ* gene was generated by subjecting the SQ171-Δ*tolC* strain (**Table 4.14**) to chemical mutagenesis and selecting *lacZ* deficient mutants. For that, an overnight culture of SQ171-Δ*tolC* was diluted 1:200 into fresh LB medium supplemented with kanamycin (30 µg/ml), grown at 37°C until reaching A_{600} of 0.1 and then exposed to 0.1% of ethyl methanesulfonate (EMS) for 1 hr. Cells were washed twice with LB medium and plated at high density on LB-agar supplemented with kanamycin (50 µg/ml), X-gal (40 µg/ml), and IPTG (0.3 mM). White colonies were selected and re-streaked on fresh kanamycin (50 µg/ml), X-gal (40 µg/ml), and IPTG (0.3 mM) LB-agar plates. The presence of mutations was detected by PCR amplification of the *lacZ* gene and sequencing. The clone designated SQ171-

ΔtolC/W3 (**Table 4.14**) contained the C2035T mutation, which changed Gln679 of the encoded β-galactosidase to a UAG stop codon.

For testing the stop codon suppressing activity of Api137, SQ171-ΔtolC/W3 cells were grown in LB medium supplemented with 50 µg/ml of kanamycin. Upon reaching A_{600} of 1.0, 0.5 ml were mixed with 3.5 mL of LB agar (0.6%) kept at 50°C and poured on an LB-agar plate containing kanamycin (50 µg/ml), IPTG (0.2 mM) and X-gal (80 µg/ml). After solidification of the soft agar, 1 µl of 50 mg/ml solution of streptomycin (100 µg) or 1 µl of 2 mM solution of Api137 (4.6 µg) were spotted on top of the cell lawn. The plate was incubated overnight at 37°C. Stop-codon read-through activity was revealed by a blue halo around the spotted antibiotic.

Purification of RF1 for cryo-EM

N-terminally 6xHis-tagged *E. coli* RF1 was overexpressed in BL21 *E. coli* cells grown at 37°C from overnight culture in LB medium and in presence of 100 µg/mL Ampicillin. Protein expression was induced at A_{600} of 0.4 by adding IPTG to a final concentration of 1 mM. RF1 was expressed from pET28-plasmid kindly provided by Rachel Green (Johns Hopkins University, Baltimore). After 1 h of expression, cells were lysed using a microfluidizer. The cell lysate was cleared by centrifugation in a SS34 rotor (Sorval) at 4°C and 44,100 x g for 30 min. Purification of His-tagged RF1 was done with Protino Ni-NTA agarose beads (Macherey-Nagel). The final eluate was applied onto a Superdex HiLoad S75 16/600 column (GE Healthcare) to yield the final concentrated protein in gel filtration buffer (50 mM HEPES pH 7.4, 50 mM KCl, 100 mM NaCl, 2% glycerol and 5 mM 2-mercaptoethanol).

Sample preparation for cryo-electron microscopy

ErmCL_S10_UAG-SRCs (stalled ribosome complexes) were generated following the same disome purification procedure as previously described (Arenz et al. 2015; Arenz et al. 2014). The 2XermCL_S10_UAG template was based on the 2XermCL_disome construct described by (Arenz et al. 2015) except that serine 10 was replaced by a UAG stop codon.

In vitro translation of the 2XermCL_S10_UAG template was performed using the Rapid Translation System RTS100 *E. coli* HY Kit (5PRIME) in the presence of 50 µM Api137. Disomes were isolated using sucrose density gradients (10–55% sucrose in buffer A, containing 50 mM HEPES-KOH, pH 7.4, 100 mM KOAc, 25 mM $Mg(OAc)_2$, 6 mM 2-mercaptoethanol, 20 µM Api137 and one Complete EDTA-free Protease Inhibitor cocktail (Roche)) as previously described (Arenz et al. 2015; Arenz et al. 2014). The final purified complex was re-incubated with a 2.5-fold excess of RF1 and 50 µM Api137 for 15 min at 37°C.

Cryo-electron microscopy and single particle reconstruction

A total of 5 A_{260}/ml Api137-RF1 complex was applied to 2 nm pre-coated Quantifoil R3/3 holey carbon supported grids and vitrified using a Vitrobot Mark IV (FEI, Eindhoven). Data collection was performed using an FEI Titan Krios transmission electron microscope equipped with a Falcon II direct electron detector with a Falcon III chip (FEI, Eindhoven) at 300 kV using a pixel size of 1.084 Å and a defocus range of 0.7–2.5 µm. The data collection yielded a total number of 5132 micrographs. Each micrograph was recorded as a series of ten frames (2.5 $e^-/Å^2$ dose per frame). All frames (accumulated dose of 28 $e^-/Å^2$) were aligned using the Motion correction software(Li et al. 2013) and power-spectra, defocus values, astigmatism and estimation of micrograph resolution were determined by CTFFIND4 (Rohou and Grigorieff 2015). Micrographs showing Thon rings beyond 3.2 Å resolution were further manually inspected for good areas and power-spectra quality. Automatic particle picking was performed using SIGNATURE (Chen and Grigorieff 2007) and single particles were processed using the FREALIGN Software package (Grigorieff 2007). Initial alignment was performed with 116,212 particles using *E. coli* 70S ribosome as a reference structure. Subsequently, particles were subjected to 3D-classification resulting in six classes with a maximum resolution extending to <3.4 Å (0.143 FSC) for class 1 (**Figure 4.25**a-c). 3D classification and initial alignment was performed using three times decimated data. The local resolution of the final maps was computed using ResMap (Kucukelbir, Sigworth, and Tagare 2014) (**Figure 4.25**e-g). The final maps were sharpened by dividing the maps by the modulation transfer

function of the detector and by applying an automatically determined negative B-factor to the maps using RELION (Scheres 2012).

Molecular modeling and map docking procedures

The molecular model of the 70S ribosome was based on *E. coli*-70S-EF-Tu structure (Fischer et al. 2015). Release factor 1 was modelled based on the previously reported RF1 structure from (PDB ID 5J3C) (Pierson et al. 2016). The Ile-tRNA model was generated based on the P-site tRNA from (Huter et al. 2016). The models were initially adjusted and refined using Coot (Emsley and Cowtan 2004). Api137 was modelled de novo into the map using Coot. The complete atomic model of the *E. coli* ribosome was refined using phenix.real_space_refine (Adams et al. 2010) with secondary structure restraints calculated by PHENIX (Adams et al. 2010). Cross-validation against overfitting (**Figure 4.25**d) was performed as described elsewhere (Brown et al. 2015). The statistics of the refined model were obtained using MolProbity (Chen et al. 2010) and are presented in **Table 4.15**.

Table 4.15: Cryo-EM data collection and refinement statistics

Data Collection and Refinement	**RF1-API-70S complex**
Particles	38,203
Pixel size (Å)	1.084
Defocus range (μm)	0.7-2.5
Voltage (kV)	300
Electron dose ($e^-/Å^{-2}$)	28
Map sharpening B factor ($Å^2$)	-73.07
Resolution (Å, 0.143 FSC)	3.4
Map CC (whole unit cell)	0.76
Map CC (around atoms)	0.78
Model Composition	
Protein residues	6205
RNA bases	4643
Validation (proteins)	
Poor rotamers (%)	0.99
Ramachandran outliers (%)	0.52
Ramachandran favored (%)	87.92
Bad backbone bonds (%)	0.00
Bad backbone angles	0.12
MolProbity score	1.99 (100^{th} percentile)
Validation (nucleic acids)	
Correct sugar puckers (%)	99.08
Good backbone conformations (%)	76.72
Bad bonds (%)	0.00
Bad angles	0.03
Clash score, all atoms	**6.98 (100^{th} percentile)**

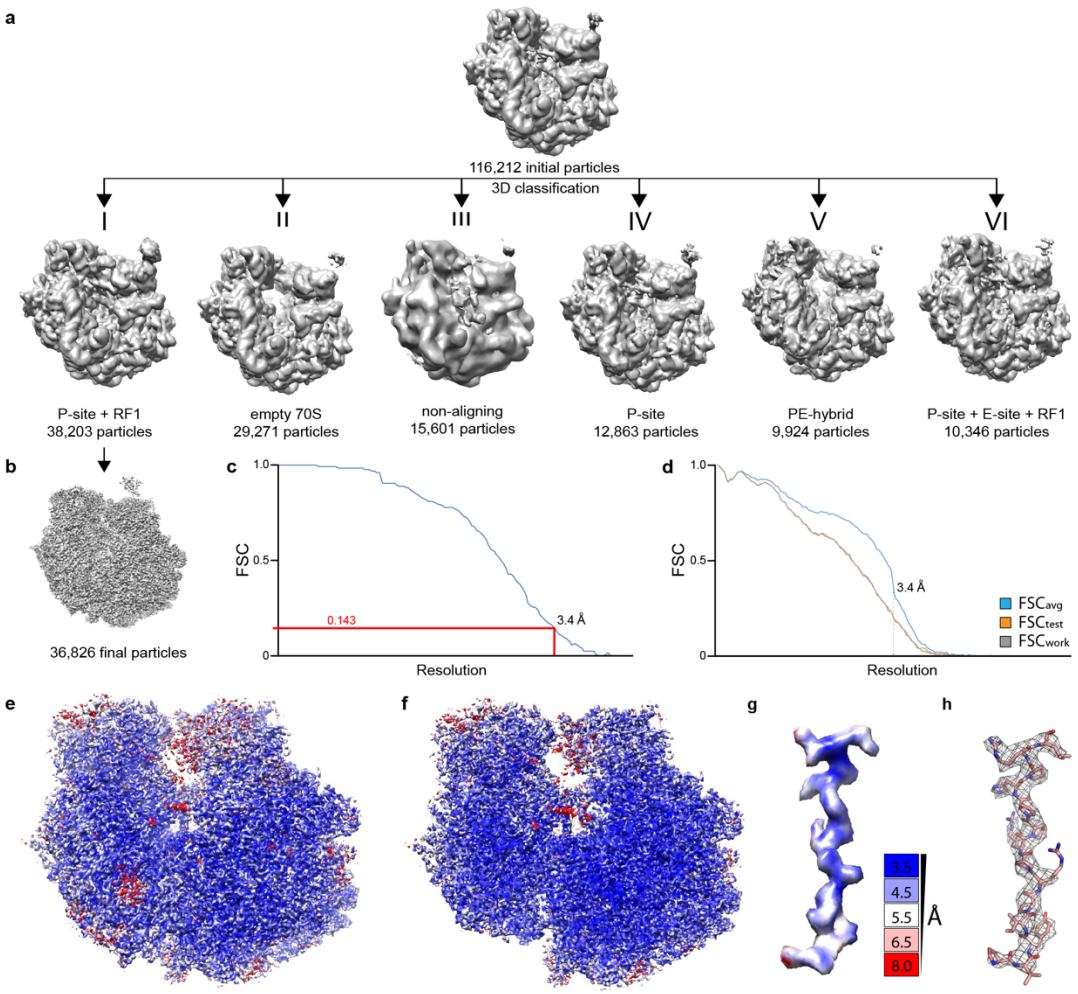

Figure 4.25: *In silico* sorting and resolution of the Api-RF1-70S complex. a, *In silico* sorting was performed with the FreAlign 9.11 software package (Grigorieff 2007). Initial alignment of 116,212 particles was followed by 3D classification, resulting in six different classes. Class 1 (38,203 particles) was further refined, yielding a (**b**) final reconstruction consisting of 36,826 particles, with (**c**) an average resolution of 3.4 Å (based on the Fourier shell correlation (FSC) curve at FSC 0.143). **d**, Validation of the fit of molecular models to cryo-EM map for the Api137-RF1-70S complex. FSC curves calculated between the refined model and the final map (blue), with the self- and cross-validated correlations in orange and black, respectively. Information beyond 3.4 Å was not used during refinement and preserved for validation. (**e**) Side view and (**f**) transverse section of the cryo-EM map of Api137-RF1-70S complex colored according to local resolution (Kucukelbir, Sigworth, and Tagare 2014). **g-h**, Cryo-EM density for Api137 (**g**) colored according to local resolution (Kucukelbir, Sigworth, and Tagare 2014) and (**h**) shown as grey mesh with molecular model for residues 5-18.

Figure preparation

Figures showing electron densities and atomic models were generated using either UCSF Chimera (Pettersen et al. 2004) or PyMol Molecular Graphic Systems (version 1.8 Schrödinger).

4.3 Experimental results

Api137 arrests ribosomes at the stop codon of mRNAs

To identify the stage of translation inhibited by Api137, we used in vitro toeprinting analysis, which determines the location of stalled ribosomes on mRNA (Hartz et al. 1988). In contrast to Onc112, which arrests translation at the start codon (Seefeldt et al. 2015; Gagnon et al. 2016) (**Figure 2.4**a), Api137 arrested translation when the stop codon entered the A site of the ribosome (**Figure 2.4**b). Similar stalling at the stop codon was obtained with other tested mRNAs when translation was carried out in the presence of Api137 or the unmodified natural apidaecin 1a (**Figure 4.27**). These results show that Api137, unlike other ribosome-targeting PrAMPs or any other known antibiotic, has the unique ability to specifically arrest the terminating ribosome.

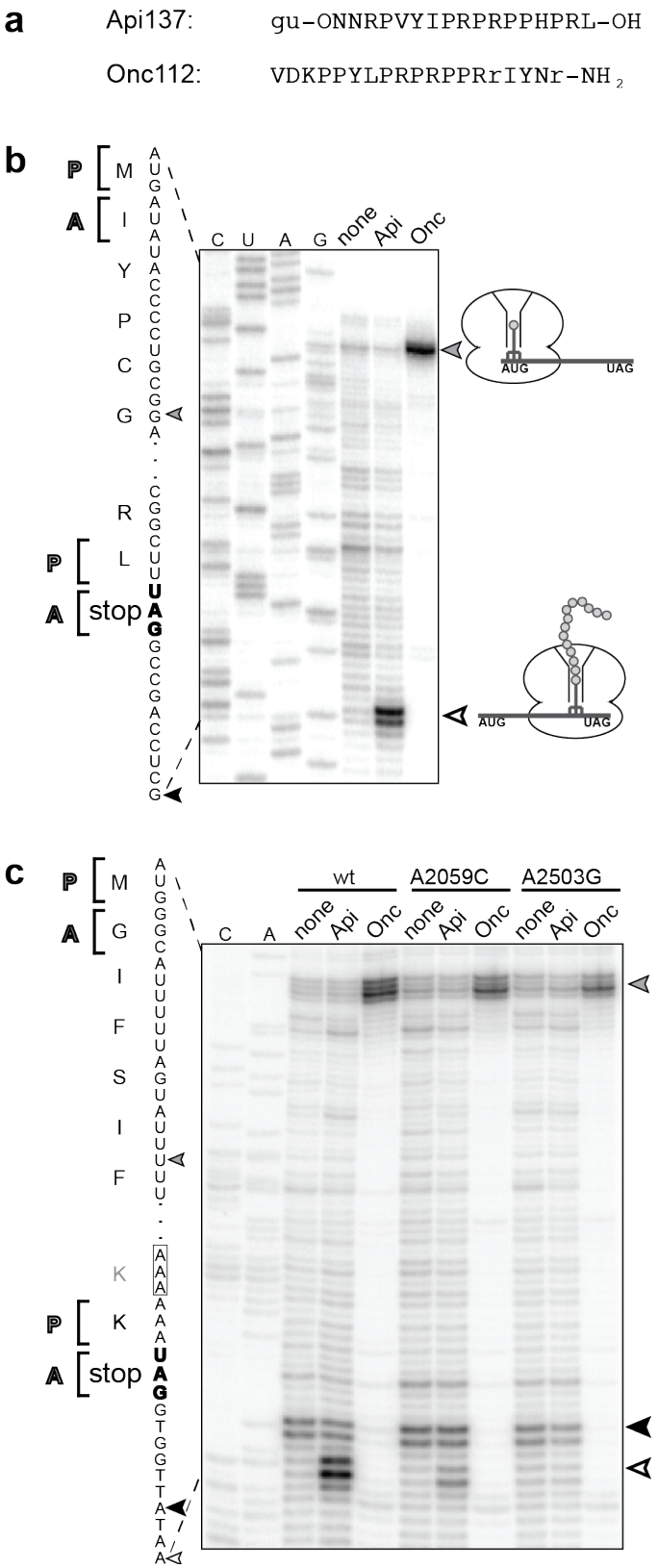

Figure 4.26: Api137 stalls ribosomes at the termination step of translation. a, Amino acid sequences of PrAMPs Api137 and Onc112. gu = N,N,N',N'-tetramethylguanidino, O = L-ornithine, r = D-arginine. **b, c,** In vitro toeprinting analysis comparing the Onc112- or Api137-mediated translation arrest on model mRNA templates derived from the *yrbA* (**b**) or *ermCL* (**c**)

genes. Positions of the toeprint bands (indicated on the gene sequence) are 16-17 nt downstream from the first nucleotide of the P-site codon. The P- and A- sites codons of the stalled ribosomes are in brackets. Toeprints in (**c**) were produced by wild-type ribosomes (wt) or by ribosomes with mutations in specific rRNA nucleotides (**Figure 4.28**a). Toeprint bands in (**b**) and (**c**) generated by Onc112-arrested ribosomes at the initiation codon are indicated with grey arrowheads; those from ribosomes arrested by Api137 at termination are marked with white arrowheads. The similar intensity of the PrAMP-independent toeprint bands marked with a white arrowhead with dotted outline in (**c**) shows that wt and mutant ribosomes translate with comparable efficiencies. Sequencing reactions are marked.

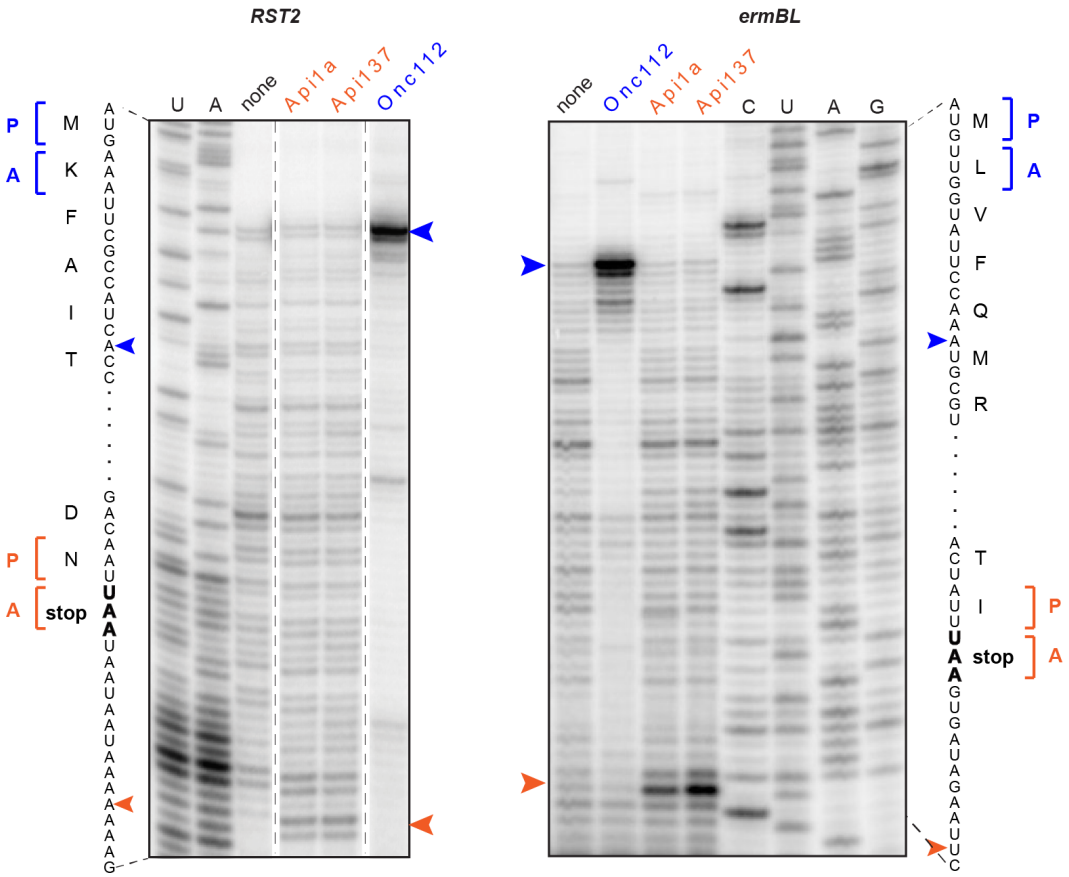

Figure 4.27: Api137-induced ribosome stalling at the end of the ORFs. Toeprinting analysis of translation arrest in the synthetic ORF RST2 (left) and the natural ORF *ermBL* (right) mediated by PrAMPs. The toeprint bands corresponding to the ribosomes arrested by Api137 or the natural apidaecin 1a (Api1a) at the stop codon of the ORF are indicated with orange arrowheads; the bands representing the ribosome arrested by Onc112 at the start codon are marked with blue arrowheads. Sequencing lanes are shown. The nucleotides corresponding to the toeprint bands are indicated in the gene sequence on the side of the gels; orange brackets indicate codons positioned in the P- and A- sites of the Api-stalled ribosome; blue brackets indicate codons in the P- and A- sites of the Onc112-stalled ribosome.

Mutations in RF1, RF2 and the ribosome confer resistance to Api137

In order to identify the components of the translation apparatus that are involved in the mechanism of Api137 action, we carried out an unbiased selection of spontaneous Api137-resistant mutants in two *E. coli* strains. We isolated three types of mutants. The resistance of the first type of mutants was caused by nonsense mutations in the *sbmA* gene (**Figure 4.28**a) encoding the transporter responsible for importing PrAMPs into the cell (Mattiuzzo et al. 2007).

Resistant mutants of the second type carried mutations in the *prfA* or *prfB* genes encoding release factors 1 and 2 (RF1 and RF2). RF1 or RF2 recognize the stop codon of the mRNA and facilitate hydrolysis of the peptidyl-tRNA ester bond, releasing the completed protein (reviewed in Korostelev 2011). Mutants isolated using *E. coli* strain SQ110 carried the mutation in the *prfA* gene, which resulted in the replacement of Asp241 of the encoded RF1 with a Gly residue (**Figure 4.28**b,c). The Api137-resistant mutant isolated with the *E. coli* strain BL21, had mutations in the *prfB* gene, resulting in substitutions of the RF2 residues Arg262 (with Cys) or Gln280 (with Leu) (**Figure 4.28**). The difference in the results obtained with two strains likely reflects the fact that SQ110, being a derivative of the K12 strain, carries an alteration in the *prfB* gene which results in replacement of Ala246 of RF2 with a Thr (Uno, Ito, and Nakamura 1996) (**Figure 4.28**d). This mutation affects the properties of RF2 (Dreyfus and Heurgue-Hamard 2011) and conceivably, could alter the interactions of the K12-type RF2 with Api137. The RF1 and RF2 mutations found in Api137 resistant strains are located in close proximity to the catalytically important GGQ motif (**Figure 4.28**b, c) suggesting that Api137 interferes with the function of RF1 and RF2.

The third type of Api137 resistant mutants had a mutation in the gene *rplP* encoding ribosomal protein uL16 (**Figure 4.28**). Subsequent testing of other ribosomal protein mutants showed that the mutations in the proteins uL22 and uL4 that are located in the nascent peptide exit tunnel also increased resistance to Api137 (**Figure 4.28**). In agreement with this observation, mutations of nearby 23S rRNA nucleotides 2059 and 2503 rendered cells Api137-resistant (**Figure 4.28**) and Api137 failed to induced pronounced arrest of the A2059C or A2503G mutant ribosomes at the stop codons in vitro (**Figure 2.4**c). Taken together, these results indicated that Api137 interferes

with translation termination by influencing functional interactions between RF1/RF2 and the ribosome.

a

E. coli strain		Minimal inhibitory concentration [μM]	Fold change
SQ171	wild type	12.5	
	23S rRNA: A2059C	100	8
	23S rRNA: A2503G	> 100	> 8
SQ110	wild type	12.5	
	SbmA: Ser251TAG (*)	> 100	> 8
	RF1: Asp241Gly (*)	> 100	> 8
BL21 (pZa-SbmA)	wild type	0.75	
	RF2: Arg262Cys (*)	> 100	> 128
	RF2: Gln280Leu (*)	50	64
	uL16: Arg81Cys (*)	6	8
AB301	wild type	12.5	
	uL4: Lys63Glu	> 100	> 8
	uL22: Δ(82-84)	> 100	> 8

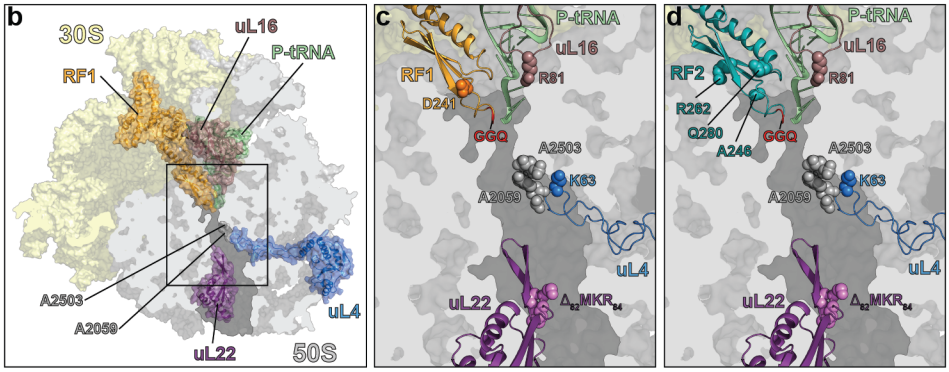

Figure 4.28: Api137-resistance mutations. a, The effect of the newly-isolated (marked by asterisks) or tested mutations on sensitivity of *E. coli* cells to Api137. The RF1 mutation is highlighted in orange; RF2 mutations, teal; rRNA mutations. grey; uL16, brown; uL4, blue; uL22, purple. **b-d**, Location of resistance mutations within the context of the terminating ribosome. **b**, Transverse section of the 50S ribosomal subunit (grey) of the 70S ribosome (30S subunit, yellow) showing the location of ribosomal proteins uL4, uL16, uL22 or 23S rRNA nucleotides (grey) whose mutations confer resistance to Api137. The region enlarged in (**c**) is boxed. **c-d**, Location of Api137 resistance mutations (spheres) in 23S rRNA (grey), ribosomal proteins uL4 (blue), uL16 (brown) and uL22 (purple), as well as (**c**) RF1 (orange) or (**d**) RF2 (teal). The GGQ motif of RF1/2 is colored red in (**c**) and (**d**).

Api137 inhibits turnover of RF1/RF2

To understand the mode of inhibition of translation termination by Api137, we used a fully reconstituted in vitro translation system. We prepared a model termination complex corresponding to the state of the ribosome prior to hydrolysis of peptidyl-tRNA (pre-hydrolysis complex, PreHC) (Kuhlenkoetter, Wintermeyer, and Rodnina 2011; Koutmou et al. 2014) (**Figure 4.29**a). Mixing the PreHC with RF1 or RF2 results in the hydrolysis of the ester bond linking fMet to the P-site tRNA, emulating the polypeptide release reaction. At a high concentration of RF1/RF2, when recycling of the factors was not required for the reaction to progress to completion, rapid and complete hydrolysis of peptidyl-tRNA was observed even in the presence of high Api137 concentrations (**Figure 4.29**b), suggesting that Api137 does not inhibit peptidyl-tRNA hydrolysis. In contrast, at limiting concentrations of RF1/RF2, when multiple rounds of binding and dissociation of the factors from PreHC were needed to achieve termination on all PreHCs, the reaction was dramatically inhibited in the presence of as little as 1 μM Api137 (**Figure 4.29**c). This result suggested that Api137 either competes with the RFs for binding to the PreHC or traps the RFs in the post-hydrolysis (PostHC) complex abolishing recycling of the factor.

To distinguish between these scenarios we directly examined the effect of Api137 on RF1 binding or dissociation using a fluorescent derivative of fMet-tRNA^{fMet} ($PreHC_{Flu}$), a quencher dye-labeled RF1 ($RF1_{Qsy}$) and following changes in fluorescence resonance energy transfer (**Figure 4.29**d). While Api137 did not affect binding of RF1 (**Figure 4.29**e), it entirely blocked RF1 dissociation (**Figure 4.29**f), demonstrating that Api137 prevents turnover of RF1/RF2 by trapping them on the ribosome.

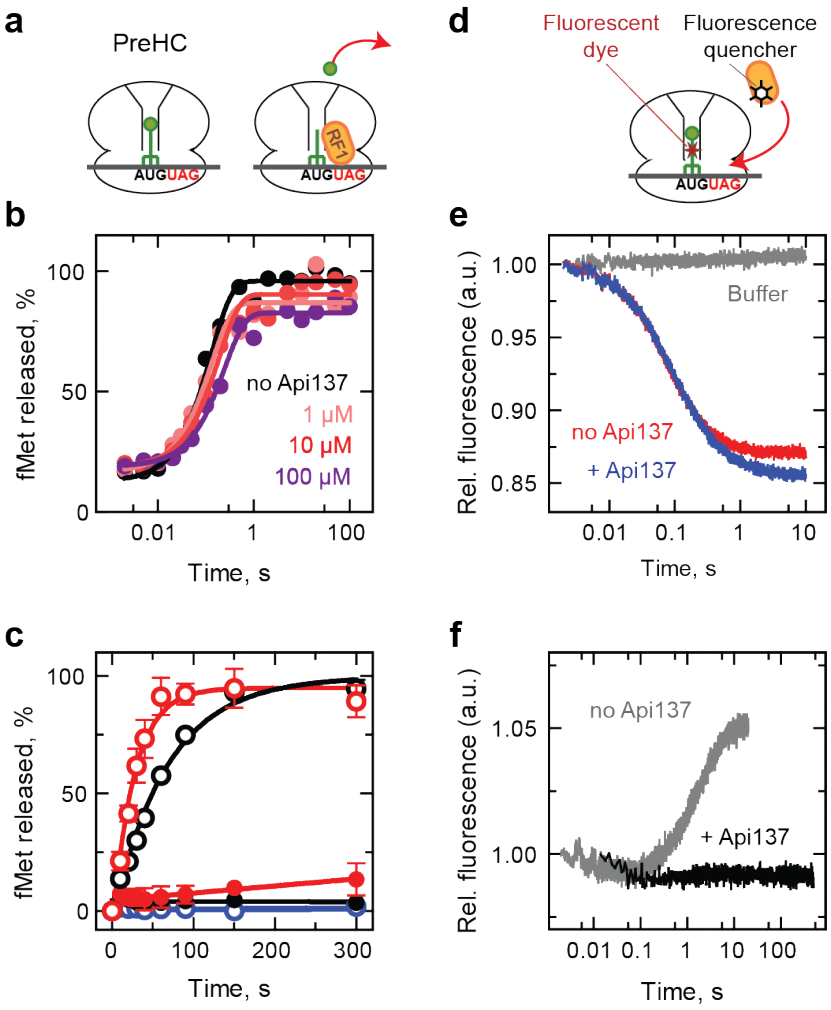

Figure 4.29: Api137 allows peptide hydrolysis but inhibits turnover of RF1/RF2 a, Schematics of the peptidyl-tRNA hydrolysis experiments. PreHC carrying f[^{3}H]Met-tRNA^{fMet} is reacted with RF1 (shown) or RF2 and the release of f[^{35}S]Met is measured. **b**, Time courses of peptide hydrolysis in PreHC in the presence of excess of RF1 without (black) or with the indicated concentrations of Api137 (colored traces).-**c**, Time courses of peptide hydrolysis in PreHC by RF1 (black circles) and RF2 (red circles) under turnover conditions in the absence (open circles) or presence of 1 μM Api137. RF3-GTP was present in all reactions. Control experiments (blue circles) lacked RF1/RF2 in the absence (open circles) or presence (closed circles) of Api137. 100% corresponds to 10 cycles of RFs binding, catalysis and dissociation. Error bars represent the s.e.m. of two independent replicates. **d**, Schematics of the RF1 binding experiments. PreHC carries fluorescein-labeled fMet-tRNA ($PreHC_{Flu}$) and RF1 carries fluorescence quencher dye ($RF1_{Qsy}$). **e**, Time courses of binding of $RF1_{Qsy}$ to $PreHC_{Flu}$ in the absence (red) or presence (blue) or Api137. Grey trace: no RF1. **f**, Time course of RF1 dissociation. $RF1_{Qsy}$ was incubated with $PreHC_{Flu}$ to generate $PostHC_{Flu}$ and then mixed with a 10-fold excess of unlabeled RF1 and RF3·GTP in the absence (grey) or in the presence (black) of Api137. See Methods for details.

When similar experiments were carried out with the Api137-resistant mutant of RF1 (**Figure 4.28**a), Api137 was unable to abolish RF1 dissociation (**Figure 4.30**a), indicating that the mutation allowed RF1 to escape Api137-mediated trapping in the PostHC complex. Similarly, the RF2 Ala246Thr mutation endemic in the K12 *E. coli* strain and located in the vicinity of the selected Api137 resistance mutations (**Figure 4.28**d), showed significantly increased tolerance to Api137 inhibition compared to the unaltered RF2 (**Figure 4.30**b). Collectively, these results showed that Api137 traps RF1 and RF2 on the ribosome after the release of the nascent protein, abolishes RF turnover and prevents disassembly of the termination complex and recycling of the ribosome for new rounds of translation.

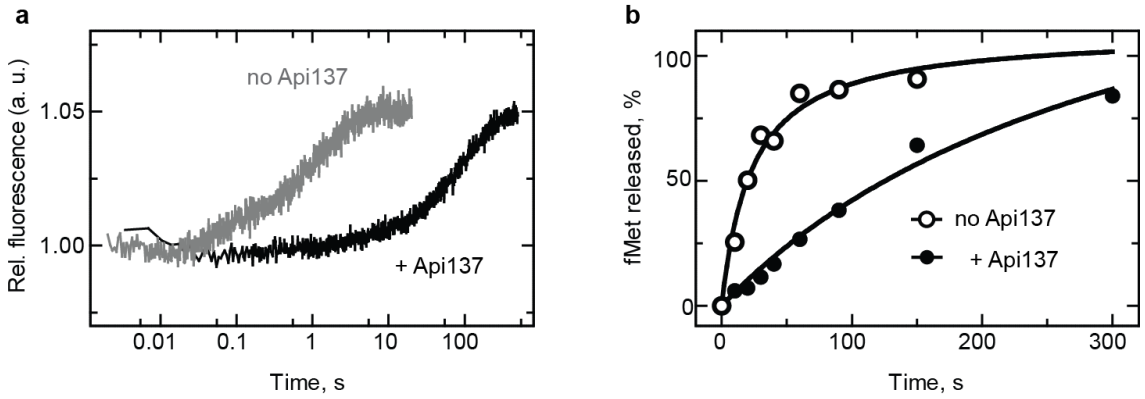

Figure 4.30: Mutations allow faster dissociation of RF1 and RF2 from the PostHC. a, Dissociation of RF1(Asp241Gly) from the PostHC in the presence of Api137**.** RF1(Asp241Gly)$_{Qsy}$ was incubated with PreHC$_{Flu}$ (0.05 μM) to generate PostHC$_{Flu}$ and then mixed with a 10-fold excess of unlabeled RF1 and RF3·GTP in the absence (grey) or in the presence (black) of Api137 (1 μM). No dissociation of wt RF1 in the presence of Api137 was observed under the same experimental conditions (**Figure 4.29**f). **b**, Peptide hydrolysis by K12 strain-specific RF2(Ala246Thr) at turnover conditions in the absence (open circles) or in the presence (closed circles) of Api137 (1 μM). In the presence of Api137, the peptide hydrolysis reaction proceeds faster when it is catalyzed by the K12 strain RF2, compared to the B strain RF2 (**Figure 4.29**c).

Interactions of Api137 with the ribosome and RF1 illuminate molecular mechanisms of RF trapping

To obtain insights into the molecular mechanism of RF1/RF2 trapping, we determined a cryo-EM structure of Api137 bound to a terminating ribosome (**Figure 4.31**a). The ribosome-nascent chain complex bearing a UAG stop codon in the A site was prepared by translating in vitro the model *ermCL* ORF in the presence of Api137, purified and subjected to cryo-EM analysis.

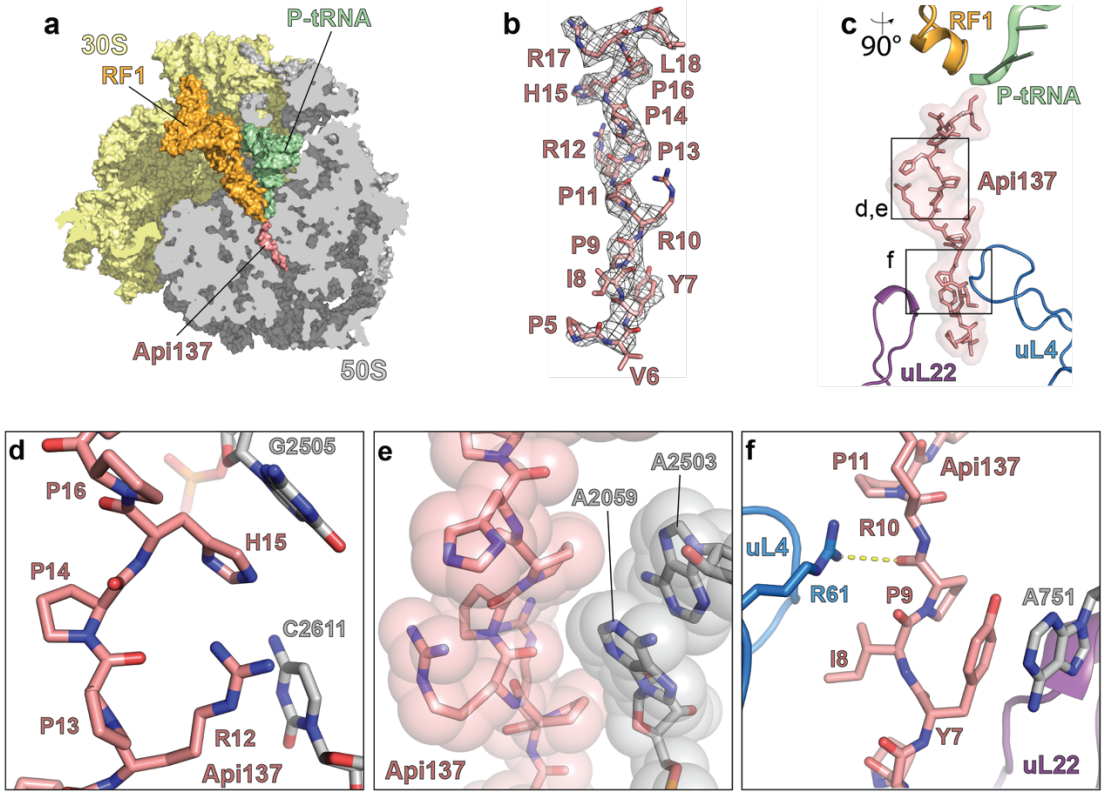

Figure 4.31: Binding of Api137 to the terminating ribosome and its interactions with the exit tunnel. a, Transverse section of the 50S subunit (grey) showing the binding site of Api137 (salmon) on the 70S ribosome (30S subunit in yellow) within the polypeptide exit tunnel relative to RF1 (orange) and the P-site tRNA (green). **b**, Cryo-EM density (mesh) and molecular model (salmon) for residues 5-18 of Api137. **c**, Placement of Api137 in the exit tunnel relative to RF1, P-site tRNA and ribosomal proteins uL4 and uL22. Boxed regions are zoomed in the panels **d-f**, showing interactions of Api137 with components of the exit tunnel, including (**d, e**) nucleotides of the 23S rRNA (grey) and (**f**) ribosomal protein uL4. In (**e**) sphere representation is used to approximate van der Waals interactions and in (**f**) a hydrogen bond is indicated with a dashed yellow line

In silico sorting of the cryo-EM data revealed a major subpopulation of ribosomes bearing a tRNA in the P site and RF1 bound in the A site (**Table 4.15** and **Figure 4.25**). A final cryo-EM reconstruction with an average resolution of 3.4 Å enabled generation of a molecular model for the entire complex (**Figure 4.31**a). In the Api137-stalled complex, the conformation of RF1 is similar to that observed previously in the PostHC during canonical termination (Korostelev et al. 2010; Pierson et al. 2016) (**Figure 4.32**a-c). Consistent with our kinetic data the P-site tRNA is deacylated, showing that RF1 has catalyzed hydrolysis of the polypeptide chain in the presence of Api137. A distinct electron density observed within the ribosomal exit tunnel could be unambiguously assigned to residues 5-18 of Api137 bound in extended conformation (**Figure 4.31**b and **Figure 4.25**g, h). The orientation of Api137 within the tunnel matches that of a nascent peptide (**Figure 4.32**d) but is opposite from that observed for other investigated PrAMPs (Gagnon et al. 2016; Roy et al. 2015; Seefeldt et al. 2016; Seefeldt et al. 2015). The C-terminal Arg17 and Leu18, which are critical for the activity of Api137 (Krizsan et al. 2014), are positioned close to the A and P sites of the PTC, respectively (**Figure 4.34**a). However, in contrast to other PrAMPs that encroach upon the PTC A site, Api137 is positioned entirely within the exit tunnel, allowing it to bind when the A site is occupied by RF1 or RF2 (**Figure 4.32**e).

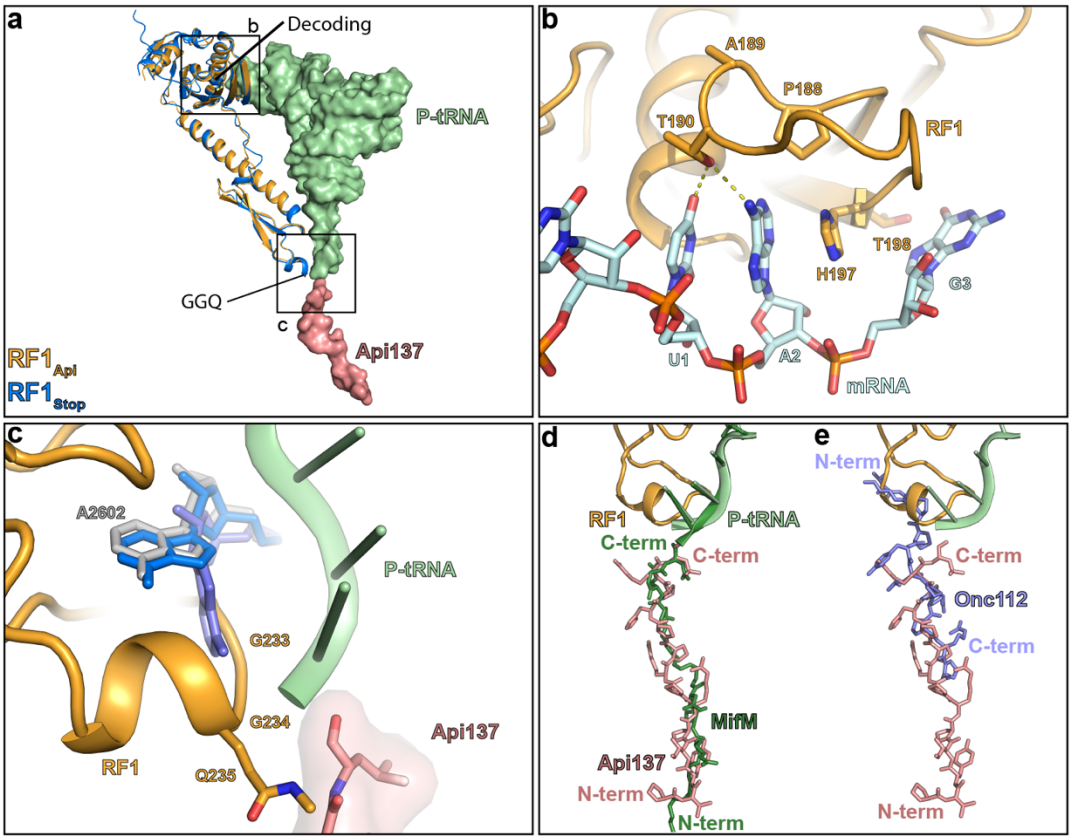

Figure 4.32: Features of the Api137-RF1-70S complex. a, RF1 (orange), deacylated P-site tRNA (green) and Api137 (salmon) in the Api137-RF1-70S complex. The position of RF1 during canonical termination is shown in blue (PDBID 5J30;(Pierson et al. 2016)). Boxed regions are zoomed in the panels (**b**) and (**c**). **b**, Interaction of the PAT motif of RF1 (orange) with the UAG stop codon of the mRNA (cyan) in the Api137-RF1-70S complex. **c**, A2602 of the 23S rRNA is in the rotated conformation as observed in previous RF1-70S structures (Laurberg et al. 2008; Korostelev et al. 2010; Svidritskiy and Korostelev 2015; Pierson et al. 2016). Conformation of A2602 (grey) in Api137-RF1-70S complex compared to A2602 (blue) during canonical termination (PDBID 5J30;(Pierson et al. 2016)) and A2602 (slate) from the pre-attack state (PDBID 1VY4;(Polikanov, Steitz, and Innis 2014)). Api137 (salmon) and P-site tRNA (green) are shown for reference. **d, e**, The binding position of Api137 (salmon) relative to the (**d**) MifM nascent chain (dark green)(Sohmen et al. 2015) or (**e**) antimicrobial peptide Onc112 (slate)(Seefeldt et al. 2015). In (**d**) and (**e**) the orientations of the peptides are indicated.

Api137 makes multiple interactions with the exit tunnel including stacking and van-der-Waals interactions with the 23S rRNA nucleotides (**Figure 4.31**d, e) and a potential hydrogen bond with the ribosomal protein uL4 (**Figure 4.31**f), clarifying how rRNA and ribosomal protein mutations could confer resistance (**Figure 4.28** and **Figure 4.33**).

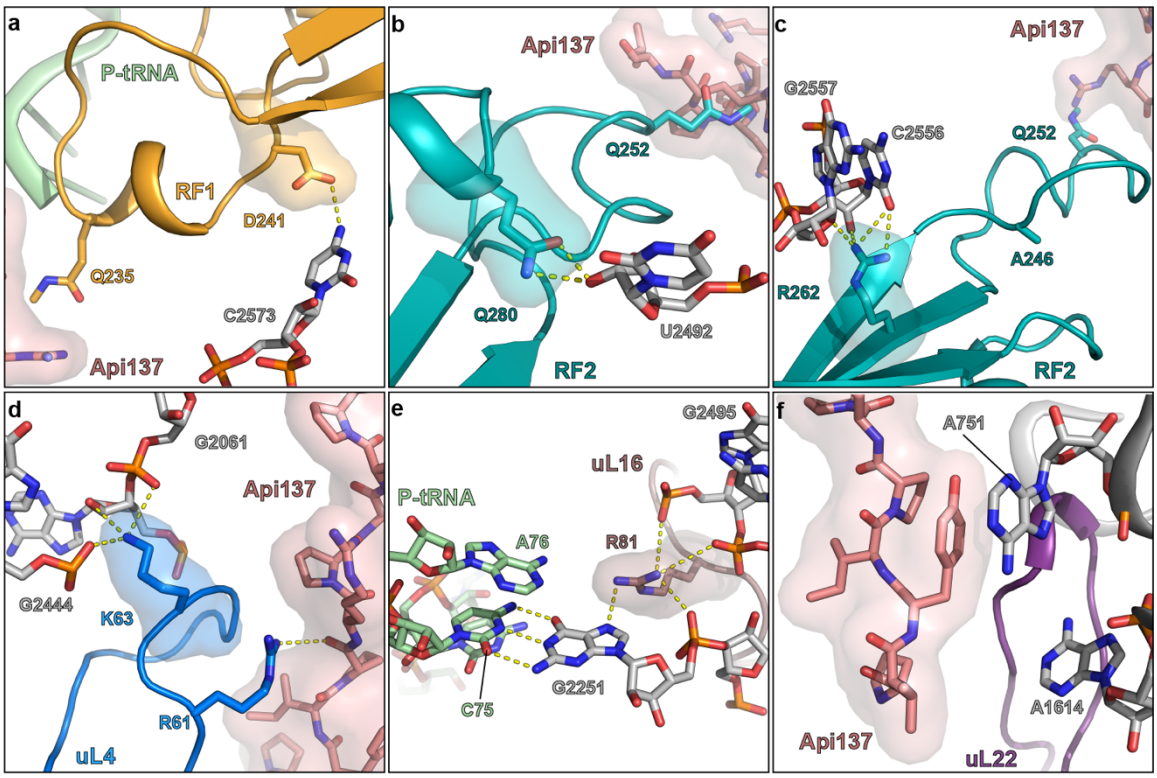

Figure 4.33: The mutations that increase resistance to Api137 (**a-c**) Location of residues in (**a**) RF1 (orange) and (**b, c**) RF2 (teal) that increase resistance to Api137 when mutated. Site of mutations are shown in stick and surface representation and Gln of the GGQ motif (Q235 in RF1 and Q252 in RF2) are shown as sticks for reference. (**d-f**) Location of Api137 resistance mutations in ribosomal proteins. (**d**) K63 in uL4 (blue) interacts with 23S rRNA residues G2061 and G2444. (**e**) Deletion of $_{82}$MKR$_{84}$ (outside of the figure boundaries) in uL22 (purple) confers resistance to Api137 presumably by changing the geometry of the uL22 exit tunnel loop and disrupting Api137 interaction with neighboring 23S rRNA nucleotides (grey), such as A751. (**f**) The mutation of R81 in uL16 (brown) may relieve Api137-mediated RF1/RF2 trapping by indirectly destabilizing interactions of deacylated tRNA with the P site mediated by G2251 of the 23S rRNA.

The interactions of the central and N-terminal segments of Api137 with the tunnel elements help to place the functionally critical C-terminal amino acids of Api137 in the vicinity of the GGQ motif of RF1 in the PTC (**Figure 4.34**a-c). The side chain of the penultimate Arg17 of Api137 is fixed in place by hydrogen bonding with the 2' hydroxyl of the G2505 ribose and O2 of the C2452 nitrogen base (**Figure 4.34**b). This network of hydrogen bonds with the nucleotides of 23S rRNA positions Arg17 for interaction with RF1. The Gln235 side chain carbonyl of RF1 is within hydrogen bonding distance from the terminal nitrogen of the Arg17 guanidinium group (**Figure 4.34**b). The contact between the Arg17 side chain and RF1 is likely to be critical because mutations of the penultimate residue of Api137 to other amino acids decrease the affinity of the PrAMP for the ribosome and reduce its inhibitory activity (Krizsan et al. 2014). Interaction between Api137 and RF1 not only helps to trap the RF on the ribosome, but also significantly stabilize binding of Api137 itself. RNA probing experiments showed that in the absence of RF1, Api137 only minimally shielded A2058, A2059, and A2062 from modification, whereas the PrAMP readily protected these nucleotides when RF1 was present (**Figure 4.34**d).

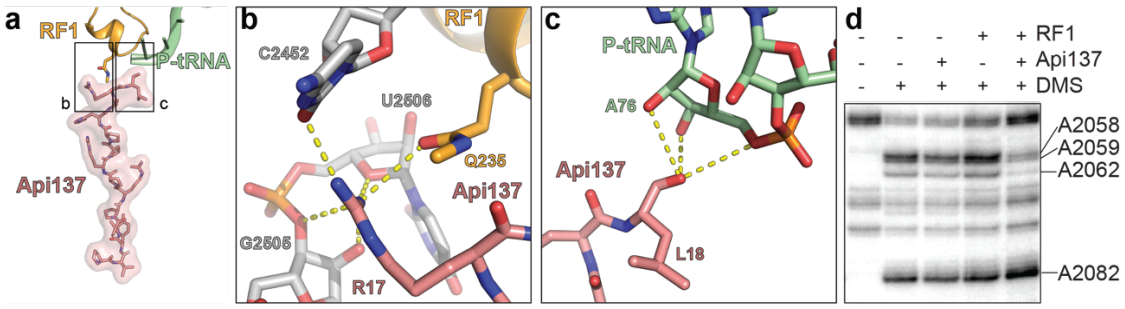

Figure 4.34: Inhibitory action of Api137 is mediated by its interactions with RF1 and P-site tRNA. a, Position of Api137 (salmon) relative to RF1 (orange) and P-site tRNA (green). The boxed regions are enlarged in panels (b,c). **b**, Interactions of Api137 with RF1. Arg17 of Api137 is coordinated by bonding with 23S rRNA nucleotides C2452, G2505 and U2506 (grey) to form a direct contact with Gln235 of the GGQ motif of RF1 (orange). **c**, The C-terminal hydroxyl of Leu18 of Api137 interacts with the ribose of A76 of deacylated P-site tRNA (green). **d**, Dimethylsulfate (DMS) probing of Api137 interaction with PostHC 23S rRNA in the absence or presence of RF1.

The C-terminal hydroxyl of Api137 is within hydrogen bonding distance from the ribose hydroxyls of A76 of the deacylated P-site tRNA (**Figure 4.34**c). These interactions could further contribute to RF1/RF2 trapping by preventing the ribosome from RF3-stimulated transitioning into the rotated state required for RF1/RF2 dissociation (Gao et al. 2007; Shi and Joseph 2016).

The results of the structural analysis not only corroborate the findings of biochemical and genetic experiments, but also illuminate the possible molecular mechanism of trapping of RF1 (and RF2) on the terminating ribosome after the release of the nascent peptide.

Api137-mediated RF depletion inhibits peptide release and stimulates stop codon read-through.

The number of ribosomes in the bacterial (*E. coli*) cell exceeds the number of RF2 and RF1 molecules by ~25-fold and ~200-fold, respectively (Bremer and Dennis 1996; Schmidt et al. 2016). Api137-mediated trapping of RF1/RF2 on a relatively small number of ribosomes should lead to a rapid depletion of the RFs. As a consequence, there would be no RF1/RF2 available to facilitate the peptide release when the remaining translating ribosomes reach a stop codon. Therefore, even though Api137 arrests the ribosome in a post-hydrolysis state, in the cells treated with Api137, most of the ribosomes should stall at stop codons in a pre-hydrolysis state carrying an intact peptidyl-tRNA.

We first tested this hypothesis in a cell-free translation system using the TnaC stalling peptide as a model. At high tryptophan concentrations (5 mM) the RF2-mediated release of TnaC peptide is impeded, leading to a well-documented accumulation of TnaC-tRNA (Gong and Yanofsky 2002) (**Figure 4.35**a). By contrast, at low concentrations of tryptophan (0.3 mM), the TnaC peptide is rapidly released at the RF2-specific UGA stop codon. Strikingly, when Api137 was present, TnaC-tRNA also accumulated at low Trp concentrations. A similar result was obtained with the *tnaC* template carrying a RF1-specific UAG stop codon (**Figure 4.35**a). These results demonstrated that as a consequence of RF1/RF2 depletion due to Api137-mediated trapping on a fraction of ribosomes, the majority of ribosomes are unable to release the TnaC peptide. Consistent with this

conclusion, the Api137-induced accumulation of TnaC-tRNA was largely rescued by supplementing the reaction with a 5-fold molar excess of RF1 over the ribosomes (**Figure 4.35**b).

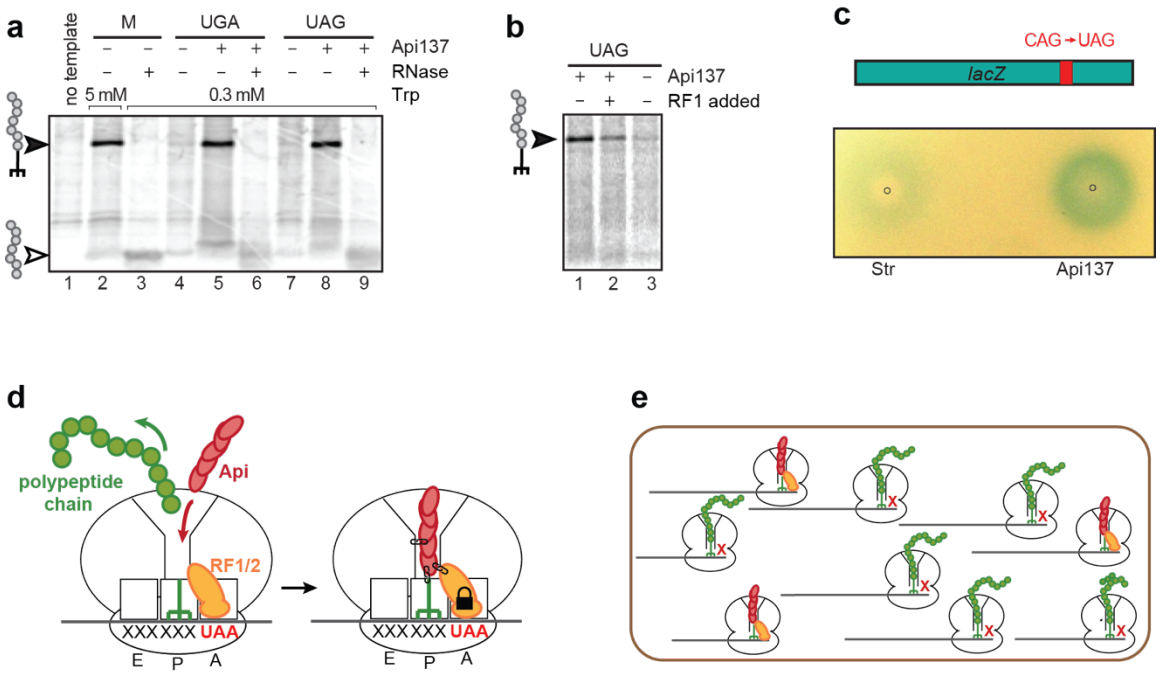

Figure 4.35: Api137 induces accumulation of peptidyl-tRNA and stop codon read-through. a, Gel electrophoresis analysis of the [^{35}S]-labeled products of the in vitro translation of the *tnaC* gene with its original UGA stop codon (lanes 1-6) or with the UAG stop codon (lanes 7-9), in the absence or presence of Api137. Where indicated, reaction products were treated with RNase. Lane 1, control reaction without mRNA. Lane 2 (labeled as M, marker) shows the band of RNase-sensitive TnaC-tRNA accumulated at high concentration of tryptophan. Lanes 5 and 8 show Api137-induced accumulation of TnaC-tRNA at low concentration of tryptophan. The bands of TnaC-tRNA and of the released TnaC peptide are shown with filled and open arrowheads, respectively. **b**, Excess of RF1 rescues Api137-induced accumulation of peptidyl-tRNA. Cell-free translation with low tryptophan was carried out in the standard conditions (lanes 1 and 3) or in the presence of a 5-fold molar excess of RF1 over the ribosomes (lane 2). **c**, The in vivo expression of the chromosomal mutant *lacZ* with a premature stop codon mediated by the stop codon read-through stimulated by the miscoding antibiotic streptomycin (Str) or by Api137. The droplet of read-through inducing agents was placed at the indicated points on the lawn of the *E. coli* cells grown on an LB/agar plate supplemented with ampicillin, IPTG and X-Gal. **d, e**, The dual mode of Api137 action. **d**, Api137 binds to the ribosome after RF1/RF2 catalyzes the release of the complete protein and traps RF1/RF2 thereby preventing its turnover. **e**, Trapping of RF1/2 depletes their available pool causing stalling of most of the ribosomes at the stop codons unable to release the nascent proteins.

When the translating ribosome reaches a stop codon, the occasional binding of a near-cognate aminoacyl-tRNA instead of the RFs may promote a stop codon read-through event. The Api137-induced depletion of the pool of free RF1/RF2 is expected to bias this competition in favor of aminoacyl-tRNA binding. Indeed, Api137 dramatically increased the read-through frequency in a reporter *E. coli* strain carrying a mutant *lacZ* allele with a premature UAG stop codon (**Figure 4.35**c). Noteworthy, the efficiency of Api137-induced read-through was significantly higher than that induced by the miscoding antibiotic streptomycin (**Figure 4.35**c). These results confirm that while Api137 traps RF1/RF2 on the ribosome after the nascent protein release, the main downstream effect of Api137 action is the arrest of the ribosomes in the pre-hydrolysis state (**Figure 4.35**d, e).

4.4 Discussion

Our biochemical, genetic and structural data reveal Api137 as the first known inhibitor that is specific for translation termination. While several inhibitors can potentially interfere with polypeptide release (Uehara, Hori, and Umezawa 1976; Svidritskiy et al. 2013), these antibiotics also target other steps of protein synthesis; in these cases, inhibition of termination is just a collateral effect of the antibiotic binding to the ribosomal centers critical for various ribosomal activities. In contrast, Api137 does not inhibit initiation or elongation of translation, but specifically arrests the ribosome at the stop codons. Api137 achieves its inhibitory action in two related, but functionally distinct ways. The primary effect of Api137 is to trap RF1 and RF2 on the ribosomes after the release of the nascent peptide (**Figure 4.35**d). This leads to depletion of the free RF pool and as a result, the majority of cellular ribosomes are arrested at the stop codons in the pre-hydrolysis state (**Figure 4.35**e). The arrested ribosome may additionally block other ribosomes on the same ORF from completing translation.

Although Api137 belongs to the broad group of ribosome-targeting PrAMPs, its mode of binding is fundamentally different from those of the previously studied derivatives of oncocin, bactenecin, pyrrhocoricin and metalnikowin (Seefeldt et al. 2016; Roy et al. 2015; Seefeldt et al. 2015; Gagnon

et al. 2016; Krizsan et al. 2015). While the binding sites of all PrAMPs overlap, the orientation of Api137 is opposite to that observed for other PrAMPs. Furthermore, the N-terminus of other PrAMPs encroaches upon the A site of the PTC, completely blocking it and hindering binding of any A site substrates (Seefeldt et al. 2016; Roy et al. 2015; Seefeldt et al. 2015; Gagnon et al. 2016), whereas Api137 binds entirely within the exit tunnel. Therefore, the binding of RF1 or RF2 to the A site is incompatible with the placement of oncocin and similar PrAMPs, whereas Api137 actually requires RF1/RF2 for efficient binding.

Due to the spatial constraints of the tunnel, direct binding of Api137 promoted by its interactions with RF1/RF2 is likely to occur only after the peptidyl-tRNA ester bond has been hydrolyzed and the newly synthesized protein has vacated the ribosome. Therefore, apidaecins have a rather narrow time window to exert their inhibitory action, namely, after departure of the newly made protein, but prior to RF1/RF2 dissociation. Within this window, Api137 has to traverse the entire length of the exit tunnel to reach its binding site close to the PTC where it can establish interactions with the RF. Thus, Api137-dependent trapping of RF1/RF2 is probably a fairly rare event in the context of the global cellular translation. However, the resulting complex is long-lived (**Figure 4.29**d), and the majority of RF1 and RF2 molecules will be eventually sequestered.

Because of the unique dual mechanism of its action, Api137 and its analogs could serve as important tools for research and medicine. Api137 could find an application in synthetic biology where interference with peptide release at engineered stop codons could stimulate the incorporation of non-canonical amino acids via stop codon suppression (Des Soye et al. 2015). The use of Api137 for medicine could go far beyond its known antibacterial action. Many human genetic disorders are caused by nonsense mutations. Although enabling premature stop codon read-through by using translation error-inducing compounds is one of the promising strategies, the decrease in translational accuracy makes such drugs highly toxic (Keeling et al. 2014). The ability of Api137 to dramatically stimulate read-through by interfering with the function of RFs provides new avenues for exploring this approach (Roy et al. 2016) and our high resolution

structure of Api137 complexed with the bacterial ribosome can serve as a starting point for the rational design of specific inhibitors of eukaryotic translation termination.

4.5 Cited Literature

Adams, P. D., P. V. Afonine, G. Bunkoczi, V. B. Chen, I. W. Davis, N. Echols, J. J. Headd, L. W. Hung, G. J. Kapral, R. W. Grosse-Kunstleve, A. J. McCoy, N. W. Moriarty, R. Oeffner, R. J. Read, D. C. Richardson, J. S. Richardson, T. C. Terwilliger, and P. H. Zwart. 2010. 'PHENIX: a comprehensive Python-based system for macromolecular structure solution', *Acta Crystallogr D Biol Crystallogr*, 66: 213-21.

Arenz, S., F. Nguyen, R. Beckmann, and D. N. Wilson. 2015. 'Cryo-EM structure of the tetracycline resistance protein TetM in complex with a translating ribosome at 3.9-A resolution', *Proc Natl Acad Sci U S A*, 112: 5401-6.

Arenz, S., H. Ramu, P. Gupta, O. Berninghausen, R. Beckmann, N. Vazquez-Laslop, A. S. Mankin, and D. N. Wilson. 2014. 'Molecular basis for erythromycin-dependent ribosome stalling during translation of the ErmBL leader peptide', *Nat Commun*, 5: 3501.

Bailey, M., T. Chettiath, and A.S. Mankin. 2008. 'Induction of *ermC* expression by ‘non-inducing’ antibiotics', *Antimicrob Agents Chemother*, 52: 866-74.

Berthold, N., P. Czihal, S. Fritsche, U. Sauer, G. Schiffer, D. Knappe, G. Alber, and R. Hoffmann. 2013. 'Novel apidaecin 1b analogs with superior serum stabilities for treatment of infections by gram-negative pathogens', *Antimicrob Agents Chemother*, 57: 402-09.

Bremer, H., and P. Dennis. 1996. 'Modulation of chemical composition and other parameters of the cell by growth rate.' in F.C. Neidhardt, Curtiss R. III, J.L. Ingraham, E.C.C. Lin, K.B. Low, B. Magasanik, W.S. Reznikoff, M. Riley, M. Schaechter and H.E. Umbarger (eds.), *Escherichia coli and Salmonella: Cellular and Molecular Biology,* (ASM Press: Washington, D.C.).

Brown, A., F. Long, R. A. Nicholls, J. Toots, P. Emsley, and G. Murshudov. 2015. 'Tools for macromolecular model building and refinement into electron cryo-microscopy reconstructions', *Acta Crystallogr D Biol Crystallogr*, 71: 136-53.

Castle, M., A. Nazarian, S. S. Yi, and P. Tempst. 1999. 'Lethal effects of apidaecin on *Escherichia coli* involve sequential molecular interactions with diverse targets', *J Biol Chem*, 274: 32555-64.

Chen, J. Z., and N. Grigorieff. 2007. 'SIGNATURE: a single-particle selection system for molecular electron microscopy', *J Struct Biol*, 157: 168-73.

Chen, V. B., W. B. Arendall, 3rd, J. J. Headd, D. A. Keedy, R. M. Immormino, G. J. Kapral, L. W. Murray, J. S. Richardson, and D. C. Richardson. 2010. 'MolProbity: all-atom structure validation for macromolecular crystallography', *Acta Crystallogr D Biol Crystallogr*, 66: 12-21.

Des Soye, B. J., J. R. Patel, F. J. Isaacs, and M. C. Jewett. 2015. 'Repurposing the translation apparatus for synthetic biology', *Curr Opin Chem Biol*, 28: 83-90.

Dreyfus, M., and V. Heurgue-Hamard. 2011. 'Termination troubles in Escherichia coli K12', *Mol Microbiol*, 79: 288-91.

Emsley, P., and K. Cowtan. 2004. 'Coot: model-building tools for molecular graphics', *Acta Crystallogr D Biol Crystallogr*, 60: 2126-32.

Fischer, N., P. Neumann, A. L. Konevega, L. V. Bock, R. Ficner, M. V. Rodnina, and H. Stark. 2015. 'Structure of the *E. coli* ribosome-EF-Tu complex at <3 A resolution by Cs-corrected cryo-EM', *Nature*, 520: 567-70.

Gagnon, M. G., R. N. Roy, I. B. Lomakin, T. Florin, A. S. Mankin, and T. A. Steitz. 2016. 'Structures of proline-rich peptides bound to the ribosome reveal a common mechanism of protein synthesis inhibition', *Nucleic Acids Res*, 44: 2439-50.

Gao, H., Z. Zhou, U. Rawat, C. Huang, L. Bouakaz, C. Wang, Z. Cheng, Y. Liu, A. Zavialov, R. Gursky, S. Sanyal, M. Ehrenberg, J. Frank, and H. Song. 2007. 'RF3 induces ribosomal conformational changes responsible for dissociation of class I release factors', *Cell*, 129: 929-41.

Gong, F., and C. Yanofsky. 2002. 'Instruction of translating ribosome by nascent peptide', *Science*, 297: 1864-7.

Grigorieff, N. 2007. 'FREALIGN: high-resolution refinement of single particle structures', *J Struct Biol*, 157: 117-25.

Hartz, D., D. S. McPheeters, R. Traut, and L. Gold. 1988. 'Extension inhibition analysis of translation initiation complexes', *Methods Enzymol*, 164: 419-25.

Huter, P., C. Muller, B. Beckert, S. Arenz, O. Berninghausen, R. Beckmann, and D. N. Wilson. 2016. 'Structural basis for ArfA-RF2-mediated translation termination on mRNAs lacking stop codons', *Nature*, 541: 546-49.

Kaji, A., M. C. Kiel, G. Hirokawa, A. R. Muto, Y. Inokuchi, and H. Kaji. 2001. 'The fourth step of protein synthesis: disassembly of the posttermination complex is catalyzed by elongation factor G and ribosome recycling factor, a near-perfect mimic of tRNA', *Cold Spring Harb Symp Quant Biol*, 66: 515-29.

Keeling, K. M., X. Xue, G. Gunn, and D. M. Bedwell. 2014. 'Therapeutics based on stop codon readthrough', *Annu Rev Genomics Hum Genet*, 15: 371-94.

Korostelev, A. A. 2011. 'Structural aspects of translation termination on the ribosome', *Rna*, 17: 1409-21.

Korostelev, A., J. Zhu, H. Asahara, and H. F. Noller. 2010. 'Recognition of the amber UAG stop codon by release factor RF1', *Embo J*, 29: 2577-85.

Koutmou, K. S., M. E. McDonald, J. L. Brunelle, and R. Green. 2014. 'RF3:GTP promotes rapid dissociation of the class 1 termination factor', *Rna*, 20: 609-20.

Krizsan, A., C. Prahl, T. Goldbach, D. Knappe, and R. Hoffmann. 2015. 'Short Proline-Rich Antimicrobial Peptides Inhibit Either the Bacterial 70S Ribosome or the Assembly of its Large 50S Subunit', *Chembiochem*, 16: 2304-8.

Krizsan, A., D. Volke, S. Weinert, N. Strater, D. Knappe, and R. Hoffmann. 2014. 'Insect-derived proline-rich antimicrobial peptides kill bacteria by inhibiting bacterial protein translation at the 70S ribosome', *Angew Chem Int Ed Engl*, 53: 12236-9.

Kucukelbir, A., F. J. Sigworth, and H. D. Tagare. 2014. 'Quantifying the local resolution of cryo-EM density maps', *Nat Methods*, 11: 63-5.

Kuhlenkoetter, S., W. Wintermeyer, and M. V. Rodnina. 2011. 'Different substrate-dependent transition states in the active site of the ribosome', *Nature*, 476: 351-4.

Laurberg, M., H. Asahara, A. Korostelev, J. Zhu, S. Trakhanov, and H. F. Noller. 2008. 'Structural basis for translation termination on the 70S ribosome', *Nature*, 454: 852-7.

Li, W., J. Tailhades, N. M. O'Brien-Simpson, F. Separovic, L. Otvos, Jr., M. A. Hossain, and J. D. Wade. 2014. 'Proline-rich antimicrobial peptides: potential therapeutics against antibiotic-resistant bacteria', *Amino Acids*, 46: 2287-94.

Li, X., P. Mooney, S. Zheng, C. R. Booth, M. B. Braunfeld, S. Gubbens, D. A. Agard, and Y. Cheng. 2013. 'Electron counting and beam-induced motion correction enable near-atomic-resolution single-particle cryo-EM', *Nat Methods*, 10: 584-90.

Mattiuzzo, M., A. Bandiera, R. Gennaro, M. Benincasa, S. Pacor, N. Antcheva, and M. Scocchi. 2007. 'Role of the *Escherichia coli* SbmA in the antimicrobial activity of proline-rich peptides', *Mol Microbiol*, 66: 151-63.

Merryman, C., and H.F. Noller. 1998. 'Footprinting and modification-interference analysis of binding sites on RNA.' in C.W.J. Smith (ed.), *RNA:Protein Interactions, A Practical Approach* (Oxford University Press: Oxford).

Milon, P., A. L. Konevega, F. Peske, A. Fabbretti, C. O. Gualerzi, and M. V. Rodnina. 2007. 'Transient kinetics, fluorescence, and FRET in studies of initiation of translation in bacteria', *Methods Enzymol*, 430: 1-30.

Orelle, C., T. Szal, D. Klepacki, K. J. Shaw, N. Vazquez-Laslop, and A. S. Mankin. 2013. 'Identifying the targets of aminoacyl-tRNA synthetase inhibitors by primer extension inhibition', *Nucleic Acids Res*, 41: e144.

Peske, F., S. Kuhlenkoetter, M. V. Rodnina, and W. Wintermeyer. 2014. 'Timing of GTP binding and hydrolysis by translation termination factor RF3', *Nucleic Acids Res*, 42: 1812-20.

Pettersen, E. F., T. D. Goddard, C. C. Huang, G. S. Couch, D. M. Greenblatt, E. C. Meng, and T. E. Ferrin. 2004. 'UCSF Chimera--a visualization system for exploratory research and analysis', *J Comput Chem*, 25: 1605-12.

Pierson, W. E., E. D. Hoffer, H. E. Keedy, C. L. Simms, C. M. Dunham, and H. S. Zaher. 2016. 'Uniformity of peptide release Is maintained by methylation of release factors', *Cell Rep*, 17: 11-8.

Polikanov, Y. S., T. A. Steitz, and C. A. Innis. 2014. 'A proton wire to couple aminoacyl-tRNA accommodation and peptide-bond formation on the ribosome', *Nat Struct Mol Biol*, 21: 787-93.

Quan, S., O. Skovgaard, R. E. McLaughlin, E. T. Buurman, and C. L. Squires. 2015. 'Markerless *Escherichia coli rrn* deletion strains for genetic determination of ribosomal binding sites', *G3*, 5: 2555-57.

Rodnina, M. V., and W. Wintermeyer. 1995. 'GTP consumption of elongation factor Tu during translation of heteropolymeric mRNAs', *Proc Natl Acad Sci USA*, 92: 1945-9.

Rohou, A., and N. Grigorieff. 2015. 'CTFFIND4: Fast and accurate defocus estimation from electron micrographs', *J Struct Biol*, 192: 216-21.

Roy, B., W. J. Friesen, Y. Tomizawa, J. D. Leszyk, J. Zhuo, B. Johnson, J. Dakka, C. R. Trotta, X. Xue, V. Mutyam, K. M. Keeling, J. A. Mobley, S. M. Rowe, D. M. Bedwell, E. M. Welch, and A. Jacobson. 2016. 'Ataluren stimulates ribosomal selection of near-cognate tRNAs to promote nonsense suppression', *Proc Natl Acad Sci U S A*, 113: 12508-13.

Roy, R. N., I. B. Lomakin, M. G. Gagnon, and T. A. Steitz. 2015. 'The mechanism of inhibition of protein synthesis by the proline-rich peptide oncocin', *Nat Struct Mol Biol*, 22: 466-9.

Schägger, H., and G. von Jagow. 1987. 'Tricine-sodium dodecyl sulfate-polyacrylamide gel electrophoresis for the separation of proteins in the range from 1 to 100 kDa', *Anal Biochem*, 166: 368-79.

Scheres, S. H. 2012. 'RELION: implementation of a Bayesian approach to cryo-EM structure determination', *J Struct Biol*, 180: 519-30.

Schmidt, A., K. Kochanowski, S. Vedelaar, E. Ahrne, B. Volkmer, L. Callipo, K. Knoops, M. Bauer, R. Aebersold, and M. Heinemann. 2016. 'The quantitative and condition-dependent Escherichia coli proteome', *Nat Biotechnol*, 34: 104-10.

Scocchi, M., M. Mardirossian, G. Runti, and M. Benincasa. 2016. 'Non-Membrane Permeabilizing Modes of Action of Antimicrobial Peptides on Bacteria', *Curr Top Med Chem*, 16: 76-88.

Seefeldt, A. C., M. Graf, N. Perebaskine, F. Nguyen, S. Arenz, M. Mardirossian, M. Scocchi, D. N. Wilson, and C. A. Innis. 2016. 'Structure of the mammalian antimicrobial peptide Bac7(1-16) bound within the exit tunnel of a bacterial ribosome', *Nucleic Acids Res*, 44: 2429-38.

Seefeldt, A. C., F. Nguyen, S. Antunes, N. Perebaskine, M. Graf, S. Arenz, K. K. Inampudi, C. Douat, G. Guichard, D. N. Wilson, and C. A. Innis. 2015. 'The proline-rich antimicrobial peptide Onc112 inhibits translation by blocking and destabilizing the initiation complex', *Nat Struct Mol Biol*, 22: 470-75.

Shi, X., and S. Joseph. 2016. 'Mechanism of translation termination: RF1 dissociation follows dissociation of RF3 from the ribosome', *Biochemistry*, 55: 6344-54.

Sohmen, D., S. Chiba, N. Shimokawa-Chiba, C. A. Innis, O. Berninghausen, R. Beckmann, K. Ito, and D. N. Wilson. 2015. 'Structure of the Bacillus subtilis 70S ribosome reveals the basis for species-specific stalling', *Nat Commun*, 6: 6941.

Svidritskiy, E., and A. A. Korostelev. 2015. 'Ribosome Structure Reveals Preservation of Active Sites in the Presence of a P-Site Wobble Mismatch', *Structure*, 23: 2155-61.

Svidritskiy, E., C. Ling, D. N. Ermolenko, and A. A. Korostelev. 2013. 'Blasticidin S inhibits translation by trapping deformed tRNA on the ribosome', *Proc Natl Acad Sci USA*, 110: 12283-8.

Uehara, Y., M. Hori, and H. Umezawa. 1976. 'Specific inhibition of the termination process of protein synthesis by negamycin', *Biochim Biophys Acta*, 442: 251-62.

Uno, M., K. Ito, and Y. Nakamura. 1996. 'Functional specificity of amino acid at position 246 in the tRNA mimicry domain of bacterial release factor 2', *Biochimie*, 78: 935-43.

Vazquez-Laslop, N., C. Thum, and A. S. Mankin. 2008. 'Molecular mechanism of drug-dependent ribosome stalling', *Mol Cell*, 30: 190-202.

Zasloff, M. 2002. 'Antimicrobial peptides of multicellular organisms', *Nature*, 415: 389-95.

5. GLOBAL ANALYSIS OF PROTEIN SYNTHESIS ARREST INDUCED BY THE TRANSLATION TERMINATION INHIBITOR APIDAECIN

5.1 Introduction

Proline-rich antimicrobial peptides (PrAMPs) are produced by many organisms to protect themselves from bacterial infection (reviewed in Graf et al. 2017; Scocchi, Tossi, and Gennaro 2011). The antimicrobial activity of PrAMPs is based on their ability of inhibiting protein synthesis in the bacterial cell by binding to the ribosome (Graf and Wilson 2019; Polikanov et al. 2018). Like other well characterized PrAMPs, such as oncocin or Bac7, Apidaecin (Api), produced by the honey bee (Casteels et al. 1989), binds to the ribosomal nascent chain exit tunnel (Florin et al. 2017; Krizsan et al. 2014). At first, this led us to believe that Api, as the other characterized PrAMPs, interferes with the initiation phase of translation (Gagnon et al. 2016; Roy et al. 2015; Seefeldt et al. 2016; Seefeldt et al. 2015). Our work, however, revealed a principally different, and rather unique, mechanism of action of Api (Florin et al. 2017). Based on *in vitro* biochemical and kinetic approaches, along with a high-resolution structure of the bacterial ribosome in complex with Api137, a derivative of the natural PrAMP Api, we propose that Api137 arrests ribosomes distinctly at stop codons, rendering Api137 to be the first described specific inhibitor of the termination phase of translation (Florin et al. 2017).

The onset of translation termination occurs when the ribosome encounters one of the three stop codons (UAA, UGA or UAG) at the end of the ORF of an mRNA. While occupying the decoding A site of the ribosome, stop codons are decoded by bacterial class I release factors RF1 or RF2 which assist the ribosome in catalyzing ester bond hydrolysis, releasing the completed protein from the peptidyl-tRNA bound in the ribosomal P site. Once in the post-hydrolysis state, the GTPase RF3 promotes dissociation of RF1/RF2 from the ribosome and the ribosome recycling factor (RRF) in conjunction with the elongation factor G (EF-G), dislodge the ribosome from mRNA and separate the ribosomal subunits to leave them ready for a new round of translation.

Our model suggests that Api137 enters the empty exit tunnel of the post-hydrolysis ribosome, right after the nascent peptide has been released and vacated the ribosome but before dissociation of RF1/RF2 has occurred. Api137 locks RF1 or RF2 in their ribosomal binding site thereby inhibiting all subsequent steps necessary for ribosome recycling (Florin et al. 2017). In addition, an implication of our model is that by depleting free RFs from the cell, Api137 action should also lead to the accumulation of ribosomes in the pre-hydrolysis state, that is, ribosomes that remain stalled at stop codons still carrying a nascent polypeptide. We further predicted that some of these pre-hydrolysis ribosomes, whose A-site is vacant, could eventually associate with an aminoacyl-tRNA and resume translation via bypassing the stop codon and continue translation downstream of it.

Even though our model for Api137 action is supported by a wealth of biochemical data, its limitation is that it is based on evidence gathered from *in vitro* experiments or from rather artificial *in vivo* systems that use single reporter genes. In addition, an aspect not considered in our model is the possibility that, in the cellular environment, Api137 could potentially also interfere with ribosomes at the initiation step of translation. This latter possibility is supported by the ability of Api137 to bind, albeit with low affinity, to the vacant ribosomes, as assessed by *in vitro* assays (Florin, Graf and Mankin, unpublished results). Therefore, the question of how Api137 inhibits translation in bacterial cells remained unanswered. Fortunately, the ribosome profiling (RiboSeq) methodology allows the analysis of the precise positioning of actively translating ribosomes within mRNAs, and thus constitutes the ideal approach for investigation of the impact of Api137 upon global translation in the living bacterial cell.

This report describes our genome-wide, unbiased and systematic investigation of Api137-induced changes of bacterial protein synthesis. For this study, we treated *E. coli* cells with Api137 and implemented RiboSeq analysis.

Consistent with our proposed model, we determined that in Api137-treated cells, ribosomes globally accumulate mainly at stop codons. Therefore, our RiboSeq analysis revealed that Api137 preferentially inhibits translation termination in the living cell. We observed that stalling at stop

codons triggers the upregulation of cellular ribosome rescue systems. In addition, we showed that Api137 treatment causes strong stop codon readthrough. Probably the most interesting and unexpected aspect of the analysis is that the observed ribosome redistribution patterns differ between genes. Although the reasons for the differential patterns are yet to be explained, in this section we describe the scoring system that we have developed to classify and quantify the variety of the detected ribosome distribution patterns. This scoring system can provide the basis for designing new experimental approaches and analytical tools to uncover the cellular factors influencing not only the detailed mechanism of Api137 action but also fundamental principles of bacterial translation regulation.

5.2 Results and Discussion

Api137 is a global inhibitor of protein synthesis

In preparation for the RiboSeq experiments, we first determined the conditions of the Api137 treatment that would result in efficient inhibition of protein synthesis. Of note, to be able to compare the Api137 related RiboSeq data with those previously obtained by our group with other ribosomal inhibitors (Kannan et al. 2014; Marks et al. 2016; Meydan et al. 2019), all the experiments were performed with the antibiotic hypersensitive *E. coli* BL21 Δ*tolC* strain (that we will call here simply *E. coli*), even though deletion of the *tolC* gene does not affect the minimal inhibitory concentration (MIC) for Api137.

We observed that treatment of *E. coli* cells for 1 min with 6.25 μM of Api137 (4-fold MIC) inhibited protein synthesis, assessed by incorporation of radiolabeled [^{35}S]-L-methionine, by as much as 90% (**Figure 5.36**, left panel). The level of residual translation did not decrease at higher concentrations of Api137 (up to 50 μM tested). In the time course experiment carried out at 6.25 μM Api137, translation was decreased to 8-15 % of the control after 2 min of treatment (**Figure 5.36**, right panel). Extending the treatment to 10 min, resulted in 3-6 % residual translation; further extension of incubation time with Api137 (up to 30 min) did not reduce residual

protein synthesis any further (data not shown). These findings imply that although Api137 rapidly interferes with cellular protein synthesis, some translation continues in the presence of the PrAMP.

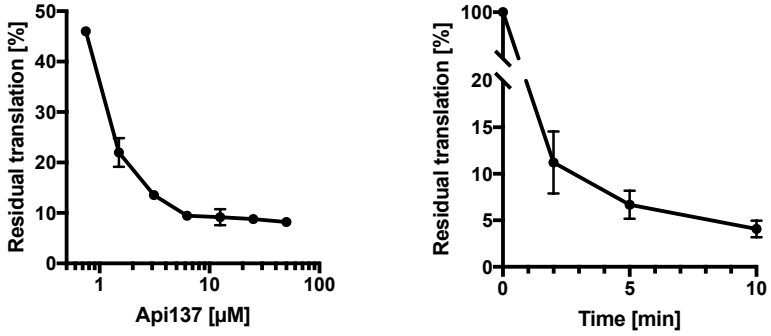

Figure 5.36: Api137 inhibits protein synthesis in *E. coli* cells. Protein synthesis of *E. coli* cells after treatment with Api137 **Left**: Exponential cells at A_{600} of 0.3 growing at 37°C in MOPS medium, devoid of L-methionine, were exposed to Api137 at the indicated concentrations. After 1 min of treatment, [^{35}S]-met was added and incubation continued for 1 min. Following trichloroacetic acid precipitation, incorporation of the radiolabel methionine was determined by scintillation counting. Radioactivity of the control cells prior to the exposure to Api137 was set to 100% translation. The labeling experiment was performed in 2 independent replicates. **Right**: *E. coli* cells were treated with 6.25 μM Api137 for the indicated times, followed by 1 min incubation with [^{35}S]-met. The plot shows the average residual translation values of 3 independent replicates.

We then proceeded to the RiboSeq analysis in order to obtain an unbiased snapshot of the distribution of ribosomes along mRNAs in bacterial cells treated with Api137. Guided by the results of the metabolic labeling experiments (**Figure 5.36**), we treated exponentially growing (in MOPS complete glucose medium) *E. coli* cells with 4-fold MIC (6.25 μM) of Api137 for 5 min. The experiment was carried out in two replicates (A and B) originated from independent cultures. For the no-treatment controls, we used an aliquot of the same exponential cultures, collected just prior to the addition of Api137. Harvesting of the cells, preparation of the library of ribosomal footprints for NGS, and data processing were performed as previously reported (Aleksashin et al. 2019).

Overview of Api137-induced ribosome distribution patterns

Analysis of the RiboSeq data clearly showed that Api137 causes a dramatic redistribution of ribosomes within mRNAs. This redistribution effect is clearly illustrated by the ribosomal density plots of the *hisLGDCBHAFI* operon (**Figure 5.37**): In the control sample, ribosomal footprints are mostly evenly distributed throughout the *his* operon open reading frames (ORFs). In contrast, in the Api137-treated cells, presence of footprints was relatively sparse within the ORFs, whereas the location of the observed density peaks suggested that ribosomes accumulated mainly towards the 5' and/or 3' ends of the ORFs or even at the intergenic regions.

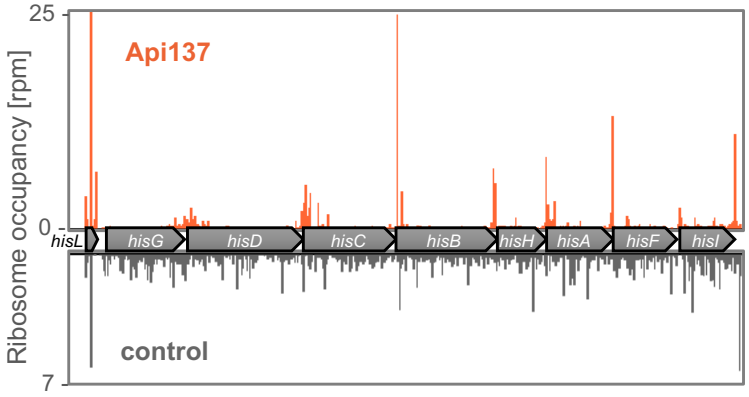

Figure 5.37: Api137 treatment leads to a redistribution of ribosomes within mRNAs. Normalized ribosome occupancies (reads per million, rpm) in the genes of the *his* operon in untreated cells (grey) or after exposure to Api137 (orange). Ribosome occupancies were visualized using MochiView software.

However, because some of the *his* operon genes overlap with each other or are separated by only a few base pairs (bp), the pilot analysis at the operon level did not reveal the precise position of ribosomes affected by the Api137 treatment. Therefore, to accurately delineate the effects at the

boundaries of the ORFs of adjacent genes, we limited our subsequent analysis to non-overlapping genes, those which are at least 50 bp apart.

To assess the redistribution of ribosomal footprints on a genome-wide scale, we performed a metagene analysis of the ribosome density at the 5' and 3' end segments of the ORFs (**Figure 5.38**).

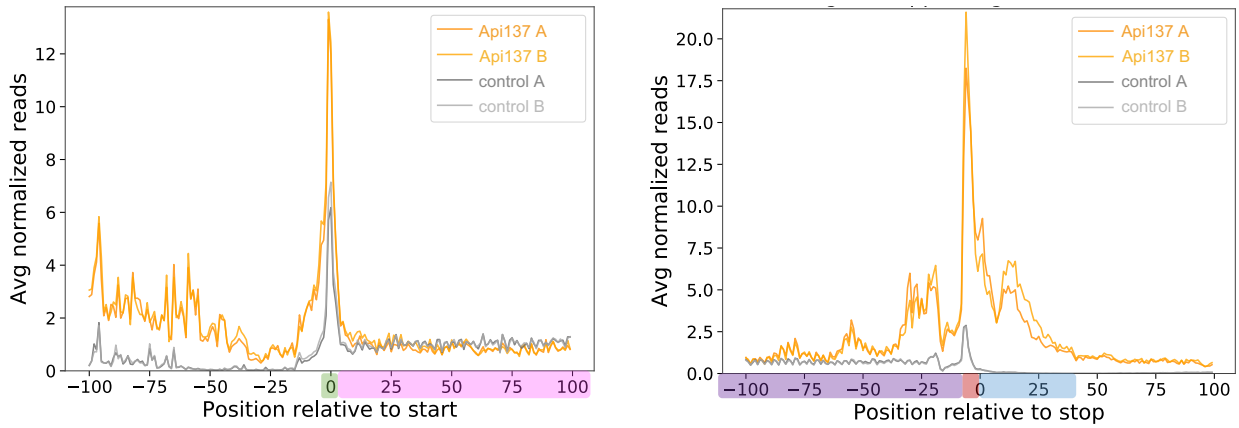

Figure 5.38: Api137 causes accumulation of ribosomes at the 5' and 3' regions of genes. Metagene analysis plots representing normalized average relative density reads in genes of *E. coli* cells exposed to Api137 (orange) or control cells (grey). Included are genes with sequencing reads mapped to at least 10% of the coding region. **Left**: Ribosome occupancy in the 5' regions. Position 0 is the first nucleotide of the start codon. Analysis was performed for 750 genes separated by at least 50 bp. **Right**: Ribosomal footprints densities at the 3' regions. Position 0 is the last nucleotide of the stop codon. The 775 genes included do not have any gene 50 bp downstream. Samples A and B represent two different replicates. Color coding of nucleotide regions corresponds to those shown in **Figure 5.39**.

The metagene analysis revealed that the action of Api137 in *E. coli* cells induced three main ribosome redistribution patterns:

i) high accumulation of ribosomes at the termination regions

ii) relatively mild accumulation of ribosomal footprints at the initiation regions

iii) increased ribosome occupancy at the intergenic regions downstream from the stop codons

In order to facilitate a systematic and quantitative evaluation of the global distribution patterns revealed by the metagene analysis, we developed a scoring system based on calculating the average ribosome occupancy of specific segments of the genes (or their flanking region) relative to the average ribosome density across the gene (**Figure 5.39** and **Table 5.16**)

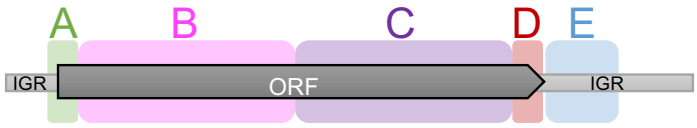

Region	Translation State	Length [nt]	Area
A	Initiation	9	nts -3 to +2 incl. start codon
B	Early elongation	gene depending	First half of ORF
C	Late Elongation	gene depending	Second half of ORF
D	Termination	9	Last 3 codons (incl. stop codon)
E	Stop codon readthrough	40	40 nt of IGR past stop codon

Figure 5.39: **The scheme of the gene regions to analyze specific distribution patterns of ribosomes according to their translational activity.** Regions for the scoring system described in **Table 5.16** are based on translation states of the ribosome. Each gene was divided into five distinct regions. Initiation region A contains the start codon and the two flanking codons. Early elongation region B encompasses the first half of the open reading frame (ORF), excluding region A. Late elongation region C includes the second half of the ORF, excluding region D. Termination region D contains the two last sense codons and the stop codon of the gene. Stop codon read through region E contains 40 nt of the intergenic region (IGR) following the stop codon.

Table 5.16: Scoring formulas used to quantify relative ribosomal footprint densities in specific gene regions. The scoring system quantifies ribosomal distribution patterns per gene. Scores determine the ratio of reads per nucleotide (nt) in the given gene regions defined as shown in **Figure 5.39**) to reads per nucleotide in the remaining gene segments. Scores are calculated using the $\log_2$ of the ratios. A score of 0 represents equal ribosome distribution. A positive score signifies enrichment, while a negative score indicates depletion of ribosomes in a given region. Scores were calculated for the 1452 *E. coli* genes included in the metagene analysis with a read density (reads per gene) of ≥ 0.5.

Score	Formula
Initiation score	$s_{in} = log_2\left(\frac{A_{nt}}{(B+C+D)_{nt}}\right)$
Termination score	$s_{term} = log_2\left(\frac{D_{nt}}{(A+B+C+)_{nt}}\right)$
Readthrough score	$s_{rt} = log_2\left(\frac{E_{nt}}{(B+C)_{nt}}\right)$

In the following sections, we will present and discuss the observed redistribution patterns caused by Api137 at specific gene segments. We will refer to both, the data from the metagene analysis and from the scoring system for regional ribosomal densities.

Api137 causes accumulation of ribosomal footprints at the initiation regions of mRNAs

The metagene analysis at the 5' end segments of the ORFs, that include the regions upstream from the start codon and the start codon itself, in both the control and Api137 treated samples, showed increased ribosome density compared to that in more internal codons (**Figure 5.38**). Increased ribosome accumulation at start sites in untreated cells has been reported in previous RiboSeq experiments in bacteria (Oh et al. 2011; Mohammad, Green, and Buskirk 2019) and reflects that initiation is one of the rate limiting steps of translation (Gualerzi and Pon 2015). Interestingly, however, the average increased density at the start codons in the Api137 treated samples is 1.9-fold more pronounced compared to the control (**Figure 5.38**). In agreement with the metagene analysis, applying our scoring system to the initiation region (region A in **Figure 5.39**) of all genes showed that the average initiation score s_{in} (**Table 5.16**) of the control samples is 0.7 while that of the Api137-treated cells is 1.6. Together, these data suggest that Api137 somehow extends the residency of ribosomes at start codons of at least some genes.

The finding that Api137 obstructs departure of ribosomes from start codons is unexpected because in our previous cell free translation experiments carried out with a handful of genes, we were unable to detect any Api137-mediated initiation inhibitory effect at initiation (Florin et al. 2017). Furthermore, superposition of the structures of Api137 bound to the ribosome (PDB ID 5O2R, (Florin et al. 2017)) with those of the initiating ribosomes (Polikanov, Steitz, and Innis 2014),

shows that the Leu-18 residue of Api137 would clash with the fMet moiety of the initiator tRNA (**Figure 5.40**, left and middle panel). However, it is conceivable that Api137 may displace the fMet residue from the active site of the peptidyl transferase center of the ribosome, thereby inhibiting the first peptide bond formation. Another possibility is that Api137 could have two binding modes: one described in our previous study with the N-terminus facing down the exit tunnel (occurring when RF1/RF2 are present) (Florin et al. 2017) and an alternative mode, where similar to PrAMPs like Bac-7 or Onc (**Figure 5.40**, right panel) (Gagnon et al. 2016; Roy et al. 2015; Seefeldt et al. 2016; Seefeldt et al. 2015), Api137 binds in an inverted orientation (C-terminus down the tunnel), in which it would transiently invade the A-site of initiating ribosomes.

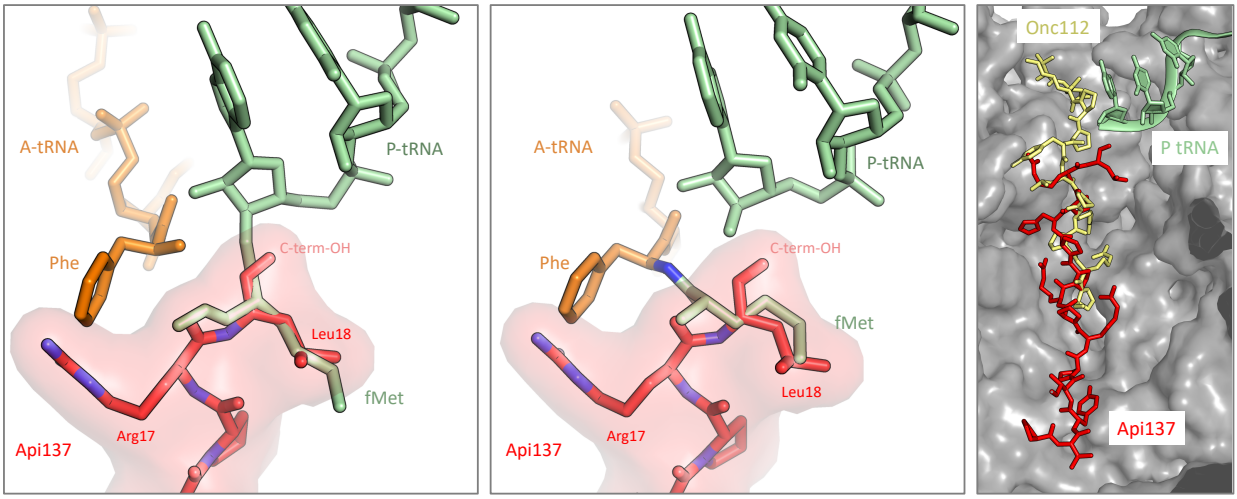

Figure 5.40: Potential clashes of Api137 with the tRNA ligands of the initiating ribosome. Superposition of Api137 (red) bound to the ribosome (PDB ID 5O2R, Florin et al., 2017) with structures of ribosomes at the translation initiation state. **Left**: Superposition with a ribosome carrying an initiator fMet-tRNA in its P-site (green) and Phe-tRNA^{Phe} in the A-site before peptide bond formation (orange, PDB ID 1VY4, Polikanov et al., 2014). The Leu-18 residue of Api137 would clash with the fMet moiety of the initiator tRNA^{fMet}. **Middle**: Superposition with a ribosome where formation of the first peptide bond has occurred. The ribosome carries a dipeptidyl-tRNA^{Phe} (orange) in its A-site and a deacylated tRNA^{fMet} (green) in the P site (PDB ID 1VY5, Polikanov et al., 2014). The C-terminal residues of Api137 would clash with the amino acids of the dipeptidyl-tRNA. **Right**: Comparison of Api137 in the nascent chain exit tunnel with the PrAmp Onc112 (yellow) (PDB ID 4ZER, Seefeldt et al., NSMB 2015) which invades the

ribosomal A-site and impedes formation of the first peptide bond (Weaver et al. 2019). Figures courtesy of Michael Graf.

A step towards understanding the action of Api137 at initiation is to determine whether Api137 equally inhibits initiation of every gene or if initiation at certain ORFs is affected more significantly compared to the others. Classification of the density scores for the initiation regions showed that in the Api137 treated samples ~ 20% of genes show a s_{in} of 2 to 3 and the s_{in} of 94 analyzed genes (~ 6%) is ≥ 4 (the s_{in} of the majority of genes in untreated samples ranges between -1 and 2 (**Figure 5.41**)). This suggests that Api137-induced initiation pausing does not occur evenly in all genes but instead, ribosomes initiating at certain genes are affected more severely by Api137. Future work will be directed towards identifying which features (the mRNA sequence, the nature of the first elongator tRNA and/or associated amino acid occupying the A-site of the initiating ribosome, etc.) define gene-specific action of Api137 at initiation.

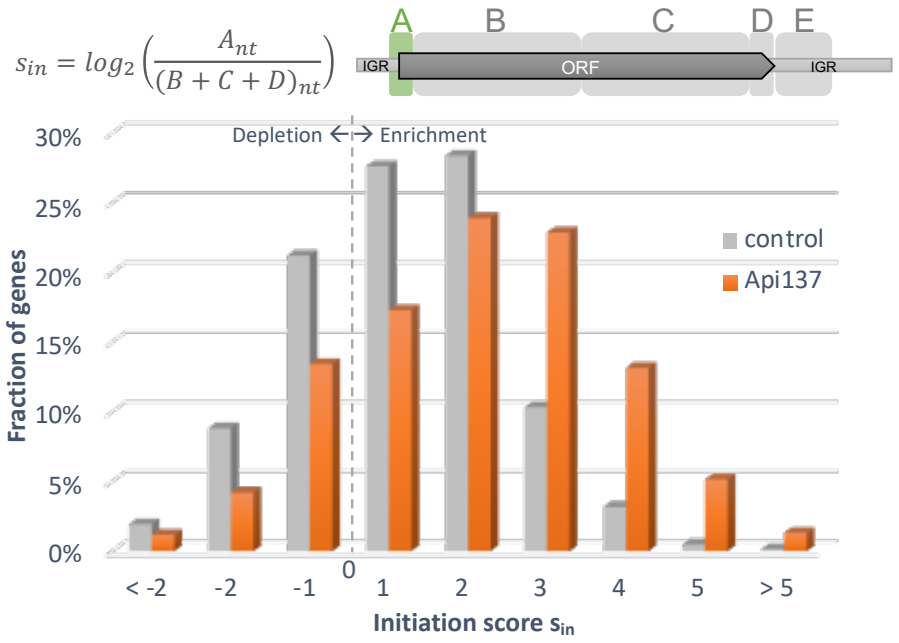

Figure 5.41: The effect of Api137 on initiation is gene specific. *E. coli* genes are binned according to their initiation scores (s_{in}). The s_{in} for each gene is averaged from 2 replicates. 1452 *E. coli* genes were included in the analysis.

Besides the ribosomal accumulation at the region immediately associated with initiation (region A in **Figure 5.39**) discussed above, we also observed higher ribosomal footprints density caused by Api137 at more distant segments of the 5' UTR of the genes (**Figure 5.38**). This effect will be discussed below.

Api137 induces high accumulation of ribosomes at termination regions

The metagene analysis at the 3' ends of ORFs, encompassing regions C to E depicted in **Figure 5.38**, showed that, compared to the control samples, there is a 10-fold accumulation of ribosomal footprints at the stop codon and the 3'UTR in the Api137 treated cells (**Figure 5.38**). Consistent with this observation, the average termination score s_{term} calculated for the genes' termination region (density of region D relative to the densities of regions B + C of **Figure 5.39**) of the Api137 treated samples is 3.2, a dramatic increase compared to the average s_{term} of 0.01 of the control cells. In full agreement with our previous biochemical and structural data (Florin et al. 2017), the

results of metagene analysis and the scoring system clearly demonstrate that Api137 globally arrests ribosomes at stop codons during cellular translation.

Similar to the effect on initiation (**Figure 5.41**), Api137 does not equally affect every termination event to the same extent. While the s_{term} of more than 85% of the analyzed genes in the Api137 treated cells is higher than 1, in 251 analyzed genes (17%) it is ≥ 5 (a range of s_{term} values not detected in any of the genes in control cells) (**Figure 5.42**), demonstrating that the effect of Api137 on the termination of certain ORFs is especially severe.

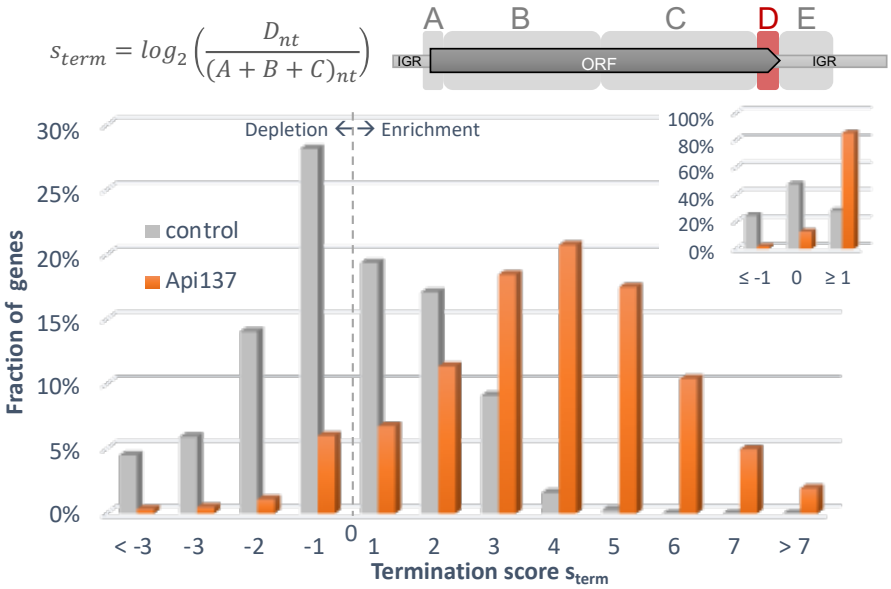

Figure 5.42: **The gene specific translation termination inhibition effect of Api137.** *E. coli* genes are binned by their termination scores (s_{term}). Included in the analysis are 1452 genes whose distance to the next ORF upstream or downstream is at least of 50 nt and their relative read density (raw reads per nucleotide) is ≥ 0.05. The s_{term} for each gene is averaged from two replicates. **Inset**: percentage of genes where the relative ribosomal occupancy at the termination region decreased, increased, or showed no change.

Among the factors that could account for the differential effect of Api137 on termination efficiencies, we considered the identity of the stop codon. For this analysis, we separately

calculated the s_{term} for the *E. coli* BL21 genes terminated with UAA (2707 genes, decoded by RF1 or RF2), UGA (1206 genes, decoded only by RF2), and UAG (281 genes, decoded only by RF1). The s_{term} for UAG terminated genes in control (untreated) cells was notably higher than that of the UAA or UGA containing ORFs, consistent with the observation that RF1-mediated termination is slower (**Figure 5.43**).

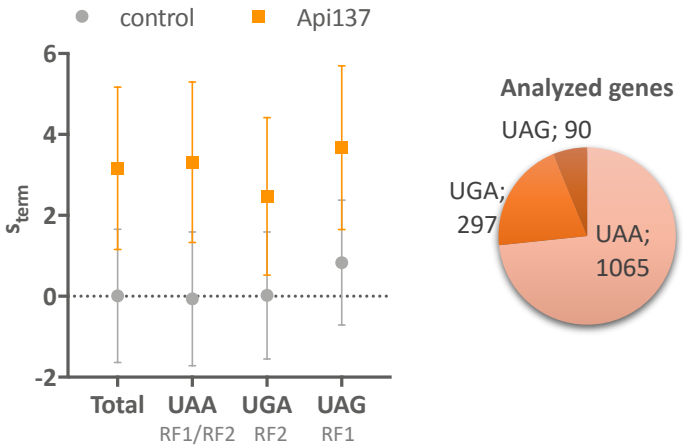

Figure 5.43: The identity of the stop codon impacts the effect of Api137 on termination efficiency. Left: Plot of average termination scores by stop codon. The release factor decoding each stop codon is indicated. Values represent the average s_{term} of two replicates of the genes within each group. The average s_{term} of genes with UAG stop in the control samples is significantly increased compared to all other genes (One-way ANOVA, Tukey's multiple comparisons test, p-value < 0.0001). In Api137 treated cells, genes with UGA stop have a significantly lower average s_{term} (One-way ANOVA, Tukey's multiple comparisons test, p-value < 0.0001). **Right**: number of analyzed genes within the specific stop codon identity groups.

The explanation for this could be that, after peptide hydrolysis, the lingering association of RF1 with the ribosome, compared to that of RF2, increases the chances of Api137 to exert its action. More puzzling is the observation that termination at the genes with UGA stop codons is relatively less affected by Api137 (average s_{term} = 2.5) compared to that of genes terminated with UAA or UAG codons (average s_{term} = 3.3) (**Figure 5.43**). Multiple factors could contribute to the less

pronounced Api137-dependent accumulation of ribosomes at UGA stop codons. One relevant observation is that RF2 seems to be less susceptible to Api137-trapping. This possibility is supported by the previously obtained kinetic data which showed that, in contrast with the complete inhibition of RF1-dependent peptide hydrolysis, 10 - 20% of hydrolyzed product in the RF2-catalyzed reaction was resilient to the action of Api137 (Florin et al. 2017).

Altogether, the analysis performed at the metagene level and using the regional scoring system firmly establishes Api137 as a potent inhibitor of translation termination *in vivo* and showed that the efficiency of its action is gene specific.

One interesting consequence of the Api137-mediated stalling of ribosomes at the stop codons is the global increase of ribosome occupancy at the 3'-terminal ORFs segments preceding the termination codon (the region colored in purple in **Figure 5.38,** which is a segment of region C in **Figure 5.39**), a general phenomenon known as queuing of colliding ribosomes (Sorensen and Pedersen 1991; Wolin and Walter 1988). Api137-triggered ribosome queuing is vividly illustrated by the profile of the *ompX* ORF (**Figure 5.44**): The unresolved Api137-induced arrest of the ribosome at termination impedes the progression of the ribosomes behind it and causes ribosome collisions.

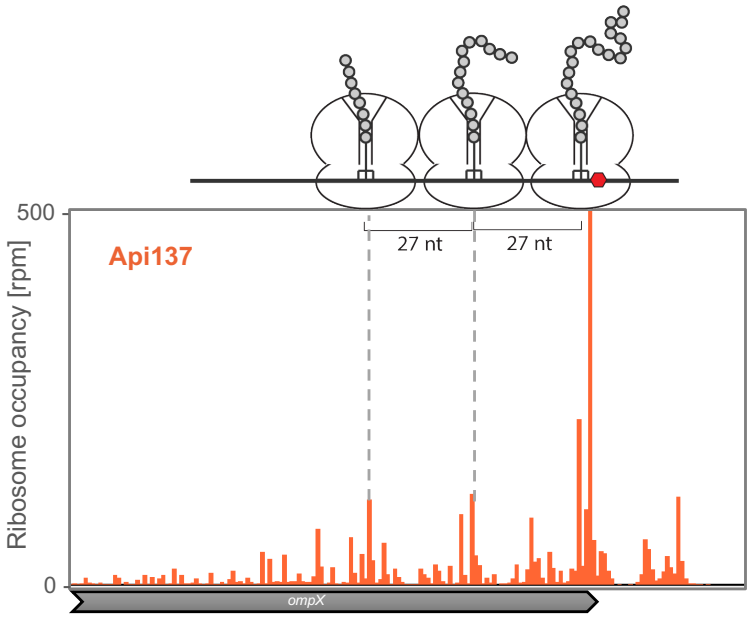

Figure 5.44: Ribosome arrest at the stop codon results in ribosome collisions. The ribosome occupancy peak at the stop codon in the *ompX* ORF is preceded by additional peaks at a distance of 24-27 nt. This distance corresponds to the mRNA fragment protected by a ribosome (depicted above the density plot) and indicates queuing of elongating ribosomes. A similar effect can be observed in the ribosome density on the *secM* gene (**Figure 5.51**).

That Api137-induced accumulation of stalled ribosomes (both stalled at the stop codons and those queued behind them) is detrimental for the cell is reflected by the upregulation in the expression of proteins involved in ribosome rescue such as *arfA*, *arfB* as well as the tmRNA gene *ssrA* (reviewed in Huter et al. 2017; Keiler 2015) (**Table 5.17** and **Figure 5.45**). Further studies could be directing to a better understanding of the cellular response to the Api137-asault.

Table 5.17: The expression of the ribosome rescue system components is induced in the presence of Api137
Expression of rescue system components, measured in reads per million per kilobase (RPKM), in Api137-treated cells compared to control samples. RPKMs are averages of two replicates. Genes encoding alternative release factor A (*arfA*) and alternative release factor B (*arfB*) are highly induced. Ribosome occupancy on the tmRNA-encoding *ssrA* transcript is enriched.

Gene	***Fold change (Api137/Control)***
arfA	69.33
arfB	4.58
ssrA	7.78

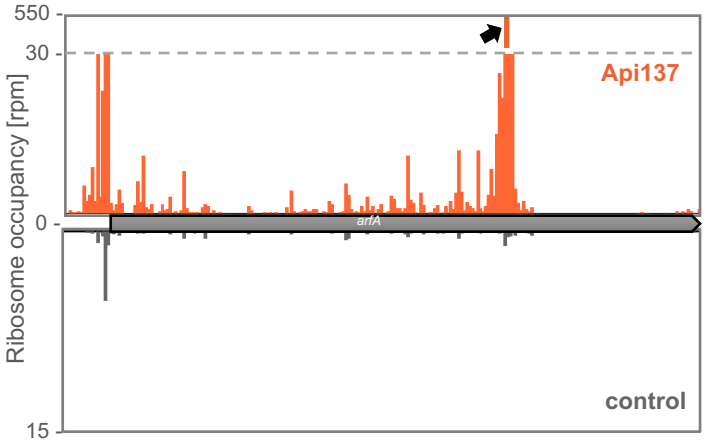

Figure 5.45: Api137-induced cellular stress triggers upregulation of ArfA expression
Translation of the *arfA* gene is dramatically increased in Api137-treated cells. The 550 rpm peak (black arrow) is located at the RNase III internal cleavage site, a critical component of ArfA expression regulation (reviewed in Huter et al. 2017; Keiler 2015).

Api137 induces stop-codon readthrough

The metagene analysis of the RiboSeq data revealed that one of the most dramatic changes caused by Api137, as detected by a 100-fold increase of ribosomal density in region E (**Figure 5.37**, light blue region, corresponding to **Figure 5.39**) as part of the 3' UTR of genes (downstream of the stop codons). Presence of ribosomal footprints downstream from the stop codons of the

ORFs fully supports the prediction derived from our model: that the Api137-mediated depletion of free RF1 and RF2 in the cell should increase the frequency of stop codon readthrough (Florin et al. 2017).

We systematically analyzed the occupancy of the 3' UTRs for each gene using the readthrough score (s_{rt}). The average s_{rt} of the Api137-treated samples is 1.9 (compare to the s_{rt} of the untreated cells which is -2.3). Accordingly, in 99% of the genes of the control samples no readthrough is detected, while 72% of the genes in the cells exposed to Api137 exhibit significant of ribosomal footprints in the 3' UTR (**Figure 5.46**).

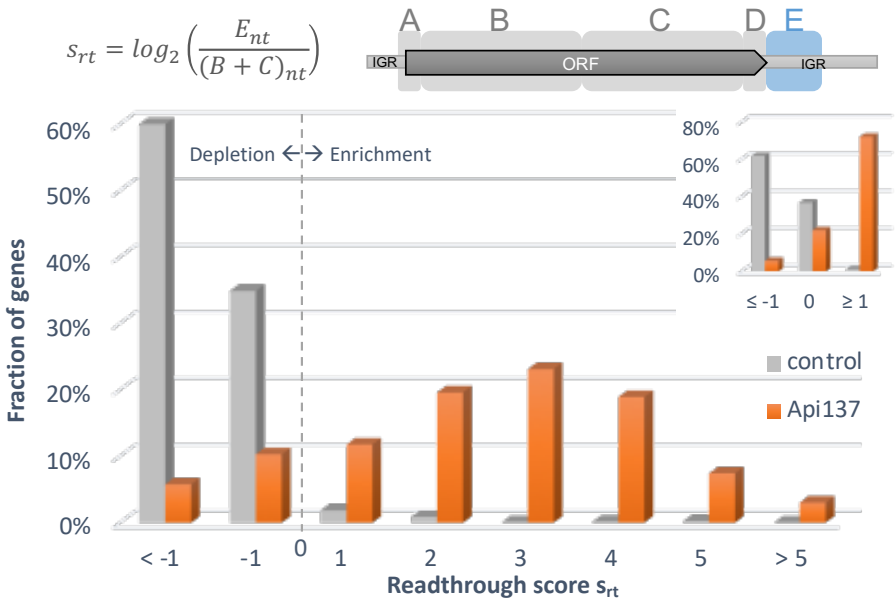

Figure 5.46: **Api137-treatment causes stop codon readthrough in the majority of genes.** *E. coli* genes are binned by their readthrough scores (s_{rt}). Included in the analysis are 1452 genes whose distance to the next ORF upstream or downstream is at least of 50 bp and their relative read density (raw reads per nucleotide) is ≥ 0.05. The s_{rt} for each gene is averaged from two replicates. **Inset** shows the percentage of genes where the relative ribosomal occupancy in the 3' UTR/IGR decreased, increased, or showed no change.

We also observed a globally higher ribosome density in the 5' UTRs (ribosomal footprints at the 100 bp regions preceding the start codon in the metagene analysis shown in **Figure 5.38**) of many genes in the Api137-treated cells. We considered the possibility that the 5' UTR ribosome footprints could originate from the ribosomes that have bypassed the stop codons of upstream genes. To test this possibility, we reasoned that detection of stop codon readthrough-footprints should be a function of the length of the intergenic regions separating the genes: the longer the UTR, the higher chances for the ribosome that bypassed the gene's stop codon to encounter another stop codon and eventually either terminate translation or remain arrested at that site. Indeed, while there is clear Api137-dependent density at the upstream regions of genes separated by 20 bp, ribosomal footprints are virtually absent within the 100 bp-upstream segment in the genes which at least 150 bp apart from each other (**Figure 5.47**). These data are compatible with the possibility that the presence of ribosomes in 5' UTRs is a consequence of Api137-mediated stop codon readthrough at the upstream genes.

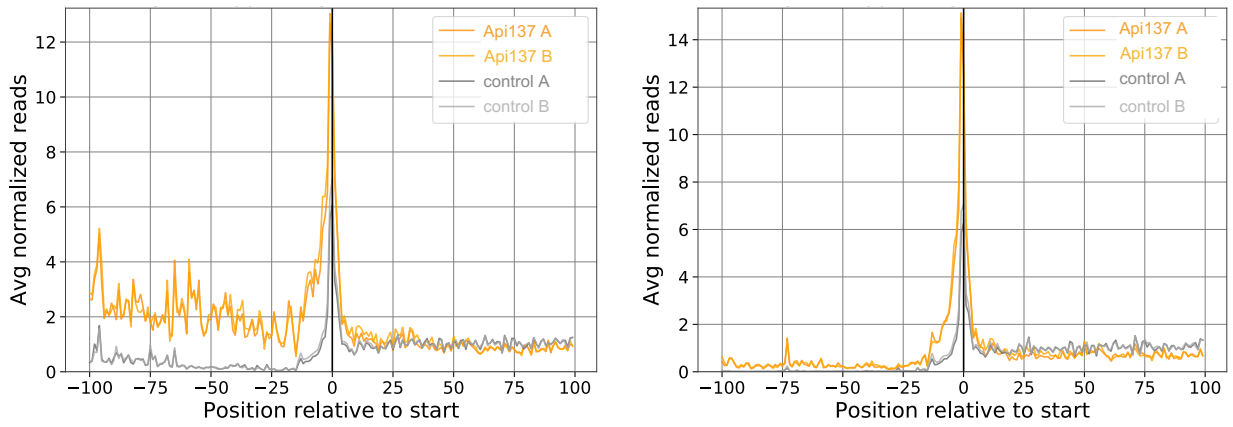

Figure 5.47: **Stop codon readthrough in upstream genes accounts for ribosome density in the 5' UTR.** Metagene analysis plots representing normalized average relative density reads in genes of *E. coli* cells exposed to Api137 (orange) or control cells (grey). Plots were generated from the corresponding data shown in **Figure 5.39**. Position 0 is the first nucleotide of the start codon. **Left**: Analysis was performed for 846 genes separated by at least 20 bp. **Right**: Analysis

was performed for 515 genes separated by at least 150 bp. Samples A and B represent two different replicates.

Similar to the differential effects on initiation and termination, our scoring system revealed that Api137-induced stop codon readthrough varies between genes (**Figure 5.46**). While 285 (20%) of the analyzed genes have a readthrough score (s_{rt}) of 1 to 2, the s_{rt} of 427 genes (29%) is higher than 3. Besides different s_{rt} values, the footprints patterns of the ribosomes present in intergenic regions are highly diverse (**Figure 5.48**).

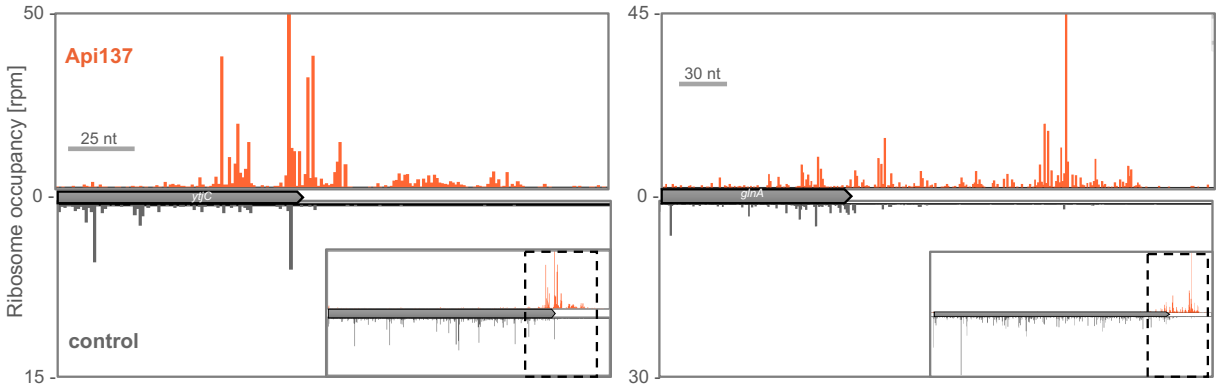

Figure 5.48: **Api137-induced ribosome density in the 3' UTR differs between genes.** Ribosome occupation (rpm) around the 3' gene ends and respective IGRs of the *ytjC* and *glnA* ORFs. **Inlet**: Ribosome distribution throughout the entire coding region. The areas shown in the main plots are boxed.

We considered the possibility that the nature of the stop codon could be one of the elements accounting for differential frequency of readthrough. However, the s_{rt} values of the genes from Api137 treated cells grouped by their stop codon identity were not significantly different from each other (**Figure 5.49**).

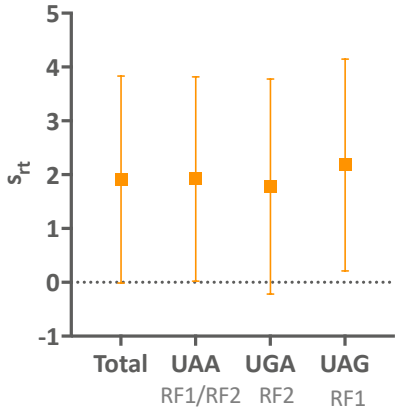

Figure 5.49: **The stop codon identity does not influence stop codon readthrough efficiency in Api137-treated cells.** Plot of average readthrough scores of genes in Api137-treated cells classified according to the identity of their stop codon (decoding RF is indicated). Values represent the average s_{rt} of two replicates of the of all genes within each group. The s_{rt} show no significant difference (One-way ANOVA, Tukey's multiple comparisons test). Number of genes in each group as in **Figure 5.43**

These data indicate that regardless of the nature of the stop codon where the termination arrests occurred, ribosomes can resume translation with comparable probabilities. For follow-up analysis, translation efficiency, mRNA structure, relative cellular amounts of tRNAs available for misincorporation, promptness to frameshifting, among other factors, could also be considered to have an impact on Api137-triggered stop codon readthrough.

Api137 can mediate ribosome stalling at some internal codons

Screening of our RiboSeq data using the visualization genome browser MochiView revealed the presence of conspicuous ribosome density peaks at some internal codons of specific genes in the Api137-treated cells (**Figure 5.50** and **Figure 5.51**).

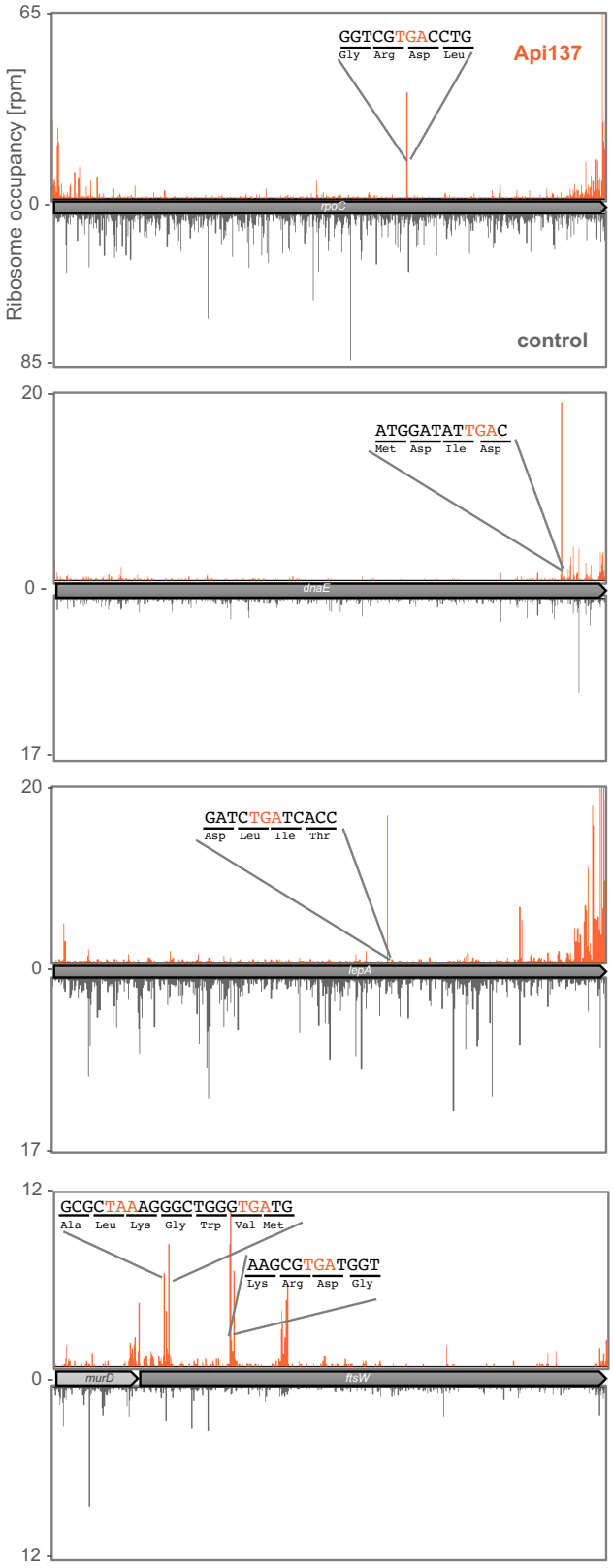

Figure 5.50: Api137 arrests ribosomes at out-of-frame (OOF) stop codons. Ribosome occupancy (rpm) in genes where ribosome density peaks were detected within the ORF. Shown are sequences around the peak in which OOF stop codons (highlighted in orange) were detected.

Because these peaks are located at single codons, they cannot be detected by our scoring system quantification, whose specified internal gene regions encompass the first or second half of the ORF (**Figure 5.39**). However, preliminary examination revealed two major classes of Api-137 dependent peaks at internal codons:

i. Some of the detected internal peaks were associated with out-of-frame (OOF) stop codons. **Figure 5.50** shows a few of such examples where the ribosome stalling event occurs at OOF stop codons present within the ORF. Potentially, these events could reflect the known termination inhibition mode of Api137. Existence of these peaks could reflect translation of alternative reading frames ending at the corresponding stop codons. This possibility is supported by the results of the recent work from our laboratory, in which the use of a specific inhibitor of translation uncovered cryptic translation start sites, including out-of-frame start sites within a number of *E. coli* genes (Meydan et al. 2019). Future work could be aimed to develop Api137-guided RiboSeq as a tool for mapping translation termination sites in bacterial genomes and identifying or validating cryptic genes.

ii. In the Api137-treated cells we also observed several peaks of ribosome density within the genes that were not associated with OOF stop codons. Two such examples, representing Api137-dependent peaks at codons 134 and 144 of the *aceE* gene are illustrated in **Figure 5.51**. The profile of this gene in the control sample reveals nothing remarkable. The other examples of this class include sites where Api137 presence seems to amplify the elongation arrest already existing under normal conditions (peaks at *secM*, *pheP*, *rpoA* in **Figure 5.51**). It is unlikely that Api137 could bind to the exit tunnel of the stalled elongating ribosome, because they carry a nascent peptide. For example, stalling at the 165th codon of *secM* (**Figure 5.51**), which is the best-characterized translation arrest event in *E. coli*, requires the presence of the nascent SecM peptide in the exit tunnel (Nakatogawa and Ito 2001, 2002). Therefore, the most feasible scenario is that Api137 plays an indirect role (*i. e*. depleting cellular factors necessary for partial release of the basal arrest) in increasing

ribosome occupancy at elongation stall sites. Characterization of the sites of this class could be used to develop Api137 as a discovery tool of translation arrest regulatory events in bacterial genomes. Future systematic analysis of this class of Api-137 density peaks could be carried out by approaches similar to those previously used by our lab to identify macrolide-dependent stall sites (Kannan et al. 2014).

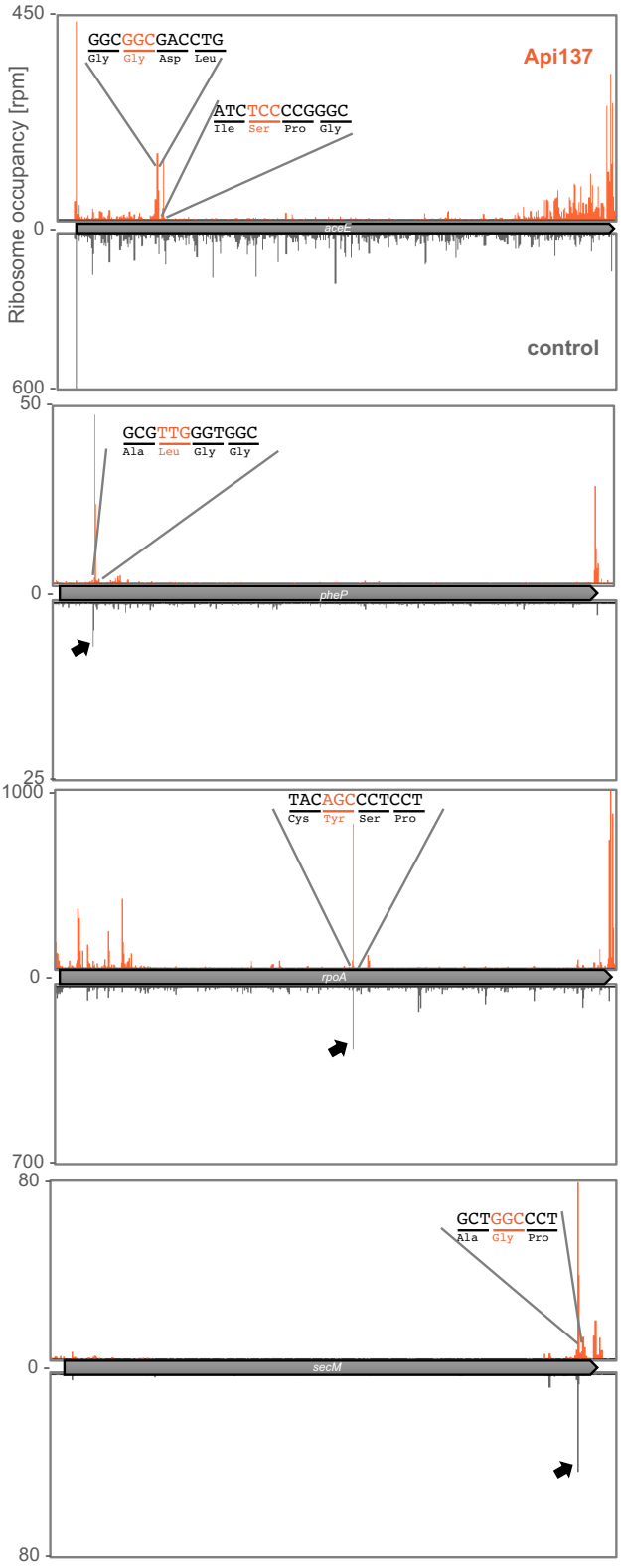

Figure 5.51: Api137 marks elongation arrest sites. Ribosome occupancy (rpm) within example ORFs without any termination signals. Given are the sequences around the peak in which the P-site of the stalled ribosome is marked in orange. In some cases, Api137 amplifies elongation arrest signals already present in the control sample (black arrows).

5.3 Cited literature

Aleksashin, N. A., M. Leppik, A. J. Hockenberry, D. Klepacki, N. Vazquez-Laslop, M. C. Jewett, J. Remme, and A. S. Mankin. 2019. 'Assembly and functionality of the ribosome with tethered subunits', Nat Commun, 10: 930.

Casteels, P., C. Ampe, F. Jacobs, M. Vaeck, and P. Tempst. 1989. 'Apidaecins: antibacterial peptides from honeybees', EMBO J, 8: 2387-91.

Florin, T., C. Maracci, M. Graf, P. Karki, D. Klepacki, O. Berninghausen, R. Beckmann, N. Vazquez-Laslop, D. N. Wilson, M. V. Rodnina, and A. S. Mankin. 2017. 'An antimicrobial peptide that inhibits translation by trapping release factors on the ribosome', Nat Struct Mol Biol, 24: 752-57.

Gagnon, M. G., R. N. Roy, I. B. Lomakin, T. Florin, A. S. Mankin, and T. A. Steitz. 2016. 'Structures of proline-rich peptides bound to the ribosome reveal a common mechanism of protein synthesis inhibition', Nucleic Acids Res, 44: 2439-50.

Graf, M., M. Mardirossian, F. Nguyen, A. C. Seefeldt, G. Guichard, M. Scocchi, C. A. Innis, and D. N. Wilson. 2017. 'Proline-rich antimicrobial peptides targeting protein synthesis', Nat Prod Rep, 34: 702-11.

Graf, M., and D. N. Wilson. 2019. 'Intracellular Antimicrobial Peptides Targeting the Protein Synthesis Machinery', Adv Exp Med Biol, 1117: 73-89.

Gualerzi, C. O., and C. L. Pon. 2015. 'Initiation of mRNA translation in bacteria: structural and dynamic aspects', Cell Mol Life Sci, 72: 4341-67.

Huter, P., C. Muller, S. Arenz, B. Beckert, and D. N. Wilson. 2017. 'Structural Basis for Ribosome Rescue in Bacteria', Trends Biochem Sci, 42: 669-80.

Kannan, K., P. Kanabar, D. Schryer, T. Florin, E. Oh, N. Bahroos, T. Tenson, J. S. Weissman, and A. S. Mankin. 2014. 'The general mode of translation inhibition by macrolide antibiotics', Proc Natl Acad Sci U S A, 111: 15958-63.

Keiler, K. C. 2015. 'Mechanisms of ribosome rescue in bacteria', Nat Rev Microbiol, 13: 285-97.

Krizsan, Andor, Daniela Volke, Stefanie Weinert, Norbert Sträter, Daniel Knappe, and Ralf Hoffmann. 2014. 'Insect-derived proline-rich antimicrobial peptides kill bacteria by inhibiting bacterial protein translation at the 70S ribosome', Angewandte Chemie (International ed. in English), 53: 12236-39.

Marks, J., K. Kannan, E. J. Roncase, D. Klepacki, A. Kefi, C. Orelle, N. Vazquez-Laslop, and A. S. Mankin. 2016. 'Context-specific inhibition of translation by ribosomal antibiotics targeting the peptidyl transferase center', Proc Natl Acad Sci U S A, 113: 12150-55.

Meydan, S., J. Marks, D. Klepacki, V. Sharma, P. V. Baranov, A. E. Firth, T. Margus, A. Kefi, N. Vazquez-Laslop, and A. S. Mankin. 2019. 'Retapamulin-Assisted Ribosome Profiling Reveals the Alternative Bacterial Proteome', Mol Cell.

Mohammad, F., R. Green, and A. R. Buskirk. 2019. 'A systematically-revised ribosome profiling method for bacteria reveals pauses at single-codon resolution', Elife, 8.

Nakatogawa, H., and K. Ito. 2001. 'Secretion monitor, SecM, undergoes self-translation arrest in the cytosol', Mol Cell, 7: 185-92.

———. 2002. 'The ribosomal exit tunnel functions as a discriminating gate', Cell, 108: 629-36.

Oh, E., A. H. Becker, A. Sandikci, D. Huber, R. Chaba, F. Gloge, R. J. Nichols, A. Typas, C. A. Gross, G. Kramer, J. S. Weissman, and B. Bukau. 2011. 'Selective ribosome profiling reveals the cotranslational chaperone action of trigger factor in vivo', Cell, 147: 1295-308.

Polikanov, Y. S., N. A. Aleksashin, B. Beckert, and D. N. Wilson. 2018. 'The Mechanisms of Action of Ribosome-Targeting Peptide Antibiotics', Front Mol Biosci, 5: 48.

Polikanov, Y. S., T. A. Steitz, and C. A. Innis. 2014. 'A proton wire to couple aminoacyl-tRNA accommodation and peptide-bond formation on the ribosome', Nat Struct Mol Biol, 21: 787-93.

Roy, Raktim N., Ivan B. Lomakin, Matthieu G. Gagnon, and Thomas A. Steitz. 2015. 'The mechanism of inhibition of protein synthesis by the proline-rich peptide oncocin', Nature structural & molecular biology.

Scocchi, M., A. Tossi, and R. Gennaro. 2011. 'Proline-rich antimicrobial peptides: converging to a non-lytic mechanism of action', Cell Mol Life Sci, 68: 2317-30.

Seefeldt, A. C., M. Graf, N. Perebaskine, F. Nguyen, S. Arenz, M. Mardirossian, M. Scocchi, D. N. Wilson, and C. A. Innis. 2016. 'Structure of the mammalian antimicrobial peptide Bac7(1-16) bound within the exit tunnel of a bacterial ribosome', Nucleic Acids Res, 44: 2429-38.

Seefeldt, Carolin A., Fabian Nguyen, Stéphanie Antunes, Natacha Pérébaskine, Michael Graf, Stefan Arenz, Kishore K. Inampudi, Céline Douat, Gilles Guichard, Daniel N. Wilson, and Axel C. Innis. 2015. 'The proline-rich antimicrobial peptide Onc112 inhibits translation by blocking and destabilizing the initiation complex', Nature structural & molecular biology, 22: 470-75.

Sorensen, M. A., and S. Pedersen. 1991. 'Absolute in vivo translation rates of individual codons in Escherichia coli. The two glutamic acid codons GAA and GAG are translated with a threefold difference in rate', J Mol Biol, 222: 265-80.

Weaver, J., F. Mohammad, A. R. Buskirk, and G. Storz. 2019. 'Identifying Small Proteins by Ribosome Profiling with Stalled Initiation Complexes', MBio, 10.

Wolin, S. L., and P. Walter. 1988. 'Ribosome pausing and stacking during translation of a eukaryotic mRNA', EMBO J, 7: 3559-69.

6. CONCLUDING REMARKS

In this thesis, we present the multifaceted studies that lead us to elucidate the mechanisms of action of several representatives of the diverse group of antimicrobial peptides (AMPs), including promising candidates for new clinical antibiotics.

Just a few years ago, based on the identification of the mode of action of only a few AMPs, it was assumed that all members of this group kill bacteria by forming pores in their cell membrane, resulting in cell lysis. However, recent and current research, including that of our group, is revealing that the lytic mechanism of AMP family members is exhibited only at high concentrations. Instead, it is becoming more and more apparent that AMPs use sophisticated mechanisms that affect the functions of diverse targets located inside the bacterial cells (Li et al. 2014; Scocchi et al. 2016; Brogden 2005).

Our studies focused on two groups of non-lytic AMPs that disrupt the protein synthesis process of bacteria. Interestingly, even though the two different kinds of AMPs target the bacterial ribosome, both their binding locations and mechanisms of actions turned out to be unique and novel

A key aspect in the elucidation of the mechanistic details of the action of ODLs and PrAMPs was the application of methodologies from diverse fields of biology, biophysics, and chemistry. For instance, the identification of ODLs as peptides involved from simple microbiological tests to sophisticated NMR and de novo chemical synthesis. Then, bioinformatic analysis uncovered the gene clusters responsible for the biosynthesis of ODLs. A combination of genetic, biochemical and structural approaches revealed the ribosome as the target of ODL action, while mouse models are being used to design therapeutic treatments with ODLs to clear bacterial infections. For the PrAMP Apidaecin (Api), it was our biochemical and kinetic studies that revealed that a stable association between Api and the ribosome critically depends on the presence of a release factor in the A site of the ribosomal catalytic center. Only then it became clear that for obtaining an Api-ribosome complex sufficiently long-lived for structural studies, RF1 needed to be included during sample preparation. Although the in vitro experiments led to the model for the unique mode of Api

action, the genome-wide approach of ribosome profiling is rendering the more comprehensive view of Api as a global inhibitor of translation termination and a general agent of stop codon readthrough.

The knowledge of the molecular mechanisms of AMPs not only can influence the design of clinical strategies to combat bacterial pathogens. It can also contribute to generate novel tools to study basic principles of protein synthesis. In fact, Api has already been used to prepare high quality termination complexes, that is, ribosomes from where the new protein have been released but that, thanks to the presence of Api, remain with stably bound RF1. The ability to prepare these complexes, which are the biological substrates for the factors involved in ribosome recycling, is allowing to make significant progress in kinetic (Adio et al. 2018) and structural studies (Graf et al. 2018) to understand the roles of RF3 in translation, which have remained highly elusive. Ribosome profiling experiments of our group, that found novel start sites in the *E. coli* genome, took advantage of the action of Api to mark the stop sites of some of those newly discovered open reading frames (Meydan et al. 2019). We expect that the use of the combination of antibiotics and AMPs serving as start and stop site markers (Meydan et al. 2019; Weaver et al. 2019) will lead to unveil new genes in different bacterial species.

The special feature of AMPs, their peptidic nature, renders them highly modular. The single building blocks, natural and unnatural or modified amino acids, can be replaced by a variety of residues to improve the AMPs chemical properties and biological activities. Thus, for example, the altered structure of the single modules of the naturally occurring compound isolated from *X. nematophila* resulted in the synthetic derivative ODL NOSO-95179, which selectively targets bacterial cells without harming higher organisms. Similarly, in collaboration with the group of Terry Moore at UIC, we are currently using chemical peptide synthesis to replace single natural amino acids of the honeybee-produced PrAMP Api not only to improve its antimicrobial activity but also to create tools for biochemical, genetic and structural studies. In parallel, taking advantage of the fact that Api is encoded in the honeybee's DNA, we are introducing the Api-coding gene in

bacterial cells to create a gene library encoding hundreds of Api-variants. Interestingly, in this case, the bacterial ribosome is both, the producer and the target of the new derivatives, a screening method that has been proposed to be used for other AMPs (Charon, Manteca, and Innis 2019) . Presently, we are testing the activity of new Api-variants in different bacterial strains to understand the requirements of each of the amino acids for Api's function and to identify candidates with a broader spectrum of antimicrobial activity.

The AMPs that were the subject of our studies represent a very small fraction of the still unexplored variety of compounds generated by immune systems. More than likely, the immune systems of all higher organisms respond to microbial invasions by producing not only one, but a variety of AMPs that work synergistically. For instance, the PrAMP drosocin is part of the complex immune systems of flies (Hanson et al. 2019) and a cocktail of AMPs is been produced by goats (Panteleev et al. 2018) and bumble bees (Rahnamaeian et al. 2015).

With today's advances in sequencing techniques and a plethora of bioinformatic tools, we are well equipped for genome-wide searches to find more AMP-encoding genes. Very recently, for example, a bioinformatic genome search led to the identification of a new bacterial ribosome acting PrAMP produced by the bottlenose dolphin *Tursiops truncates* (Mardirossian et al. 2018). In a related approach, researchers are mining genomes of potential antibiotic producers for resistance genes. Those genes are important for the producer to protect itself from getting harmed by its own weapons and their identification can lead us to the actual antimicrobial compound. Notably, efficient screening of the "self-resistome" requires knowledge of the different modes of action that antibiotics can employ. Our lab contributes to this approach by identifying novel mechanisms of protein synthesis inhibition.

To put it in a nutshell, collaborative, multifaceted research applied to elucidate the molecular mechanisms of AMPs should contribute to find better antimicrobials and to uncover novel strategies to inhibit bacterial growth.

6.1 Cited Literature

Adio, S., H. Sharma, T. Senyushkina, P. Karki, C. Maracci, I. Wohlgemuth, W. Holtkamp, F. Peske, and M. V. Rodnina. 2018. 'Dynamics of ribosomes and release factors during translation termination in E. coli', Elife, 7.

Brogden, K. A. 2005. 'Antimicrobial peptides: pore formers or metabolic inhibitors in bacteria?', Nat Rev Microbiol, 3: 238-50.

Charon, J., A. Manteca, and C. A. Innis. 2019. 'Using the Bacterial Ribosome as a Discovery Platform for Peptide-Based Antibiotics', Biochemistry, 58: 75-84.

Graf, M., P. Huter, C. Maracci, M. Peterek, M. V. Rodnina, and D. N. Wilson. 2018. 'Visualization of translation termination intermediates trapped by the Apidaecin 137 peptide during RF3-mediated recycling of RF1', Nat Commun, 9: 3053.

Hanson, M. A., A. Dostalova, C. Ceroni, M. Poidevin, S. Kondo, and B. Lemaitre. 2019. 'Synergy and remarkable specificity of antimicrobial peptides in vivo using a systematic knockout approach', Elife, 8.

Li, W., J. Tailhades, N. M. O'Brien-Simpson, F. Separovic, L. Otvos, Jr., M. A. Hossain, and J. D. Wade. 2014. 'Proline-rich antimicrobial peptides: potential therapeutics against antibiotic-resistant bacteria', Amino Acids, 46: 2287-94.

Mardirossian, M., N. Perebaskine, M. Benincasa, S. Gambato, S. Hofmann, P. Huter, C. Muller, K. Hilpert, C. A. Innis, A. Tossi, and D. N. Wilson. 2018. 'The Dolphin Proline-Rich Antimicrobial Peptide Tur1A Inhibits Protein Synthesis by Targeting the Bacterial Ribosome', Cell Chem Biol, 25: 530-39 e7.

Panteleev, P. V., I. A. Bolosov, A. A. Kalashnikov, V. N. Kokryakov, O. V. Shamova, A. A. Emelianova, S. V. Balandin, and T. V. Ovchinnikova. 2018. 'Combined Antibacterial Effects of Goat Cathelicidins With Different Mechanisms of Action', Front Microbiol, 9: 2983.

Rahnamaeian, M., M. Cytrynska, A. Zdybicka-Barabas, K. Dobslaff, J. Wiesner, R. M. Twyman, T. Zuchner, B. M. Sadd, R. R. Regoes, P. Schmid-Hempel, and A. Vilcinskas. 2015. 'Insect antimicrobial peptides show potentiating functional interactions against Gram-negative bacteria', Proc Biol Sci, 282: 20150293.

Scocchi, M., M. Mardirossian, G. Runti, and M. Benincasa. 2016. 'Non-Membrane Permeabilizing Modes of Action of Antimicrobial Peptides on Bacteria', Curr Top Med Chem, 16: 76-88.

APPENDICES

APPENDIX A

Table A1: ^{1}H and ^{13}C chemical shifts of Odilorhabdin A (1296 Da) measured in water at 280 K.

Residue	Group	^{1}H (ppm)	^{13}C (ppm)
Lys[1]			
	HN		
	$C_\alpha H$	3.8	53.00
	$C_\beta H2$	1.66-1.62	30.4
	$C_\gamma H2$	1.20	21.1
	$C_\delta H2$	1.45	26.3
	$C_\varepsilon H2$	2.78	39.0
	NH2	-	
Dab(βOH)[2]			
	HN	8.83	
	$C_\alpha H$	4.28	56.3
	$C_\beta H(OH)$	3.89	67.4
	$C_\gamma H2$	2.99-2.79	41.9
	NH2	-	
Dab(βOH)[3]			
	HN	8.63	
	$C_\alpha H$	4.33	56.3
	$C_\beta H(OH)$	3.93	67.7
	$C_\gamma H2$	2.98-2.80	41.5
	NH2	-	
Gly[4]			
	HN	8.37	
	$C_\alpha H2$	3.80	42.1
Orn[5]			
	HN	8.15	
	$C_\alpha H$	4.46	51.2
	$C_\beta H2$	1.66-1.62	27.5
	$C_\gamma H2$	1.49-1.40	23.2
	$C_\delta H2$	2.74	39.0
	NH2	-	
Pro[6]			
	$C_\alpha H$	4.10	60.4
	$C_\beta H2$	1.98-1.60	29.5

	$C_{\gamma}H2$	1.72	24.3
	$C_{\delta}H2$	3.48-3.38	47.7
His[7]			
	HN	8.49	
	$C_{\alpha}H$	4.46	52.0
	$C_{\beta}H2$	3.93	67.7
	$C_{\gamma 2}H2$	2.98-2.80	41.5
	$C_{\varepsilon 1}H$	8.33	134.0
Dhl[8]			
	HN	8.41	
	$C_{\alpha}H$	4.12	53.8
	$C_{\beta}H2$	1.70	27.0
	$C_{\gamma}H2$	1.36-1.26	30.0
	$C_{\delta}H\delta$-OH	3.62	67.0
	$C_{\varepsilon}H2$	2.86-2.63	44.5
	NH2	-	
Dha[9]			
	HN	9.6	
	C_{α}	-	-
	$C_{\beta}H$	6.17	132
	$C_{\gamma}H2$	2.20	26.5
	$C_{\delta}H2$	3.10	39.5
	HN_{ε}	7.00	
	C(NH2)=NH	-	-
Dhl[10]			
	HN	8.05	
	$C_{\alpha}H$	4.06	54.0
	$C_{\beta}H2$	1.65	27.0
	$C_{\gamma}H2$	1.27	30.0
	$C_{\delta}H$-OH	3.60	67.0
	$C_{\varepsilon}H2$	2.86-2.63	44.5
Dbt[11]			
	HN	8.05	
	$C_{\alpha}H2$	2.95	39.5
	$C_{\beta}H2$	1.30	25.3
	$C_{\gamma}H2$	1.40	24.0
	$C_{\delta}H2$	2.80	39.0
	NH2		

APPENDIX A (continued)

Table A2: Minimal inhibitory concentrations (MICs) of NOSO-95179 and other translation inhibitors against *E. coli* SQ110 strain carrying indicated mutations in the 16S rRNA. NOS – NOSO-95179, TET – tetracycline, TIG – tigecycline, GEN – gentamicin, KAN – kanamycin, and CHL – chloramphenicol.

***E. coli* strain**	**Mutation**	**MIC (μg/ml)**					
		NOS	**TET**	**TIG**	**GEN**	**KAN**	**CHL**
SQ110	WT	8	1	0.25	0.25	2	8
	16S: C962A	>64	2	0.25	0.25	4	8
	16S: G973U	>64	2	0.25	0.25	2	8
	16S: G973A	>64	2	0.25	0.25	2	8
	16S: ΔU982	>64	1	0.25	0.25	2	8
	16s: A983G	64	1	0.125	0.25	2	8
	16S: ΔG1048	>64	1	0.25	0.5	4	8
	16S: U1049A	32	1	0.25	0.25	2	8
	16S: ΔG1050	>64	1	0.25	0.125	2	8
	16S: U1052A	>64	0.5	0.25	0.25	2	8
	16S: U1052G	>64	0.5	0.5	0.5	4	8
	16S: G1058C[a]	64	0.5	ND	ND	ND	ND
	16S: C1200A	64	2	0.25	0.25	2	8
	16S: C1200U	64	1	0.125	0.125	1	8
	16S:A1201G	64	1	≤0.125	0.5	4	8
	S10: H56Y	>64	2	0.25	0.5	4	8
BL21	WT[b]	32	0.125	ND	ND	ND	ND
	TetM[c]	16	16	ND	ND	ND	ND

[a] Previously engineered mutant in the SQ110 Δ*tolC* cells (Polikanov et al., 2014); MIC for TET is from the same work.
[b] BL21 cells transformed with an empty vector pET11a (Polikanov et al., 2014).
[c] BL21 cells transformed with the plasmid pET11a carrying the *tetM* gene (Polikanov et al., 2014).

APPENDIX A (continued)

Table A3: Antibacterial activity of NOSO-95179 and comparators against carbapenem-resistant *Enterobacteriaceae* strains. NOS – NOSO-95179, CTR – ceftriaxone, CIP – ciprofloxacin, GEN – genciproflo, GEN – gentamicin, IMI – imipenem, and POL – polymyxin B.

Microorganism (Strain)	Genotype	MIC (µg/mL)					
		NOS	**CTR**	**CIP**	**GEN**	**IMI**	**POL**
K. pneumoniae ATCC BAA-1904	KPC-2	8	>64	>64	32	>64	0.5
K. pneumoniae ATCC BAA-1904	KPC-3	4	>64	**0.5**	**16**	**64**	**0.5**
K. pneumoniae NCTC 13438	KPC-3	8	>64	**>64**	**2**	**>64**	**0.5**
K. pneumoniae NCTC 13439	VIM-1	4	>64	32	1	64	0.5
K. pneumoniae ATCC BAA-2146	NDM-1	4	>64	>64	>64	>64	1
K. pneumoniae ATCC BAA-2472	NDM-1	4	>64	>64	>64	>64	0.5
K. pneumoniae ATCC BAA-2473	NDM-1	4	>64	>64	>64	>64	0.5
K. pneumoniae NCTC 13443	NDM-1	**4**	**>64**	**>64**	**>64**	**>64**	**0.5**
K. pneumoniae NCTC 13442	OXA-48	4	8	8	0.25	>64	0.5
K. pneumoniae ATCC BAA-2473	OXA-48	4	>64	1	>64	>64	0.5
E. coli ATCC BAA-2340	KPC	16	>64	>64	1	32	0.5
E. coli ATCC BAA-2452	NDM-1	16	>64	<0.125	>64	>64	0.5
E. coli ATCC BAA-2469	NDM-1	16	>64	>64	>64	>64	0.5
E. cloacae ATCC BAA-2468	NDM-1	16	>64	>64	>64	>64	0.5

APPENDIX B

CHAPTER 2 as published in Molecular Cell, Volume 70, Issue 1, 5 April 2018, Pages 83-94.
"Odilorhabdins, Antibacterial Agents that Cause Miscoding by Binding at a New Ribosomal Site"
Lucile Pantel, Tanja Florin, Malgorzata Dobosz-Bartoszek, Emilie Racine, Matthieu Sarciaux, Marine Serri, Jessica Houard, Jean-Marc Campagne, Renata Marcia de Figueiredo, Camille Midrier, Sophie Gaudriault, Alain Givaudan, Anne Lanois, Steve Forst, André Aumelas, Christelle Cotteaux-Lautard, Jean-Michel Bolla, Carina Vingsbo Lundberg, Douglas L. Huseby, Diarmaid Hughes, Philippe Villain-Guillot, Alexander S. Mankin, Yury S. Polikanov, Maxime Gualtieri

How authors can use their own journal articles

Authors publishing in Elsevier journals have wide rights to use their works for teaching and scholarly purposes without needing to seek permission.

Table of Author's Rights

	Preprint version (with a few exceptions- see below *)	Accepted Author Manuscript	Published Journal Articles
Use for classroom teaching by author or author's institution and presentation at a meeting or conference and distributing copies to attendees	Yes	Yes	Yes
Use for internal training by author's company	Yes	Yes	Yes
Distribution to colleagues for their research use	Yes	Yes	Yes
Use in a subsequent compilation of the author's works	Yes	Yes	Yes
Inclusion in a thesis or dissertation	Yes	Yes	Yes
Reuse of portions or extracts from the article in other works	Yes	Yes with full acknowledgement of final article	Yes with full acknowledgement of final article
Preparation of derivative works (other than for commercial purposes)	Yes	Yes with full acknowledgement of final article	Yes with full acknowledgement of final article
Preprint servers	Yes	Yes with the specific written permission of Elsevier	No
Voluntary posting on open web sites operated by author or author's institution for scholarly purposes	Yes (author may later add an appropriate bibliographic citation, indicating subsequent publication by Elsevier and journal title)	Yes, with appropriate bibliographic citation and a link to the article once published	Only with the specific written permission of Elsevier
Mandated deposit or deposit in or posting to subject-oriented or centralized repositories	Yes under specific agreement between Elsevier and the repository	Yes under specific agreement between Elsevier and the repository**	Yes under specific agreement between Elsevier and the repository
Use or posting for commercial gain or to substitute for services provided directly by journal	Only with the specific written permission of Elsevier	Only with the specific written permission of Elsevier	Only with the specific written permission of Elsevier

** Voluntary posting of Accepted Author Manuscripts in the arXiv subject repository is permitted.

APPENDIX C

CHAPTER 3 as published in Nucleic Acids Research, Volume 44, Issue 5, 18 March 2016, Pages 2439–2450.
"Structures of proline-rich peptides bound to the ribosome reveal a common mechanism of protein synthesis inhibition"
Matthieu G. Gagnon, Raktim N. Roy, Ivan B. Lomakin, Tanja Florin, Alexander S. Mankin, Thomas A. Steitz.

Author Reuse and Self-Archiving

As an author of an Oxford University Press title, published by our Academic, Trade, Reference, Science and/or Medical books groups, there are certain rights granted to you in the area of Reuse and Self Archiving. This policy sets out the way in which you, as authors of these titles, may reuse pre and post publication versions of your work for your own teaching, publishing and self-archiving purposes, without the need to obtain written permission from OUP.

OUP is pleased to grant this permission for the following uses:

- posting on the your own personal website or in an institutional or subject based repository after a **12 month** period for **Science and Medical** titles and a **24 month** period for **Academic, Trade and Reference** titles;
- inclusion in scholarly, not-for-profit derivative reuses, (these can include the extension of your contribution to a book-length work, or inclusion in an edited collection of your own work, or any work of which you are an author or editor);
- reproduction within coursepacks or e-coursepacks for your own teaching purposes, (with the proviso that the coursepacks are not sold for more than the cost of reproduction);
- inclusion within your thesis or dissertation.

Permission for these reuses is granted on the following conditions:

- that the material you wish to reuse is your own work and has already been published by OUP;
- that the intended reuse is for scholarly purposes, for publication by a not-for-profit publisher;
- that full acknowledgement is made of the original publication stating the specific material reused [pages, figure numbers, etc.], [Title] by/edited by [Author/editor], [year of publication], reproduced by permission of Oxford University Press [link to OUP catalogue if available, or OUP website];
- In the case of joint-authored works, it is the responsibility of the authors to obtain permission from co-authors for the work to be reuse/republished.
- that reuse on personal websites and institutional or subject based repositories includes a link to the work as published in an OUP online product (e.g. Oxford Scholarship Online), and/or or to the OUP online catalogue entry; and that the material is not distributed under any kind of Open Access style licences (e.g. Creative Commons) which may affect the Licence between yourself and OUP.

APPENDIX D

CHAPTER 4 as published in Nature Structural & Molecular Biology, Volume 24, Issue 9, 24 July 2017, Pages 752-757

“An antimicrobial peptide that inhibits translation by trapping release factors on the ribosome”

Tanja Florin, Cristina Maracci, Michael Graf, Prajwal Karki, Dorota Klepacki, Otto Berninghausen, Roland Beckmann, Nora Vázquez-Laslop, Daniel N Wilson, Marina V Rodnina & Alexander S Mankin

Author Request (from Springer Nature)

VITA

Tanja Florin

EDUCATION

2015 - present	Doctoral Candidate (Medicinal Chemistry and Pharmacognosy) University of Illinois at Chicago, Chicago, IL
2012 - 2015	M. S. (Biochemistry and Molecular Biology) University of Potsdam, Germany
2008 - 2011	B. Eng. (Biotechnology) University of Applied Sciences Jena, Germany

PUBLICATIONS

Pantel L, **Florin T**, Dobosz-Bartoszek M, Racine E, Sarciaux M, Serri M, Houard J, Campagne JM, de Figueiredo RM, Midrier C, Gaudriault S, Givaudan A, Lanois A, Forst S, Aumelas A, Cotteaux-Lautard C, Bolla JM, Vingsbo Lundberg C, Huseby DL, Hughes D, Villain-Guillot P, Mankin AS, Polikanov YS, Gualtieri M (2018). Odilorhabdins, Antibacterial Agents that Cause Miscoding by Binding at a New Ribosomal Site. *Molecular Cell 70*, 83–94.e7.

Highlighted in: Preview: A much needed boost for the dwindling antibiotic pipeline (*Molecular Cell*)

Florin T, Maracci C, Graf M, Karki P, Klepacki D, Berninghausen O, Beckmann R, Vázquez-Laslop N, Wilson DN, Rodnina MV, Mankin AS (2017). An antimicrobial peptide that inhibits translation by trapping release factors on the ribosome, *Nature Structural & Molecular Biology* 24(9):752-757

Gagnon MG, Roy RN, Lomakin IB, **Florin T**, Mankin AS & Steitz TA (2016). Structures of proline-rich peptides bound to the ribosome reveal a common mechanism of protein synthesis inhibition. *Nucleic Acids Research* 44(5):2439-50.

Orelle C, Carlson ED, Szal T, **Florin T**, Jewett MC & Mankin AS (2015). Protein synthesis by ribosomes with tethered subunits. *Nature* 524: 119-124

Highlighted in: Molecular Biology: inseparable ribosomes (*Nature Methods*) & Synthetic Biology: Ribosomal ties that bind. (*Nature*)

Kannan K, Kanabar P, Schryer D, **Florin T**, Oh E, Bahroos N, Tenson T, Weissman JS & Mankin AS (2014). The general mode of translation inhibition by macrolide antibiotics. *Proceeding of the National Academy of Sciences of the United States of America* 111: 15958–63

RESEARCH EXPERIENCE

Ph.D. Thesis Project — Mar 2016 – present
University of Illinois at Chicago, Chicago, IL
Title: Antimicrobial peptides and their mechanisms of protein synthesis inhibition
Advisors: Drs. Alexander Mankin and Nora Vázquez-Laslop

Pre-doctoral Training — Apr 2015 – Jul 2015
University of Illinois at Chicago, Chicago, IL
Studying the mode of inhibition of different proline-rich antimicrobial peptides
Advisors: Drs. Alexander Mankin and Nora Vázquez-Laslop

Master's Thesis Project — May 2014 – Dec 2014
University of Illinois at Chicago, Chicago, IL
Thesis: An Orthogonal Tethered Ribosome as a Tool for the Investigation of the Role of Functionally Critical Nucleotides in the Peptidyl Transferase Center
Advisor: Dr. Alexander Mankin

Research Assistant — Oct 2013 – Apr 2014
University of Potsdam, Potsdam, Germany
Development of an expression system based on yeast artificial chromosomes
Advisor: Dr. Katrin Messerschmidt

Student Internship — Feb 2014
Fraunhofer Institute for Biomedical Engineering, Golm, Germany
Lighthouse project Cell-free Bioproduction
Training in techniques of cell-free protein synthesis
Advisor: Dr. Stefan Kubick

Research Internship — Jul 2013 – Sep 2013
University of Illinois at Chicago, Chicago, IL
Investigation of the general mode of action of macrolide antibiotics
Advisor: Dr. Alexander Mankin

Bachelor's Thesis Project — Apr 2011 – Nov 2011
In.vent Diagnostica GmbH, Hennigsdorf, Germany in cooperation with
Charité Institute for Rheumatology and Clinical Immunology, Berlin, Germany
Thesis: Optimization of the Purification of the Autoimmune-Biomarker PPP2R1A for the Development of a Diagnostic Assay in the Field of Rheumatoid Arthritis
Advisors: Dr. Karl Skriner and Anja Gräfe

Student Assistant — Jun 2010 – Jan 2011
University of Applied Sciences Jena, Germany
Analysis of different black tea compounds using GC/MS and data interpretation
Advisors: Drs. Karl-Heinz Feller and Christine Bartzsch

ORAL PRESENTATIONS

Apr 2017 — American Society for Biochemistry and Molecular Biology (ASBMB) Annual Meeting, Chicago, IL
An antimicrobial peptide that turns the ribosome into a release factor trap

Mar 2017 — Center for Biomolecular Sciences Positive Thinking Seminars, University of Illinois at Chicago, IL
Mechanisms of antimicrobial peptides to inhibit ribosomal functions

Sep 2016 — Graduate Women in Science (GWIS) Eta Chapter, Chicago Science Talk, Chicago, IL
Apidaecin – An antimicrobial peptide with a unique mode of action

Jan 2016 — Chicago RNA Club, University of Chicago, Chicago, IL
Ribosome-targeting antimicrobial peptide inhibits translation termination at preferred stop codons

POSTER PRESENTATIONS

Feb 2019 — College of Pharmacy Research Day, University of Illinois at Chicago, Chicago, IL
Global analysis of protein synthesis arrest induced by the translation termination inhibitor apidaecin (Florin T, Klepacki D, Kefi A, Vázquez-Laslop N, Mankin AS)

Jan 2019 — 2019 Ribosome, Structure and Function, Mérida, Mexico
Global analysis of protein synthesis arrest induced by the termination inhibitor apidaecin (Florin T, Klepacki D, Kefi A, Vázquez-Laslop N, Mankin AS)

Feb 2018 — College of Pharmacy Research Day, University of Illinois at Chicago, Chicago, IL

Global analysis of protein synthesis arrest induced by the translation termination inhibitor apidaecin (Florin T, Klepacki D, Kefi A, Vázquez-Laslop N, Mankin AS)

Oct 2017 Rustbelt RNA meeting, Indianapolis, IN
Global analysis of protein synthesis arrest induced by the translation termination inhibitor apidaecin (Florin T, Klepacki D, Kefi A, Vázquez-Laslop N, Mankin AS)

Sep 2017 EMBO Conference: Protein Synthesis and Translational Control, Heidelberg, Germany
Global analysis of protein synthesis arrest induced by the translation termination inhibitor apidaecin (Florin T, Klepacki D, Kefi A, Vázquez-Laslop N, Mankin AS)

Aug 2017 Riback/SURF summer research mini-symposium, University of Illinois at Chicago
Novel strategy to study the mechanism of action of apidaecin, an antimicrobial peptide that traps release factors (Colón S, Florin T, Vázquez-Laslop N, Mankin AS)

May 2017 Molecular Biology Research Building (MBRB) Research Day, University of Illinois at Chicago
An antimicrobial peptide that turns the ribosome into a release factor trap (Florin T, Maracci C, Graf M, Karky P, Rodnina M, Wilson D, Vázquez-Laslop N, Mankin AS)

Apr 2017 MIKI Medicinal Chemistry Meeting, University of Minnesota, Minneapolis, MN
An antimicrobial peptide that turns the ribosome into a release factor trap (Florin T, Maracci C, Graf M, Karky P, Rodnina M, Wilson D, Vázquez-Laslop N, Mankin AS)

Feb 2017 College of Pharmacy Research Day, University of Illinois at Chicago, Chicago, IL
An antimicrobial peptide that turns the ribosome into a release factor trap (Florin T, Maracci C, Graf M, Karky P, Rodnina M, Wilson D, Vázquez-Laslop N, Mankin AS)

Oct 2016 Rustbelt RNA Meeting, Cleveland, OH
Ribosome-targeting antimicrobial peptide exhibits a unique mode of inhibition of translation (Florin T, Maracci C, Karky P, Rodnina M, Vázquez-Laslop N, Mankin AS)

Jul 2016 EMBO Conference on Ribosome Structure and Function, Strasbourg, France
Ribosome-targeting antimicrobial peptide inhibits translation termination by interfering with peptide release (Florin T, Klepacki D, Vázquez-Laslop N, Mankin AS)

Apr 2016 MIKI Medicinal Chemistry Meeting, University of Iowa, Iowa City, IA
Proline-rich antimicrobial peptide apidaecin exhibits a unique mode of inhibition of translation (Florin T, Vázquez-Laslop N, Mankin AS)

Feb 2016 College of Pharmacy Research Day, University of Illinois at Chicago, Chicago, IL
Proline-rich antimicrobial peptide apidaecin exhibits a unique mode of inhibition of translation (Florin T, Vázquez-Laslop N, Mankin AS)

Oct 2015 Chicago Biomedical Consortium Symposium, Chicago, IL
Proline-rich antimicrobial peptide apidaecin exhibits a unique mode of inhibition of translation (Florin T, Vázquez-Laslop N, Mankin AS)

AWARDS, GRANTS & FELLOWSHIPS

2019, 2017, 2016 Student Presenter Award, Graduate College, University of Illinois at Chicago, Chicago, IL

2019, 2017, 2016 Travel Award, Graduate Student Council, University of Illinois at Chicago, Chicago, IL

Dec 2018 Travel Award for Ph.D. Students (TAPS), College of Pharmacy, University of Illinois at Chicago, Chicago, IL

Feb 2018 Charles Wesley Petranek Memorial Scholarship, College of Pharmacy, University of Illinois at Chicago, Chicago, IL

May 2017 1st Place Poster Award, Category Biomolecules and Structural Biology, MBRB Research Day, University of Illinois at Chicago, Chicago, IL

May 2017-May 2018 Full scholarship for Ph.D. students (DAAD, German Academic Exchange Service)

Feb 2017	Horizon Award for Excellence in Research, Scientific Poster Session Award Winner, 2nd Place, Biology Category at College of Pharmacy's 2017 Research Day, University of Illinois at Chicago
2013 - 2014	Program for the enhancement of mobility of German students (PROMOS) Scholarship (DAAD, German Academic Exchange Service)

SERVICE & SCIENCE OUTREACH

Apr 2019	Workshop Coordinator and Mentor for Science Explorers Program (Northwestern University) visiting the Mankin/Vázquez-Laboratory, UIC
Apr 2019	Workshop assistant for Science Night at Christopher Elementary School, Chicago, IL
Mar 2019	Workshop assistant at Expanding Your Horizons Chicago, UIC
Oct 2019	Participation at the German Academic Exchange Service (DAAD) alumni meeting in Atlanta, GA: *Knowledge, Trust and the Future of Democracy: Transatlantic Perspectives on the Role of Scholarship and Science in Society*
July 2018-present	Mentor of a scholar of the Portal to Biomedical Research Careers Postbaccalaureate Research Education Program at UIC (UIC PBRC PREP) in the Mankin laboratory, UIC
May 2018-May 2019	Mentor for incoming international students as part of the First Friend program of the Office of International Services, UIC
Apr 2018	Volunteer for Taste of Science Chicago
Mar 2018	Workshop assistant at Expanding Your Horizons (University of Chicago, Chicago, IL)
Mar 2018	Judge at Chicago Science Fair (Museum of Science and Industry, Chicago, IL)
Oct 2017-May 2019	Mentor of a UIC Honors College's Biology undergraduate student in the Mankin laboratory, UIC
Aug 2017	Judge at Riback/SURF summer research mini-symposium, UIC
Jun 2017-April 2018	Chair of the poster session committee for the student-organized Medicinal Chemistry Meeting MIKI at UIC in Chicago, IL
Jun - Aug 2017	Mentor of an undergraduate student in the Mankin laboratory as part of the Summer Undergraduate Research Fellowship (SURF) program of the College of Pharmacy, UIC
Jan - Apr 2017	Mentor of a high school student intern in the Mankin laboratory, UIC
Aug 2016 - present	Coordinator of weekly seminar series (Center for Biomolecular Sciences, UIC, Chicago, IL)
Mar 2016	Judge at Chicago Science Fair (Museum of Science and Industry, Chicago, IL)
Jan 2016 - Mar 2019	Mentor for Science Club weekly afterschool program, Science in Society (True Value Boys and Girls Club, Chicago, IL)
Jan 2016	Judge at AVI-3 Regional Network Science Fair, Chicago, IL
Aug 2015-May 2017	Teaching Assistant for the course Principles of Drug Action and Therapeutics, UIC
Dec 2015	Judge at Science Fair at Mark T. Skinner Fine Art & Technology School, Chicago, IL

MEMBERSHIPS

2019 - present	American Association for the Advancement of Science (AAAS)
2015 - present	Graduate Women in Science (GWIS), Eta chapter, Chicago
2010 - present	Biotechnological Students Association, Germany